

Design and Characterization of a Dual Electro-Hydrostatic Actuator

A Thesis Submitted to
the School of Graduate Studies
in Partial Fulfillment of the Requirements
for the Degree of Master of Applied Science
in the Department of Mechanical Engineering,
McMaster University, Hamilton
Canada

By

Kevin Ronald McCullough

MASTER OF APPLIED SCIENCE (2011)

McMaster University

(Mechanical Engineering)

Hamilton, On

TITLE: Design and Characterization of a Dual Electro-Hydrostatic Actuator

AUTHOR: Kevin McCullough, B.Eng.Mgmt. (McMaster University)

SUPERVISOR: Professor S.R. Habibi

NUMBER OF PAGES: xviii, 170

Permission to Use

In presenting this thesis in partial fulfillment of the requirements for a Postgraduate degree from McMaster University, I agree that the Libraries of this University may make it freely available for inspection. I further agree that the permission for copying this thesis in any manner, in whole or in part for scholarly purposes, may be granted by the professors who supervised my thesis work or, in their absence, by the Head of the Department or the Faculty Dean in which my thesis work was conducted. It is understood that any copying or publication or use of this thesis or parts thereof for financial gain shall not be allowed without my written permission. It is also understood that due recognition shall be given to me and McMaster University in any scholarly use which may be made of any material in my thesis. Requests for permission to copy or to make other use of material in this thesis, in whole or part, should be addressed to:

Head of the Department of Mechanical Engineering
McMaster University
Faculty of Engineering
1280 Main Street West
Hamilton, Ontario L8S 4L6
Canada

Abstract

Actuation of flight surfaces in aircraft have evolved over the last century from systems using simple mechanical linkages actuated by the pilot to complex electronic systems that maneuver large loads and have some form of redundancy. The latest form of flight surface actuation uses Power-By-Wire (PBW) systems, which are modulated, lean and fault tolerant actuators embedded in the flight surface that require only the attachment of power and control wires. This research will focus on a specific form of PBW system called an Electro-Hydrostatic Actuator (EHA), which is seen on modern aircraft such as the Lockheed F-35 Lightning and the Airbus A380.

An EHA is a closed-loop form of hydraulic system which controls an actuator's movement by routing fluid to it via a fixed-displacement pump attached to a servomotor. The two primary components of the EHA's hydraulic circuit are a bi-directional external gear pump and an actuator, but the system incorporates an accumulator, a bi-directional relief valve, a by-pass valve and a series of check valves for full functionality. The minimal components and the closed-loop architecture lend itself to be lightweight, modular and independent of other hydraulic systems on an aircraft.

This research will focus on developing a design based on a dual EHA system used for the rudder of the F-35. The design objective is to reduce the comparative weight. The dual EHA allows for continued actuation of the airfoil in the event that one of the EHA's malfunction. The design produced in this research incorporates a new inner-circuit which allowed the system to be 12% lighter than the F-35 rudder EHA. A prototype developed from this design was produced but was augmented with additional components that allow for simulation of fault conditions in the future. With a prototype produced several experiments were performed to determine the level of internal leakage and damping inside the system. Experiments showed that internal leakage increases linearly with the increase of back pressure on the pump and that the bulk of the leakage occurs at the pump itself. Experiments also showed that the damping in the system is non-linear and that it is best described by a LuGre friction model.

Black-box system identification techniques were applied to the EHA to determine piece-wise linear models. These trials showed that the non-linear friction as well as the seals in the actuator forced the system to have two major piece-wise linear regions. These experiments also showed that when the mean velocity of the actuator increases so does the system bandwidth.

Enclosed in this dissertation are details of the design of the dual EHA and the experimental results performed on it.

Acknowledgements

The author would like to express his gratitude to his supervisor, Dr. S.R. Habibi, for his guidance, advice and support during the course of this research and the writing of this dissertation. The technical assistance provided by Mr. Ron Lodewyks, Mr. Mark Mackenzie, Mr. Jim McLaren, Mr. J.P. Talon and Mr. Joseph Verhaeghe is also greatly appreciated.

Financial support provided by the School of Graduate Studies, the Department of Mechanical Engineering and the Ontario Government's Graduate Scholarship Program is acknowledged.

Special gratitude must be conveyed to fellow graduate students Andrew Gadsden and Mohammed El-Sayed for their assistance, technical expertise and support during this research.

I would also like to express my gratitude to my family, friends and girlfriend Allison for their encouragement and support.

Table of Contents

Permission to Use.....	ii
Abstract	iii
Acknowledgements	v
List of Figures	iv
List of Tables	ix
Nomenclature	x
Chapter 1 Introduction	1
1.1 Preliminary Remarks.....	1
1.2 Research Objectives.....	2
1.3 Thesis Outline	3
Chapter 2 Conventional Flight Surface Actuator Systems.....	4
2.1 Flight Controls on an Aircraft	4
2.2 Using Mechanical Linkages for Flight Surface Actuation	5
2.3 Flight Surface Actuation using Hydraulic Systems.....	7
2.3.1 Hydraulic Systems using Mechanical Linkages	7
2.3.2 Hydraulic Systems using Fly-By-Wire (FBW) Technology	10
2.4 Flight Surface Actuation using Power-by-Wire (PBW) Systems	21
2.4.1 Electro-Mechanical Actuators (EMA)	23
2.5 Conclusion	28
Chapter 3 Hydrostatic Actuation Systems	29
3.1 Variable-Displacement Piston Pump Hydrostatic Actuation Systems	29
3.2 Electro-Hydrostatic Actuator (EHA)	36
3.2.1 EHA Mathematical Model	37
3.2.2 EHA Advantages and Disadvantages.....	55
3.3 Conclusion	55
Chapter 4 Design of a dual Electro-Hydrostatic Actuator	56
4.1 Dual Electro-Hydrostatic Actuator	56

4.2 Dual Electro-Hydrostatic Actuator Specifications.....	57
4.3 Dual Electro-Hydrostatic Actuator Prototype Circuit Architecture	59
4.4 Dual Electro-Hydrostatic Actuator Design Process.....	60
4.5 Physical Design of the Dual Electro-Hydrostatic Actuator	66
4.6 Physical Design of the Dual Electro-Hydrostatic Actuator Prototype.....	73
4.6.1 System Reservoir and Filter Circuit (Assembly 1)	78
4.6.2 External Leakage Circuit (Assembly 2)	78
4.6.3 Variable Bulk Modulus External Circuit (Assembly 3)	79
4.6.4 Charging Circuit (Assembly 4)	81
4.6.5 Offline Rectifying Filtration Circuit (Assembly 5).....	83
4.6.6 Axis A and B Connect Valves (Assembly 6).....	84
4.6.7 Axis A and B Blocking Valves (Assembly 7).....	84
4.6.8 Axis A and B Throttling Valves (Assembly 8).....	85
4.7 Finite Element Analysis of the Dual Electro-Hydrostatic Actuator	89
4.8 Servomotor Drive Amplifier and System Controller	95
4.9 Conclusion	97
Chapter 5 Experimental Determination of EHA Parameters	98
5.1 Verification of the Hydraulic Gain	98
5.2 Determination of the Overall Leakage Coefficient	99
5.3 Determination of the Cylinder Damping Coefficient	103
5.4 Determination of the EHA Bulk Modulus.....	111
5.5 Review.....	113
5.6 Conclusion	114
Chapter 6 EHA System Identification	115
6.1 System Identification Theory.....	115
6.2 System Identification Initial Tests.....	119
6.3 System Identification of the Servomotor	127
6.4 System Identification of the Combined EHA System	132
6.5 Review.....	142
6.6 Conclusion	143
Chapter 7 Control of the Electro-Hydrostatic Actuator.....	144
7.1 State Conversion for Feedback Purposes.....	144

7.1.1 Design of an IIR filter	144
7.2 Design of a Closed-Loop Controller	147
7.3 Conclusion	148
Chapter 8 Conclusions and Recommendations	149
8.1 Summary	149
8.2 Outcomes	149
8.3 Conclusions.....	151
8.4 Recommendations for Future Research.....	151
References	153
Appendix A – Description of Electrical Components and Full Electrical Diagram of the Siemens Servodrive	156
A.1 Sensors Used for System Analysis	156
A.1.1 Differential Pressure Transducer	156
A.2.1 Noise Characteristics of the Rotary Encoder	160
A.2.3 Differential Pressure Noise Characteristics	163
A.3 Data Acquisition Cards (DAQ)	164
A.3.1 National Instruments PCI-6229 Multifunction DAQ	164
A.3.2 Measurement Computing PCI-QUAD04 Encoder DAQ	164
A.3.3 Siemens PCI-Profibus Interface Card	165
A.4 EHA Electrical Circuit Diagram.....	165
Appendix B – Additional Friction and Internal Leakage Data	167

List of Figures

Figure 2.1. Primary and secondary flight surfaces for the Boeing 777 [2].	4
Figure 2.2. Airplane controls, movement and axes of rotation [1].	5
Figure 2.3. Flight surface actuation using mechanical linkages.	6
Figure 2.4. Examples of hydraulic actuators with mechanical linkages for flight surface actuation [4].	8
Figure 2.5. Fly-By-Wire flight surface actuation system [4].	10
Figure 2.6. Layout of a common servo valve [6].	11
Figure 2.7. Simplified servovalve block diagram [6].	12
Figure 2.8. Block diagram incorporating the dynamics of a servo valve spool.	17
Figure 2.9. Spool valve, actuator and load configuration [7].	18
Figure 2.10. Closed-loop hydraulic block diagram for a servovalve controlled actuator.	19
Figure 2.11. Hydraulic system network on the Boeing 767 [8].	20
Figure 2.12. Layout of power-by-wire systems in a commercial aircraft [11].	22
Figure 2.13. Basic Structure of a power-by-wire system.	23
Figure 2.14. Basic Structure of an EMA.	24
Figure 2.15. An EMA for high-power flight controls [13].	24
Figure 2.16. Electrical motor block diagram.	26
Figure 2.17. Closed-loop servomotor block diagram.	26
Figure 2.18. Closed-loop EMA control block diagram [12].	27
Figure 3.1. Hydrostatic actuation system.	29
Figure 3.2. Dynamically significant components of a hydrostatic system.	30
Figure 3.3. Forces acted upon a swash plate in an axial piston pump [15].	33
Figure 3.4. Variable-displacement piston pump hydrostatic actuation system control block diagram [15].	35
Figure 3.5. TRW Aeronautical Systems variable-displacement piston pump PBW flight surface actuator [13].	35
Figure 3.6. Schematic of the Electro-Hydrostatic Actuator (EHA) [16].	36
Figure 3.7. Deadband effect in the pump and motor in the EHA [18].	42
Figure 3.8. Representation of equation 3.26.	43
Figure 3.9. Block diagram of Inner-loop control strategy.	43
Figure 3.10. Closed-loop diagram of hydraulic system with flow as the input and velocity as the output.	52
Figure 3.11. Closed-loop diagram of hydraulic system with motor speed as the input and position as the output.	52
Figure 3.12. Closed-loop diagram of the overall system.	53
Figure 3.13. Block diagram or EHA control strategy	53

Figure 4.1. Depiction of the Parker Aerospace F-35 Rudder EHA [23]	58
Figure 4.2. Surface architecture of the Parker Aerospace F-35 Rudder EHA [23].....	58
Figure 4.3. Circuit architecture of the dual EHA prototype.	59
Figure 4.4. Hawe RKO check valve [26].....	64
Figure 4.5. Hawe RB2 check valve [26].....	65
Figure 4.6. Hawe AC13 Accumulator [27].....	65
Figure 4.7. Hydraforce CR10-28 Pressure Relief Valve.....	65
Figure 4.8. Hydraforce SV08-24 By-Pass Valve [28].	66
Figure 4.9. Inner circuit housing component.....	67
Figure 4.10. Inner circuit housing component.....	68
Figure 4.11. Pump housing component, front view and back view	69
Figure 4.12. Pump housing component, front view and back view	70
Figure 4.13. Inner circuit housing sandwiched between the two pump housings.	71
Figure 4.14. Dual EHA minus the actuators	72
Figure 4.15. Dual EHA assembly.....	72
Figure 4.16. Siemens 1FK7080-5AF71-1AG2 servomotor.....	74
Figure 4.17. R+W America BK2/60/83 shaft coupling [30].	75
Figure 4.18. Pump-servomotor interface with coupling.....	75
Figure 4.19. Higginson MH2511400BXN12D double rod, double acting actuator.....	76
Figure 4.20. Complete hydraulic circuit diagram of the dual EHA prototype.....	77
Figure 4.21. System reservoir and filter.	78
Figure 4.22. External Leakage Circuit.	79
Figure 4.23. External Bulk Modulus Circuit.....	80
Figure 4.24. Charging circuit.	82
Figure 4.25. Rectified filtration circuit.....	83
Figure 4.26. Axis A and B connect valves.....	84
Figure 4.27. Axis A blocking valve.	85
Figure 4.28. Axis A throttling assembly.	86
Figure 4.29. Axis B throttling assembly.	87
Figure 4.30. Complete dual EHA with all peripherals.....	87
Figure 4.31. Load (in red) and constraints (in blue) for the inner circuit.	90
Figure 4.32. Applied loads on the pump housing.....	90
Figure 4.33. Constraints on the pump housing.	91
Figure 4.34. Load (in red) and constraints (in blue) on the hatch.	91
Figure 4.35. Inner circuit mesh.	92
Figure 4.36. Pump housing mesh.	92
Figure 4.37. Hatch mesh.	93
Figure 4.38. Stress distribution in the inner circuit.	93
Figure 4.39. Stress distribution in the pump housing.	94
Figure 4.40. Hatch stress distribution.....	94
Figure 4.41. Dual EHA electrical and control configuration.	97

Figure 5.1. Measured actuator velocity vs. pump velocity.....	99
Figure 5.2. Schematic of setup used to determine the overall pump leakage.....	100
Figure 5.3. Flow vs. pressure at a pump speed of 1000rpm for Axis A	101
Figure 5.4. Leakage vs. pressure at a pump speed of 1000rpm for Axis A.....	101
Figure 5.5. Volumetric efficiency vs. pressure at a pump speed of 1000rpm for Axis A.....	102
Figure 5.6. Leakage areas of an external gear pump.....	103
Figure 5.7. Friction interface between two surfaces at the microscopic level [35].....	105
Figure 5.8. Static friction vs. velocity of actuator with no load for the axis A forward operating mode.	107
Figure 5.9. Actuator friction vs. velocity for the axis A forward operating mode.....	108
Figure 5.10. Actuator friction vs. velocity for Axis A forward operating mode.	109
Figure 5.11. Actuator friction vs. velocity for Axis A reverse operating mode.....	110
Figure 5.12. Effect of entrapped air on the bulk modulus of a hydraulic system [37].	112
 Figure 6.1. ARX model structure.	116
Figure 6.2. ARMAX model structure.....	117
Figure 6.3. Box-Jenkins model structure.	117
Figure 6.4. Output Error model structure.....	117
Figure 6.5. Break frequency test ETFE for the servomotor.....	120
Figure 6.6. Break frequency test ETFE for the combined EHA system.	121
Figure 6.7. ETFE's for the servomotor using different input levels. Used to determine the highest input voltage range before saturation effects occur.....	122
Figure 6.8. ETFE's for the combined EHA using different input levels. Used to determine the highest input voltage range before saturation effects occur.....	122
Figure 6.9. ETFE's to determine the piece-wise linearity of the motor.....	123
Figure 6.10. ETFE's to determine the piece-wise linearity of the combined system.	124
Figure 6.11. a) SVD and b) ARX-structure order estimates of the servomotor.....	125
Figure 6.12. a) SVD and b) ARX-structure order estimates of the combined system.	125
Figure 6.13. ETFE and Output Error model of the servomotor.	128
Figure 6.14. System response and model response for a 3V (94.2rad/sec) step input for the servomotor.	129
Figure 6.15. System response and model response for a $\pm 1.5V$ ($\pm 47.1\text{rad/s}$) chirp input for the servomotor.	129
Figure 6.16. System and model response for a chirp input between 0-2 seconds.	130
Figure 6.17. System and model response for a chirp input between 5.5-6 seconds.	130
Figure 6.18. System and model response for a chirp input between 12.25-12.5 seconds.....	131
Figure 6.19. System and model response for a sawtooth input of 20Hz with a magnitude between 0-94.2rad/sec.	131
Figure 6.20. ETFE and Output Error model of the first piecewise linear region of the combined system.	133
Figure 6.21. Chirp input response showing the system operating in the deadband of the first piecewise linear region.	133

Figure 6.22. System and model response for the low velocity linear range in the combined system.....	134
Figure 6.23. System response and model response for a $\pm 1.5V$ ($1.71E-2m/s$) chirp input for the combined system low velocity linear region.....	135
Figure 6.24. System response and model response for a $\pm 1.5V$ ($1.71E-2m/s$) chirp input for the combined system low velocity linear region, 0-2 seconds.....	135
Figure 6.25. System response and model response for a $\pm 1.5V$ ($1.71E-2m/s$) chirp input for the combined system low velocity linear region, 3-4 seconds.....	136
Figure 6.26. System response and model response for a $\pm 1.5V$ ($1.71E-2m/s$) chirp input for the combined system low velocity linear region, 4.5-5 seconds.....	136
Figure 6.27. System response and model response for a sawtooth input of 16Hz with a magnitude between $\pm 1.5V$ ($1.71E-2m/s$).	137
Figure 6.28. ETFE and Output Error model for the high velocity linear region for the combined system.	138
Figure 6.29. System and model step response for the high velocity linear range in the combined system.	139
Figure 6.30. System and model chirp response for the high velocity linear range in the combined system.	139
Figure 6.31. System and model chirp response for the high velocity linear range in the combined system, 0-1 seconds.	140
Figure 6.32. System and model chirp response for the high velocity linear range in the combined system, 1.75-2 seconds.	140
Figure 6.33. System and model chirp response for the high velocity linear range in the combined system, 2.5-2.75 seconds.	141
Figure 6.34. System and model sawtooth response for the high velocity linear range in the combined system.....	142
 Figure 7.1. Bode plot for a lowpass Butterworth filter with a bandwidth of 350rad/sec.	146
Figure 7.2. Step input and response for a proportional controller.	147
Figure 7.3. Resultant velocity of the step response shown in figure 7.2.....	148
 Figure A.1. Differential pressure transducer attached to the actuator.....	156
Figure A.2. Omegadyne PX80B0-1KDI differential pressure transducer.	157
Figure A.3. Principle components of a linear encoder [43].	159
Figure A.4. Fagor MX-35-5 encoder with linear rail and actuator shaft coupling.....	160
Figure A.5. Rotary encoder velocity signal using 3V (94.24rad/sec) step input.	161
Figure A.6. Power spectral density of the rotary encoder velocity signal.	161
Figure A.7. Linear Encoder velocity signal using 3V ($3.41E-2m/s$) step input.....	162
Figure A.8. Power spectral density of the linear encoder velocity signal.....	162
Figure A.9. Measurement noise in the differential pressure transducer.	163

Figure A.10. Power spectral density of the measurement noise in the differential pressure transducer.....	163
Figure A.11. National Instruments PCI-6229 multi-function data acquisition card.	164
Figure A.12. Measurement Computing PCI-QUAD04 encoder data acquisition card.	165
Figure A.13. Siemens PCI-Profibus Interface Card.	165
Figure A.14. EHA electrical diagram.	166
Figure B.1. Static friction vs. velocity for Axis A reverse operating mode.	167
Figure B.2. Static friction vs. velocity for Axis B forward operating mode.	167
Figure B.3. Static friction vs. velocity for Axis B reverse operating mode.	168
Figure B.4. Actuator friction force vs. velocity for Axis B forward operating mode.	168
Figure B.5. Actuator friction vs. velocity for Axis B reverse operating mode.	169
Figure B.6. Volumetric flow vs. pressure for axis B.	169
Figure B.7. Leakage flow vs. pressure for axis B.	170
Figure B.8. Volumetric Efficiency vs. pressure for axis B.	170

List of Tables

Table 4.1. Potential faults in the EHA and corresponding flight surface [22].....	57
Table 4.2. Specifications of the Parker Aerospace F35 Rudder EHA [23].....	58
Table 4.3. Annealed 15-5PH stainless steel material properties [24]	61
Table 4.4. Specifications for the Infranor ICM-14N servomotor [25].....	63
Table 4.5. Resultant specifications form dual EHA design process.....	66
Table 4.6. Description of inner circuit housing.	67
Table 4.7. Inner circuit housing components.....	68
Table 4.8. Pump housing component description.	69
Table 4.9. Pump housing assembly components.	70
Table 4.10. Breakdown of the mass of the Dual EHA designed for comparison against the F-35 Rudder EHA.	73
Table 4.11. Specifications for the 1FK7080-5AF71-1AG2 servomotor [29].	74
Table 4.12. Dual EHA added components and sub-assemblies.	77
Table 4.13. System reservoir and filter components.	78
Table 4.14. External Leakage Circuit Components.....	79
Table 4.15. External Bulk Modulus Circuit Components.	81
Table 4.16. Charging circuit components.	82
Table 4.17. Rectifier circuit components.	83
Table 4.18. Axis A and B connect valve components.	84
Table 4.19. Axis A throttling assembly components.	86
Table 4.20. Axis B throttling assembly components.	87
Table 4.21. EHA parameters determined by design.....	88
Table 5.1. Static friction and standard deviation for all operating modes.	107
Table 5.2. LuGre friction parameters for all operating modes.	110
Table 5.3. Experimental EHA parameters for both Axes.	113
Table 6.1. Delay and deadband of the servomotor and combined system.....	125

Nomenclature

A	Piston surface area (m^2)
A_s	Servovalve spool end area (m^2)
A_p	Cross-sectional area of a piston in a variable-displacement piston pump (m^2)
A_i	Actuator shaft cross-sectional area (m^2)
a_{n-1} to a_1	Lowpass Butterworth filter continuous transfer function exponents
B	System damping (Ns/m)
$B_{A,For}$	EHA axis A damping coefficient in the forward direction (Ns/m)
$B_{A,Rev}$	EHA axis A damping coefficient in the reverse direction (Ns/m)
$B_{B,For}$	EHA axis B damping coefficient in the forward direction (Ns/m)
$B_{B,Rev}$	EHA axis B damping coefficient in the reverse direction (Ns/m)
c_p	Partial derivative of the load flow with respect to the load pressure
c_x	Partial derivative of the load flow with respect to the spool position
C_{ep}	Leakage flow to the case drain (m^3/sPa)
c_v	Loss factor for viscous friction
c_c	Coulombic friction coefficient
D_{couple}	EMA dynamic coupling term
D_p	Pump volumetric displacement (m^3/rad)
D_{pv}	Instantaneous variable-displacement pump volumetric displacement (m^3/rad)
D	Inner diameter of the pipe (m)
d_i	Piston shaft diameter (m)
d_o	Piston head diameter (m)
d_{io}	Maximum allowable diameter of the inlet/outlet ports (m)

e	Error input
F	Loading force (N)
F_{ap}	Applied force (N)
f	Dimensionless pipe friction factor
F_n	Required actuator force (N)
F_s	Static friction (N)
F_c	Coulombic friction (N)
F_v	Viscous friction (N)
F_f	Friction force (N)
F_{fss}	Steady-state actuator friction (N)
f	System output
f'	Output derivative
G_1	Servomotor electrical transfer function
G_2	Servomotor mechanical transfer function
G_{me}	Transfer function for EMA servomotor dynamics
G_{load}	System load transfer function
G_b	EMA deadzone gain
G_c	Transfer function that converts positional error into a velocity error
G_T	EMA Backlash compliance transfer function
G_{inner}	EMA inner-loop transfer function
G_s	Variable-displacement pump control gain
G_p	Variable-displacement pump gain (m^3/srad)
G_{PI}	Inner-loop proportional-integral controller
$g(\dot{x})$	Stribeck friction function

H	Converts the feedback position into feedback velocity in the EMA
H_a	Hankel matrix
i	Input current to the servovalve (A)
Im	Impulse response
J	Lowpass Butterworth filter response magnitude
J_m	Servomotor rotary inertia (Kg/m^2)
J_{pm}	Rotary inertia of the pump and motor combined (Kg/m^2)
J_c	Coupling rotary inertia (Kgm^2)
J_p	Pump rotary inertia (Kgm^2)
K_{im}	Servovalve torque motor gain (Nm/A)
K_q	Servovalve armature-flapper transfer function (m/N)
K_a	Servovalve hydraulic amplifier flow gain (m^2/s)
K_{sp}	Servovalve feedback wire stiffness (N)
K_{ser}	Servovalve armature-flapper constant (N/m)
k	Valve constant
K	System stiffness (N/m)
K_e	Servomotor electrical circuit gain (Ω^{-1})
K_c	Servomotor gain (Nm/A)
K_{conv}	Servomotor amplifier gain (V/m)
K_{conv2}	EMA second conversion factor (V s/rad)
K_{mv}	Servomotor viscous friction (Ns/rad)
K_{is}	Coefficient of inertial swash plate torque (Nm/rad)
K_{pr}	Coefficient of pressure swash plate torque (Nm/Pa)
K_v	Resistance to flow in the check valve (m^3/Pa)

$K_{p_{visc}}$	Oil viscosity coefficient (Nms/rad)
K_{fric}	External gear pump coefficient of friction (Nms/rad)
K_w	Back-emf constant (V/rad)
K_p	Inner-loop proportional gain
K_i	Inner-loop integral gain
K_{pipe}	Coefficient relating flow to pressure drop in the pipe (Ns ² /m ⁸)
K_h	Hydraulic gain (m/rad)
k_s	Time iteration (sec)
L_c	Servomotor winding inductance (H)
L	EHA actuator leakage (m ³ /sPa)
L_T	Combined EHA leakage (m ³ /sPa)
l	Pipe length (m)
M	System mass (Kg)
M_a	Mass of actuator piston (Kg)
M_L	Mass of the load (Kg)
M_p	Mass of a single piston in a variable displacement piston pump (Kg)
m	Air index of compression
N	Ballscrew lead (m/rad)
N_p	Number of pistons in a variable displacement piston pump
n	Stribeck exponent
n_m	Servomotor noise output
n_c	Combined EHA system noise output
P_s	System supply pressure (Pa)
P_1	Pressure in actuator chamber 1 (Pa)

P_2	Pressure in actuator chamber 2 (Pa)
P_r	System reservoir pressure (Pa)
P_l	Linearized load pressure (Pa)
\dot{P}_1	Pressure increase rate in chamber 1 (Pa/s)
P_a	Port a pressure (Pa)
P_b	Port b pressure (Pa)
P_{lp}	Operating load pressure point (Pa)
P_{ac}	Accumulator pressure (Pa)
P_{vb}	Check valve cracking pressure (Pa)
P_{case}	Case drain pressure (Pa)
P_{pipe}	Pressure drop in the pipe (Pa)
PC	Outer-loop controller transfer function
P_n	System nominal pressure (Pa)
P_w	EHA required power output (W)
P_{diff}	Pressure differential (Pa)
P	System static pressure (Pa)
P_o	Atmospheric pressure (Pa)
p	Lowpass Butterworth filter order
q	Time shift operator
ΔQ	Hydraulic amplifier differential flow (m^3/s)
Q_1	Fluid flow in chamber 1 of the actuator (m^3/s)
Q_2	Fluid flow in chamber 2 of the actuator (m^3/s)
Q_l	Linearized flow (m^3/s)
Q_h	Net volumetric flow into the connecting hose (m^3/s)

Q_a	Port a pump flow (m^3/s)
Q_b	Port b pump flow (m^3/s)
Q_{ac1}	Fluid flow from the accumulator to chamber 1 (m^3/s)
Q_{ac2}	Fluid flow from the accumulator to chamber 2 (m^3/s)
$Q_{ac,in}$	Flow coming into the inner circuit from the case drain (m^3)
Q_{case}	Case drain flow (m^3/s)
Q_L	EHA load flow (m^3/s)
Q_n	Nominal fluid flow (m^3/s)
r	Piston pitch radius in a variable displacement piston pump (m)
R_c	Servomotor winding resistance (Ω)
s	Continuous Laplace transform
sgn	Sign function
T_m	Servomotor torque (Nm)
T_{load}	Load of the ballscrew and flight surface actuator (Nm)
$T_{mstatic}$	EMA servomotor static friction (Nm)
T_{static}	EMA flight surface static friction (Nm)
T_{dist}	EMA torque disturbances (Nm)
T_v	Variable-displacement pump torque (Nm)
T_{db}	External gear pump deadband torque (Nm)
T	Sample period (s)
$TF_{A,For}$	EHA Axis A forward transfer function
$TF_{A,Rev}$	EHA Axis A reverse transfer function
$TF_{B,For}$	EHA Axis B forward transfer function
$TF_{B,Rev}$	EHA Axis B reverse transfer function

U	Singular value decomposition unitary matrix
V_c	Servomotor input voltage (V)
V_{s_0}	Nominal servo piston volume in a variable-displacement pump (m^3)
V_a	Fluid volume in chamber a of the EHA circuit (m^3)
V_b	Fluid volume in chamber b of the EHA circuit (m^3)
V	Velocity of fluid in the pipe (m/s)
V_o	Nominal volume of each chamber of the EHA (m^3)
ΔV	Change in volume of the system (Pa)
v_s	Stribeck velocity (m/s)
V_d	Singular value decomposition diagonal matrix
V_n	Maximum loaded velocity of the actuator (m/s)
W	Singular value decomposition unitary matrix
w_c	Cut-off frequency (rad/s)
w_{ser}	Servovalve natural frequency (rad/s)
\dot{w}_m	Servomotor rotational acceleration (rad/s ²)
w_p	Pump shaft speed (rad/s)
w_{pop}	Pipe operating flow (m^3/s)
w_{nh}	Hydraulic natural frequency (rad/s)
x_f	Servovalve flapper displacement (m)
x_s	Servovalve spool displacement (m)
x_{sp}	Operating spool position (m)
x	Actuator position (m)
\dot{x}	Actuator velocity (m/s)
\ddot{x}	Actuator acceleration (m/s ²)

x_d	Demanded actuator position (m)
\dot{x}_d	Demanded actuator velocity (m/s)
\ddot{x}_d	Demanded actuator acceleration (m/s^2)
\tilde{x}	Actuator positional error (m)
$\dot{\tilde{x}}$	Actuator velocity error (m/s)
$\ddot{\tilde{x}}$	Actuator acceleration error (m/s^2)
x_o	Mean position of the EHA actuator (m)
z	Discrete Laplace transform
β_s	Variable displacement pump hydrostatic system bulk modulus (Pa)
β_e	Effective bulk modulus of the fluid (Pa)
β_o	Bulk modulus of oil (Pa)
β_v	Combined system bulk modulus (Pa)
τ	Torque input to the armature-flapper in the servovalve (Nm)
τ_e	Servomotor electrical time constant (s)
τ_n	EHA nominal torque (Nm)
τ_i	Integral action time (s)
ζ_{ser}	Servovalve damping ratio
ζ_h	Hydraulic damping coefficient
$\dot{\theta}_m$	Rotor velocity of the servomotor (rad/s)
α	Piston pump swash plate angle (rad)
$\dot{\alpha}$	Piston pump swash plate velocity (rad/s)
γ	Pressure carry-over angle in a variable-displacement piston pump (rad)
ξ	External gear pump cross-port leakage (m^3/sPa)
ρ	Fluid density (kg/m^3)

ε_V	EHA volumetric efficiency
μ	Dynamic coefficient of viscosity (Kg/sm)
φ	Pre-sliding displacement (m)
σ_o	Micro-asperity stiffness of the contact between the seals and bore (N/m)
σ_1	Micro-asperity damping coefficient during the pre-sliding displacement (Ns/m)
σ_2	Coefficient of viscous friction in the gross-sliding regime (Ns/m)
φ_{ss}	Steady-state piston/rod seal deflection (m)
δ	Air/oil volumetric ratio
η	Impulse response input magnitude (V)

Chapter 1 Introduction

1.1 Preliminary Remarks

Hydraulic systems have been widely used in industry for decades in applications where it is advantages to have the following features:

- The ability to maneuver large loads.
- High force/torque-to-mass ratio.
- Obtain accurate control of a state of interest (i.e. position, velocity).
- Have a self-lubricating system (oil acts as a lubricant).

Due to these features hydraulic systems have found applications in aerospace systems, farm equipment, off-road equipment and heavy machinery. In this study, their application to the aerospace industry will be investigated. The dual Electro-Hydrostatic Actuator (EHA) is used to actuate the aircrafts' flight surfaces. In particular, this study will investigate a prototype developed at McMaster University that uses a unique architecture that employs a leaner system compared to current models in industry.

An EHA is a form of hydrostatic system that uses the flow from the pump to control an actuator as opposed to a directional valve seen in common hydraulic systems. Hydrostatic systems have been widely used in industry, primarily in off-road and farm equipment as transmissions, for many years. The primary difference between traditional hydrostatic systems and the EHA is the manner in which fluid is routed to the actuator by the pump. Traditional hydrostatic systems employ a variable-displacement pump attached to single speed motor, which controls the output flow depending on the input angle of the pump swash plate. The EHA employs a fixed-displacement piston pump attached to a servomotor in which the output flow is proportional to the servomotor rotary speed. Due to the fixed-displacement pump the EHA only requires on-demand rotation of the servomotor. This can greatly enhance energy efficiency. The primary components of the EHA design considered in this research include a fixed-displacement bi-directional external gear pump, a servomotor, a symmetrical linear actuator, an accumulator, a series of check valves, a by-pass valve and pressure relief valves. Compared to common directional valve actuated systems, the EHA has the following advantages:

- Increased power-to-weight ratio.
- Increased energy efficiency.
- Increased modularity of the system.

The increased power-to-weight ratio is achieved by creating an integrated unit where all components are combined into a lumped, modular system. The resulting reduction in weight makes the EHA ideal for aerospace, especially since the performance and fuel efficiency are becoming increasingly important. In aircraft it is especially important to have systems that are fault tolerant and have some form of redundancy. An EHA can satisfy this by combining two systems in tandem so that one can compensate for the other in the event of a malfunction. A dual EHA was developed for this research which is an integrated, lumped unit. The result of this is reduced weight and an enhanced fault tolerant architecture. The final prototype developed is such an integrated unit, but is also augmented so that the system can be easily adapted to incorporate fault condition simulations for future research.

1.2 Research Objectives

The objectives of this research are as follows:

- To design a dual EHA as an integrated, lumped unit so that it has the same performance characteristics as the EHA used for the rudder of the F-35 Lightning fighter jet produced by Parker Aerospace but is 10% lighter.
- To develop a prototype that incorporates all components of the dual EHA design previously mentioned minus the actuator, and incorporates extra components that can be used to perform fault condition analysis.
- To develop and investigate a mathematical model for the EHA in a linearized form that can be used to develop future control and fault detection models.
- To determine two major physical model parameters, namely internal leakage and damping.
- To investigate the linearity of the EHA system and to produce piece-wise linear models where possible.
- To design a filter to feedback several states to a controller and to implement a basic proportional controller for the EHA.

The outline of the research which incorporates these objectives can be seen in section 1.3.

1.3 Thesis Outline

The outline of this dissertation is as follows:

- Chapter 2 provides a literature review of the history of flight surface actuators which includes mechanical linkages, hydraulic systems, Fly-By-Wire (FBW) systems and Power-By-Wire (PBW) systems.
- Chapter 3 describes the concept of hydrostatic actuation using variable-displacement and fixed-displacement pumps. The latter of these two encompasses the EHA.
- Chapter 4 provides a detailed description of the design and prototyping of a dual EHA that has weight savings compared to the F-35 rudder EHA.
- Chapter 5 describes the process for determining the internal leakage and damping characteristics for the dual EHA prototype and will present their final values.
- Chapter 6 describes the process and results for system identification performed on the EHA prototype.
- Chapter 7 investigates the design of a digital filter used for feedback purposes and the implementation of a closed-loop proportional controller implemented on a single EHA.

Chapter 2 Conventional Flight Surface Actuator Systems

This chapter provides an introduction into the concept of flight surface actuators used in aircraft. Common mechanisms and their associated mathematical models are discussed along with their advantages and disadvantages. Conventional mechanical and hydraulic systems that are relevant to flight surface actuation are discussed in detail.

2.1 Flight Controls on an Aircraft

Flight control systems on an airplane are typically classified into two categories: primary and secondary. Primary systems in an aircraft typically control all components that safely guide an airplane during flight, which include the ailerons, the elevator and the rudder [1]. Secondary flight controls improve the performance characteristics of the aircraft or relieve the pilot of using excessive control force [1]. Examples of secondary flight controls include the landing gear, flaps and trim systems. Figure 2.1 shows all of the primary flight surfaces and a select number of the secondary flight surfaces on the Boeing 777 aircraft.

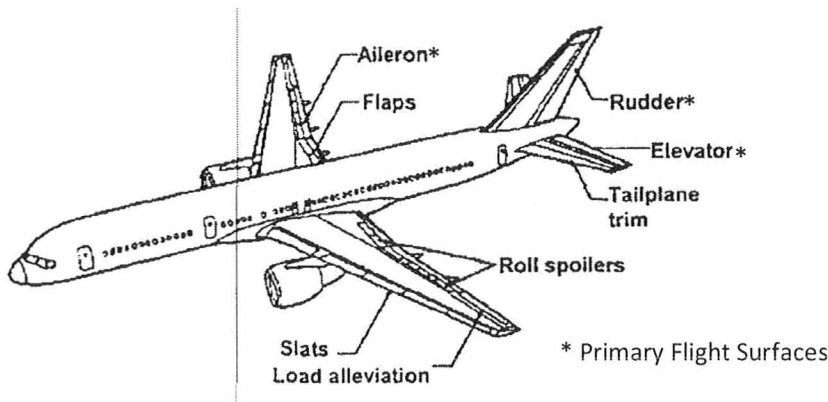


Figure 2.1. Primary and secondary flight surfaces for the Boeing 777 [2].

The primary flight surfaces control the three main axes of the aircraft's orientation which are yaw, pitch and roll. The rudder, elevator and ailerons control these respectively. A depiction of the movement of an aircraft can be seen in figure 2.2. The focus of this research is in the systems that actuate the primary flight control surfaces. The following sections will describe the types of flight surface actuators used in the history of flight:

- Mechanical linkages.
- Hydraulic actuation controled by mechanical linkages.

- Fly-By-Wire (FBW) systems.
- Power-By-Wire (PBW) systems.

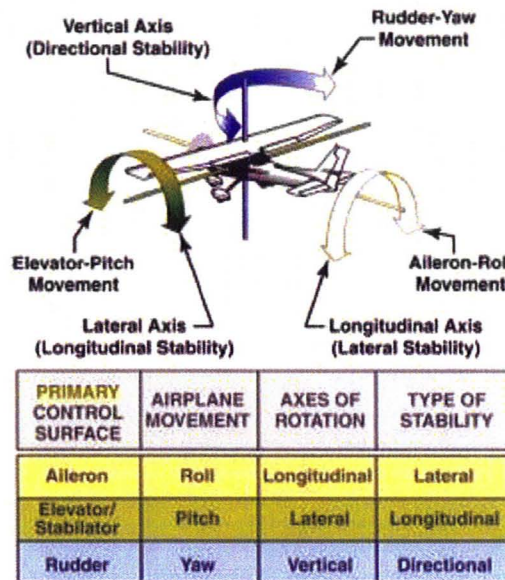


Figure 2.2. Airplane controls, movement and axes of rotation [1].

2.2 Using Mechanical Linkages for Flight Surface Actuation

When aircraft were in their primitive development phase in the early 20th century their limited size and speed allowed their primary flight surfaces to be actuated using only the force exerted by the pilot on the controls. Linkages using taught wires, pulleys and sometimes counterweights would connect the joystick and foot pedals in the cockpit to the flight surface. This method was simple and reliable but was limited to the size and performance of the aircraft since the power needed to move the flight surface is solely provided by the pilot. With the advent of larger aircraft, particularly after 1931, this method needed to be replaced by systems where the power was provided by an auxiliary system [3]. The replacements included hydraulic and mechanical actuators which were later incorporated into Fly-By-Wire systems and then more recently into Power-By-Wire systems. Even though, mechanical linkages between the cockpit and the flight surface still exist in aircraft such as the Cessna Skyhawk and gliders due to the small size and simplicity of these aircraft.

Figure 2.3 shows a simple depiction of a flight surface actuated by mechanical linkages. Control input is given by the pilot through pivoting the control stick which in turn translates motion to taught wires. The taught wires are oriented around the structure of the aircraft using a series of pulleys. At the

opposite end of the taught wire is a pivot which is rigidly attached to the flight surface. This pivot will rotate and move the flight surface.

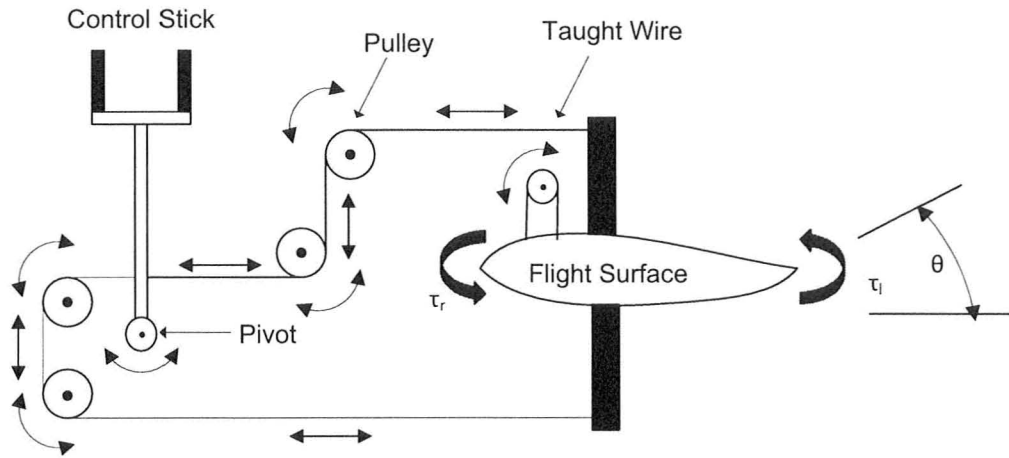


Figure 2.3. Flight surface actuation using mechanical linkages.

The control stick is often used to control the ailerons and the elevator. Movements to the left and right move the ailerons while movements forwards and backwards move the elevators. To control the yaw foot pedals are typically employed in the cockpit, which is attached to the rudder in a similar fashion seen in figure 2.3. This control setup has remained the common choice in flight surface actuation throughout history.

In the event where the flight surface is weighed down due to gravity a counterweight is often employed so that the pilot does not need to force the flight surface to the level position. The advantages of flight surface actuation using mechanical linkages are:

- Simple to design and implement.
- Feedback from disturbances on the flight surface can easily be felt by the pilot.
- A secondary power source is not required to move the flight surface.

The disadvantages of flight surface actuation using mechanical linkages are:

- Limited to flight surfaces that can only be actuated by the power input of the pilot. This limitation is compounded by friction in the controls-to-flight surface connection.
- Requires bulky pulleys, wires and counterweights.
- Multiple, independent actuation systems for redundancy are extremely difficult to implement.

2.3 Flight Surface Actuation using Hydraulic Systems

From the dawn of flight up until the early 1930's flight control was dominated by the use of simplistic mechanical linkages where all power to move the surface was provided by the pilot [3]. As the power demands grew due to larger aircraft and control surfaces an auxiliary power assist system was needed. To achieve this hydraulic actuators were employed in the flight surfaces using directional valves. From the 1930's to the early 1970's the directional valve was connected to mechanical linkages that were actuated by using manual controls from the cockpit. From the 1970's and on, with the emergence of communication technology, control of the directional valve has been performed by sending electrical control signals. This concept created the emergence of Fly-By-Wire (FBW) systems where flight surface controls were increasingly being replaced by computerized systems. Both hydraulic actuation through mechanical systems and FBW will be discussed below.

2.3.1 Hydraulic Systems using Mechanical Linkages

Initially, the use of hydraulic systems for flight surface actuation was an extension of using mechanical linkages. Instead of moving the flight surface itself the mechanical linkage controlled a hydraulic directional valve that allowed fluid to move an actuator in a controlled manner. A classical example of this control architecture can be seen in figure 2.4.

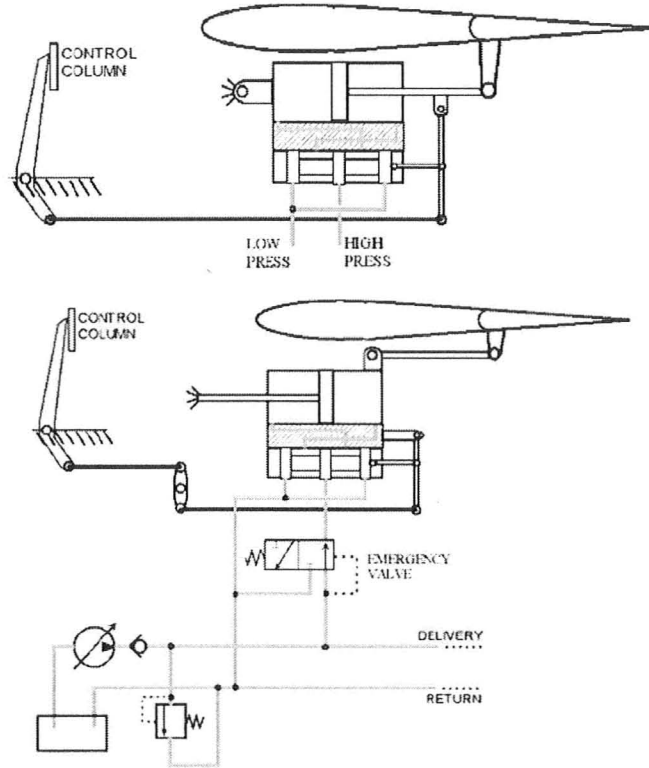


Figure 2.4. Examples of hydraulic actuators with mechanical linkages for flight surface actuation [4].

Figure 2.4 shows two common hydraulic servomechanisms. In the first example the piston rod, directional valve spool and mechanical linkage are all rigidly attached. Control inputs from the cockpit will initially force the valve spool to move in the desired direction, allowing fluid to move into one of the actuator chambers. As the actuator moves to its desired position the valve spool will gradually move to the neutral position, thus settling the actuator. In the second example the piston rod in the actuator is rigidly attached to the aircraft with the cylinder attached to the flight surface. In the same manner as the first example the valve spool will gradually move back to neutral as the desired actuator position is achieved. Both examples share the same basic hydraulic circuit architecture seen at the bottom of figure 2.4. Both also have the two basic features: the system is controlled in a proportional way in that the actuator response is a function of the pilot's input through the mechanical linkages; the pilot with little effort to move the control valve has maneuver intensity feedback [4]. For the latter of the two the pilot will experience feedback but will not experience the full load condition experienced on the flight surface.

This form of hydraulic transmission system is termed as an open-loop style controlled using directional valves. The electric motor is attached to either a fixed or variable-displacement pump

though a flexible or rigid coupling. The type of pump can be either an internal gear, an external gear, a vane or piston pump. A relief valve is typically positioned close to the outlet of the pump. This prevents the pressure of the fluid from exceeding a maximum threshold and protects the system from burst failure. The check valve placed just past the outlet of the pump allows the actuator to maintain static pressure without assistance from the pump. This saves energy when the flight surface is in a non-neutral position and requires static hydraulic pressure to hold it in place. In some cases a pressurized accumulator is placed after the check valve to allow pressurized fluid to be stored to assist the pump when the demanded flow-rate is high. The accumulator from the supply system (pump and accumulator) also provides a constant supply pressure, dampens pressure spikes and decreases coupling effects between actuators. The flow then passes through the valve which controls the fluid entering the actuator. In the case seen in figure 2.4 there is an emergency valve connected to the delivery segment of the circuit. If the pressure drops at this section due to loss of electrical power, rupture in the hydraulic lines, etc., it will link the control valve inlet to the reservoir [4]. This will allow the pilot to manually actuate the cylinder.

The advantages of flight surface actuation with hydraulic actuators coupled to mechanical linkages are:

- Larger surfaces can be actuated with little effort from the pilot.
- The pilot will experience positional feedback through the controls
- Relatively simple architecture is employed.

The disadvantages of flight surface actuation with hydraulic actuators coupled to mechanical linkages are:

- An artificial feel system needs to be employed so the pilot can experience the load condition on the flight surface.
- A secondary power system is required to move the flight surfaces.
- Multiple, independent actuation systems for redundancy is still extremely difficult to implement due to mechanical linkages being used.
- Requires bulky hydraulic components.

2.3.2 Hydraulic Systems using Fly-By-Wire (FBW) Technology

In the early 1970's the concept of flight actuation through sending electrical signals to control valves was coming into fruition due to emerging communication technology. This idea would replace the mechanical linkages between the cockpit and control valves and replace them with distributed centralized electrical communication architectures that would be controlled by computers [15]. This concept was termed as Fly-by-Wire (FBW), which eliminated the necessity of mechanical linkages to actuate the flight surface control mechanism by replacing them with electrically controlled valves. As these systems were further developed a distributed communication architecture became the system of choice due to reduced load on a centralized flight control computer and increased flexibility during architecture development [15]. Another significant advantage of FBW systems is that signals can be inputted to the control valve without any command from the pilot. An example of a FBW system can be seen in the figure below.

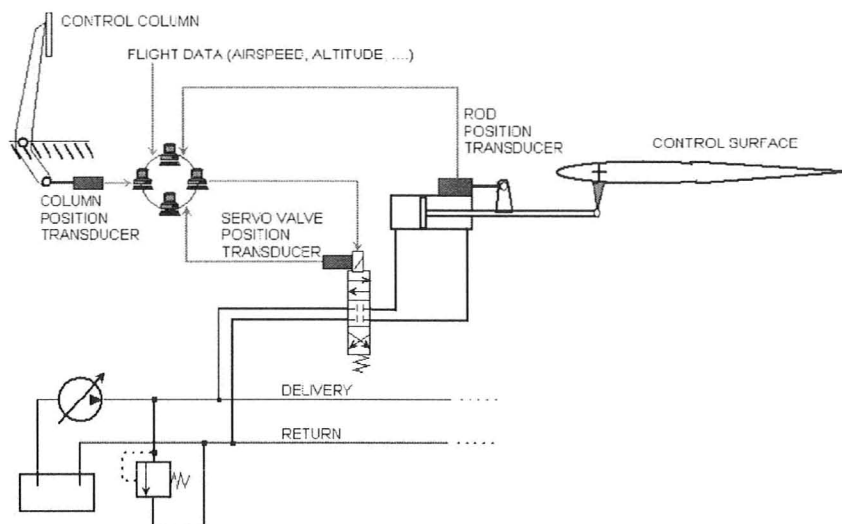


Figure 2.5. Fly-By-Wire flight surface actuation system [4].

In the figure above control input to the directional valve and positional feedback of the flight surface are performed using electrical signals. In many cases there is also a positional sensor on the directional valve itself. Initially in FBW systems, all control was performed using analog signals but recently these have been switched to digital control. All of these signals along with the control input from the pilot and other flight data are processed by computers inside the aircraft.

Electrically signaled directional valves are generally controlled either by proportional or servo action. Proportional valves are moved by solenoids that are balanced by opposing springs. The force

given to the solenoid (which is proportional to valve opening) is controlled by the amount of current it receives. Higher performance proportional valves have Linear Variable Differential Transducers (LVDT) that feedback spool position for flow control. For flows higher than $2.5 \times 10^{-3} \text{ m}^3/\text{s}$ (40 GPM) the force required to move the spool is much greater than what a solenoid can provide. In these applications two spools are employed: a pilot spool and main spool. The solenoid actuates the pilot spool which allows pressurized fluid to move the main spool back and forth. Proportional valves that use lower flows tend to use only one spool.

Servovalves use a small torque motor attached to a flapper to control the fluid pressure, which in turn, moves the valve spool through pilot-actuation on both ends of the valve. Proportional valves are less complicated, are less susceptible to contamination and inexpensive compared to servo valves. However, servovalves have a quicker response time since the torque motor only controls the pressure and does not have to overcome spring forces and LVDT inertia [5]. Servovalves are more appropriate for high precision applications. Servovalves are bi-directional and are able to channel the return flow to the reservoir. A depiction of a typical servo valve can be seen in figure 2.6.

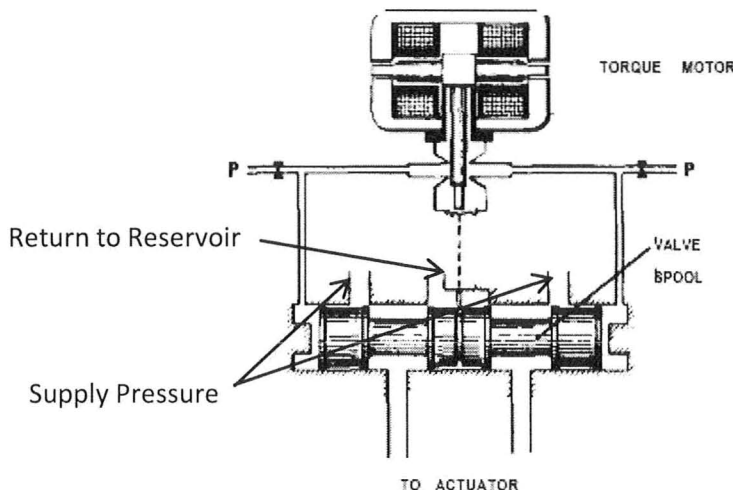


Figure 2.6. Layout of a common servo valve [6].

2.3.2.1 Modeling of Servovalve Controlled Actuators in Flight Surface Actuators

A simplified block diagram describing the model for the servovalve can be seen in figure 2.7.

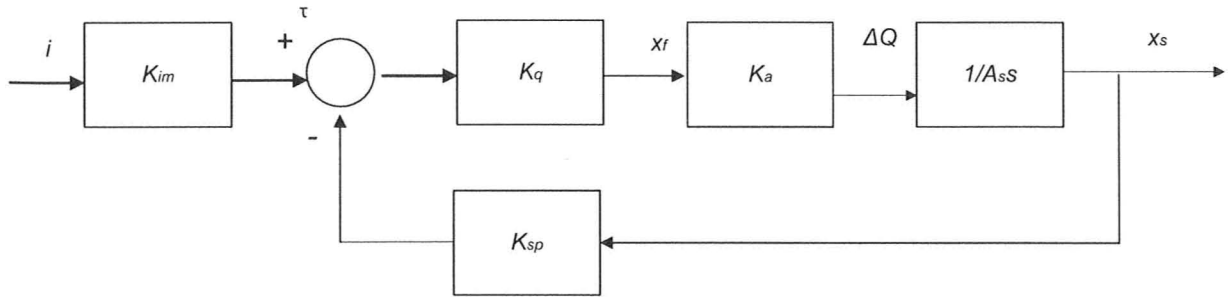


Figure 2.7. Simplified servovalve block diagram [6].

Where i is the input current (A), K_{im} is the torque motor gain (Nm/A), K_q is the armature-flapper transfer function (m/N), K_a is the hydraulic amplifier flow gain (m^2/s), A_s is the spool end area (m^2), K_{sp} is the feedback wire stiffness (N), τ is the torque input to the armature-flapper, x_f is the flapper displacement (m), ΔQ is the hydraulic amplifier differential flow (m^3/s) and x_s is the spool displacement (m). The transfer function for the armature flapper is shown below [6]:

$$K_q = \frac{x_f(s)}{\tau(s)} = \frac{1/K_{ser}}{1 + \left(\frac{2\zeta_{ser}}{w_{ser}}\right)s + \left(\frac{s}{w_{ser}}\right)^2} \quad (2.1)$$

Where K_{ser} is the armature-flapper constant (N/m), ζ_{ser} is the damping ratio and w_{ser} is the natural frequency (rad/s). The complete linearized mathematical model for a servovalve is shown by the following third order transfer function:

$$\frac{x_s(s)}{i(s)} = \frac{\frac{K_a w_{ser}^2}{A_s K_{ser}}}{s^3 + 2w_{ser}\zeta_{ser}s^2 + w_{ser}^2 s + \frac{K_{sp} K_a w_{ser}^2}{A_s K_{ser}}} \quad (2.2)$$

The proportional or servo valve usually has 4 ports and 3 positions and is generally configured to be closed centre, meaning that the flow is blocked when the spool is not actuated. All the flow returning to the reservoir passes through a filter that captures small particles that over time can wear the components of the system if not removed. When the valve is actuated flow is directed to one side of a hydraulic actuator such as a piston. The most common piston is an asymmetrical, single rod type

since they are compact and cost-effective. The problem with asymmetrical actuators is that the maximum velocity, force and flow vary according to the direction of motion.

When mathematically modeling open-loop hydraulic systems the components that need to be analyzed are the proportional/servo valve and the actuator with a connected load. The only information needed from the power supply going into the valve is the supply pressure and maximum flow. The model shown here is presented by Habibi [7]. The valve is analyzed by relating the output flow from the valve to the actuator and the pressure difference across the orifice of the spool. This relationship can be seen in the following equation:

$$Q_1 = kx_s \sqrt{P_s - P_1} \quad (2.3)$$

Where Q_1 is the flow to the actuator (m^3/s), k is the valve constant, x_s is the displacement of the spool (m), P_s is the supply pressure (Pa) and P_1 is the pressure in actuator chamber 1. Resistance is also caused by flow from the opposite chamber passing through the valve back to the reservoir. This is governed by the same principle seen in equation 2.3 and is shown below:

$$Q_2 = kx_s \sqrt{P_2 - P_r} \quad (2.4)$$

Where Q_2 is the flow back to the reservoir (m^3/s), P_2 is the pressure in actuator chamber 2 (Pa) and P_r is the reservoir pressure (Pa). To create an overall linear model of the system equations 2.3 and 2.4 must be linearized. To do this the new variables P_l and Q_l are introduced. P_l and Q_l are the load pressure (Pa) and load flow (m^3/s) respectively. In this case the actuator is a double acting, double rod type where the volume in both chambers are equal, meaning that Q_1 and Q_2 are the same. Assuming the valve has negligible leakage the following relationship is obtained:

$$\sqrt{P_s - P_1} = \sqrt{P_2 - P_r} \quad (2.5)$$

In the majority of cases the reservoir pressure is at atmospheric which is significantly less compared to the supply (typically around 10-15MPa), making P_r negligible. This assumption gives form to the following equation:

$$P_s = P_1 + P_2 \quad (2.6)$$

The load pressure is simply the pressure differential between the two actuator chambers:

$$P_l = P_1 - P_2 \quad (2.7)$$

Substituting equation 2.6 into 2.7 yields:

$$P_1 = \frac{P_s + P_l}{2} \quad (2.8)$$

and

$$P_2 = \frac{P_s - P_l}{2} \quad (2.9)$$

The load flow can now be represented in terms of P_l :

$$Q_l = \frac{kx_s}{2} \left(\sqrt{P_s - P_1} + \sqrt{P_2 - P_r} \right) \quad (2.10)$$

Substituting equations 2.8 and 2.9 into 2.10 yields the equation that relates the load flow to the spool position and the load pressure:

$$\begin{aligned} Q_l &= \frac{kx_s}{2} \left(\sqrt{\frac{P_s - P_l}{2}} + \sqrt{\frac{P_s - P_l}{2}} \right) \\ Q_l &= \frac{kx_s}{\sqrt{2}} \left(\sqrt{P_s - P_l} \right) \end{aligned} \quad (2.11)$$

Equation 2.11 is a non-linear relationship which can be linearized about an operating point using a Taylor Series Expansion. The input variables here are the spool position and the load pressure. The operating spool position and load pressure point are x_{sp} and P_{lp} respectively. The Taylor Series Expansion is shown in the following equation:

$$Q_l(P_l, x_s) = Q_l(P_{lp}, x_{sp}) + \frac{\partial Q_l}{\partial P_l} \Bigg|_{x_s=x_{sp}, P_l=P_{lp}} \Delta P_l + \frac{\partial Q_l}{\partial x_s} \Bigg|_{x_s=x_{sp}, P_l=P_{lp}} \Delta x_s \quad (2.12)$$

Where

$$\Delta x_s = x_s - x_{sp} \quad (2.13)$$

$$\Delta P_l = P_l - P_{lp} \quad (2.14)$$

Solving for the partial derivative of Q_l with respect to P_l yields:

$$-c_p = \frac{\partial Q_l}{\partial P_l} \Bigg|_{x_s=x_{sp}, P_l=P_{lp}} = -\frac{kx_s}{2\sqrt{2}\sqrt{P_s - P_l}} \Bigg|_{x_s=x_{sp}, P_l=P_{lp}} \quad (2.15)$$

Solving for the partial derivative of Q_l with respect to x_s yields:

$$c_x = \frac{\partial Q_l}{\partial x_s} \Bigg|_{x_s=x_{sp}, P_l=P_{lp}} = \frac{k}{\sqrt{2}} \sqrt{P_s - P_l} \Bigg|_{x_s=x_{sp}, P_l=P_{lp}} \quad (2.16)$$

Note that c_p and c_x will be used for convenience. c_p is shown with a negative sign in equation 2.15 in order to derive a simplified model in the following equations. Substituting equations 2.15 and 2.16 into equation 2.12 yields:

$$Q_l(P_l, x_s) = Q_l(P_{lp}, x_{sp}) + c_x \Delta x_s - c_p \Delta P_l \quad (2.17)$$

or

$$\Delta Q_l(P_l, x_s) = c_x \Delta x_s - c_p \Delta P_l \quad (2.18)$$

Where,

$$\Delta Q_l(P_l, x_s) = Q_l(P_l, x_s) - Q_l(P_{lp}, x_{sp}) \quad (2.19)$$

The Laplace transform of equation 2.19 is:

$$\Delta Q_l(s) = c_x \Delta x_s(s) - c_p \Delta P_l(s) \quad (2.20)$$

Equation 2.20 presents the linearized form of a valve model about a preselected operating point. Once the operating point is selected equations 2.15 and 2.16 are used to calculate c_p and c_x respectively.

Now that the valve has been modeled the actuator and the attached load must be considered. The model of the actuator can be seen in the equation below:

$$F(s) = AP_l(s) \quad (2.21)$$

Where F is the load (N) and A is the area of the actuating piston (m^2). Due to its linearity the equation above can be represented by:

$$\Delta F(s) = A\Delta P_l(s) \quad (2.22)$$

The flow rate of the piston is represented by the equation below:

$$Q_l(t) = A\dot{x}(t) \quad (2.23)$$

Where \dot{x} is the actuator velocity (m/s). In its Laplace transform the equation above becomes:

$$Q_l(s) = Asx(s) \quad (2.24)$$

Due to its linearity the equation above can be represented by:

$$\Delta Q_l(s) = As\Delta x(s) \quad (2.25)$$

The relationship above can be combined with equation 2.20 to yield:

$$As\Delta x(s) = c_x \Delta x_s(s) - c_p \Delta P_l(s) \quad (2.26)$$

Substituting equation 2.22 yields:

$$As\Delta x(s) = c_x \Delta x_s(s) - c_p \Delta F(s) / A \quad (2.27)$$

Rearranging the equation above to solve for the force yields:

$$\Delta F(s) = \frac{Ac_x}{c_p} \left(\Delta x_s(s) - \frac{As}{c_x} \Delta x(s) \right) \quad (2.28)$$

The above equation shows that the force acted on the load of the system is a function of the valve spool position and the position of the actuator. With this knowledge the force applied to the actuator by the load can be considered. Equation 2.28 can also be represented by the following block diagram:

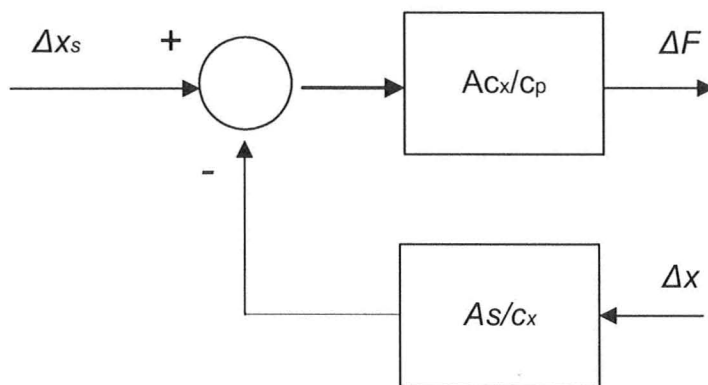


Figure 2.8. Block diagram incorporating the dynamics of a servo valve spool.

Now the load attached to the actuator can be considered. The load on flight surface actuators in its most basic form can be shown as a mass-damper system. A depiction of this system in its basic form can be seen in the figure 2.9.

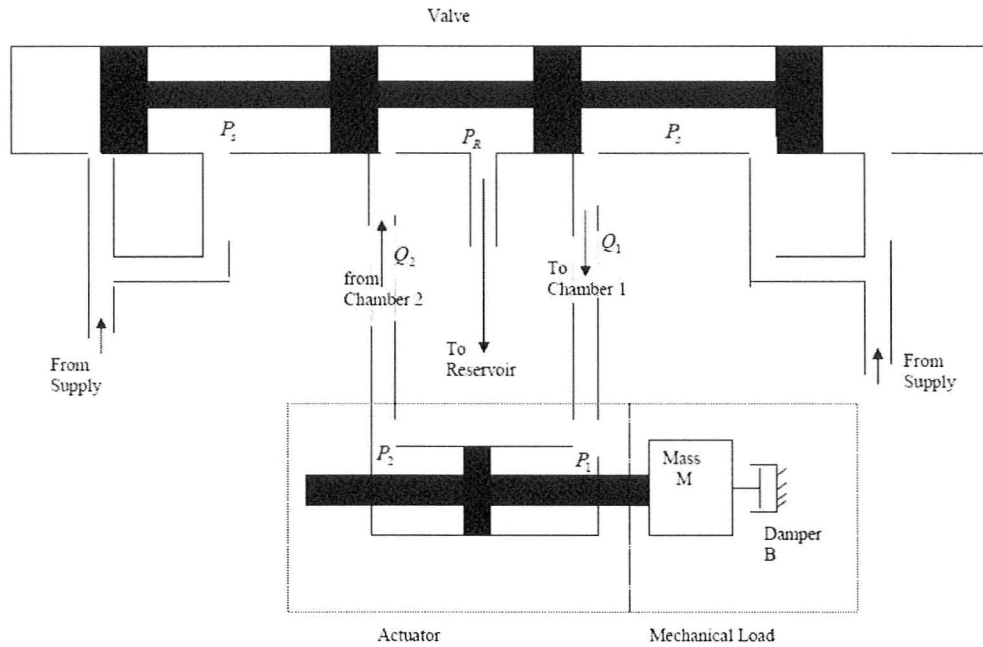


Figure 2.9. Spool valve, actuator and load configuration [7].

The relationship between the force, mass and damping of a system is seen in the equation below:

$$F(t) = M\ddot{x}(t) + B\dot{x}(t) \quad (2.29)$$

Where M is the mass of the load (Kg) and B is the system damping (Ns/m). The above equation is linear and can be represented by the following Laplace transform:

$$\Delta F(s) = (Ms^2 + Bs)\Delta x(s) \quad (2.30)$$

Combining the relationship above with equation 2.28 yields:

$$\frac{Ac_x}{c_p} \left(\Delta x_s(s) - \frac{As}{c_x} \Delta x(s) \right) = (Ms^2 + Bs)\Delta x(s) \quad (2.31)$$

Rearranging, the overall transfer function becomes:

$$\frac{\Delta x(s)}{\Delta x_s(s)} = \frac{\frac{Ac_x}{Mc_p}}{s^2 + \left(\frac{B}{M} + \frac{A^2}{Mc_p}\right)s} \quad (2.32)$$

The overall closed-loop block diagram becomes:

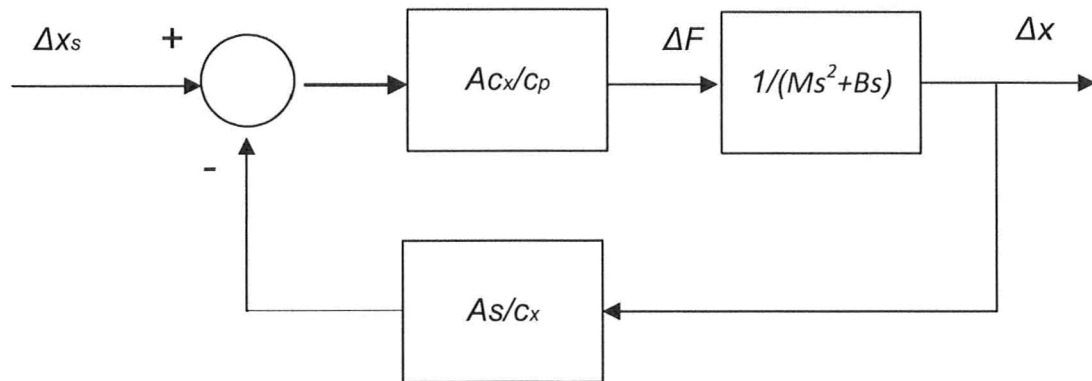


Figure 2.10. Closed-loop hydraulic block diagram for a servoactuator controlled actuator.

This shows that a servoactuator can be modeled as a 2nd order, type 1 system. This is a simplified model that does not account for elasticity effects such as the bulk modulus of the oil and the flexibility of any hoses. Equation 2.32 can be combined with equation 2.2 to create an overall transfer function that links the current input into the servoactuator to the position of the actuator.

With the advent of FBW systems more involved hydraulic systems were added to aircraft to increase redundancy in the event of any system failure. Although not always the case, several commercial aircraft use 3 separate and independent hydraulic systems that can control the same or separate flight surface actuator or system. The importance of each flight actuator/system will determine the number of hydraulic systems connected to it (i.e. the rudder may have all three hydraulic systems attached for added redundancy while the tail skid may only have one) [8]. An example of this form of hydraulic system is seen on the Boeing 767. A depiction of the hydraulic systems can be seen in figure 2.11.

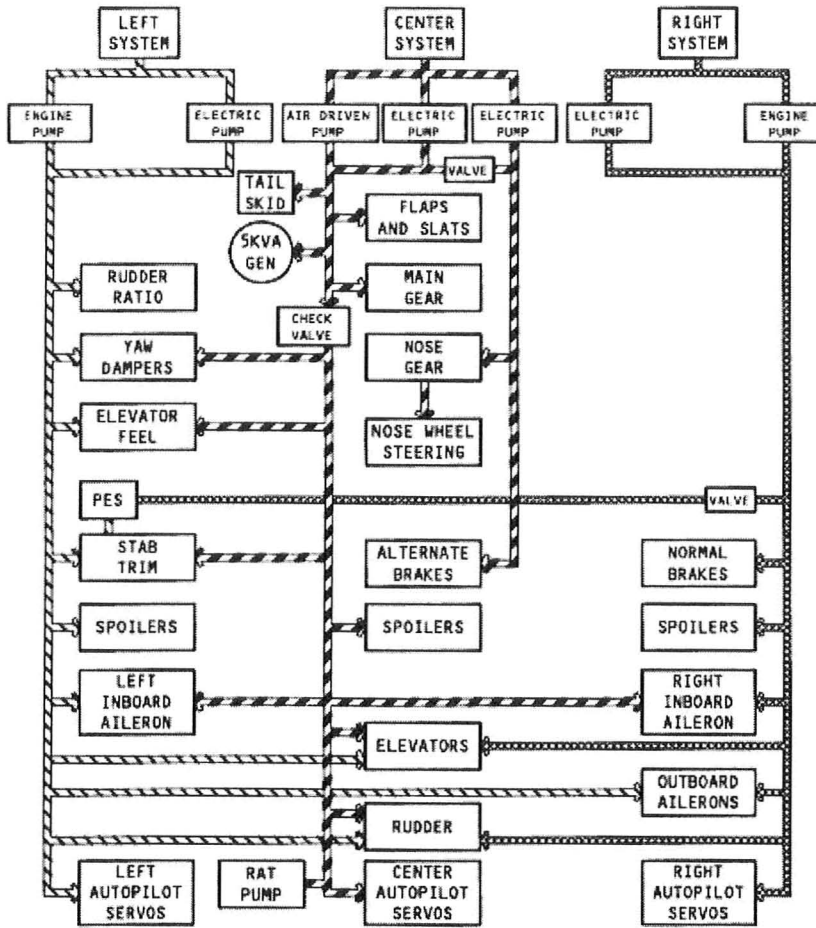


Figure 2.11. Hydraulic system network on the Boeing 767 [8].

This network shows that the primary system is in the centre. This system uses two separate electric pumps and a Ram Air Turbine (RAT) (air driven pump), which uses a turbine that is deployed under the fuselage to generate power in the event where main electrical power is lost. The left and right systems each use an electric pump and a pump connected directly to the engines on the main wings. The primary flight surfaces can be actuated by all three hydraulic systems combined, by each system alone or a combination of several. This example shows that FBW systems can be employed to more complex aircraft to increase the functionality, redundancy and efficiency of the actuation systems.

The advantages of flight surface actuation using FBW systems are:

- Weight reduction due to the elimination of mechanical linkages.
- The introduction of computer assisted control allows for added features such as increased stability, the ability to tune the pilot's control demands to protect the aircraft from exceeding airframe load factors, turbulence suppression, thrust vectoring, etc.
- Increased redundancy since several hydraulic systems in parallel can be employed.
- More control surfaces can be added such as trim for the rudder and other flight surfaces.

The disadvantages of flight surface actuation using FBW systems are:

- All electrically actuated systems mean that a failure in electrical power will severely limit aircraft control.
- Added complexity increases development costs.
- Hydraulic failure in one system can still affect the functionality of another system.

2.4 Flight Surface Actuation using Power-by-Wire (PBW) Systems

Over the last few decades the performance demands for flight surface actuation have increased and led to the desire of replacing FBW systems with Power-By-Wire (PBW) systems [9]. Although FBW systems give a significant performance advantage compared to conventional mechanical and hydraulic systems previously discussed, there are several disadvantages that still need to be addressed, which include [10].

- Higher complexity and weight.
- Energy efficiency: they must maintain hydraulic pressure of 21-42MPa (3000-6000psi) at all times, regardless of demand.
- System reliability: a fault in one of the hydraulic lines potentially leads to complete hydraulic failure in the aircraft.

The PBW concept has evolved into the more electric aircraft concept where flight surface actuation is achieved by using modular subsystems rather than centralized hydraulics. Figure 2.12 shows the layout of the PBW systems in the F-35 Lightning. This aircraft employs a combination of Electro-Hydrostatic Actuators (EHA's) and Electric Drive Units.

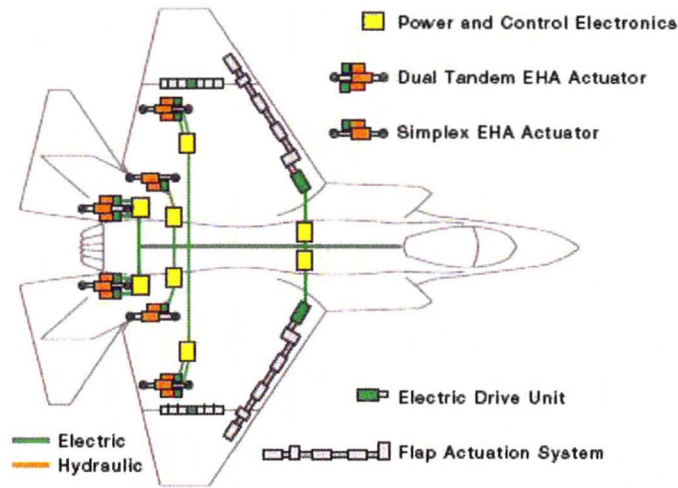


Figure 2.12. Layout of power-by-wire systems in a commercial aircraft [11].

Some of the features of modular PBW systems include [10].

- Control power comes directly from the aircraft's electrical grid, not a centralized hydraulic unit.
- Modular design decreases the overall weight required for all actuation systems.
- Modularity reduces maintenance costs and simplifies maintenance procedures since the repair of a unit can easily be performed by removing it from the flight surface and replacing it with a new one.
- Modularity increases reuse in multiple aircraft platforms hence reducing development costs.
- Fault tolerance: one fault in a centralized hydraulic system can cause failure in other systems or reduce overall performance. If a fault occurs in a modular PBW system, it can easily be shut-off and the actuation can be performed by a redundant system.
- Power-on-demand feature reduces the overall energy consumption of the aircraft.

Figure 2.13 shows the basic structure of a modular PBW flight surface actuation system used in the more electric aircraft concept.

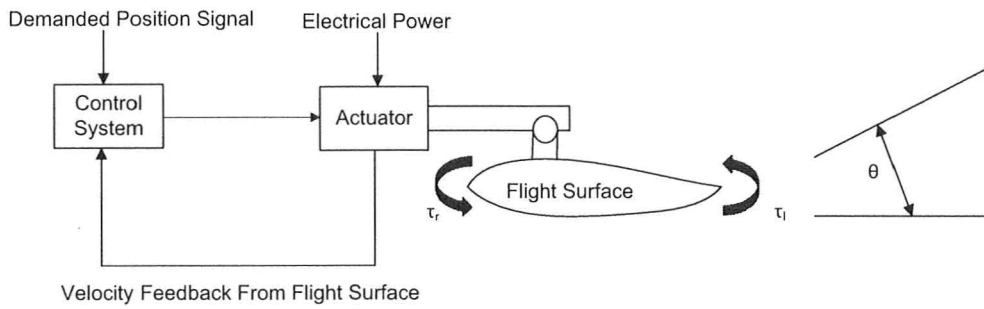


Figure 2.13. Basic Structure of a power-by-wire system.

The two types of systems typically used for modular power-by-wire flight surface actuation are Electro-Mechanical Actuators (EMA) and Electro-Hydrostatic Actuators (EHA). The EMA will be reviewed briefly in this chapter while the EHA will be discussed in significant detail in chapter 3, as it is the focus of this research.

2.4.1 Electro-Mechanical Actuators (EMA)

In the EMA, a drive motor is connected to a ball screw in order to translate rotary motion into linear motion. The basic components include [12]:

- A control system.
- A brushless, permanent magnet electric servomotor with a velocity feedback sensor.
- A ballscrew.
- A mechanical linkage between the ballscrew and flight surface.
- The flight surface.

A depiction of a typical EMA structure can be seen in figure 2.14.

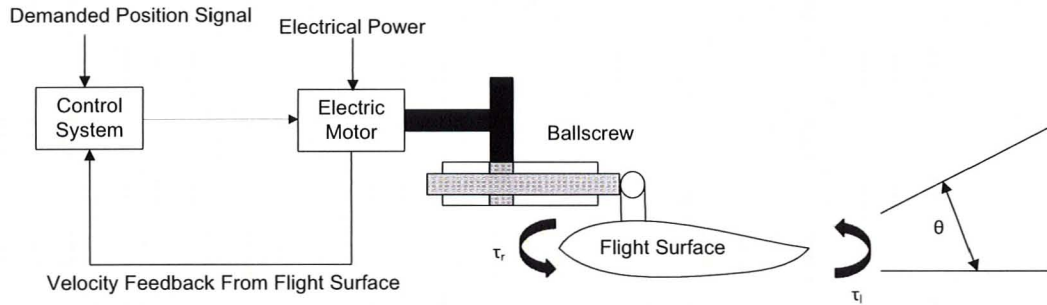


Figure 2.14. Basic Structure of an EMA.

An example of an EMA developed by TRW Aeronautical Systems can be seen in the figure 2.15:

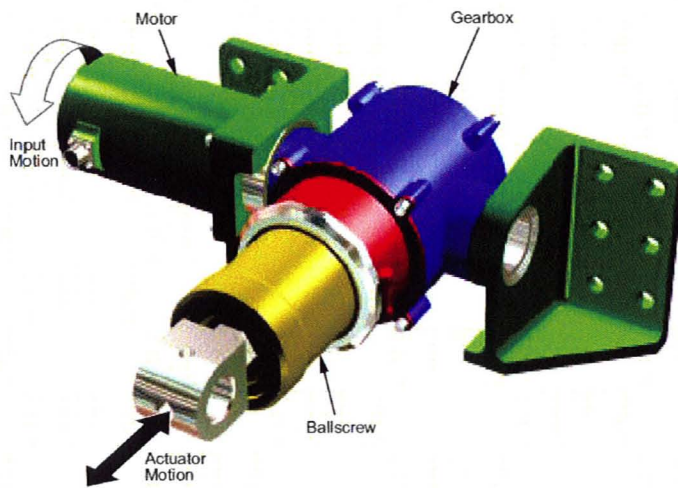


Figure 2.15. An EMA for high-power flight controls [13].

Typically there are no sensors on the flight surface that feedback position to the controller due to reliability concerns as the sensor would be exposed to harsh environments. However, there are some cases where there is position feedback. Some fighter aircraft have this where the feedback sensor is highly insulated from the environment.

Habibi, Roach and Luecke developed an overall mathematical model of an EMA system and used this model to develop novel inner-loop control strategies [12]. The first step was to understand the torque output of the servomotor. The mathematical model of a brushless servomotor is well understood. The first step in modeling pertains to the servomotor. The torque output from a brushless servomotor is described by equations 2.33-2.35 [12].

$$T_m = K_c i \quad (2.33)$$

$$i = G_1(V_c - K_w \dot{\theta}) \quad (2.34)$$

$$G_1 = \frac{1/R_c}{(L_c/R_c)s + 1} \quad (2.35)$$

Where T_m is the motor torque (Nm), K_c is the motor gain (Nm/A), i is the input current (A), V_c is the input voltage (V), K_w is the back-emf constant (V/rad), $\dot{\theta}$ is the rotational speed of the servomotor (rad/s), R_c is the resistance of the servomotor windings (Ω), L_c is the inductance of the servomotor windings (H), K_e is the electrical circuit servomotor gain (Ω^{-1}) and τ_e is the servomotor electrical time constant (s).

The mechanical torque exerted on the load is given by equation 2.36 [12].

$$T_m = J_m \ddot{\theta}_m + K_{mv} \dot{\theta}_m + \frac{T_{load}}{N} + T_{mstatic} \quad (2.36)$$

Where J_m is the rotary inertia of the motor (Kg/m^2), $\dot{\theta}_m$ is the acceleration of the servomotor's rotor (rad/s^2), K_{mv} is the servomotor viscous friction (Ns/rad), $\dot{\theta}_m$ is the velocity of the servomotor's rotor (rad/s), T_{load} is the load of the ballscrew and the flight surface actuator (Nm), N is the ballscrew lead (m/rad) and $T_{mstatic}$ is the static friction experienced at startup (Nm).

The first two terms of equation 2.36 are linked to the construction of the servomotor, leading to the following transfer function:

$$G_{me} = \frac{1/K_{mv}}{\frac{J_m}{K_{mv}}s + 1} \quad (2.37)$$

Where G_{me} is the transfer function for the motor dynamics. From equations 2.33-2.37 the servomotor block diagram can be constructed as shown in figure 2.16.

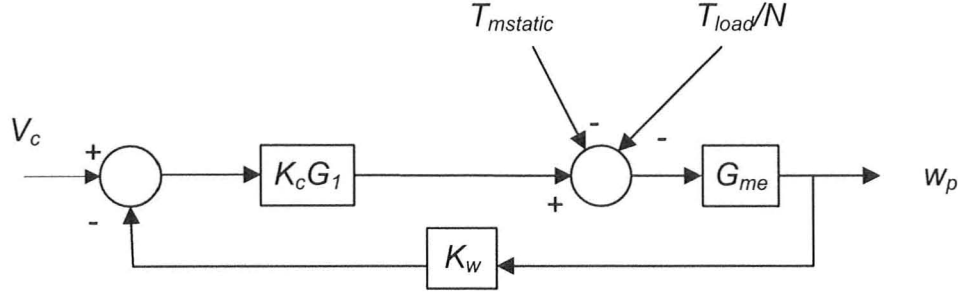


Figure 2.16. Electrical motor block diagram.

Since the input to the system is the demanded position the conversion between the input voltage and the demanded position is given by equation 2.38.

$$K_{conv} = \frac{V}{x} \quad (2.38)$$

The control strategy used in [12] involves Proportional-Integral-Derivative (PID) gains, G_{PID} , and requires consideration in the amplifier gain K_{conv} (V/m) as shown in figure 2.17. Furthermore, the model of the load is shown by equations 2.39 and 2.40.

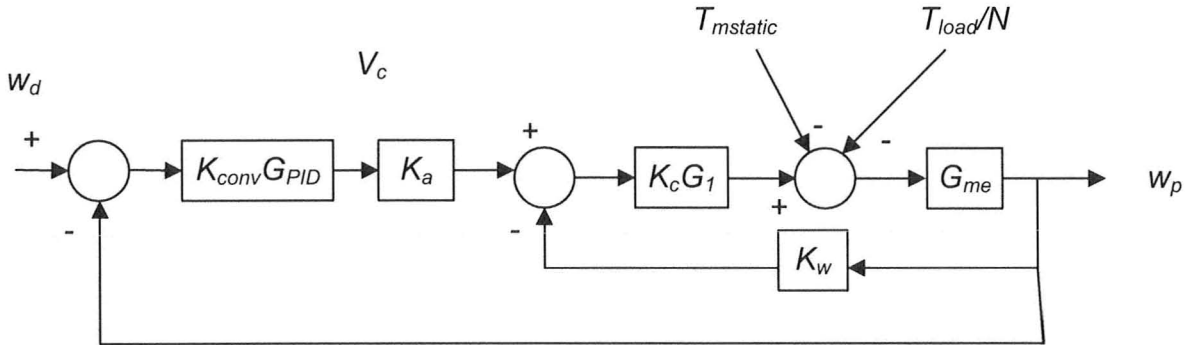


Figure 2.17. Closed-loop servomotor block diagram.

$$T_{load} = M\ddot{x} + B\dot{x} + Kx + T_{dist} \quad (2.39)$$

$$G_{load} = \frac{1}{Ms^2 + Bs + K} \quad (2.40)$$

Where K is the system stiffness (N/m), T_{dist} is any torque that acts as a disturbance (Nm) and G_{load} is the load transfer function.

The linkage between the load and the motor is obtained by the intermeshing of the ballscrew and the gear attached to the motor. The model at this point becomes highly non-linear due to the backlash in the gears. The backlash is modeled as $G_b(\theta)$ and G_T in [12]. The overall EMA block diagram with the outer-feedback loop can be seen in figure 2.18.

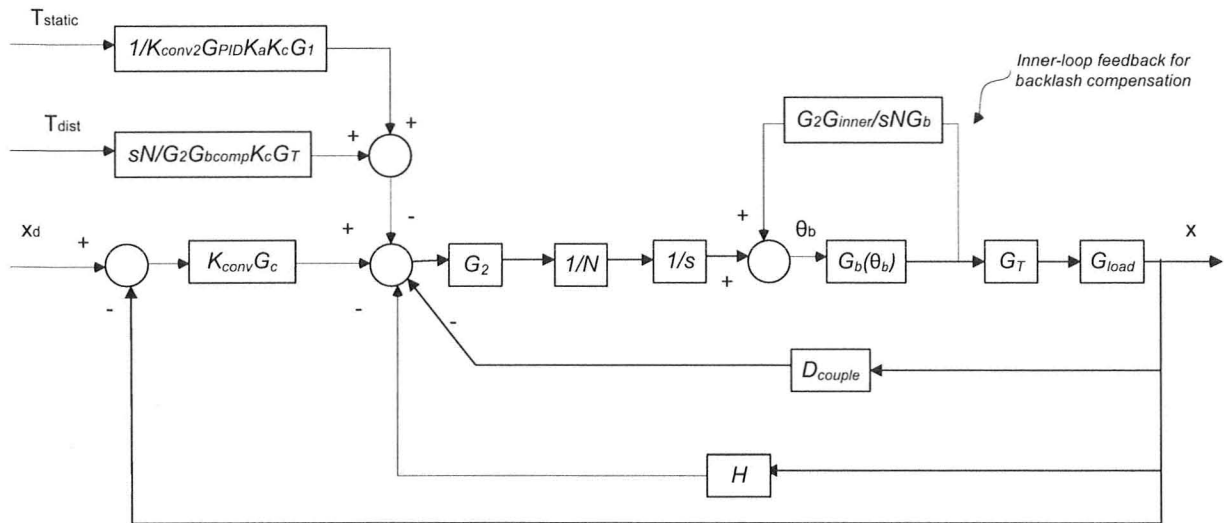


Figure 2.18. Closed-loop EMA control block diagram [12].

Where T_{static} is the torque element for static friction (Nm), T_{dist} is any torque disturbances in the system (Nm), G_2 is the closed-loop servomotor transfer function in figure 2.17, G_c is the transfer function that converts the positional error input to velocity error input, D_{couple} is the dynamic coupling term that takes into account the meshing between the ballscrew and the gear on the servomotor, H converts the feedback position into feedback velocity, G_T is the transfer function for backlash compliance, G_{inner} is the inner-loop feedback transfer function, N is the lead in the ballscrew (rad/m), G_b is the deadzone gain and K_{conv2} is another conversion factor (Vs/rad). Refer to [12] for complete details on all of the parameters listed above and the overall model.

The EMA is a practical solution for modular PBW flight surface actuation and is used in several modern aircraft. The main advantages of the EMA include:

- Modular design, which lends itself to simple maintenance and use across several platforms.
- Ease of control.
- Does not leak since fluid is not used for power transmission.

Their disadvantages include:

- The use of a ballscrew adds backlash.
- There is a safety concern due to a failure mode that involves jamming of the actuator because of solid contaminants.

2.5 Conclusion

The basic concept of flight surface actuation was introduced in this chapter along with several conventional systems used to actuate flight surfaces throughout the history of flight. Mathematical models were presented for centralized electro-hydraulic actuators and EMA's. Chapter three will discuss in detail the concept of hydrostatic actuation systems and will introduce the Electro-Hydrostatic Actuator (EHA), which is the focus of this research.

Chapter 3 Hydrostatic Actuation Systems

This chapter details the concept of hydrostatic actuation systems and provides insight into their current and potential application to PBW systems. The two main forms of hydrostatic actuation systems are the variable-displacement piston pump and the fixed-displacement external gear pump types. This chapter details the architecture and mathematical models of both. The fixed-displacement external gear pump driven system is the basis of the Electro-Hydrostatic Actuator (EHA), and will be discussed in greater detail as it is the focus of this research.

3.1 Variable-Displacement Piston Pump Hydrostatic Actuation Systems

As mentioned in chapter 2 there are some major deficiencies to valve controlled centralized hydraulic systems for flight surface actuation. The most serious of these drawbacks is their inefficient use of energy. A different form of hydraulic actuation system exists that does not involve energy loss due to orifice flow or channeling of fluid over a relief valve when all of the input flow is not required during actuation. A hydrostatic actuation system has a closed-loop architecture in that the return flow from the actuator goes directly back to the inlet of the pump. This closed-loop architecture allows it to be developed into a PBW system. This form of architecture can be seen in figure 3.1.

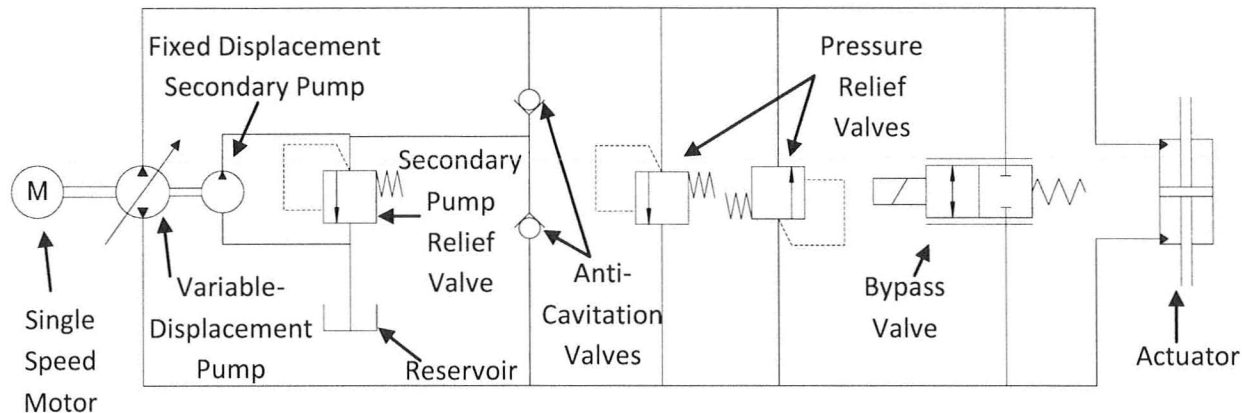


Figure 3.1. Hydrostatic actuation system.

The main difference between this and a conventional hydraulic actuation system is that the flow is controlled by the pump itself. In figure 3.1, flow control is achieved by a variable displacement pump. The main types of variable displacement pumps are the axial piston type and the vane type. Axial piston pumps use a series of pistons attached to a common swash plate. The pitch of this swash plate is varied

through active control or passive pressure feedback to alter the flow output. Piston pumps provide high output flows and pressures but tend to be bulky and complex. Variable vane pumps operate by using a series of extending and retracting plates (or vanes) whose position is dependent on the rotary orientation of the central lobe they are attached to. To vary the volumetric displacement the lobe is shifted in its containment chamber back and forth to alter the volume of fluid the vanes can capture. Although simple and compact variable vane pumps are not employed in hydrostatic circuits for flight surface actuators since they require a speed of at least 52.4rads/sec (500rpm) and they cannot displace enough fluid at a high enough pressure [14]. For this reason the majority of flight surface actuation systems have employed an axial piston pump in the past.

Note that in figure 3.1 there is a proportional bypass valve. This allows the actuator in some circumstances to be controlled more accurately since partial flow is allowed to cross ports [13]. This is advantages for high accuracy control since a variable-displacement pump is highly non-linear and difficult to model, as will be seen later in this section. There is also smaller fixed displacement secondary pump that provides extra fluid to the inlet to make up for leakage. This pump also ensures that there is a large enough static pressure to prevent cavitation.

When mathematically modeling a hydrostatic system such as the one seen in figure 3.1, if it is designed correctly, the significant dynamics of the system can be reduced down to the motor, pump, actuator and the stiffness of the system. The following modeling process will ignore the effects of the throttling valve since it will assume the axial piston pump sizing is performed correctly.

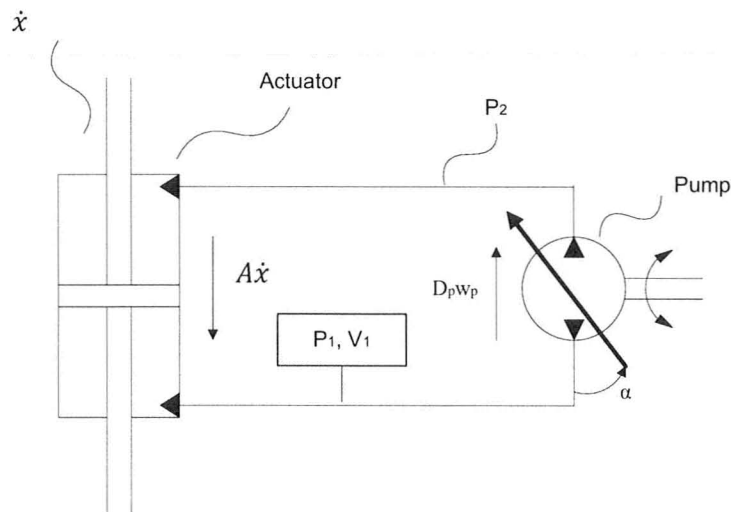


Figure 3.2. Dynamically significant components of a hydrostatic system.

Where α is the swash plate angle of the variable-displacement pump (rad), D_p is the volumetric displacement of the pump (m^3/rad) and w_p is the pump shaft speed (rad/s). Modeling of each section is shown below.

3.1.1 Modeling of the Actuator with Attached Load for the Hydrostatic System

To find the acceleration of the actuator Newton's second law can be applied along with equation 2.29, which gives the following relationship:

$$M_a \ddot{x} = F_{ap} - M_L \ddot{x} - B \dot{x} \quad (3.1)$$

Where M_a is the mass of the actuator piston (Kg), F_{ap} is the applied force (N), M_L is the mass of the load (Kg), and B is the damping caused by the actuator (Ns/m). The applied force across the piston can be expressed as:

$$F_{ap} = A(P_1 - P_2) \quad (3.2)$$

Combining equations 3.1 and 3.2 and solving for the acceleration yields:

$$\ddot{x} = \frac{A(P_1 - P_2) + B\dot{x}}{M_L + M_a} \quad (3.3)$$

Knowing that the combined load is $M = M_a + M_L$ the acceleration can be simplified using the following equation:

$$\ddot{x} = \frac{AP_1}{M} - \frac{AP_2 + B\dot{x}}{M} \quad (3.4)$$

Note that for the rest of the variable-displacement pump hydrostatic system analysis, it will be assumed that P_1 is the high pressure side.

3.1.2 Modeling of the Dynamics of the Hose in the Hydrostatic System

Assuming that P_1 is the high pressure side modeling of its pressure rise, \dot{P}_1 , is described by the following equation [15]:

$$\dot{P}_1 = \frac{\beta_s}{V_1} Q_h \quad (3.5)$$

Where β_s is the combined stiffness of the system (Pa), V_1 is the volume of fluid in the hose and the actuator in chamber 1, and Q_h is the net volumetric flow into the hose only. For simplicity leakage will be ignored here. Therefore, flow into the hose can also be modeled by the following equation [15]:

$$Q_h = G_p \alpha - A \dot{x} \quad (3.6)$$

Where G_p is the variable-displacement pump gain (m^3/srad). Combining equations 3.5 and 3.6 yields the following relationship:

$$\dot{P}_1 = \frac{\beta_s}{V_1} G_p \alpha - \frac{\beta_s}{V_1} A \dot{x} \quad (3.7)$$

3.1.3 Modeling of a Variable-Displacement Axial Piston Pump for Hydrostatic Systems

Modeling of a variable-displacement piston pump for a hydrostatic system was performed by Manring and Luecke [15] with using a hydraulic motor as the actuator. The following analysis will use the model from [15] but will augment it with a double-acting, double rod cylinder instead of a hydraulic motor. The major components of a variable-displacement piston pump can be seen in figure 3.3.

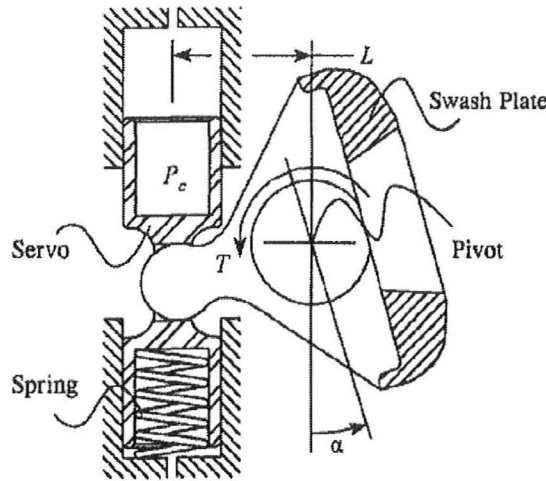


Figure 3.3. Forces acted upon a swash plate in an axial piston pump [15].

A relationship for the naturally induced torque on the swash plate, T_v (Nm), is used to model the dynamics of the pump. This can be seen in equation 3.8 [15].

$$T_v = K_{is}\alpha - K_{pr}(P_1 - P_2) \quad (3.8)$$

Where K_{is} is the coefficient of inertial swash plate torque (Nm/rad) and K_{pr} is the coefficient of pressure swash plate torque (Nm/Pa) as defined in equations 3.9 and 3.10 respectively.

$$K_{is} = \frac{N_p M_p r^2 w_p^2}{2} \quad (3.9)$$

$$K_{pr} = \frac{N_p A_p r \gamma}{2\pi} \quad (3.10)$$

Where N_p is the number of pistons in the pump, M_p is the mass of a single piston (kg), r is the piston pitch-radius (m), A_p is the cross-sectional area of the piston (m^2) and γ is the pressure carry-over angle on the plate.

The swash plate angle at any given time is complex to model since it is a function of other variables besides demanded position. Manring and Luecke developed a relationship and a control

strategy for the swash plate angle as defined by equation 3.11 [15]. The equation below has been augmented so that it applies to a linear actuator instead of a hydraulic motor.

$$\dot{\alpha} = \frac{AG_s}{A_s L D_{pv}} \dot{x} - \frac{V_{so}}{V_2} \frac{K_{pr}}{(A_s L)^2} (G_p \alpha - A \dot{x}) \quad (3.11)$$

Where G_s is the control gain, A_s is the area of the servo piston seen in figure 3.3 (m^2), L is the swash plate arm length (m), D_{pv} is the instantaneous volumetric displacement of the pump (m^3/rad), \dot{x} is the error between the demanded and actual velocity of the actuator (m/s) and V_{so} is the nominal servo piston volume (m^3). Note that the instantaneous volumetric displacement of the pump is calculated using the following relationship:

$$D_{pv} = \frac{G_p \alpha}{w_p} \quad (3.12)$$

To obtain the overall dynamic model equations 3.4, 3.7 and 3.11 are combined in state-space form in equation 3.13 [15].

$$\begin{bmatrix} \ddot{x} \\ \dot{P}_1 \\ \dot{\alpha} \end{bmatrix} = \begin{bmatrix} -a & b & 0 \\ -d & 0 & f \\ (g_1 - g_2) & 0 & -j \end{bmatrix} \begin{bmatrix} \dot{x} \\ P_1 \\ \alpha \end{bmatrix} + \begin{bmatrix} -u \\ 0 \\ w \end{bmatrix} \quad (3.13)$$

Where,

$$a = \frac{B}{M}, \quad b = \frac{A}{M}, \quad d = \beta_s \frac{A}{V_1}, \quad f = \beta_s \frac{G_p}{V_1}, \quad g_1 = \frac{AV_{so}K_{pr}}{V_1(A_sL)^2}, \quad g_2 = \frac{AG_s}{A_s L D_{pv}}, \quad j = \frac{V_{so}K_{pr}G_p}{V_1(A_sL)^2}$$

$$u = -\frac{A}{M} P_2, \quad w = g_2 \dot{x}_d$$

Where \dot{x}_d is the desired actuator velocity (m/s). The transient response of the system can be determined by solving for the eigenvalues of 3.13 [15]. The corresponding block diagram for equation 3.13 is shown in figure 3.4.

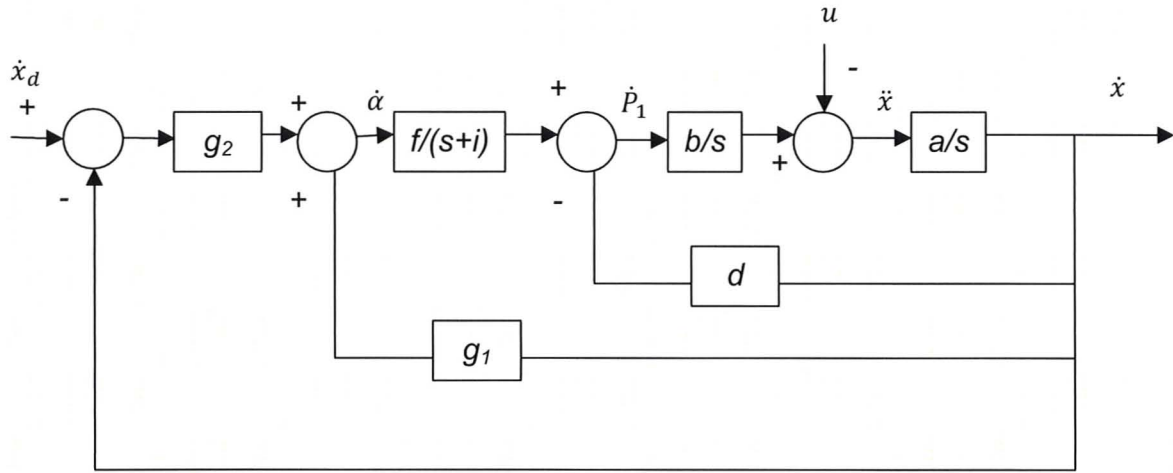


Figure 3.4. Variable-displacement piston pump hydrostatic actuation system control block diagram [15].

The proposed system of figure 3.4 can be used for flight control but has some inefficiencies. These include the need for a heavy variable displacement pump, a secondary pump and a small reservoir. Although this hydrostatic system is more efficient than a traditional hydraulic system, there is still power lost by the smaller pump forcing fluid over its corresponding relief valve and the motor continuously turning when the swash plate is at the neutral position. An example of a dual variable-displacement piston pump PBW flight surface actuator can be seen in figure 3.5.

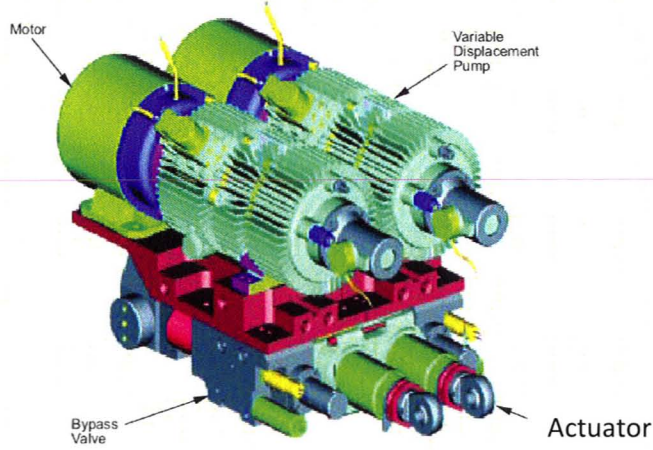


Figure 3.5. TRW Aeronautical Systems variable-displacement piston pump PBW flight surface actuator [13].

An updated form of a hydrostatic circuit has been developed which is more energy efficient and lighter than the variable-displacement pump hydrostatic actuator described above. This system is called the Electro-Hydrostatic Actuator (EHA) and will form the basis of this research. This circuit substitutes

the variable-displacement piston pump with a fixed-displacement external gear pump that uses a servomotor for control.

3.2 Electro-Hydrostatic Actuator (EHA)

The main differences between the variable-displacement piston pump hydrostatic system and the EHA are the type of pump used, the layout of the inner circuitry and the control strategy. In the EHA, the motion is controlled solely by a servomotor attached to a fixed-displacement gear pump as shown in figure 3.6.

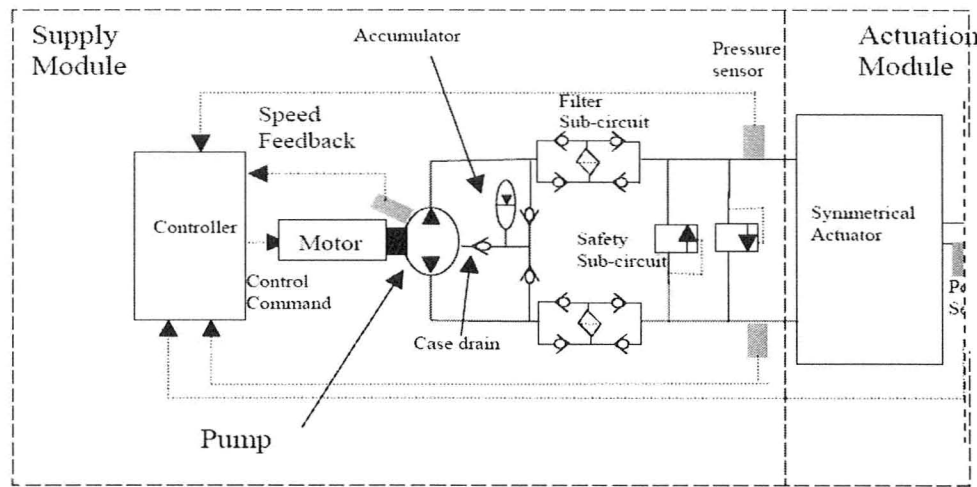


Figure 3.6. Schematic of the Electro-Hydrostatic Actuator (EHA) [16].

Substituting for the secondary make-up fluid pump is an inner circuit that combines an accumulator and a series of check valves. A check valve attached to the case drain allows fluid to be routed to the accumulator, circumventing the requirement for a reservoir. For bi-directional pumps a case drain is always required since internal leakage cannot be routed back to the inlet of the pump, which is the case in single direction pumps. The accumulator holds excess fluid that is available in case of two scenarios. The first is to prevent cavitation. Cavitation is the formation of vapour bubbles in a liquid that is very close to vacuum pressure [6]. These bubbles form in the inlet of the pump and then travel to the outlet through the pumping motion. When these bubbles become pressurized they implode and cause the gears and/or pump housing to pit. This wears the pump and introduces large contaminants into the system. The presence of the accumulator ensures that the inlet side of the pump does not go below atmospheric pressure, minimizing the chance of vapour bubbles forming. The accumulator holds a charge of 275-689KPa (40-100psi). This is enough pressure to avoid cavitation but it is also low enough

to allow flow from the case drain back into the circuit. If the pressure was too high the case drain check valve would not open and would cause the pump gears to vibrate and damage their casing.

The second scenario is providing make-up fluid for any dynamic leakage. Dynamic leakage occurs in the rod seals attached to the actuator and the shaft seal attached to the pump. Dynamic leakage is needed so that lubrication becomes available to the seals [14]. Dynamic leakage builds-up over time and if it is not compensated for, air bubbles can enter the system.

The filtering sub-circuit provides fluid conditioning for both sides of the fluid in a rectified manner. This means that irrespective of the flow direction, filtration flow is preserved in only one direction. In our analysis the filtering sub-circuit is excluded since it offers impedance to flow, which degrades the performance of the EHA by decreasing its bandwidth.

An external bi-directional gear pump is used due to its high power-to-weight ratio compared to piston pumps. External gear pumps can exert up to 20.86MPa (3000psi) of system pressure and have a volumetric efficiency of 85-90% [14]. Vane pumps can be manufactured to function bi-directionally but cannot develop high enough pressures, which eliminate their potential use.

3.2.1 EHA Mathematical Model

Symmetry in hydraulic systems simplifies the dynamic complexity of the model and it results in the same dynamic performance in both directions [16]. The majority of the pump leakage occurs across the ports and is modeled by a cross-port leakage coefficient ξ . The remainder of the pump leakage flows to the case drain and externally through the pump shaft seal. The latter is considered negligible and is often not taken into account.

The dynamic model of the pump can be described in terms of output flow. The factors that affect the output flow include:

- Volumetric displacement per revolution
- Cross-port leakage
- External leakage to case drain
- Compressibility of oil during pressure changes

3.2.1.1 Fixed-Displacement External Gear Pump Mathematical Model

The equations for pump flow on both ports are described below [17]:

$$Q_a = D_p w_p - \xi(P_a - P_b) - C_{ep}(P_a - P_r) - \frac{V_a}{\beta_e} \frac{dP_a}{dt} \quad (3.14)$$

$$Q_b = D_p w_p - \xi(P_a - P_b) + C_{ep}(P_b - P_r) + \frac{V_b}{\beta_e} \frac{dP_b}{dt} \quad (3.15)$$

Where Q_a, Q_b are the respective pumps flows though ports a and b (m^3/s), ξ is the cross-port leakage (m^3/sPa), P_a, P_b are the respective pressures at ports a and b (Pa), C_{ep} is the leakage flowing externally and to the case drain (m^3/sPa), V_a, V_b are the respective volumes of fluid in the circuit connected to ports a and b (m^3), and β_e is the effective bulk modulus of the fluid (Pa). $D_p w_p$ represents the volumetric flow, $-\xi(P_a - P_b) - C_{ep}(P_a - P_r)$ and $-\xi(P_a - P_b) + C_{ep}(P_b - P_r)$ represent the leakage flows and $-\frac{V_a}{\beta_e} \frac{dP_a}{dt}$ and $\frac{V_b}{\beta_e} \frac{dP_b}{dt}$ represent the compressibility flows.

Note that a smaller volumetric displacement of the pump implies less flow per revolution, giving a higher control resolution. As a consequence the maximum actuator speed and bandwidth would be reduced. A trade-off exists between the actuator velocity and its positional accuracy.

3.2.1.2 Hydraulic Actuator Mathematical Model

When designing a hydraulic circuit that requires a linear actuator the following parameters must be considered:

- Velocity
- Stroke
- Force
- Desired system pressure
- Accuracy

The actuator is the first component to be chosen in a hydraulic circuit since the pump and motor must be selected to satisfy the actuator performance. The actuator used in the EHA should be symmetrical such as a double-acting, double rod type seen in figure 3.6. Symmetry results in the same dynamic performance irrespective of flow direction, reduces the circuit complexity and increases overall reliability. Their disadvantage is they require a dead space to accommodate the side of the piston that is not connected to the load.

The dynamic model of the actuator can be described in terms of output flow. The factors that affect the output flow include:

- Working area of piston
- Linear velocity of actuator
- Internal and external leakage
- Compressibility of oil

The equations for actuator flow are as follows [17]:

$$Q_1 = A\dot{x} + \frac{A(x_o + x)}{\beta_e} \frac{dP_1}{dt} + LP_1 \quad (3.16)$$

$$Q_2 = A\dot{x} - \frac{A(x_o + x)}{\beta_e} \frac{dP_2}{dt} - LP_2 \quad (3.17)$$

Where x_o is the mean position of the actuator (m), and L is the actuator leakage coefficient (m^3/sPa).

3.2.1.3 Hydraulic Accumulator Mathematical Model

An accumulator takes advantage of the compressibility of gas to allow the storage of pressurized hydraulic fluid. Accumulators for hydraulic systems are widely used and provide features such as [14]:

- Shock pulsation damping
- Assist the pump to move an actuator
- Maintain system pressure in the event of leakage

The three main types of accumulators are gas charged, spring loaded, or weight loaded. The three types of gas charged accumulators are bladder, diaphragm and piston. The type employed in the EHA is a diaphragm type.

The model used for the accumulator in the inner circuit is as follows [18]:

$$\begin{aligned}
P_{ac} - P_a > P_{vb}, \quad & Q_{ac1} = K_v(P_{ac} - P_a) \\
P_{ac} - P_a < P_{vb}, \quad & Q_{ac1} = 0 \\
P_{ac} - P_b > P_{vb}, \quad & Q_{ac2} = K_v(P_{ac} - P_a) \\
P_{ac} - P_b < P_{vb}, \quad & Q_{ac2} = 0 \\
P_{case} - P_{ac} > P_{vb}, \quad & Q_{ac,in} = Q_{case} \\
P_{case} - P_{ac} < P_{vb}, \quad & Q_{ac,in} = 0
\end{aligned} \tag{3.18}$$

Where P_{ac} is the pressure of the accumulator (Pa), P_{vb} is the pressure needed to lift the poppet in the check valve off of its seat (Pa), Q_{ac1} , Q_{ac2} are the flows going from the accumulator to chambers 1 and 2 respectively (m^3/s), K_v is the resistance to flow in the check valves (m^3/Pa), P_{case} is the case drain pressure (Pa), $Q_{ac,in}$ is the flow coming into the inner circuit from the case drain (m^3/s) while Q_{case} is the flow through the case drain.

If the flow from the case drain exceeds the flow going back to the main chambers from the inner circuit then the accumulator charges with fluid. If this flow is gradual it is isothermal. The equation for isothermal expansion and compression of gas is [18]:

$$P_{ac} = \frac{P_{ac_{initial}} V_{ac_{initial}}}{V_{ac_{initial}} + \int Q_{ac} dt} \tag{3.19}$$

Although an accumulator is present in the system for purposes of mathematical modeling its dynamics are not included since it is assumed that they are insignificant [18].

3.2.1.4 Pressure Relief Valve Mathematical Model

The pressure relief valves ensure that the differential pressure between both ports does not exceed a maximum operating pressure. In terms of their effect on the model itself all they add is a saturation component to the pressure and do not affect any other parameter.

3.2.1.5 Servomotor/ Pump System Model

The dynamics of the servomotor and the pump attached to it play an important role in the overall model of the EHA. The pump defines the volumetric displacement of the fluid which affects the actuator speed and resolution as previously discussed. The servomotor becomes dynamically significant if the poles of

its continuous transfer function are less than ten times the magnitude of the poles of the hydraulic continuous transfer function. Pump and motor selection are crucial to the desired performance and should be carefully chosen. The required power of the system, which can be determined by the actuator speed and maximum pressure, along with the volumetric displacement, torque, servomotor rotational speed and pump efficiency must be balanced to obtain the optimum performance. When considering the servomotor a sensor that can feedback velocity for control purposes should be taken into account since they are usually integrated into the motor housing. Resolvers and rotary optical encoders are the main types that are used in industry.

The servomotors' mechanical and electrical time constants are combined to determine its overall transfer function. The relationship of the field current and input voltage is shown in equations 2.34 and 2.35 but is also shown below for convenience.

$$G_1 = \frac{i}{V_c - K_w \dot{\theta}_m}$$

$$G_1 = \frac{1/R_c}{(L_c/R_c)s + 1} = \frac{K_e}{\tau_e s + 1} \quad (3.20)$$

The torque generated by the motor is seen in equation 2.33 and is also shown below for convenience:

$$T_m = K_c i \quad (3.21)$$

Given that the servomotor is connected directly to the pump the torque exerted on the pump is given by the following equation [19]:

$$T_m = J_{pm} \dot{w}_p + (K_{p_{visc}} + K_{fric}) w_p + T_{db} + D_p (P_a - P_b) \quad (3.22)$$

Where J_{pm} is the rotary inertia of the servomotor and pump combined (Nms^2/rad), \dot{w}_p is the rotary acceleration of the pump (rad/s), $K_{p_{visc}}$ is the oil viscosity coefficient (Nms/rad), K_{fric} is the coefficient of friction (Nms/rad) and T_{db} is the deadband torque (Nm). The deadband torque is non-linear since it includes factors such as static friction and is affected by the gap between the gear teeth at the start of pump motion. Figure 3.7 shows the effect that deadband can have on the output speed of the

servomotor for a given input. This issue can be resolved using a high gain inner-loop controller for the motor, which will be discussed later in this chapter.

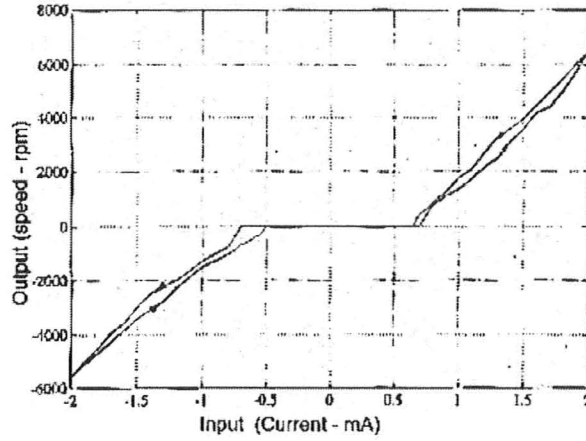


Figure 3.7. Deadband effect in the pump and motor in the EHA [18].

Since the torque of the servomotor equals the torque exerted by the pump equations 3.21 and 3.22 are combined to form:

$$K_c i = J_{pm} \dot{w}_p + (K_{pvisc} + K_{fric}) w_p + T_{db} + D_p(P_a - P_b) \quad (3.23)$$

Inserting equation 3.20 into 3.23 and taking the Laplace transform yields:

$$w_p (J_{pm}s + K_{pvisc} + K_{fric}) = K_c G_1 (V_c - K_w \dot{\theta}) - T_{db} - D_p(P_a - P_b) \quad (3.24)$$

The coupling used between the motor and pump allows zero backlash, meaning that $w_p = \dot{\theta}$. From this w_p can be isolated and the following relationship results:

$$w_p = \frac{K_c G_1 V_c - T_{db} - D_p(P_a - P_b)}{(J_{pm}s + K_{pvisc} + K_{fric} + K_c K_w G_1)} \quad (3.25)$$

$$w_p = G_2 (K_c G_1 V_c - T_{db} - D_p(P_a - P_b)) \quad (3.26)$$

Where:

$$G_2 = \frac{1}{J_{pm}s + K_{p_{visc}} + K_{fric} + K_c K_w G_1} \quad (3.27)$$

The resulting block diagram becomes:

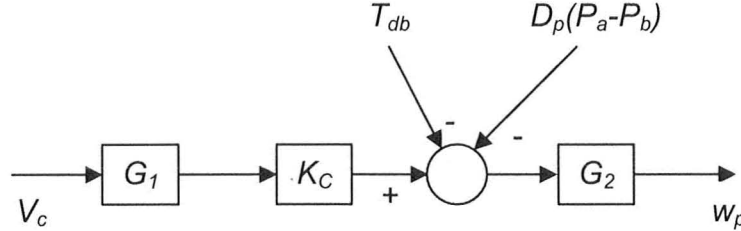


Figure 3.8. Representation of equation 3.26.

Since the servomotor uses a high gain inner-loop control (explained later in this chapter) strategy that minimizes the effects of the friction at the pump and motor figure 3.8 transforms into 3.9 below.

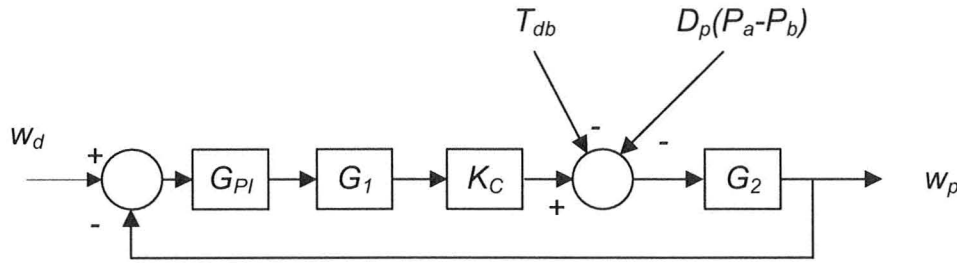


Figure 3.9. Block diagram of inner-loop control strategy.

Where w_d is the demanded velocity of the motor and G_{PI} is the high gain controller, represented by:

$$G_{PI} = \frac{K_p s + K_I}{s} \quad (3.28)$$

Where K_p and K_I are the proportional and integral gains respectively. The resulting motor and pump closed-loop relationship is expressed by:

$$w_p = \frac{G_2(G_{PI}G_1K_c w_d - T_{db} - D_p(P_a - P_b))}{1 + G_2G_{PI}G_1K_c} \quad (3.29)$$

Equation 3.29 shows that the effect of T_{db} and $D_p(P_a - P_b)$ can be minimized by using a high gain inner-loop velocity controller ($G_2 G_{PI} G_1 K_c w_d \gg G_2$) [16].

3.2.1.6 Hydraulic Subsystem Model

When mathematically modeling the hydraulic subsystem dynamics, several assumptions must be made for linearization:

- All tubing that connects the components together is rigid. The elasticity of steel tube is high enough that the resulting expansion under pressure can be ignored. The casings for all other components are assumed to be rigid as well.
- The motor-to-pump coupling is torsionally rigid, meaning that $w_p = \dot{\theta}$.

Knowing that the flow in and out of the pump are equal to the flow in and out of the actuator the load flow, Q_L , can be determined as follows:

$$Q_L = \frac{Q_a + Q_b}{2} = \frac{Q_1 + Q_2}{2} = D_p w_p \quad (3.30)$$

There are two potential operating modes the system is exposed to, one where the inner circuit is negligible and one where it is dynamically significant. The first mode to be evaluated will be the mode where the inner circuit is dynamically insignificant. This occurs during normal operation. If the inner circuit dynamics are negligible then the pressure difference of the pump is $P_a - P_b$. If P_b falls below P_r , the inner circuit dynamics are not-negligible and the pressure difference of the pump is $P_a - P_r$.

3.2.1.7 EHA model under Mode 1

Substituting equations 3.14 through 3.17 into 3.30 yields:

$$\begin{aligned} A\dot{x} + \frac{A(x_o + x)}{\beta_e} \frac{dP_1}{dt} + LP_1 + A\dot{x} - \frac{A(x_o - x)}{\beta_e} \frac{dP_2}{dt} - LP_2 \\ = D_p w_p - \xi(P_a - P_b) - C_{ep}(P_a - P_r) - \frac{V_a}{\beta_e} \frac{dP_a}{dt} + D_p w_p \\ - \xi(P_a - P_b) + C_{ep}(P_b - P_r) + \frac{V_b}{\beta_e} \frac{dP_b}{dt} \end{aligned} \quad (3.31)$$

The connection between the pump and the actuator has a resulting pressure drop, P_{pipe} , which is modeled by using the Darcy-Weisbach pipe flow equation [20]:

$$P_{pipe} = \frac{f l \rho}{D} V^2 \quad (3.32)$$

Where f is the dimensionless friction factor of the pipe, l is length of the pipe (m), ρ is the density of the fluid (kg/m^3), D is the inner diameter of the pipe (m) and V is the velocity of the fluid. For convenience the Darcy-Weisbach pipe flow equation is stated in terms of the flow and a single parameter that encompasses the physical characteristics of the pipe:

$$P_{pipe} = \frac{f l \rho}{D} V^2 = K_{pipe} Q_1^2 = K_{pipe} D_p^2 w_p^2 \quad (3.33)$$

Where K_{pipe} is the coefficient relating flow to pressure drop in the pipe (Ns^2/m^8). In its linearized form it can be expressed at the operating flow w_{pop} as:

$$\Delta P_{pipe} \approx 2K_{pipe} D_p^2 \Delta w_p w_{pop} \quad (3.34)$$

From this the relationship between the pump port and actuator port pressures can be modeled as:

$$P_a = P_1 + P_{pipe} \quad (3.35)$$

$$P_b = P_2 - P_{pipe} \quad (3.36)$$

It is important to note that the following relationships exists:

$$V_a = V_o + Ax \quad (3.37)$$

$$V_b = V_o - Ax \quad (3.38)$$

Where V_o is the pipe plus mean actuator chamber volume (m^3). It is also assumed that $\frac{dP_a}{dt} \approx \frac{dP_1}{dt}$ and $\frac{dP_b}{dt} \approx \frac{dP_2}{dt}$ [11]. Using these assumptions, knowing that $V_o = Ax_o$ and substituting equations 3.35 through 3.38 into 3.31 the following relationship results:

$$\begin{aligned} 2A\dot{x} + \frac{V_o}{\beta_e} \left(\frac{dP_1}{dt} - \frac{dP_2}{dt} \right) + L(P_1 - P_2) + \frac{Ax}{\beta_e} \left(\frac{dP_1}{dt} + \frac{dP_2}{dt} \right) \\ = 2D_p w_p - C_{ep}(P_1 - P_2 + 2P_{pipe}) - \frac{V_o}{\beta_e} \left(\frac{dP_1}{dt} - \frac{dP_2}{dt} \right) \\ - 2\xi(P_1 - P_2 + 2P_{pipe}) - \frac{Ax}{\beta_e} \left(\frac{dP_1}{dt} + \frac{dP_2}{dt} \right) \end{aligned} \quad (3.39)$$

Due to symmetry of the actuator $\frac{dP_1}{dt} \approx -\frac{dP_2}{dt}$. Taking this into account and rearranging equation 3.39 yields:

$$\begin{aligned} D_p w_p = A\dot{x} + \frac{V_o}{\beta_e} \left(\frac{dP_1}{dt} - \frac{dP_2}{dt} \right) + \frac{L}{2}(P_1 - P_2) \\ + \left(\frac{C_{ep}}{2} + \xi \right) (P_1 - P_2 + 2P_{pipe}) \end{aligned} \quad (3.40)$$

The load on the EHA is a horizontal mass and can be modeled using the following equation for force:

$$F = (P_1 - P_2)A = M\ddot{x} + B\dot{x} \quad (3.41)$$

$$(P_1 - P_2) = \frac{M\ddot{x} + B\dot{x}}{A} \quad (3.42)$$

$$\left(\frac{dP_1}{dt} - \frac{dP_2}{dt} \right) = \frac{M\ddot{x} + B\dot{x}}{A} \quad (3.43)$$

Substituting equations 3.42 and 3.43 into equation 3.40 yields:

$$\begin{aligned}
D_p w_p = A\dot{x} + \frac{V_o}{\beta_e} \left(\frac{M\ddot{x} + B\ddot{x}}{A} \right) + \frac{L}{2} \left(\frac{M\ddot{x} + B\dot{x}}{A} \right) \\
+ \left(\frac{C_{ep}}{2} + \xi \right) \left(\frac{M\ddot{x} + B\dot{x}}{A} + 2P_{pipe} \right)
\end{aligned} \tag{3.44}$$

Expanding equation 3.44 yields:

$$\begin{aligned}
D_p w_p &= A\dot{x} + \frac{V_o M \ddot{x}}{A \beta_e} + \frac{V_o B \ddot{x}}{A \beta_e} + \frac{LM \ddot{x}}{2A} + \frac{LB \dot{x}}{2A} + \frac{C_{ep} M \ddot{x}}{2A} + \frac{C_{ep} B \dot{x}}{2A} + C_{ep} P_{pipe} + \frac{\xi M \ddot{x}}{A} + \frac{\xi B \dot{x}}{A} + 2P_{pipe} \xi \\
D_p w_p &= \left(\frac{V_o M}{A \beta_e} \right) \ddot{x} + \left(\frac{V_o B}{A \beta_e} + \frac{LM}{2A} + \frac{C_{ep} M}{2A} + \frac{\xi M}{A} \right) \ddot{x} + \left(A + \frac{LB}{2A} + \frac{C_{ep} B}{2A} + \frac{\xi B}{A} \right) \dot{x} + C_{ep} P_{pipe} + 2P_{pipe} \xi \\
D_p w_p - P_{pipe} (C_{ep} + 2\xi) &= \left(\frac{V_o M}{A \beta_e} \right) \ddot{x} + \left(\frac{V_o B + LM \beta_e / 2 + C_{ep} M \beta_e / 2 + \xi M \beta_e}{A \beta_e} \right) \ddot{x} \\
&\quad + \left(\frac{A^2 \beta_e + LB \beta_e / 2 + C_{ep} B \beta_e / 2 + \xi B \beta_e}{A \beta_e} \right) \dot{x}
\end{aligned} \tag{3.45}$$

Substituting equation 3.34 into 3.45 yields:

$$\begin{aligned}
D_p w_p (1 - 2K_{pipe} D_p w_{pop} (C_{ep} + 2\xi)) &= \left(\frac{V_o M}{A \beta_e} \right) \ddot{x} + \left(\frac{V_o B + LM \beta_e / 2 + C_{ep} M \beta_e / 2 + \xi M \beta_e}{A \beta_e} \right) \ddot{x} \\
&\quad + \left(\frac{A^2 \beta_e + LB \beta_e / 2 + C_{ep} B \beta_e / 2 + \xi B \beta_e}{A \beta_e} \right) \dot{x}
\end{aligned} \tag{3.46}$$

Taking the Laplace transform of 3.46 in the form $G(s) = \frac{x(s)}{w(s)}$ yields:

$$\begin{aligned}
\frac{x(s)}{w(s)} &= \frac{D_p (1 - 2K_{pipe} D_p w_{pop} (C_{ep} + 2\xi))}{\left(\frac{V_o M}{A \beta_e} \right) s^3 + \left(\frac{V_o B + LM \beta_e / 2 + C_{ep} M \beta_e / 2 + \xi M \beta_e}{A \beta_e} \right) s^2 + \left(\frac{A^2 \beta_e + LB \beta_e / 2 + C_{ep} B \beta_e / 2 + \xi B \beta_e}{A \beta_e} \right) s}
\end{aligned} \tag{3.47}$$

It can be assumed that $2K_{pipe}D_p w_{pop}(C_{ep} + 2\xi) \ll 1$ in practice, which leaves the equation:

$$\frac{x(s)}{w(s)} = \frac{D_p}{\left(\frac{V_o M}{A\beta_e}\right)s^3 + \left(\frac{V_o B + LM\beta_e/2 + C_{ep}M\beta_e/2 + \xi M\beta_e}{A\beta_e}\right)s^2 + \left(\frac{A^2\beta_e + LB\beta_e/2 + C_{ep}B\beta_e/2 + \xi B\beta_e}{A\beta_e}\right)s} \quad (3.48)$$

In the general form the hydraulic transfer function can be described as:

$$\frac{x(s)}{w(s)} = \frac{\frac{A\beta_e D_p}{V_o M}}{s^3 + \left(\frac{B}{M} + \left(\frac{L}{2} + \frac{C_{ep}}{2} + \xi\right)\frac{\beta_e}{V_o}\right)s^2 + \left(A^2 + \left(\frac{L}{2} + \frac{C_{ep}}{2} + \xi\right)B\right)\frac{\beta_e}{V_o M}s} \quad (3.49)$$

It is clear from equation 3.49 that the overall leakage is represented by $\frac{L}{2} + \frac{C_{ep}}{2} + \xi$. For convenience a lumped representation is used such that, $L_T = \frac{L}{2} + \frac{C_{ep}}{2} + \xi$. The final transfer function for the hydraulic subsystem becomes:

$$\frac{x(s)}{w(s)} = \frac{\frac{A\beta_e D_p}{V_o M}}{s^3 + \left(\frac{B}{M} + \frac{L_T\beta_e}{V_o}\right)s^2 + (A^2 + L_T B)\frac{\beta_e}{V_o M}s} \quad (3.50)$$

Equation 3.50 is third order, type 1 and in its general form can be represented by:

$$\frac{x(s)}{w(s)} = \frac{K_h w_{nh}^2}{s(s^2 + 2\zeta_h w_{nh}s + w_{nh}^2)} \quad (3.51)$$

Where:

$$w_{nh} = \sqrt{(A^2 + L_T B) \frac{\beta_e}{V_o M}} \quad (3.52)$$

$$\zeta_h = \left(\frac{B}{M} + \frac{L_T \beta_e}{V_o} \right) \frac{1}{2w_{nh}} \quad (3.53)$$

$$K_h = \frac{AD_p}{A^2 + L_T B} \quad (3.54)$$

The hydraulic natural frequency, the damping ratio and the gain show how parameters should be minimized or maximized for optimal performance. It can be seen that increasing the bulk modulus, β_e , and piston area, A , increases the natural frequency while increasing the overall volume, V_o , and mass, M , decreases the natural frequency. Intuitively this makes sense and resembles the general equation for the natural frequency assuming there is no leakage [21]:

$$w_{nh} = \sqrt{\frac{4A^2 \beta_e}{MV_o}} \quad (3.55)$$

This equation was developed assuming that fluid acts on one side of the cylinder. This equation multiplies the numerator by 2 instead of 1 which is shown by equation 3.52. Note that in equation 3.52 it is assumed that $A^2 \gg L_T B$, meaning that the effect of leakage is negligible.

If the goal of designing the EHA is to increase its bandwidth then equation 3.52 shows that it is preferable to have a high natural frequency. This means that the volume and mass of the system must be minimized while the bulk modulus and the area must be maximized. This comes at the cost of decreasing the damping ratio which could lead to potentially large oscillations at the natural frequency. As previously mentioned there is a balance between the accuracy of the system response and the maximum speed of the actuator. Neglecting leakage, equation 3.54 provides the hydraulic gain as:

$$K_h \approx \frac{D_p}{A} \quad (3.56)$$

A larger hydraulic gain will result in increased speed. The gain is proportional to the ratio of the volumetric displacement compared to the piston surface area. A larger volumetric displacement compromises the metering of the fluid flow and as a consequence sacrifices the accuracy of the response. The parameter used to tune the balance between desired system accuracy and actuator velocity is the hydraulic gain.

3.2.1.8 EHA model under Mode 2

In this case it is assumed that the inlet pressure equals the case drain pressure, $P_b \approx P_r$. This means that there is negligible pressure differential across the check valve between the case drain and the inlet. Since there is negligible pressure differential to open this check valve it can be assumed that there is no flow moving from the case drain to the inlet, so $C_{ep} \approx 0$. This also insinuates that there is no pressure differential occurring in the inlet of the pump, which means $\frac{dP_2}{dt} \approx \frac{dP_r}{dt} \approx 0$. Using these assumptions equation 3.39 changes into the form shown in 3.57:

$$\begin{aligned} 2A\dot{x} + \frac{V_o}{\beta_e} \frac{dP_1}{dt} + L(P_1 - P_2) + \frac{Ax}{\beta_e} \frac{dP_1}{dt} \\ = 2D_p w_p - \frac{V_o}{\beta_e} \frac{dP_1}{dt} - 2\xi(P_1 - P_2 + 2P_{pipe}) - \frac{Ax}{\beta_e} \frac{dP_1}{dt} \end{aligned} \quad (3.57)$$

Using the same assumptions as in mode 1 equation 3.57 can be simplified into 3.58:

$$\begin{aligned} A\dot{x} + \frac{Ax}{\beta_e} \left(\frac{dP_1}{dt} \right) + \frac{V_o}{\beta_e} \left(\frac{dP_1}{dt} \right) + \frac{L}{2}(P_1 - P_2) \\ = D_p w_p - \xi(P_1 - P_2 + 2P_{pipe}) \end{aligned} \quad (3.58)$$

When substituting for the pressure differentials equation 3.43 was used. Assuming that $\frac{dP_2}{dt} \approx 0$, equation 3.43 turns into equation 3.59:

$$\frac{dP_1}{dt} = \frac{M\ddot{x} + B\dot{x}}{A} \quad (3.59)$$

Equation 3.58 turns into equation 3.60:

$$\begin{aligned}
A\dot{x} + \frac{Ax}{\beta_e} \left(\frac{M\ddot{x} + B\ddot{x}}{A} \right) + \frac{V_o}{\beta_e} \left(\frac{M\ddot{x} + B\ddot{x}}{A} \right) + \frac{L}{2} \left(\frac{M\ddot{x} + B\dot{x}}{A} \right) \\
= D_p w_p - \xi \left(\frac{M\ddot{x} + B\dot{x}}{A} + 2P_{pipe} \right)
\end{aligned} \tag{3.60}$$

Solving for $D_p w_p$ yields:

$$\begin{aligned}
D_p w_p = A\dot{x} + \frac{(V_o + Ax)}{\beta_e} \left(\frac{M\ddot{x} + B\ddot{x}}{A} \right) + \frac{L}{2} \left(\frac{M\ddot{x} + B\dot{x}}{A} \right) \\
+ \xi \left(\frac{M\ddot{x} + B\dot{x}}{A} + 2P_{pipe} \right)
\end{aligned} \tag{3.61}$$

Equation 3.61 shows that this mode has a non-linear component $\frac{(V_o + Ax)}{2\beta_e} \left(\frac{M\ddot{x} + B\ddot{x}}{A} \right)$ which is due to the lack of symmetry in the system. To obtain a transfer function the position x must be linearized about a point. In this case it will be linearized about $x = 0$, or when the actuator is at its starting position. Equation 3.61 becomes:

$$\begin{aligned}
D_p w_p = A\dot{x} + \frac{V_o}{2\beta_e} \left(\frac{M\ddot{x} + B\ddot{x}}{A} \right) + \frac{L}{2} \left(\frac{M\ddot{x} + B\dot{x}}{A} \right) \\
+ \xi \left(\frac{M\ddot{x} + B\dot{x}}{A} + 2P_{pipe} \right)
\end{aligned} \tag{3.62}$$

By using the same procedure as in mode 1 the resulting transfer function becomes:

$$\frac{x(s)}{w(s)} = \frac{\frac{A\beta_e D_p}{V_o M}}{s^3 + \left(\frac{B}{M} + \left(\frac{L}{2} + \xi \right) \frac{\beta_e}{V_o} \right) s^2 + \left(A^2 + \left(\frac{L}{2} + \xi \right) B \right) \frac{\beta_e}{V_o M} s} \tag{3.63}$$

Note that the difference from mode 1 is that the total leakage is represented by $L_T = \frac{L}{2} + \xi$ instead of $L_T = \frac{L}{2} + \frac{c_{ep}}{2} + \xi$.

3.2.1.9 Combined Motor, Pump and Hydraulic System Model

Before a general model of the EHA system can be calculated, a control strategy must be developed. The control strategy used in the EHA proposed in [18] uses two feedback loops. The first is the inner-loop feedback using the velocity of the pump-motor. This controller takes advantage of a high PI gain which aims to desensitize the system to the deadband as previously discussed. The second is an outer-loop feedback control of the position. Before an overall model can be obtained the hydraulic portion must be known where the input is flow and the output is actuator velocity. This is shown in a block diagram form in figure 3.10.

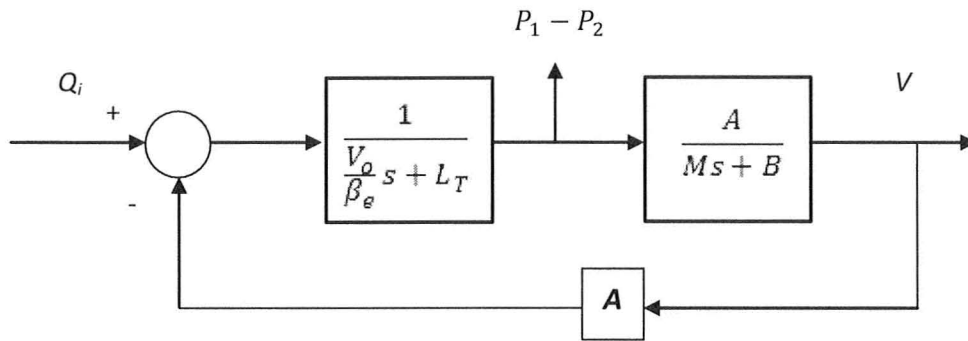


Figure 3.10. Closed-loop diagram of hydraulic system with flow as the input and velocity as the output.

In figure 3.10, Q_i is the volumetric flow into the actuator (m^3/s) and V is the velocity of the actuator (m/s). Note that cross-port pressure can be detected here which is useful when coupling the hydraulic portion with the pump-servomotor. Altering figure 3.10 to show the input and output variables of equation 3.50 yields the block diagram shown in figure 3.11.

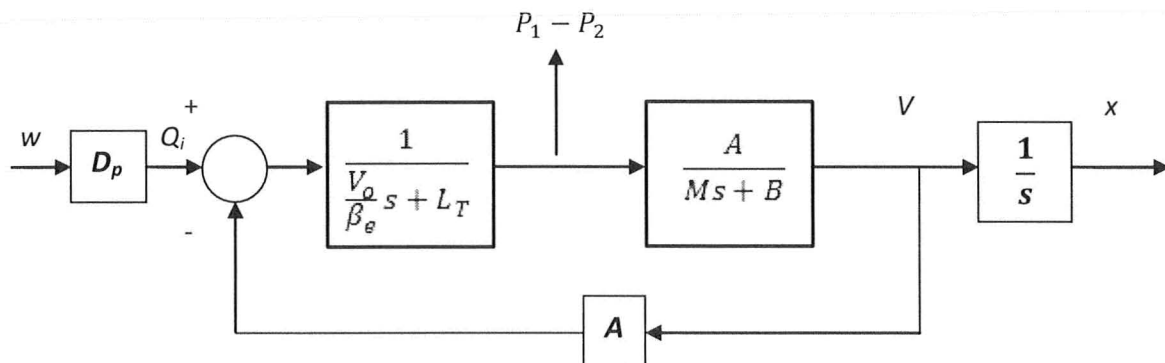


Figure 3.11. Closed-loop diagram of hydraulic system with motor speed as the input and position as the output.

Combining figure 3.11 with the servomotor and closing the position loop yields the block diagram shown in figure 3.12.

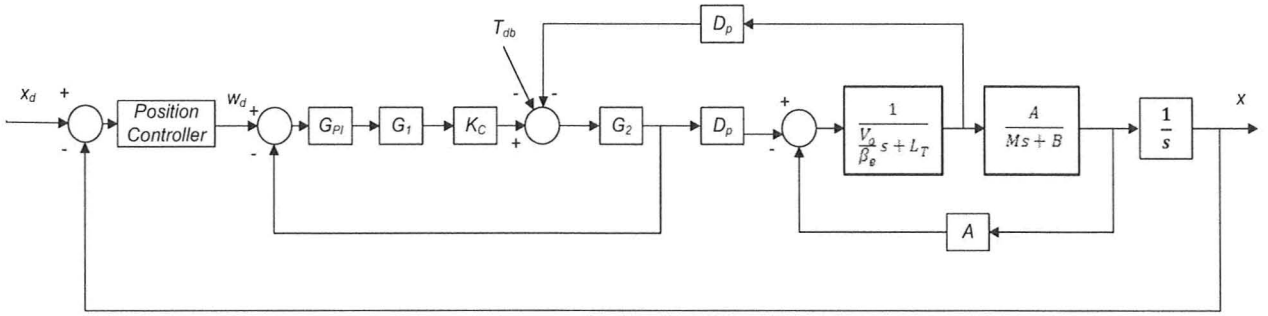


Figure 3.12. Closed-loop diagram of the overall system.

Note that the cross-port differential pressure in this form can be multiplied by the volumetric displacement in order to model the real-time torque applied to the pump. As previously mentioned the effect of this dynamic coupling manifested by the pressure fluctuations at the pump (i.e. $D_p(P_a - P_b)$) is minimized by using the high gain inner-loop control strategy of the motor, provided that the servomotor torque is not saturated. If this term is negligible then the servomotor and pump transfer function can be multiplied directly with the hydraulic system model as shown in figure 3.13.

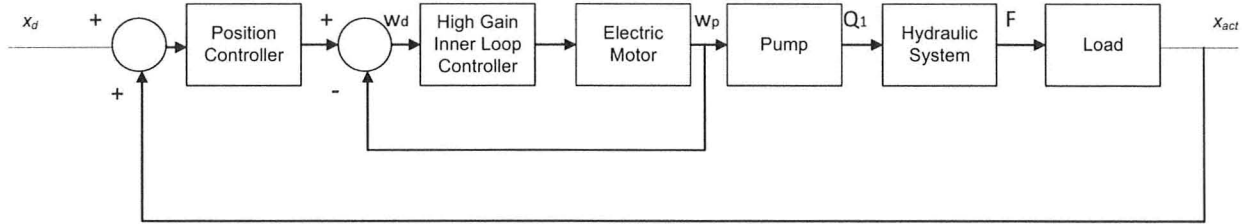


Figure 3.13. Block diagram or EHA control strategy

For a higher gain inner-loop gain, the overall transfer function can be approximated as:

$$\frac{w_p(s)}{w_d(s)} * \frac{x(s)}{w_p(s)} = \frac{G_2 G_{PI} G_1 K_c}{1 + G_2 G_{PI} G_1 K_c} * \frac{\frac{A \beta_e D_p}{V_o M}}{s^3 + \left(\frac{B}{M} + \frac{L_T \beta_e}{V_o}\right) s^2 + (A^2 + L_T B) \frac{\beta_e}{V_o M} s}$$

$$\frac{x(s)}{w_d(s)} = \frac{A \beta_e D_p G_2 G_{PI} G_1 K_c}{V_o M D_{en}(s)} \quad (3.64)$$

Where:

$$Den(s) = (1 + G_2 G_{PI} G_1 K_c) s^3 + (1 + G_2 G_{PI} G_1 K_c) \left(\frac{B}{M} + \frac{L_T \beta_e}{V_o} \right) s^2 + (1 + G_2 G_{PI} G_1 K_c) (A^2 + L_T B) \frac{\beta_e}{V_o M} s \quad (3.65)$$

The position controller converts the positional error into a velocity input to the motor and is represented by equation 3.66:

$$\frac{w_d(s)}{\tilde{x}(s)} = PC(s) \quad (3.66)$$

Where \tilde{x} is the positional error (m) and $PC(s)$ is the transfer function for the controller. Combining this with equation 3.64 yields:

$$\frac{x(s)}{\tilde{x}(s)} = \frac{A \beta_e D_p G_2 G_{PI} G_1 K_c PC(s)}{V_o M Den(s)} \quad (3.67)$$

Closing the positional loop yields the final overall EHA linear transfer function:

$$\begin{aligned} \frac{x(s)}{x_d(s)} &= \frac{\frac{A \beta_e D_p G_2 G_{PI} G_1 K_c PC(s)}{V_o M Den(s)}}{1 + \frac{A \beta_e D_p G_2 G_{PI} G_1 K_c PC(s)}{V_o M Den(s)}} \\ \frac{x(s)}{x_d(s)} &= \frac{\frac{A \beta_e D_p G_2 G_{PI} G_1 K_c PC(s)}{V_o M Den(s)}}{\frac{V_o M Den(s)}{V_o M Den(s)} + \frac{A \beta_e D_p G_2 G_{PI} G_1 K_c PC(s)}{V_o M Den(s)}} \\ \frac{x(s)}{x_d(s)} &= \frac{A \beta_e D_p G_2 G_{PI} G_1 K_c PC(s)}{V_o M Den(s) + A \beta_e D_p G_2 G_{PI} G_1 K_c PC(s)} \end{aligned} \quad (3.68)$$

Where:

$$Den(s) = (1 + G_2 G_{PI} G_1 K_c) s^3 + (1 + G_2 G_{PI} G_1 K_c) \left(\frac{B}{M} + \frac{L_T \beta_e}{V_o} \right) s^2 + (1 + G_2 G_{PI} G_1 K_c) (A^2 + L_T B) \frac{\beta_e}{V_o M} s \quad (3.69)$$

3.2.2 EHA Advantages and Disadvantages

The main advantages of the EHA include:

- Modular design which lends itself to simple maintenance and re-use across several platforms.
- Ease of control.
- Safe failure modes.

Although they are a very practical solution, there have some disadvantages which include:

- Prone to leakage.
- System is complex which leads to higher development costs.

3.3 Conclusion

This chapter introduced the concept of hydrostatic actuation systems, namely variable-displacement and fixed-displacement pump controlled types. A mathematical model for variable-displacement piston pump hydrostatic actuation systems was presented and their use for flight surface actuators was explored. The fixed-displacement pump Electro-Hydrostatic Actuation (EHA) system was also introduced in significant detail, including its design and mathematical model. Chapter 4 will introduce the design of a dual-EHA prototype that was manufactured specifically for this research.

Chapter 4 Design of a dual Electro-Hydrostatic Actuator

This chapter describes in detail the design of the dual EHA prototype developed for this research. The design parameters, process of manufacturing and the hardware-software interface used will be reported. The design parameter information introduced here will allow modeling, dynamic analysis and control of the EHA as discussed in chapters 6 and 7.

4.1 Dual Electro-Hydrostatic Actuator

Due to rigorous requirements from the aerospace industry to produce systems that are reliable and fail-safe the design of the EHA must be tailored in order to satisfy their concerns. The main focus for the design of the EHA prototype is to produce a system that is fail-safe, or in other words, will still have partial functionality in the event of a fault in the system. Before the design was performed the potential faults that could occur in the EHA and the flight system were investigated. Table 4.1 lists some of these potential faults.

When using a dual EHA system there are two methods in which they can be setup: parallel or series. A parallel setup implies that two individual EHA's are attached to the flight surface independently. A series setup implies that both EHA's are attached by the end of each actuator and that they are integrated into a lumped unit. The parallel approach creates two systems that have more independence from one another in that they only share the same flight surface they are attached to. If one of these EHA's fails the only effect the failed system would have on the other is that both actuators must still displace concurrently in the same path. Because of this, a provision must be made so that the failed actuator ports are cross-connected and decoupled from the pump so the faulty actuator can move freely. Using a lumped unit in which both systems are integrated with actuators attached in series allows for a better power-to-weight ratio compared to the parallel layout. The integration of the two however increases the linkage between both systems and decreases its fail-safe capability.

Selection between both layouts is dependent on the application. In commercial aircraft applications where the balance between fail-safe capabilities of a system to its power-to-weight ratio leans more towards the former using two systems attached in parallel is more suitable. In military aircraft applications the latter is more important. The design of the EHA prototype for this research is based on the specifications of the rudder for the F-35 Joint Strike Fighter (JSF). The focus is on producing a system with a higher power-to-weight ratio compared to the existing F-35 system.

Table 4.1. Potential faults in the EHA and corresponding flight surface [22].

Fault	Effect
Seal Wear in the Actuator	Change in friction characteristics and potential external leakage.
Oil Degradation	Change in viscous friction
External leakage due to loose fittings	System failure and contamination to the environment
Shaft seal wear in the pump	Contamination to the environment
Gear teeth wear	Reduction in volumetric efficiency and increased noise
Case drain seal failure	Excessive external leakage into accumulator, low efficiency, increase in accumulator pressure during operation, oil temperature increases and decrease in actuator velocity
Clogged or stuck check valves due to debris	Inability to build up pressure due to large flow going to inner circuit and oil temperature rises.
Clogged or stuck relief valve due to debris	Partial amount of flow will go through relief valve, causing a decrease in actuator speed. Oil temperature rises as well.
The coils of the motor wear out, causing the motor to fail (Note that the EHA prototype has a current sensor which limits the maximum current that can go to the motor).	System does not operate.
Mechanical Coupling between the motor and pump wears or fails	Wears the bearings and gear teeth of the pump causing excessive vibration and internal leakage. System could fail as well.

4.2 Dual Electro-Hydrostatic Actuator Specifications

The main specifications for the dual EHA for the JSF designed by Parker Aerospace are listed in table 4.2. Figures 4.1 and 4.2 show a depiction of the F-35 system and its architecture respectively.

Table 4.2. Specifications of the Parker Aerospace F35 Rudder EHA [23].

Stroke	$\pm 3.37E-2m (\pm 1.33in)$
Actuator Weight	41.82Kg (92 lbs)
Output Power	4.82KW (6.5HP)
No-Load Velocity	0.13-0.14m/s (5.04in/s-5.83in/s)
Loaded Velocity	7.62E-2 – 9.19E-2m/s (3.00-3.62in/s) at 62.28KN (14,000lbs)
Stall Force	56.49KN (12,700lbs)
Frequency Response	3.80Hz at -3dB and -90deg

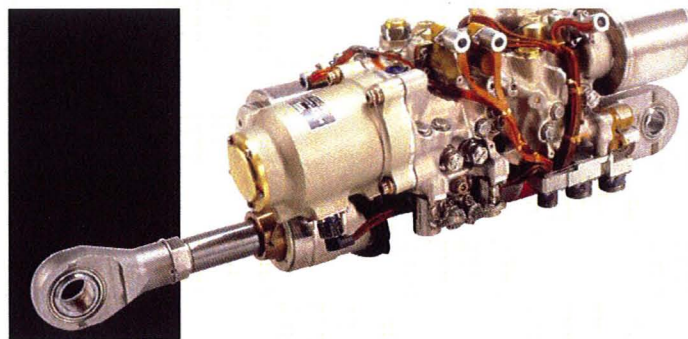


Figure 4.1. Depiction of the Parker Aerospace F-35 Rudder EHA [23].

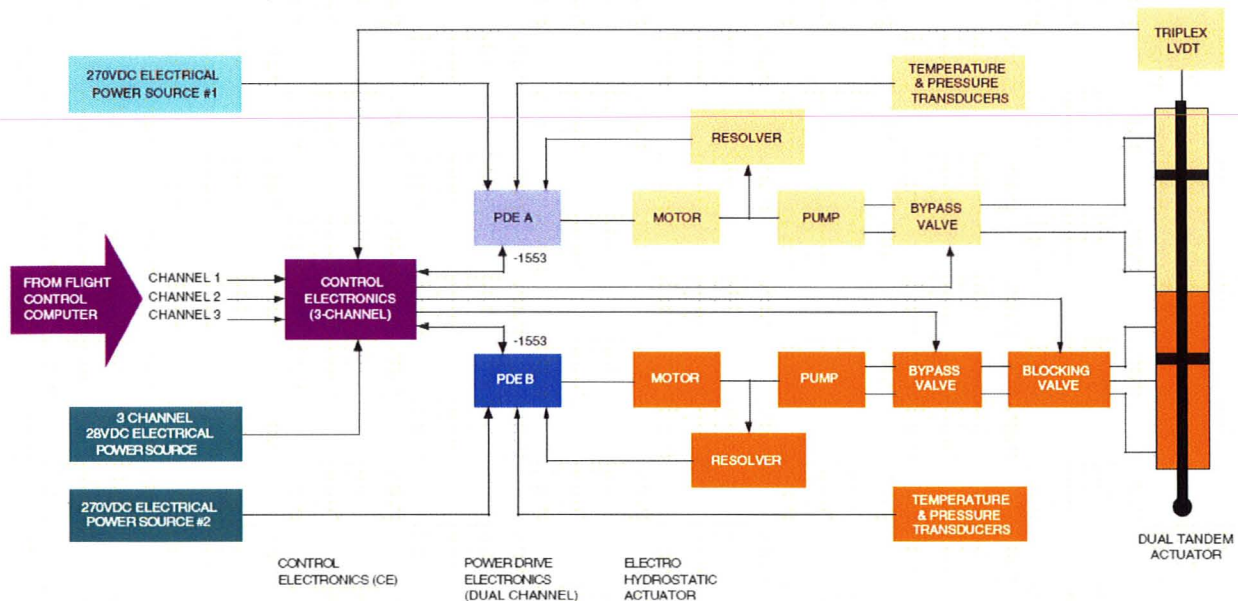


Figure 4.2. Surface architecture of the Parker Aerospace F-35 Rudder EHA [23].

Figure 4.1 shows a lumped dual EHA where the actuators are connected in series to form a dual tandem actuator. Incorporated into each hydrostatic circuit is a bypass valve as shown in figure 4.2. These decouple a pump from one side of the dual tandem actuator in the event of a fault. This allows one pump to drive the actuator with little resistance from the other circuit. A blocking valve is incorporated in one of the circuits which acts as a load holding device when the flight surface is held at a pitch in which high forces are applied. The motor is not required in these situations to hold the surface at that pitch via the pump. Note that the F-35 Rudder EHA does have position feedback from the actuator which is uncommon.

The design of the EHA presented in this research will attempt to replicate or exceed the performance specifications surface architecture shown in figure 4.2, with a particular emphasis on a better power-to-weight ratio.

4.3 Dual Electro-Hydrostatic Actuator Prototype Circuit Architecture

Since the focus for this design is to produce a system with a high power-to-weight ratio a series connection will be made to connect the two EHA's into a dual unit. Figure 4.3 shows the circuit architecture of the main components of the dual EHA prototype designed as a part of this research by attaching both actuators at the shaft.

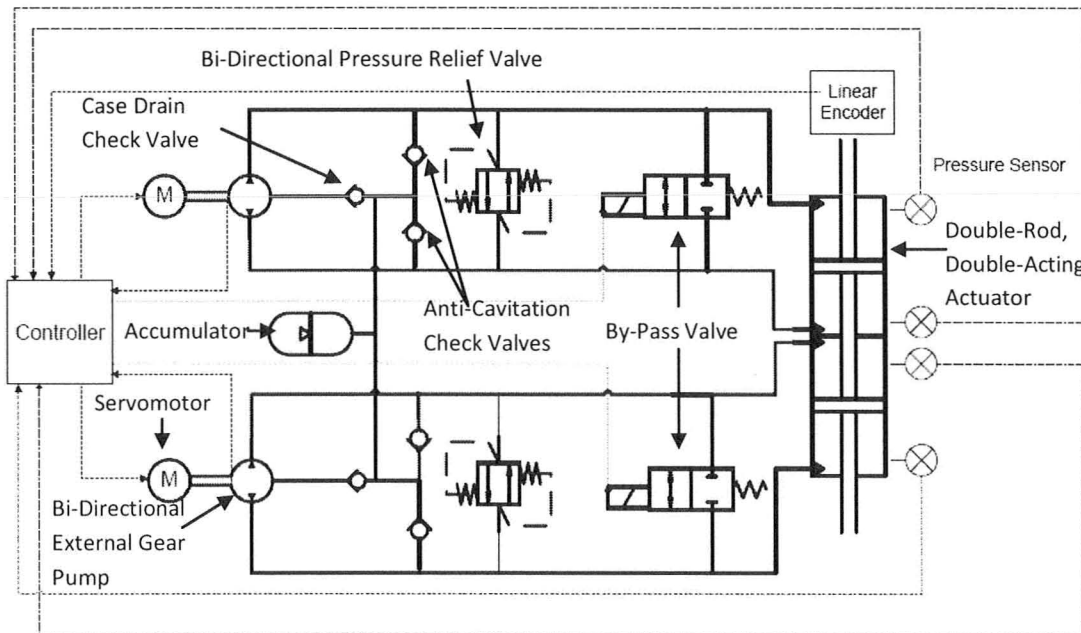


Figure 4.3. Circuit architecture of the dual EHA prototype.

This architecture has similarities to that seen in figure 4.2. The main difference lies within the inner circuit. The Parker EHA employs two charged reservoirs, one for each circuit. In the prototype designed for this research one charged reservoir (or accumulator) is shared between both circuits to reduce the weight. The single accumulator still has the capability to prevent cavitation and make-up for dynamic leakage in both systems.

Note that figure 4.3 does not contain a load holding valve. This was omitted since its addition would introduce significant non-linearities into the system which would decrease the frequency response, and hence increase the complexity of the control algorithm. It also increases the weight. The flight surface can still be held by the servomotor in static applications.

4.4 Dual Electro-Hydrostatic Actuator Design Process

In this section the process for designing a dual EHA is described. This process was used to design and build an experimental apparatus which will be described later in this chapter.

Typically when hydraulic systems are designed the process starts by selecting an actuator and a nominal operating pressure. The majority of the component selection depends on the dimensions of the actuator and the pressure rating. Two types of actuators were considered: a linear symmetrical actuator and a double rod, double acting cylinder. The first form only employs one rod, eliminating the need for dead space on the back end of the EHA. As a consequence it requires a larger bore diameter and is more cumbersome to attach two together in series. It was decided to employ two double rod, double acting cylinders in series in order to reduce the amount of material used and the complexity of mating the rods. The choice of actuator was made based on three parameters which were the stroke, load, and system pressure. If hydraulic cushioning is required then this needs to be taken into account as well. A system pressure of 20.68MPa (3000psi) has been chosen since this is the maximum pressure in which external gear pumps are still efficient at delivering flow [14]. Knowing that the maximum load is 62.28KN from table 4.2 the area of the piston in the actuator can be determined. The effective maximum load for each circuit is 31.14KN since it is shared. Calculating the piston area is given by the following formula:

$$A = \frac{F_n}{P_n} \quad (4.1)$$

Where F_n is the required actuator force (N) and P_n is the system nominal pressure. The calculated piston area is 1.48E-3m². Before the actuator dimensions are chosen, the maximum load applied to the shaft must be determined. The material and the safety factor must be known before the shaft diameter is chosen.

In systems that require high power-to-weight ratios the material used to contain the high loads must exhibit the same quality. Also, due to the extreme environments, especially those where there is a high concentration of moisture, the material chosen must be highly corrosion resistant. The material chosen for the housing of the dual EHA is annealed 15-5PH Stainless Steel. This material has a high yield and tensile strength, has excellent fatigue properties, is highly corrosion resistant, dissipates heat well, has low ferrite content, is weldable and can be machined using standard practices [24]. These characteristics make it an excellent choice to use for a flight surface actuator. Table 4.3 shows the properties inherent to annealed 15-5PH Stainless Steel.

Table 4.3. Annealed 15-5PH stainless steel material properties [24].

0.2% Yield Strength	963MPa
Ultimate Tensile Strength	1110MPa
Rockwell C Hardness	35HRC
Density	7780Kg/m ³
Thermal Conductivity	17.9W/m-K at 149°C

An acceptable safety factor used for the design of this prototype is a burst pressure set at six times the maximum normal operating pressure. Given a material yield strength of 963MPa the maximum allowable stress in the material at any time is 160.5MPa. Knowing that the maximum load applied to the shaft connected to the flight surface is 62.28KN (from table 4.2) using equation 4.1 gives a minimum shaft area of 3.88E-4m². The diameter of the shaft is related to area by the following formula:

$$A_i = \frac{\pi}{4} d_i^2 \quad (4.2)$$

Where A_i is the shaft area (m²) and d_i is the shaft diameter (m). Isolating for the shaft diameter yields:

$$d_i = \sqrt{\frac{4A_i}{\pi}} \quad (4.3)$$

The diameter of the shaft becomes 22.2mm. Since this diameter is not equal to any standard size it was decided to choose a shaft diameter one size up from this, which is 25.4mm (1in). Determining the area of the actuator piston with an attached shaft is given by the following formula:

$$A = \frac{\pi}{4} (d_o^2 - d_i^2) \quad (4.4)$$

Where A is the piston area (m^2) and d_o is the piston diameter (m). Isolating for the piston diameter yields:

$$d_o = \sqrt{\frac{4A}{\pi} + d_i^2} \quad (4.5)$$

This yields a piston diameter of 5.03E-2m. Choosing the closest standard size to this value is 5.08E-2m (2in). From table 4.2 it is known that the stroke of the cylinder is $\pm 3.37\text{E}-2\text{m}$ without accounting for the cushions.

With the shaft and piston diameters along with the stroke calculated the actuator can be designed. In review the major actuator parameters are:

- Shaft diameter: 25.4mm (1in)
- Piston diameter: 50.8mm (2in)
- Effective piston area (A): $1.52\text{E}-3\text{m}^2$
- Stroke: $\pm 3.37\text{mm}$ ($\pm 1.33\text{in}$)

Given the area of the piston and the maximum actuator velocity, the maximum required flow rate can be calculated by the following formula:

$$Q_n = V_n A \quad (4.6)$$

Where Q_n is the flow rate (m^3/s) and V_n is the maximum loaded velocity of the actuator from table 4.2. The calculated flow rate is $1.39\text{E-}4\text{m}^3/\text{s}$. The maximum flow rate determines the volumetric displacement of the pump and the maximum rotational velocity of the servomotor. From these requirements the pump can be selected along with the power requirements of the servomotor. The required maximum power of the system is 4.82KW (2.41KW per servomotor) from table 4.2. The servomotor chosen to meet the torque and speed requirements is the Infranor ICM-14N, which has the following specifications:

Table 4.4. Specifications for the Infranor ICM-14N servomotor [25].

Stall Torque	16.1Nm
Nominal Torque	7.1Nm
Nominal Speed	314.59rad/s (3000rpm)
Nominal Power	2.23KW
Mass	9.2Kg
Rotor Inertia	$3.36\text{E-}03\text{Kgm}^2$
Winding Resistance	0.64Ω
Winding Inductance	4.5mH

With a nominal speed of the motor being 314.59rad/sec the required volumetric displacement is calculated using the following formula:

$$D_p = \frac{Q_n}{w_n} \quad (4.7)$$

Where D_p is the volumetric displacement of the pump (m^3/rad). The volumetric displacement of the pump is calculated as $4.42\text{E-}07\text{m}^3/\text{rad}$. Instead of designing a custom gear pump for this application it was decided to use the gears and bushings of one that is available in industry with approximately the same volumetric displacement. The pump chosen is a Marzocchi ALP1-4 model, which has a volumetric displacement of $4.38\text{E-}07\text{m}^3/\text{rad}$. Using this value the nominal torque of the system can be calculated using the following formula:

$$\tau_n = \frac{P_w}{w_n} \quad (4.8)$$

Where τ_n is the nominal torque (Nm) and P_w is the required power output (W). At the nominal speed the required torque is 7.66Nm, which is above the nominal torque of the motor of 7.1Nm calculated using the equation above. This means that the motor cannot run continuously at this torque. Since the EHA does not continuously function this is an acceptable value. The consequence of this is that the servomotor can only run at maximum torque intermittently. For this project the above servomotor/pump combination is considered acceptable for the experimental setup.

Once the major parameters have been determined the selection of the inner-circuit components, by-pass valve and pressure relief valves can be performed. The case drain check valve is sized by knowing the maximum flow of the pump and the approximate internal leakage at the highest pressure. The pump is rated for approximately 15% internal leakage at its highest operating pressure and speed, which equates to $2.085E-5m^3/s$. It is preferable to reduce the backpressure in the case drain caused by the resistance to flow from the check valve. The smallest cracking pressure for the check valve should therefore be used. The case drain check valve chosen is Hawe RKO, which has a cracking pressure of 5KPa and a negligible resistance at the given flow rate. This can be seen in figure 4.4.



Figure 4.4. Hawe RKO check valve [26].

The anti-cavitation check valves not only need to rout fluid from the case drain back to the inlet of the pump but must allow a larger flow to enter in the event of cavitation. A larger check valve was chosen that would accommodate a flow rate equal to the maximum flow of the pump to reduce the back pressure as much as possible. The check valve chosen is Hawe RB2, which has a cracking pressure of approximately 7KPa and a resistance of 10KPa at full system flow. This can be seen in figure 4.5.



Figure 4.5. Hawe RB2 check valve [26].

As previously mentioned the accumulator serves two purposes. It prevents cavitation and provides make-up fluid for any external leakage. When cavitation occurs the amount of extra fluid needed is minimal since the cavitation compensation process occurs extremely quickly. Therefore, the accumulator should be sized based on the maximum amount of fluid that is allowed to leak before maintenance is required. Since the maintenance interval for fighter aircraft occurs much more frequently compared to commercial aircraft the required accumulator can be very small. The accumulator chosen is Hawe AC13 which has a volumetric capacity of 13cm^3 .



Figure 4.6. Hawe AC13 Accumulator [27].

Pressure relief must occur between each side of a circuit in both directions and must not create too much back-pressure at maximum flow. The relief valve chosen is a Hydraforce CR10-28 which is bi-directional, meaning only one is required for each circuit.



Figure 4.7. Hydraforce CR10-28 Pressure Relief Valve.

The by-pass valve must be bi-directional and also must reduce the amount of back pressure at full system flow. The by-pass valve chosen is a Hydraforce SV08-24 which creates a back pressure of approximately 137KPa at full flow.

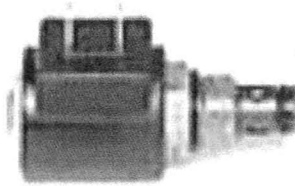


Figure 4.8. Hydraforce SV08-24 By-Pass Valve [28].

In summary table 4.5 provides the major specifications of the dual EHA:

Table 4.5. Resultant specifications form dual EHA design process.

Nominal Pressure (P_n)	20.68MPa (3000psi)
Nominal Actuating Force (F_n)	62.28KN total (31.14KN each)
Effective Piston Area (A)	1.52E-3m ²
Maximum Volumetric Flow (Q_n)	1.39E-4m ³ /s
Maximum Actuator Velocity (V_n)	9.19E-2m/s
Pump Volumetric Displacement (D_p)	4.38E-07m ³ /rad
Pump Nominal Speed (w_n)	314.59rad/s (3000rpm)
Nominal Torque (τ_n)	7.1Nm

4.5 Physical Design of the Dual Electro-Hydrostatic Actuator

With all the major parameters of the EHA defined and the components chosen, the remaining pump/routing elements of the EHA are designed as a lumped unit. The first portion designed was the inner circuit for both systems which shares a common accumulator. It was decided that the inner circuit, minus the anti-cavitation check valves would be incorporated into one machined part. This part is sandwiched between both pump housings in order to save as much space as possible. Figure 4.9 shows a depiction of this part. Figure 4.10 shows a depiction of the part with its inner channels shown and the accumulator and case drain check valves attached. The green channels are the flow lines between the case drain and anti-cavitation check valves. The red channels are the flow lines between the pumps and the case drain. The block is symmetric on both sides.

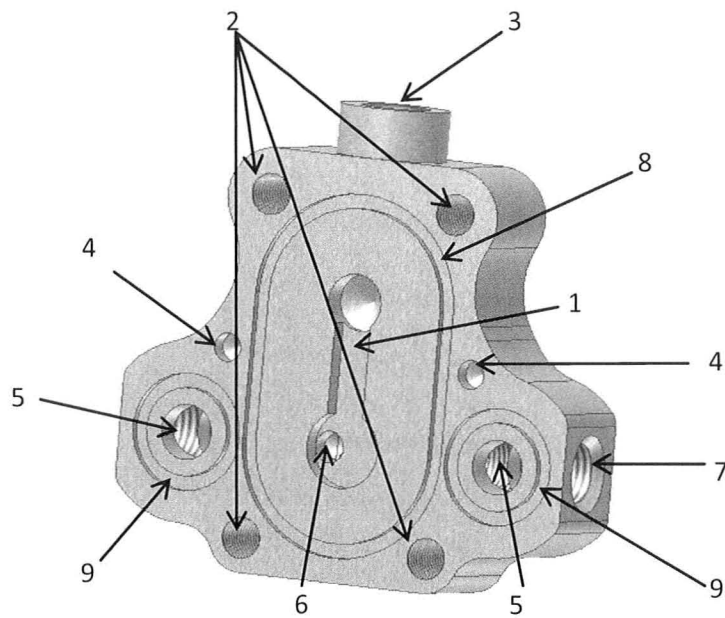


Figure 4.9. Inner circuit housing component.

Table 4.6. Description of inner circuit housing.

1	Channels for routing case drain leakage to the inner circuit.
2	Threaded holes to fasten both pump housings to inner circuit housing.
3	Hole in which the accumulator threads into.
4	Alignment holes that ensure proper orientation with the pump housing.
5	Outlet ports from inner circuit where fluid routs to the anti-cavitation check valves.
6	Case drain inlet port.
7	Hole which houses the case drain check valve.
8	Pump face O-ring groove.
9	Anti-cavitation check valve face O-ring groove.

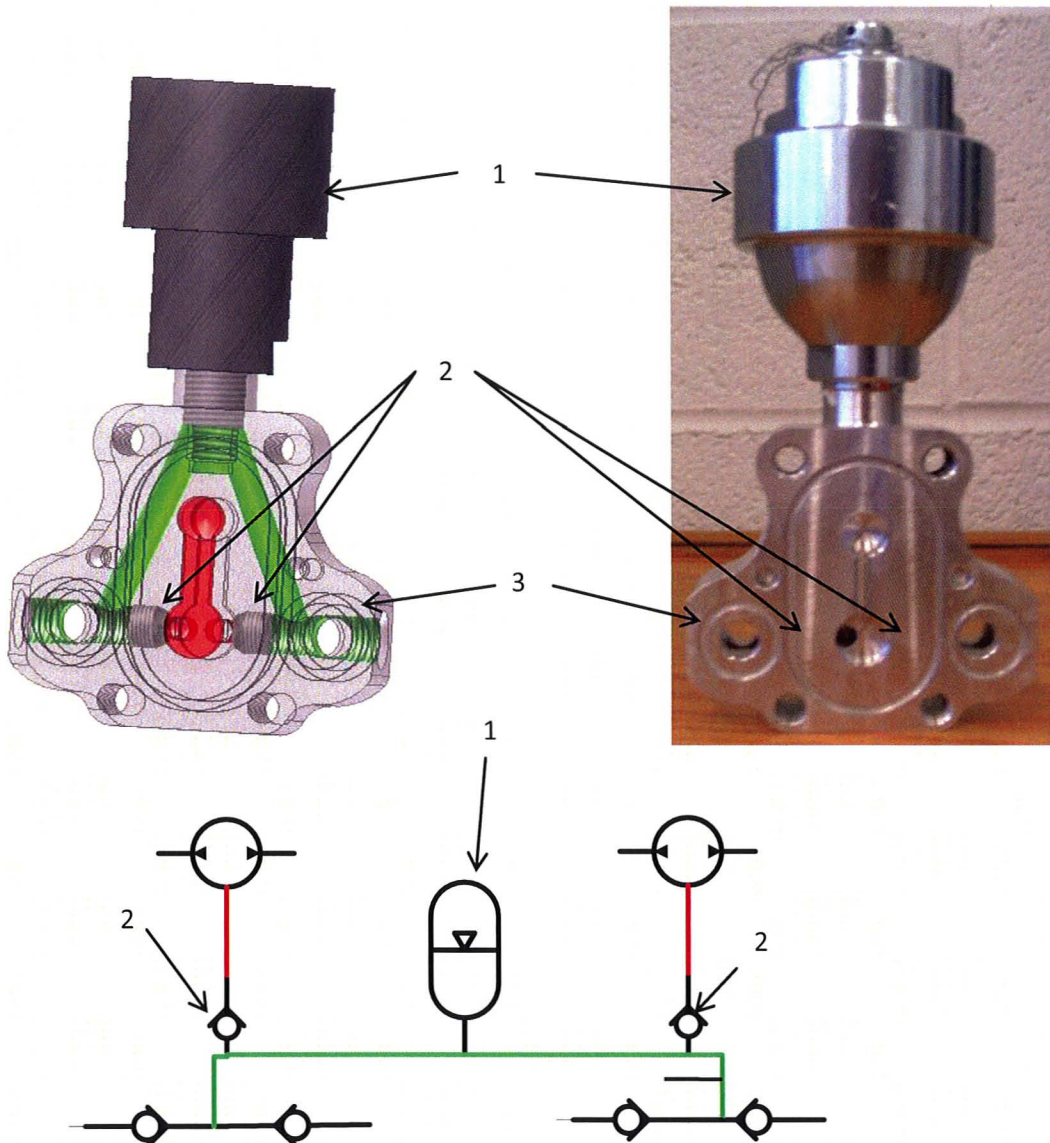


Figure 4.10. Inner circuit housing component.

Table 4.7. Inner circuit housing components.

1	Accumulator
2	Case drain check valves
3	Inner circuit housing

Note that the O-Ring grooves in the inner circuit housing were designed so that there is a 20% squeeze when both pump housings are secured tightly. This means that the depth of the groove is sized to be approximately 80% of the O-ring diameter. This is an industry standard when designing hydraulic equipment rated up to 20.68MPa [14]. In this application BUNA-N seals, which are soft with a

durometer of 50, were used due to their cost effectiveness. In applications where there are higher temperatures or the life-cycle of the seal must be high more robust seals made out of materials such as Viton should be used.

This design provides a compact and lightweight method to integrate the inner circuit, weighing only 0.49Kg.

The two pump housings sandwich the assembly seen in figure 4.10 and also integrate the anti-cavitation check valves, pressure relief valves and by-pass valves. This is made clear in figure 4.12. Figure 4.11 shows a depiction of this pump block alone.

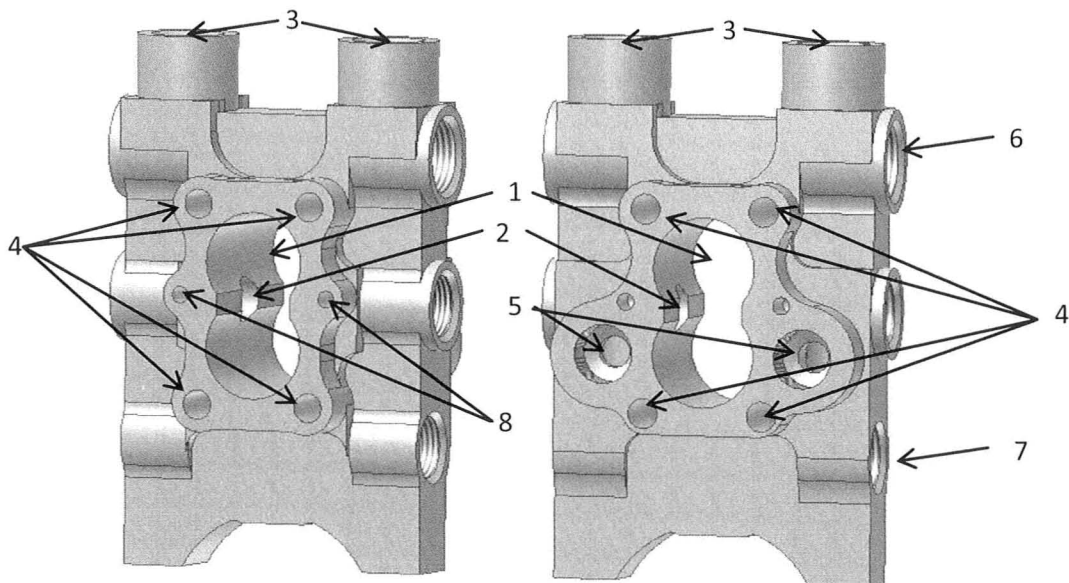


Figure 4.11. Pump housing component, front view and back view.

Table 4.8. Pump housing component description.

1	External gear pump enclosure.
2	Pump inlet/outlet ports.
3	Channels which connect, pump, relief and bypass ports together.
4	Bolt holes.
5	Anti-cavitation check valve enclosure.
6	Pressure relief valve enclosure.
7	By-pass valve enclosure.
8	Alignment holes.

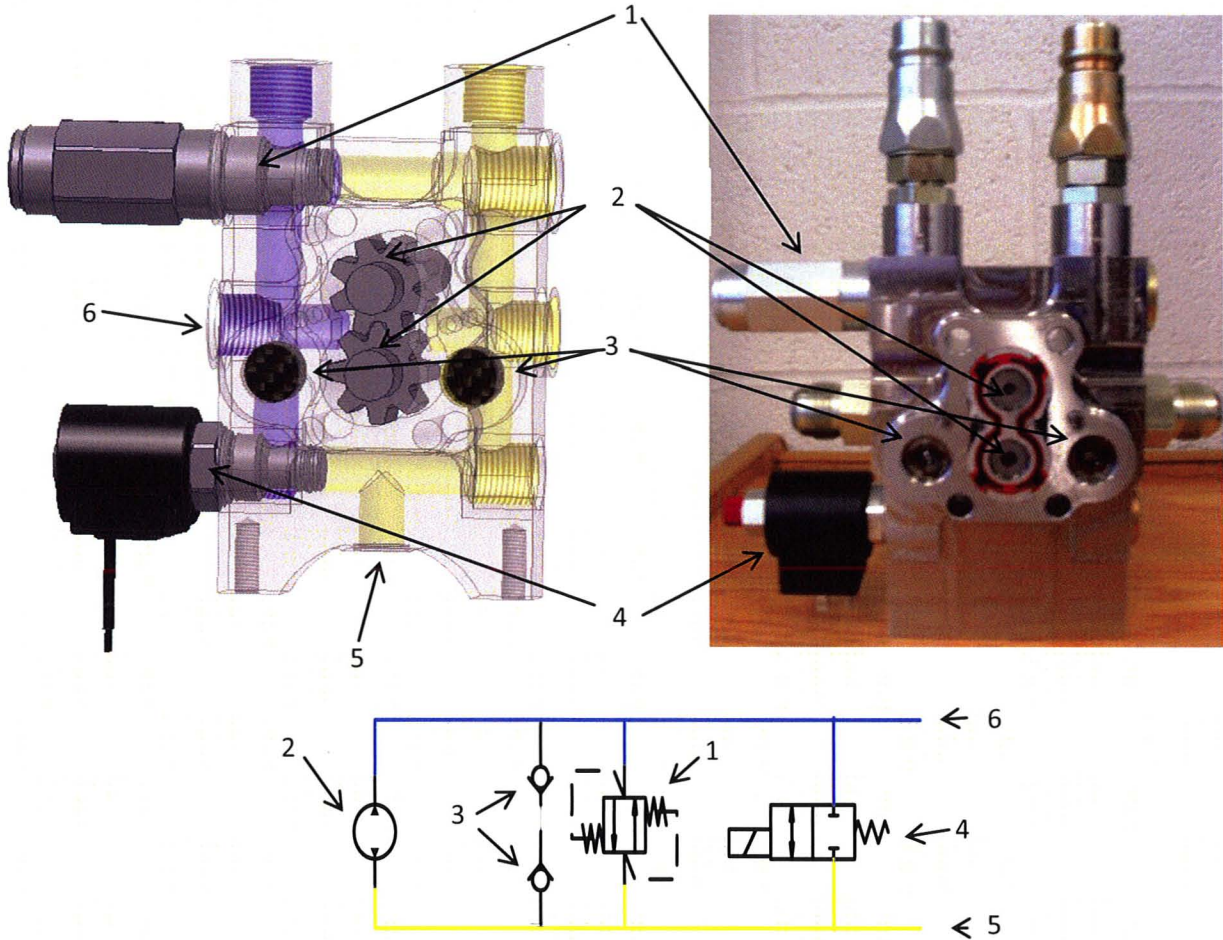


Figure 4.12. Pump housing component, front view and back view.

Table 4.9. Pump housing assembly components.

1	Bi-directional relief valve
2	External gear pump
3	Anti-cavitation check valves
4	Bypass valve
5	Inlet/outlet port to one side of actuator
6	Inlet/outlet port to other side of actuator

It must be noted that the efficiency of an external gear pump is extremely sensitive to the clearance between the housing components and the gears themselves. For high pressure external gear pumps (up to 20.68MPa) the clearances must be within 0.5-5 μ m [14]. This will be discussed further in the next chapter.

A depiction of the inner circuit housing sandwiched between the two pump housing blocks can be seen in figure 4.13.

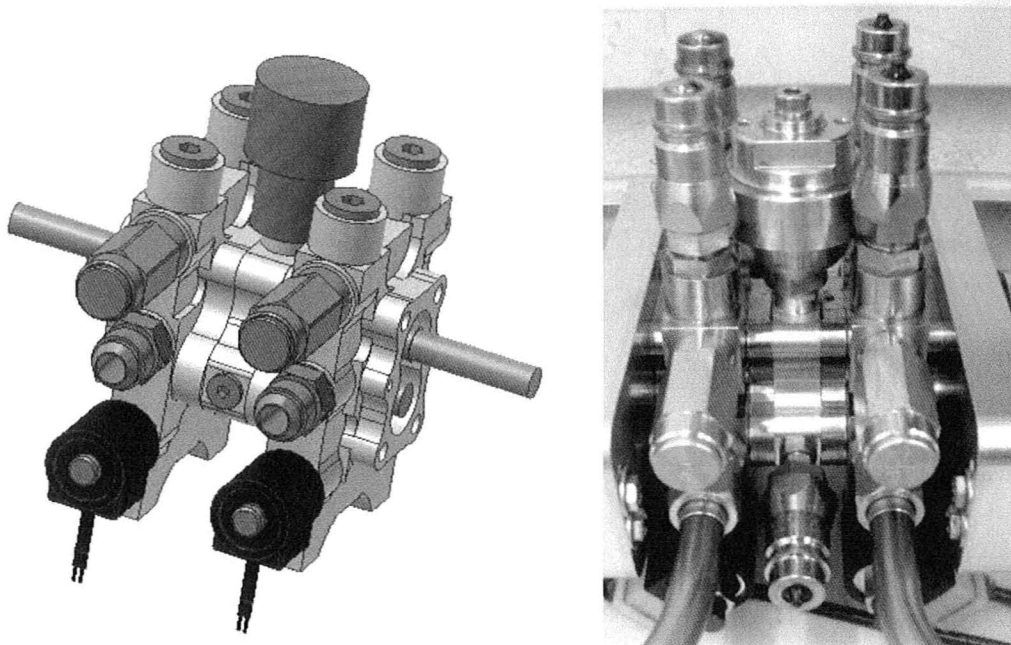


Figure 4.13. Inner circuit housing sandwiched between the two pump housings.

A depiction of figure 4.13 coupled with the Infranor servomotor and its interfacing block can be seen in figure 4.14. Figure 4.15 shows a depiction of the entire dual EHA assembled together. Note that the connections between the pump housing and actuator are performed by using tubing on the blue side of the circuit seen in figure 4.12. For the yellow side fluid is routed to the bottom of the pump block and directly into the connection cap between both actuators, which directs fluid into the corresponding chamber. The size of these channels is determined by the maximum velocity allowed, which depends on whether it is an inlet or an outlet. The maximum velocity allowed for the inlet of a pump should not exceed 1.22m/s (4ft/s) and the outlet velocity should not exceed 6.10m/s (20ft/s) [14]. Any higher velocity could potentially cause cavitation at the inlet and too much back pressure at the outlet. Since both sides interchange between the inlet and outlet, the diameter of the channels were designed so that the maximum flow does not exceed 1.22m/s. To calculate this the following equation is used:

$$d_{io} = \sqrt{\frac{4Q_a}{\pi V_{io}}} \quad (4.9)$$

Where d_{io} is the maximum allowable diameter of the inlet/outlet ports (m) and V_{io} is the maximum allowable velocity of the inlet/outlet ports set at 1.22m/s. This equates to a diameter of 1.20E-2m (0.474in). The next size up was chosen to be the minimum diameter of all channels which was 1.27E-2m (0.5in).

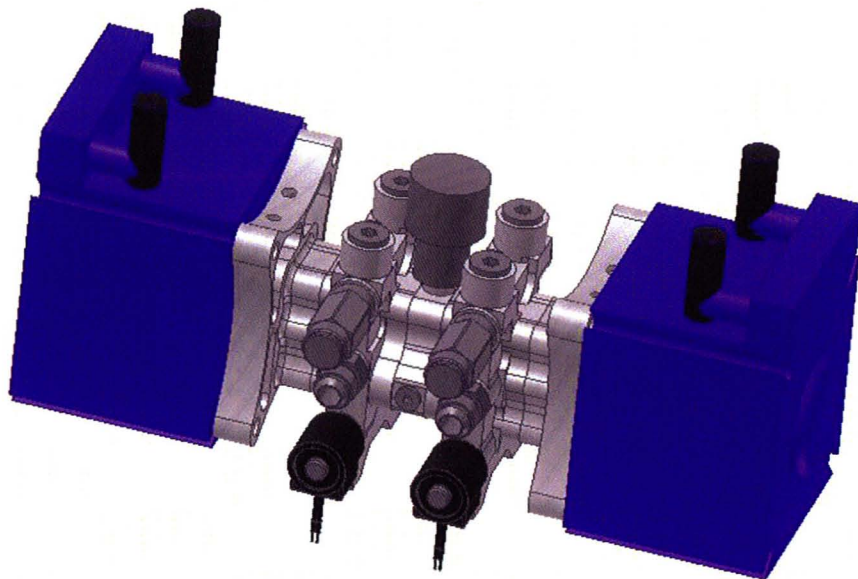


Figure 4.14. Dual EHA minus the actuators

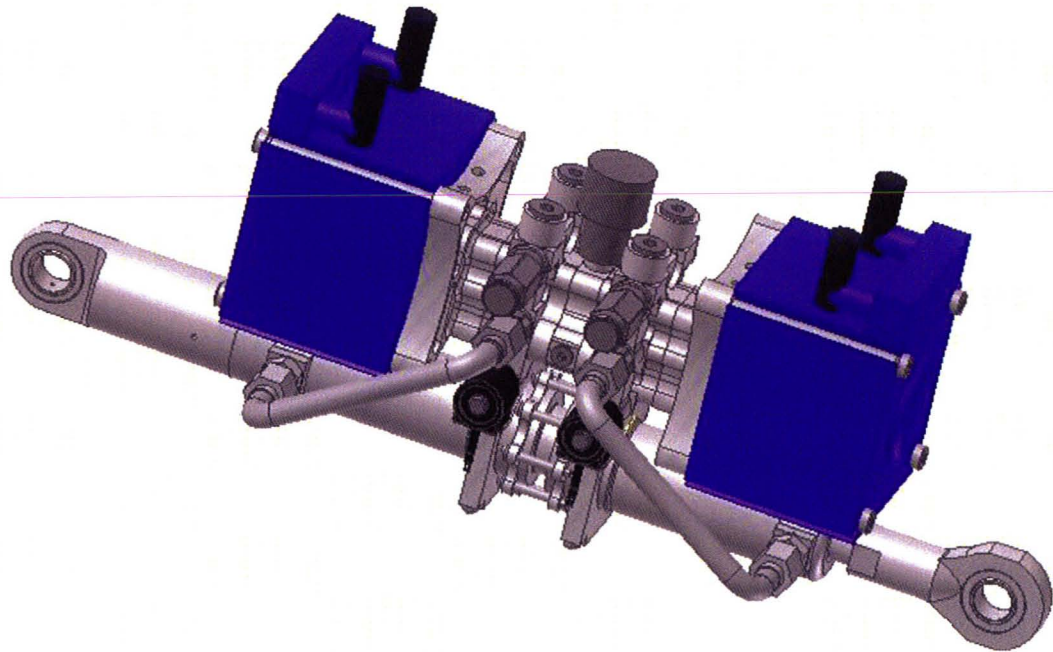


Figure 4.15. Dual EHA assembly.

The mass of this system combined is 36.74Kg which is approximately 12% lighter than the EHA developed by Parker for the F-35 rudder. Table 4.10 gives a breakdown of the mass of all major components of this system.

Table 4.10. Breakdown of the mass of the Dual EHA designed for comparison against the F-35 Rudder EHA.

Infranor Servomotors	18.6Kg (9.3 Kg each)
Valving	0.85Kg
Inner Circuit and Accumulator	0.79Kg
Pump housings and motor/pump interface	4.46Kg
Pump gears and motor coupling	0.72Kg
Pump and actuator bearings	0.91Kg
Dual Actuator	6.63Kg
Oil	0.62Kg
Fitting, bolts, seals and tubing	3.16Kg
Overall Mass	36.74Kg

For the dual EHA prototype developed for research purposes there were many substantial differences compared to the one seen in figure 4.15. The reasons for this include:

- A Siemens Simodrive 611U servomotor and drive amplifier were already available in McMasters' research facilities. Purchasing a new Infranor servomotor and drive would be a substantial cost, so it was decided to use the existing equipment available.
- To obtain a dual actuator seen in figure 4.15 would require a substantial amount of machining that was undesirable. It was decided to purchase two actuators that attach at the shaft instead.

The next section provides details of the dual EHA prototype that was manufactured for experimentation.

4.6 Physical Design of the Dual Electro-Hydrostatic Actuator Prototype

The similarity of the dual EHA design shown above and the dual EHA prototype produced is the inner circuit and pump housings seen in figure 4.13. The valves and fittings seen in figure 4.13 do not change as well. Therefore, the information that describes the depictions in figures 4.3 to 4.13 give an accurate summary of how this portion of the dual EHA was designed. The only differences are that the CR10-28

relief valve is set to 3.44MPa (500psi) instead of 20.68MPa and the gears are a slightly different size. Another difference is instead of the Infranor ICM 14N servomotor, a Siemens 1FK7080-5AF71-1AG2 servomotor was employed. The specifications for this motor are provided in table 4.11.

Table 4.11. Specifications for the 1FK7080-5AF71-1AG2 servomotor [29].

Stall Torque	8Nm
Nominal Torque	6.8Nm
Nominal Speed	314.59rad/s (3000rpm)
Nominal Power	2.14KW
Mass	10Kg
Rotor Inertia	1.5E-03Kgm ²
Winding Resistance (R_c)	1.04Ω
Winding Inductance (L_c)	14mH
Back emf constant (K_w)	0.98V/rad/s (102.5V/1000rpm)
Torque Constant (K_c)	1.61 Nm/A



Figure 4.16. Siemens 1FK7080-5AF71-1AG2 servomotor.

Unlike the Infranor servomotor the Siemens servomotor has a straight shaft, requiring a large coupling to attach it to the pump. It also requires a large interface to mount the pump and servomotor together. The coupling used needs to have a very large rotational stiffness so that it can be assumed to be rigid, and hence dynamically insignificant for control purposes. The coupling chosen is a bellows type, which is made by R+W America. The model is BK2/60/83 which can be seen in figure 4.17.



Figure 4.17. R+W America BK2/60/83 shaft coupling [30].

This coupling has a rotary inertia of $3.2E-04\text{Kgm}^2$ and a stiffness of $7.6E+04\text{Nm/rad}$. This increases the overall rotary inertia of the system to $1.82E-04\text{Kgm}^2$. This also implies that knowing the maximum torque output is 8Nm the maximum rotary deflection of the coupling is $1.1E-04\text{rad}$, which will be assumed to be negligible. The machined pump-servomotor interface can be seen in figure 4.18.

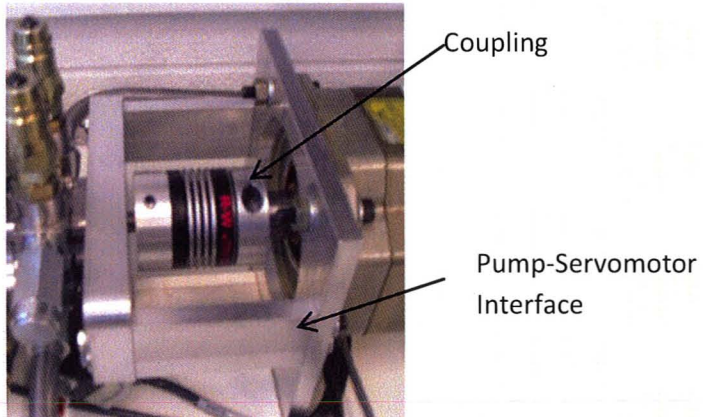


Figure 4.18. Pump-servomotor interface with coupling.

The pump chosen is similar to that selected for the pump described for the design to match the Parker dual EHA but is slightly larger. The Marzocchi ALP-5 series was chosen due to the non-availability of the ALP-4 from the manufacturer. Geometrically the only difference between these two series is that the ALP-5 is 2mm thicker, requiring the pump housing to be thickened by the same value. The volumetric displacement of this pump is $5.57E-07\text{m}^3/\text{rad}$ and has a rotary inertia of $1.57E-05\text{Kgm}^2$. Calculating the overall rotary inertia is performed using the following equation:

$$J_{pm} = J_c + J_p + J_m \quad (4.10)$$

Where J_{pm} is the overall rotary inertia (Kgm^2), J_c is the coupling rotary inertia (Kgm^2), J_p in the pump rotary inertia (Kgm^2), and J_m is the servomotor rotary inertia (Kgm^2). Using the equation above the total rotary inertia of the servomotor, pump and coupling is $1.98E-04\text{Kgm}^2$.

As previously mentioned the dual actuator for the EHA prototype is simply two double rod, double acting cylinders attached at the shaft. The area required for this cylinder is the same as the one derived for the design of the F-35 rudder dual EHA but with a larger stroke. The cylinders chosen are manufactured by Higginson with the model number MH2511400BXN12D, which have a piston diameter of $5.08E-2\text{m}$ (2in), a rod diameter of $2.54E-2\text{m}$ (1in) and a stroke of 0.30m (12in). There is cushioning on both ends of the cylinders to reduce the impact if they are dead ended. The pressure rating of these cylinders is 10.34MPa (1500psi) with a safety factor of 4. This component has the lowest pressure rating compared to all others in the circuit. This gives the entire system a burst pressure rating of 10.34MPa . The mass of the piston inside the actuator (M_p) is 3.688Kg . Both cylinders are foot mounted and were placed on a flat plate, which minimizes the vertical misalignment of the shafts. Dial gauges were used to shift the cylinders to minimize the horizontal and angular misalignment. A depiction of one of these cylinders can be seen in figure 4.19.



Figure 4.19. Higginson MH2511400BXN12D double rod, double acting actuator.

In addition to the dual circuit shown in figure 4.3 several peripheral components were added to increase the functionality to the system to allow simulation of fault conditions. Figure 4.20 shows the circuit diagram of the entire experimental prototype. Table 4.12 gives a description of each sub-circuit. Note that since there are two identical circuits attached to one another one side will be termed Axis A while the other will be termed Axis B.

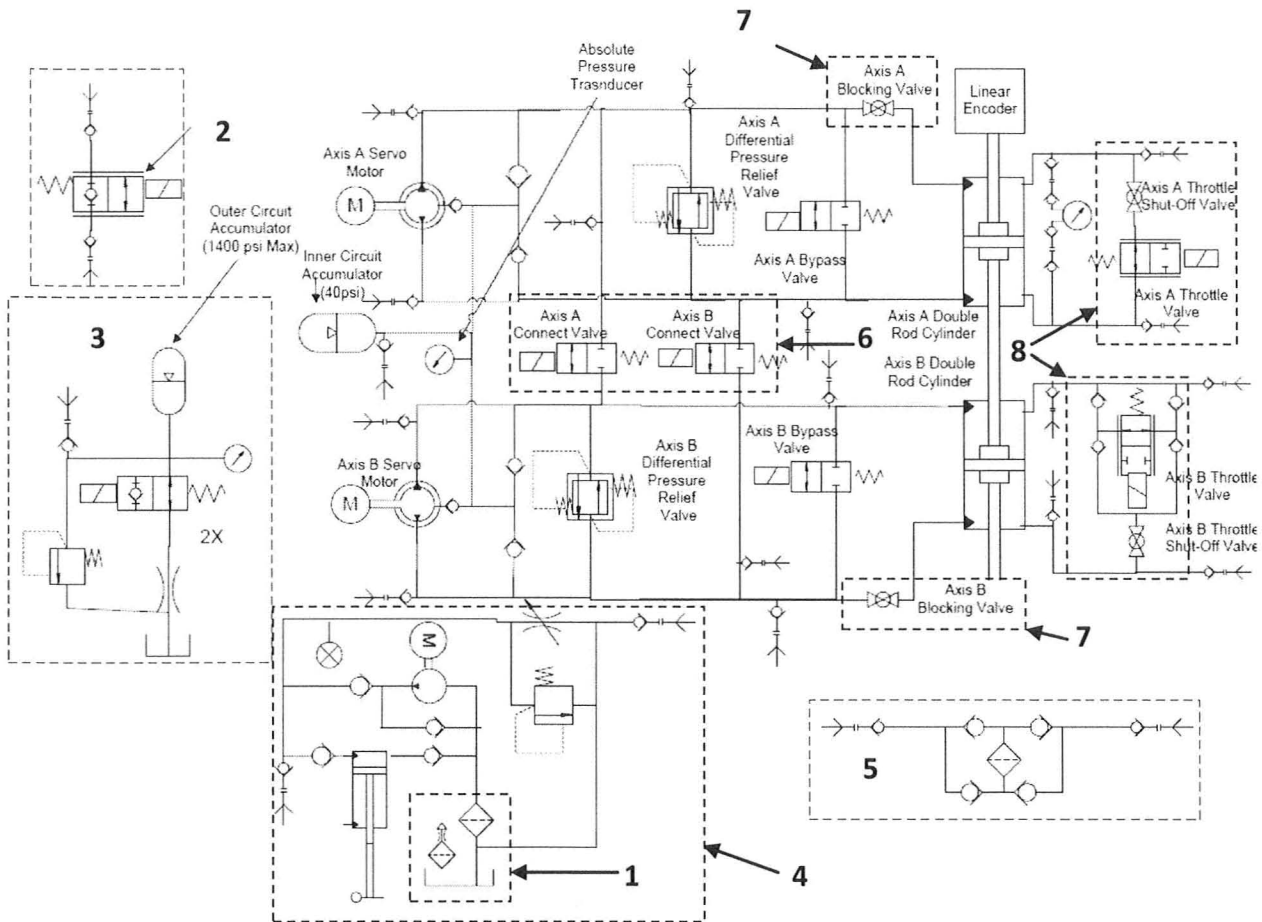


Figure 4.20. Complete hydraulic circuit diagram of the dual EHA prototype.

Note that every added component and sub-assembly are surrounded by broken lines.

Table 4.12. Dual EHA added components and sub-assemblies.

1	System Reservoir and Filter Circuit
2	External Leakage Circuit
3	Variable Bulk Modulus External Circuit
4	Charging Circuit
5	Rectified Offline Filtration Circuit
6	Axis A and B Connect Valves
7	Axis A and B Blocking Valves
8	Axis A and B Throttling Valves

4.6.1 System Reservoir and Filter Circuit (Assembly 1)

A reservoir is employed to supply and receive flow from many of the subassemblies of the dual EHA, which will be discussed later in this chapter. A depiction of this sub-assembly can be seen in figure 4.21 and a description of each component can be seen in table 4.13. The reservoir, (1), is wall mounted and has a capacity 1.89E-02m³ (5 Gallons). This also has a small 10micron filter, (2), which is connected between the outlet of the reservoir and the inlet of the pump. This provides extra fluid conditioning in addition to the rectified offline filtration circuit (assembly 5).

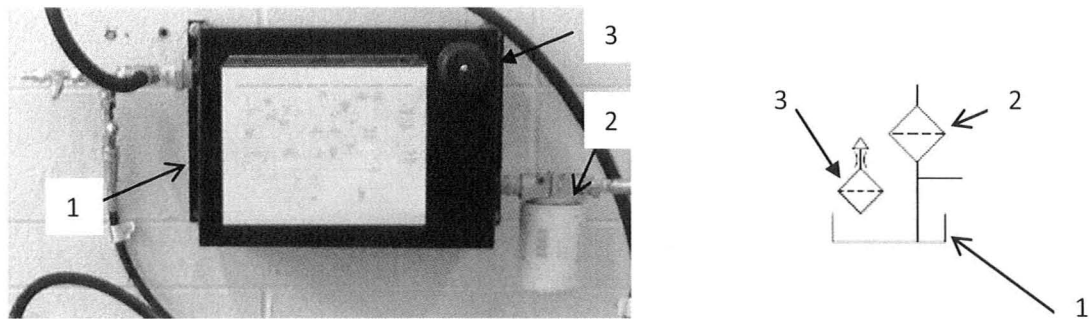


Figure 4.21. System reservoir and filter.

Table 4.13. System reservoir and filter components.

1	Reservoir
2	10micron filter
3	Reservoir Breather Cap

4.6.2 External Leakage Circuit (Assembly 2)

The external leakage circuit enables experiments to be performed in the future that relate to fault detection analysis. A depiction of this assembly can be seen in figure 4.22 and a description of each component can be seen in table 4.14. To simulate external leakage a proportional valve, (1), is used to vary the restriction in the valve that allows flow back to the reservoir. The type of valve used is a Hydraforce SP08-20 normally closed, 2-way. This is controlled using a Hydraforce 4000165 DIN coil mount proportional valve controller. This controller takes a 0-10V input from a data acquisition card and converts it to a 0-1.2A current, which in turn controls the position of the poppet in the valve.

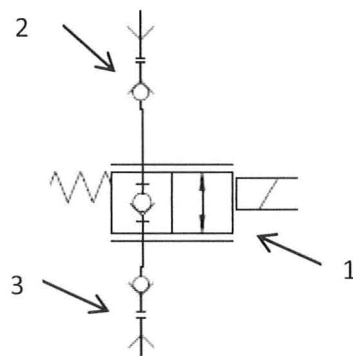
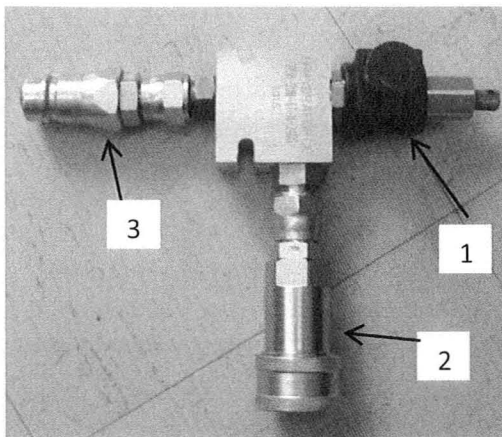


Figure 4.22. External Leakage Circuit.

Table 4.14. External Leakage Circuit Components.

1	Hydraforce SP08-20 normally closed proportional valve
2	Quick connect coupling to be connected to the dual EHA
3	Quick connect nipple to be connected to the reservoir

4.6.3 Variable Bulk Modulus External Circuit (Assembly 3)

A variable bulk modulus external circuit is added to enable the user to control the stiffness of the system, which in turn changes its natural frequency. A depiction of this circuit can be seen in figure 4.23 and a description of each component can be seen in table 4.15. This is used for fault detection purposes for which experiments will be performed in the future. There are two of these assemblies, each to be connected to both chambers on either axis.

The basis behind this circuit is that it changes two major parameters in the system: the volume and the bulk modulus. Added volume is provided by the extra fluid in the accumulator, (3), and the rest of the sub-assembly. The change in bulk modulus is provided by the added nitrogen pocket which is on the opposite side of the diaphragm in the accumulator. This acts as an air pocket in the system. The larger the percentage volume of air entrapped in the system fluid the lower the bulk modulus. This circuit allows the user to control either how much fluid is charged into the accumulator and/or the static charge on the other side of the diaphragm. This can be accomplished by using the charging circuit (assembly 4) to add oil or a nitrogen bottle to charge the top side of the accumulator.

The accumulator employed in this assembly, (3), uses the same model as in the inner circuit, the Hawe AC13, which has a volumetric capacity of $1.3E-05m^3$. There are three valves used in this assembly; one for flow control, (4), one for pressure relief, (5), and another that opens flow back to tank when shut off, (1). The flow control valve, (4), is a Hydraforce FC08-20F with an orifice check. The pressure relief valve, (5), is a Hydraforce RV08-20, which has a fixed setting of 9.65MPa (1400psi). The solenoid valve, (1), is a Hydraforce is a SV08-21, which allows 2-way flow and is normally open. The accumulator can be charged up to 9.65MPa but should be no more than 9.30MPa. The pressure relief valve exists due to the potential presence of the high static charge of the oil. Since the cross-over relief valves are pre-set to 3.44MPa and the static pressure can be set to 9.30MPa if a cylinder is dead-ended the system pressure can exceed the sum of these pressures, which is 12.74MPa. This value is larger than the rated pressure of the system of 10.34MPa. (5) acts as an absolute pressure relief valve and will ensure the pressure in each chamber does not exceed the system rated pressure, even when back pressure due to high flow occurs. Due to the dangers of discharging high pressures manually and to ensure that the static pressure does not remain when the system is turned off, valve (1) is used. When the system is turned on the solenoid will activate and close the link between the reservoir and both chambers, allowing for static pressure to be present. (4) is present to ensure that when (5) is turned off the flow going back to tank is gradual. This flow is routed through a hose which uses a quick connect coupling to connect back to the reservoir. A Measurement Specialties M5154-000004-2K5PG pressure transducer, (2), is attached to each of these blocks to monitor the static pressure at any given time.

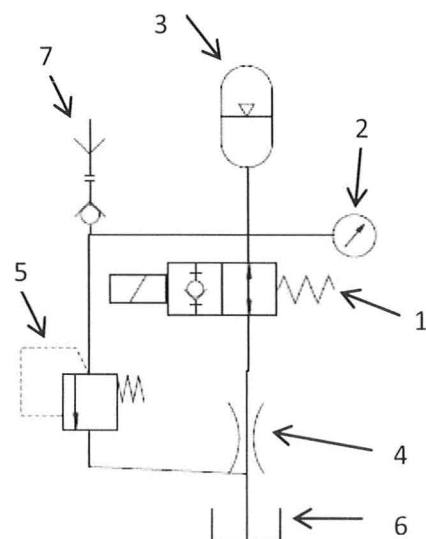
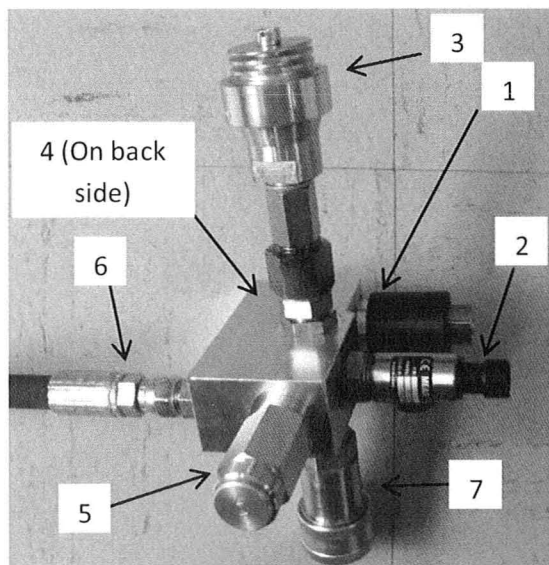


Figure 4.23. External Bulk Modulus Circuit..

Table 4.15. External Bulk Modulus Circuit Components.

1	Hydraforce SV08-21 Normally Open Solenoid Valve
2	Measurement Specialties M5154-000004-2K5PG pressure transducer
3	Hawe AC13 Accumulator
4	Hydraforce FC08-20F Flow Control Valve
5	Hydraforce RV08-20 Pressure Relief Valve
6	Return hose back to reservoir with quick connect coupling
7	Quick connect coupling which attaches the external bulk modulus circuit to the dual EHA

4.6.4 Charging Circuit (Assembly 4)

The charging circuit is used to prime the dual EHA with fluid and to charge it to whatever static pressure is desired. A depiction of this circuit can be seen in figure 4.24 and a description of each component can be seen in table 4.16. This can be performed manually or automatically. Manually, the system is charged by a Hydraforce HP10-21 hand pump, (2). Automatically, the system is charged by a single direction external gear pump, (6), with a volumetric displacement of $2.83E-7m^3/rad$. The motor used to turn this is the same Siemens servomotor, (3), used to drive the EHA. Since this motor can rotate in both directions, but the pump is single direction, caution must be exercised to ensure the pump is not rotated in the wrong direction. To rotate the pump in the correct direction a negative control voltage signal (-10-0V) must be given to the servomotor. If a positive voltage is given by mistake a check valve (5) has been installed between the inlet and outlet of the gear pump that allows fluid to move from the inlet to the outlet. This will avoid high pressures being generated if the pump runs in the wrong direction which minimizes any potential excess wear. There is also a check valve, (8), at the outlet of the gear pump that avoids displacement from the hand pump turning the gear pump when it is idle.

A quick connect coupling attaches both pumps to any nipple in the circuit that is available and hence can charge any portion desired. A variable Hydraforce RV10-20 relief valve, (7), is attached to the outlet of both pumps to ensure that the fluid cannot be charged above the set value. A Hydraforce

NV08-20 needle valve, (1), is also attached to the outlet of the pump to lower the pressure of the portion of the circuit charged in the event that it is pressurized over the desired value.

Note that the addition of an automatic charging component allows the system to be charged in real-time experiments. This is especially useful when using the external bulk modulus circuit. Real-time discharging of the circuit can be performed by the external leakage circuit. These external systems allow for real-time variations of the system pressure and fault condition simulations when used together.

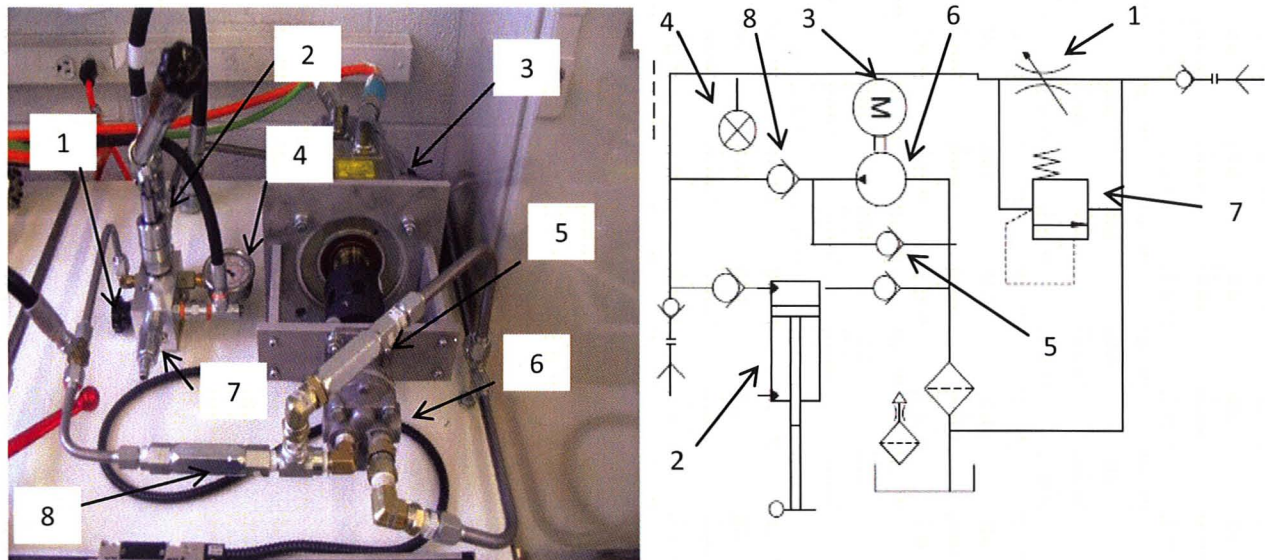


Figure 4.24. Charging circuit.

Table 4.16. Charging circuit components.

1	Hydraforce NV08-20 needle valve
2	Hydraforce HP10-21 hand pump
3	Siemens servomotor
4	0-20MPa pressure gauge
5	Check Valve connecting the inlet and outlet of the pump
6	2.83E-7m ³ /rad displacement external gear pump
7	Hydraforce RV10-20 relief valve
8	Check valve on outlet of gear pump

4.6.5 Offline Rectifying Filtration Circuit (Assembly 5)

Due to the stringent standards of oil cleanliness in hydraulic systems, especially in hydrostatic systems, it is proper to use filtration to minimize any contaminants. An offline system is employed so that it can be used at intervals when filtration is required. A depiction of this circuit can be seen in figure 4.25 and a description of each component can be seen in table 4.17. An online system is undesirable since it changes the overall dynamics of the system. A rectified unit using four check valves, (2), is employed that forces fluid to enter the filter in one direction, regardless of the direction in which fluid enters the sub-circuit. A Pall UR209 filter, (1), with a 10micron element is used to filter the circuit. It is recommended that this circuit be used after one hour of use of either axis. When running fluid though the filter using the bi-directional external gear pumps they should operate for at least five minutes.

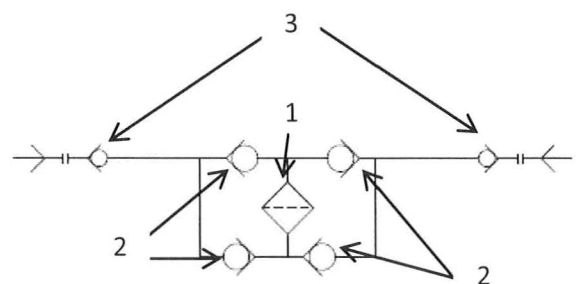
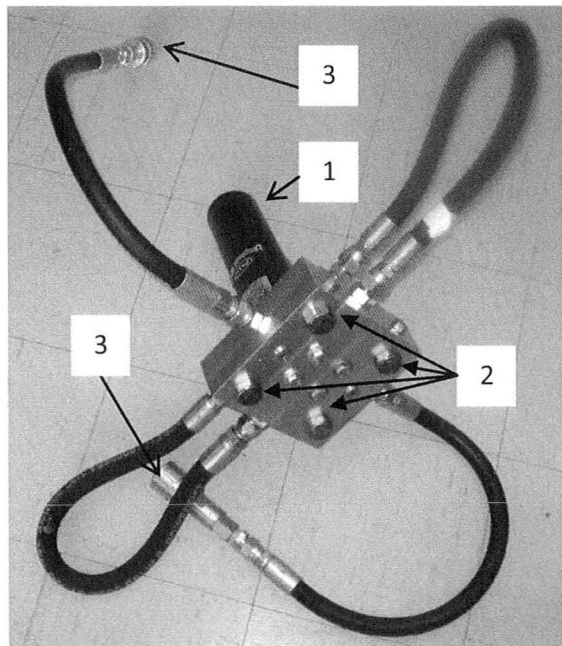


Figure 4.25. Rectified filtration circuit.

Table 4.17. Rectifier circuit components.

1	Pall UR209 10micron filter
2	Rectifying check valves
3	Quick connect couplings

4.6.6 Axis A and B Connect Valves (Assembly 6)

In addition to the components already shown in the dual EHA circuit in figure 4.3 there are several valves permanently attached to the system to increase functionality. Figure 4.26 shows the inclusion of valves named Axis A and B connect valves. Table 4.18 describes each component. These valves, (1) and (2), allow two pumps to drive one of the actuators, which is useful for applications where increased velocity is needed. This application is employed to obtain the damping relationship of each axis which is explained in chapter 5. Since both axes are not perfectly symmetrical and both servomotors do not give the exact same output even when given the same input (due to any noise input and inexact dynamics of each servomotor), these valves can be opened to relieve any stress at the actuator shaft coupling caused by unequal input flows. The valves employed here are Hydraforce SV10-28 2-way, normally closed blocking valves.

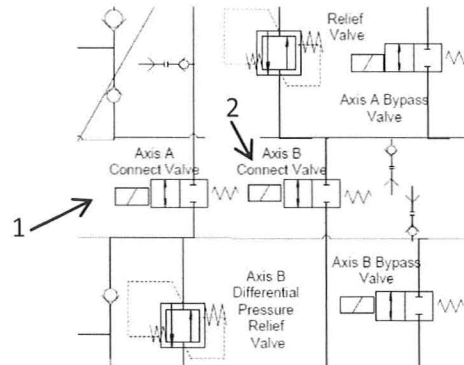
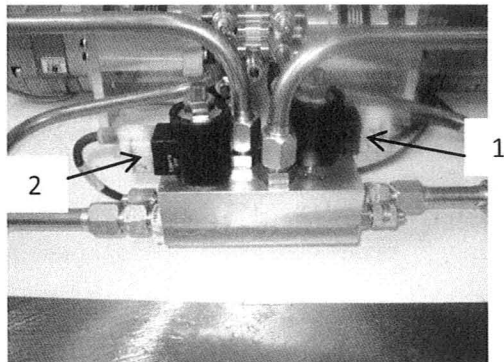


Figure 4.26. Axis A and B connect valves.

Table 4.18. Axis A and B connect valve components.

1	Hydraforce SV10-28 Axis A connect valve
2	Hydraforce SV10-28 Axis B connect valve

4.6.7 Axis A and B Blocking Valves (Assembly 7)

There is an axis A and B blocking valve that blocks sub-circuit flow between each pump and its corresponding actuator. These are manual ball valves that minimize any line restriction when they are open. These serve several purposes which include:

- If one is shutoff and another is open, it allows the axis with the open ball valve to drive the actuator of the other axis and force its fluid to go through its corresponding proportional throttling valve. This simulates a load on the axis with the open ball valve. This is performed to determine the leakage coefficient of each axis, which is described in chapter 5.
- If one valve is shut and the other is open then it allows both pumps to drive one actuator, provided that Axis A and B connect valves are open. This is useful in the application where the speed of the actuator must be increased.

The ball valves employed here are the Hydac KHB-16SAE model. These have a positive seal which creates a seal with negligible leakage. These can be seen in figure 4.27.

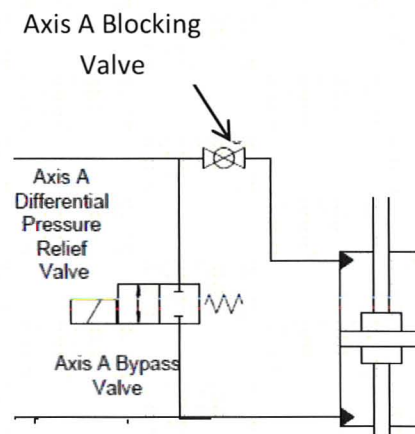
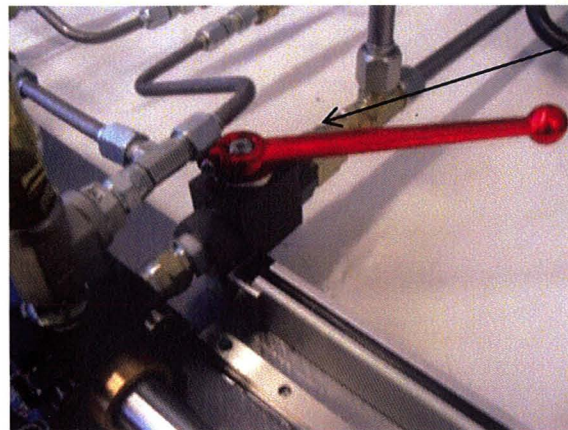


Figure 4.27. Axis A blocking valve.

4.6.8 Axis A and B Throttling Valves (Assembly 8)

The axis A and B throttling valves are used to restrict flow and create variable load conditions. This allows one axis to drive the actuator of the other axis with a variable restriction, as previously mentioned. A depiction of the Axis A and B throttling valves and their corresponding blocking ball valves can be seen in figures 4.28 and 4.29 respectively. Tables 4.19 and 4.20 describe the components for each of these respective assemblies. These valves can create fault conditions such as increased load (which can be also simulated as increased friction) and increased internal leakage. When simulating increased internal leakage both throttling valves must be used in conjunction. One is used to increase the load by throttling fluid of the actuator that is blocked from its corresponding pump, while the other is used to control the cross-port leakage of the other actuator being driven by its corresponding pump. The type of proportional valve used here is a Hydraforce SP08-25 2-way, normally open, bi-directional type, (2). They are controlled by the same Hydraforce 4000165 DIN coil mount proportional valve

controller which receives 0-10V inputs from the controller. Beside these throttling valves are ball valves, (1), which completely seal off each chamber from the other on each axis when closed. These are placed here since the throttling valves are normally open, which would have to be fully activated by its corresponding proportional solenoid to be closed. Since the throttling valves also use a spool instead of a poppet they can leak even when closed. The ball valves eliminate the necessity to use the throttling valves when they are not needed for any operation. The ball valves employed here are the Hydac KHB-10SAE model. Axis B uses the same configuration but the throttle valve is encased in a rectifier circuit. This allows fluid to enter the proportional valve only through the bottom end of the cartridge regardless of which direction the actuator is moving. This provides symmetry to the throttling process.

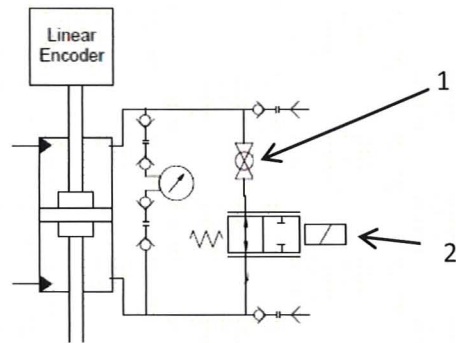
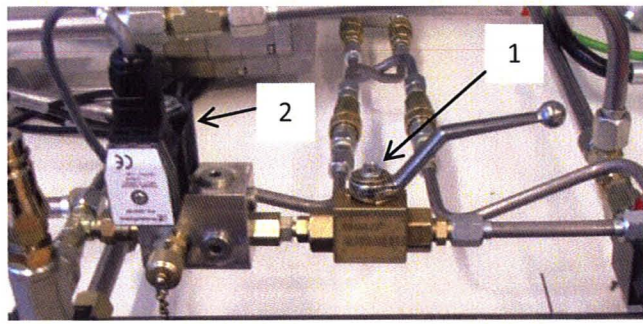


Figure 4.28. Axis A throttling assembly.

Table 4.19. Axis A throttling assembly components.

1	Axis A throttling shutoff valve
2	Axis A throttling valve

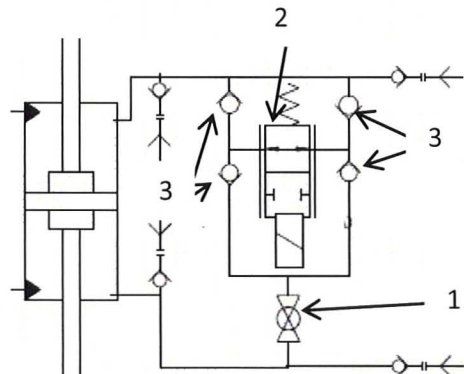
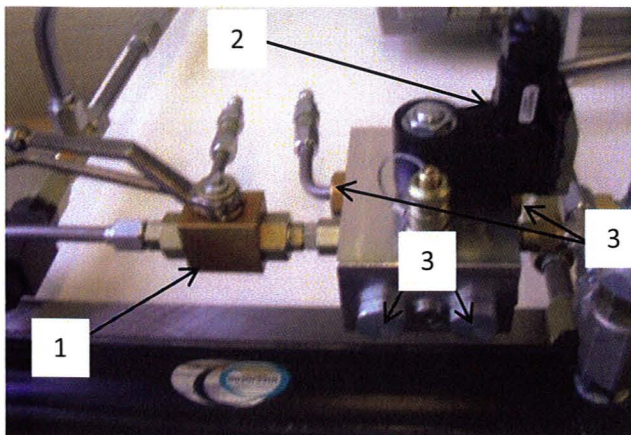


Figure 4.29. Axis B throttling assembly.

Table 4.20. Axis B throttling assembly components.

1	Axis B throttling shutoff valve
2	Axis B throttling valve
3	Rectifying check valves

4.6.9 Combined EHA Prototype

A depiction of the combined system can be seen in figure 4.30.

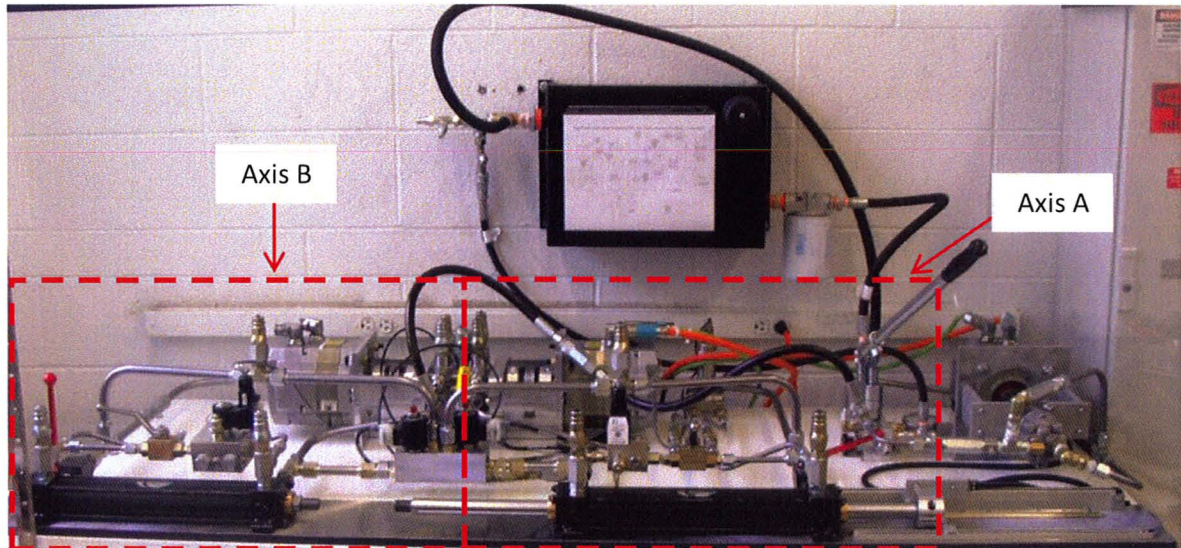


Figure 4.30. Complete dual EHA with all peripherals.

The connecting lines attached to the reservoir are all flexible hose which allows easy connection to the corresponding sub-circuits. The connections in axis A and B all use rigid tubing to avoid decreasing the stiffness of the system. This avoids decreasing the bandwidth of the system and also makes the calculation for the bulk modulus of the system simpler. External connections are either flexible hose or tubing. All the tubing and flexible hose can be seen in figure 4.30. The combined volume of each axis, $V_{o,a}$ and $V_{o,b}$, is $1.08E-3m^3$. Note that there is no added mass to the actuator so the mass of the piston, M_p , is equal to the total mass, M .

The above describes in detail the design of the dual EHA prototype produced. In summary the major parameters derived from the above, which are required for control purposes, are shown in table 4.21. Note that these parameters are similar for both axes.

Table 4.21. EHA parameters determined by design.

Volumetric Displacement (D_p)	$5.57E-07m^3/rad$
Effective piston area (A)	$1.52E-3m^2$
Winding Resistance (R_c)	1.04Ω
Winding Inductance (L_c)	$14mH$
Back emf constant (K_w)	$0.98V/rad/s (102.5V/1000rpm)$
Torque Constant (K_c)	1.61 Nm/A
Rotary Inertia (J_{pm})	$1.98E-03Kgm^2$
System Volume ($V_{o,a}, V_{o,b}$)	$1.08E-3m^3$
Actuating Mass (M)	3.688Kg

Note that these parameters are necessary for the servomotor and hydraulic models previously introduced. For convenience the hydraulic and servomotor transfer functions are restated as follows:

$$\frac{x(s)}{w(s)} = \frac{\frac{A\beta_e D_p}{V_o M}}{s^3 + \left(\frac{B}{M} + \frac{L_T \beta_e}{V_o}\right) s^2 + (A^2 + L_T B) \frac{\beta_e}{V_o M} s} \quad (4.11)$$

$$\frac{w_p(s)}{w_d(s)} = \frac{G_2 G_{PI} G_1 K_c}{1 + G_2 G_{PI} G_1 K_c} \quad (4.12)$$

Where $G_1 = \frac{1/R_c}{(L_c/R_c)s+1}$, $G_2 = \frac{1}{J_{pm}s + K_{p_{visc}} + K_{fric} + K_c K_w G_1}$, and $G_{PI} = \frac{K_p s + K_I}{s}$. Note that equations 4.11 and 4.12 require parameters that are not shown in the table 4.21. The first parameter not shown is the bulk modulus, β_e . From [16] the bulk modulus is 210MPa, which will be the assumed value for this research. For the damping coefficient, B , Habibi and Goldenberg determined a value of 800Ns/m [16]. The next chapter will investigate the damping coefficient as it relates to actuator velocity. The leakage coefficient, L_T , determined in [16] was 5.0E-13m³/s/Nm⁻². The next chapter will also investigate the overall leakage coefficient. The pump viscosity and friction coefficients, $K_{p_{visc}}$ and K_{fric} respectively, added together is 2.0E-4Nm/rad/s from [16]. This will also be the assumed value for $K_{p_{visc}}$ and K_{fric} in this research.

4.7 Finite Element Analysis of the Dual Electro-Hydrostatic Actuator

Finite Element Analysis (FEA) was performed on the components shown in figure 4.13 plus the pump hatch to verify the safety factor for the system with a burst pressure of 20.68MPa that was at least 6 times the maximum operating pressure. The program used was ANSYS Workbench. The analysis can be performed in two ways. The first is by having all components assembled together then applying the loads. The second is to evaluate each component individually with their respective loads and apply boundary conditions that simulate the component when assembled (i.e. apply a force to the part that results from pretension caused by tightening the casing bolts). The second approach was used since it minimizes the computing power needed to obtain a solution. The first approach was attempted but the computers available did not have the required memory to produce a solution.

When using the second approach all components are fastened together using four 5/16-24 UNF Grade 8 bolts with a pretension of 50Nm. 50Nm was the pretension used for the outer casing of the Marzocchi pumps and hence replicated on this prototype. This equates to a pretension force of 2.97E5N per bolt or 1.19E6N in total. This was added to each part as an initial load/constraint for each simulation. Figure 4.31 shows the applied loads and constraints for the inner circuit. For all simulations the nominal pressure used was 20.68MPa (3000psi).

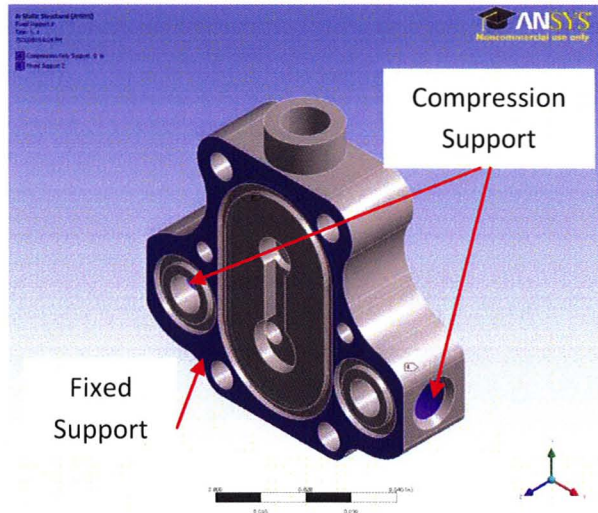
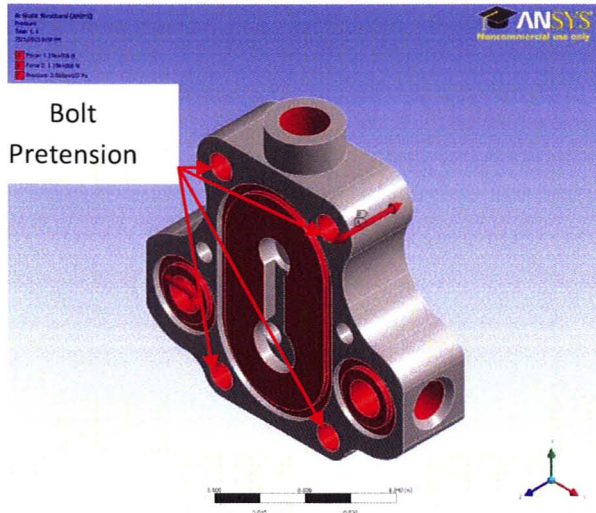


Figure 4.31. Load (in red) and constraints (in blue) for the inner circuit.

Notice that there is a compression support for the inner circuit. This is where a hydraulic fitting is placed. The fixed support is provided by the pump housings on both sides. Although these ends do not provide a complete fixed support it was assumed that the resultant friction on the surfaces was so high due to the bolt pretension that it could be simulated as fixed. Also notice that there is a load due to the bolt pretension. The bolts thread into this portion and pull from both sides.

The applied load to the pump housing can be seen in figure 4.32.

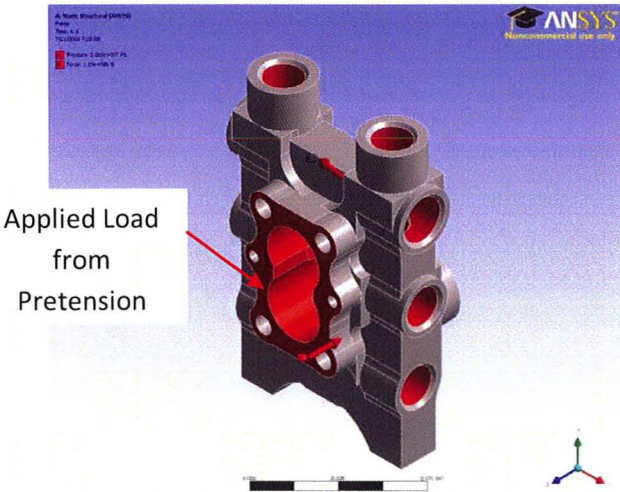


Figure 4.32. Applied loads on the pump housing.

Note that figure 4.32 shows the applied load from pretension distributed on one of the faces. Since these are through holes the pretension acts as an equivalent force onto the pump face. The remaining

coloured portion is the applied pressure. The opposite face is used as the fixed constraint, which can be seen in the figure below along with all other constraints.

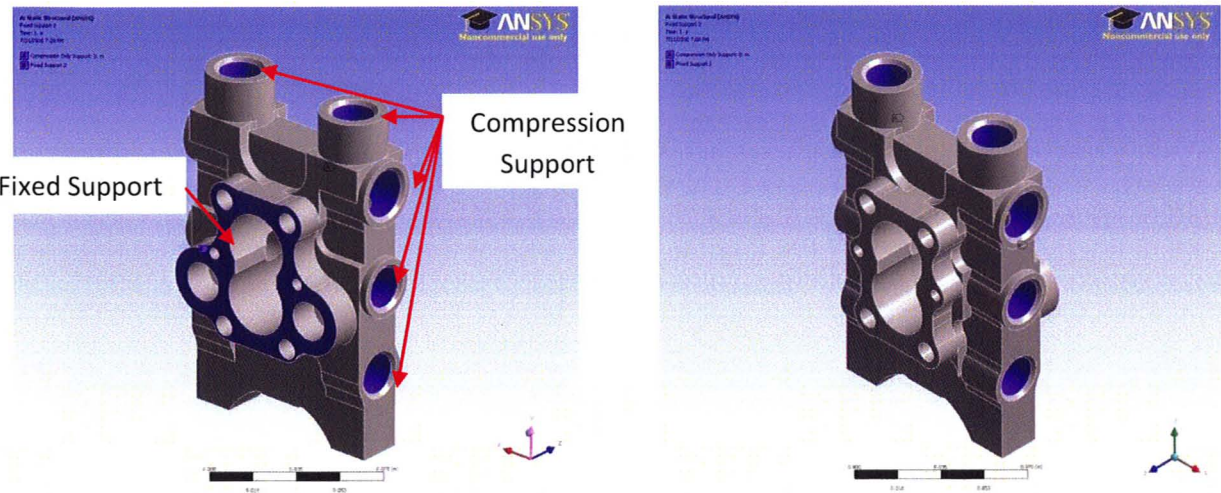


Figure 4.33. Constraints on the pump housing.

The applied load and constraints for the hatch can be seen in figure 4.34. Note that there is a load from the pretension of the bolts and the system pressure.

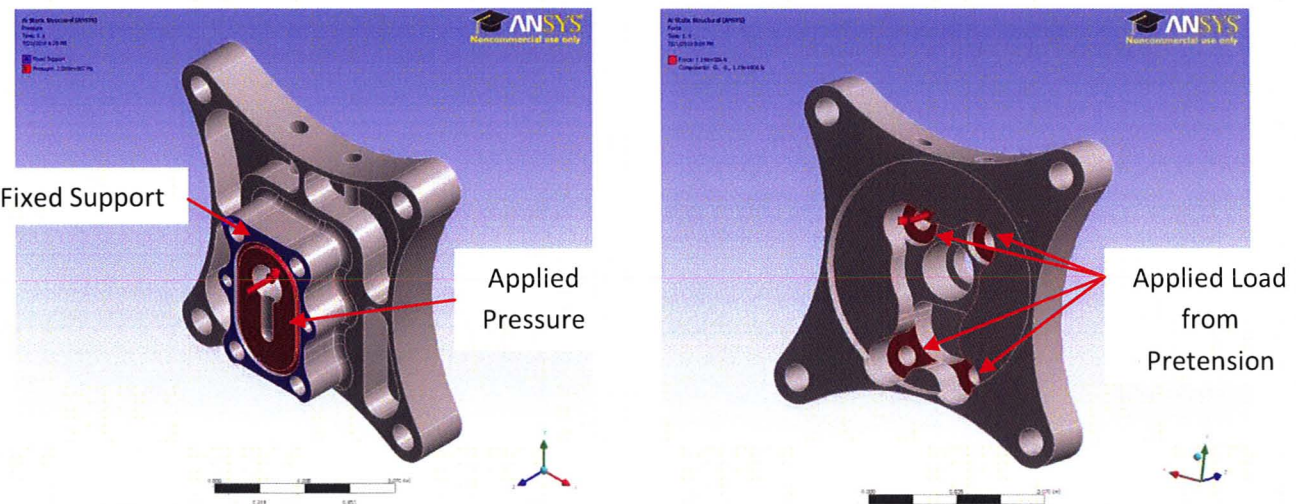


Figure 4.34. Load (in red) and constraints (in blue) on the hatch.

The mesh resolution used was 3mm with ANSYS defined element types termed as SOLID187 and SURF154. SOLID187 is a 10 node, 3-dimensional element suited for irregular element meshes due to its quadratic behaviour [31]. SURF154 is a 2-dimensional element that overlays the 3-dimensional elements and is used as the contact element for all loads and constraints [31]. It was determined that

these two elements were most applicable for all simulations performed. Figures 4.35-4.37 show the mesh for the inner circuit, pump housing and hatch respectively.

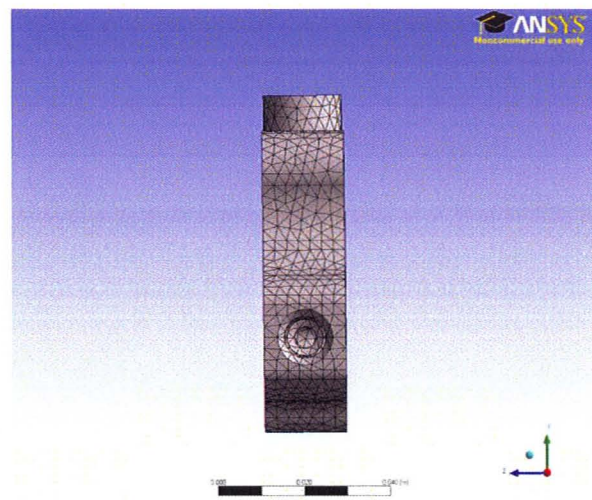


Figure 4.35. Inner circuit mesh.

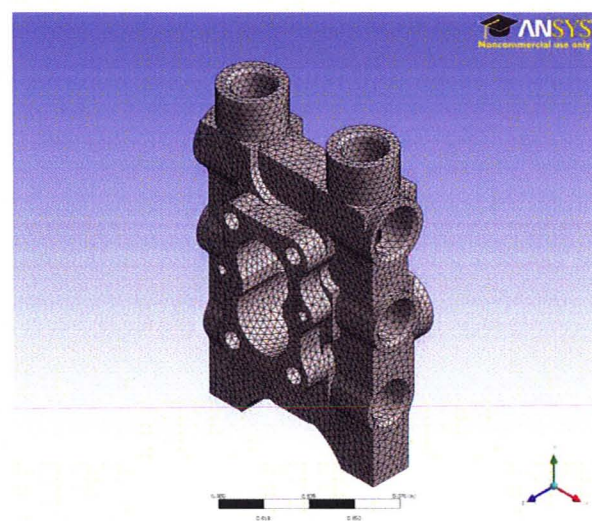
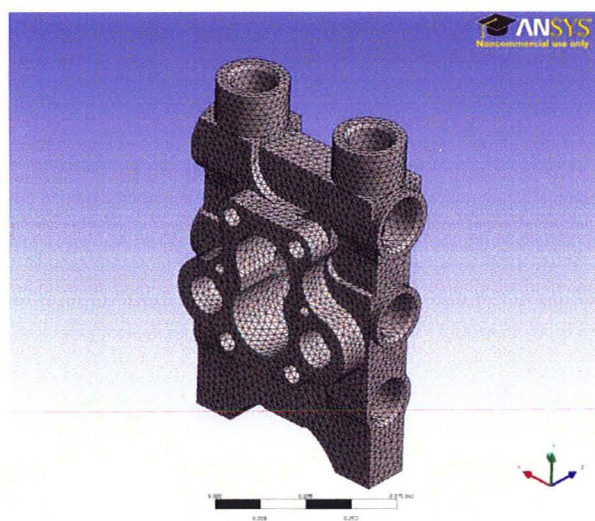


Figure 4.36. Pump housing mesh.

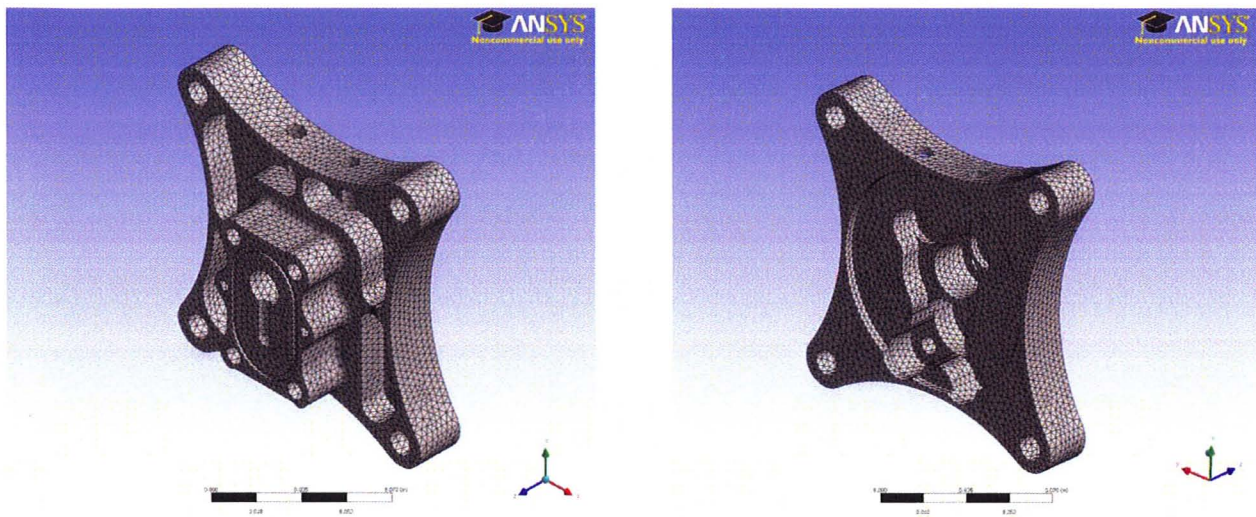


Figure 4.37. Hatch mesh.

The results from the inner circuit simulation can be seen in figure 4.38. This shows that the largest amount of stress occurs where two holes cross at 90° to allow fluid through the anti-cavitation check valve. The largest amount of stress is 107.31 MPa and the safety factor is 8.97, which is above the minimum required value of 6.

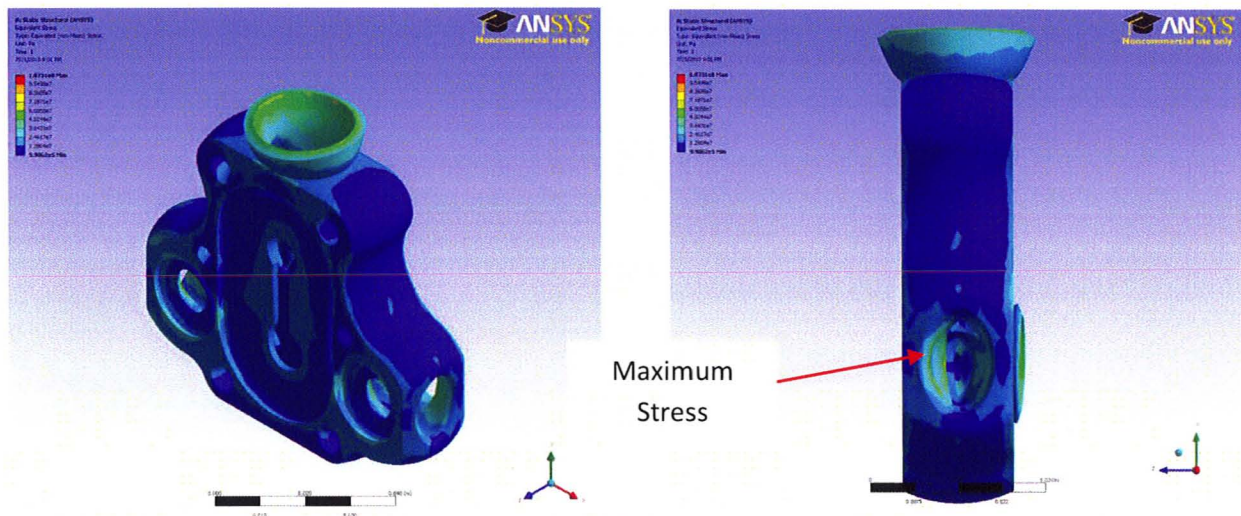


Figure 4.38. Stress distribution in the inner circuit.

The results from the pump housing simulation can be seen in figure 4.39. This shows that the largest amount of stress occurs at edges inside the body where the pressure relief valve and the fittings which attach to the inlet and outlet are placed. The largest amount of stress is 167.02 MPa and the safety

factor is 5.77. Although this is slightly below the safety factor of 6 it was determined that this is still acceptable.

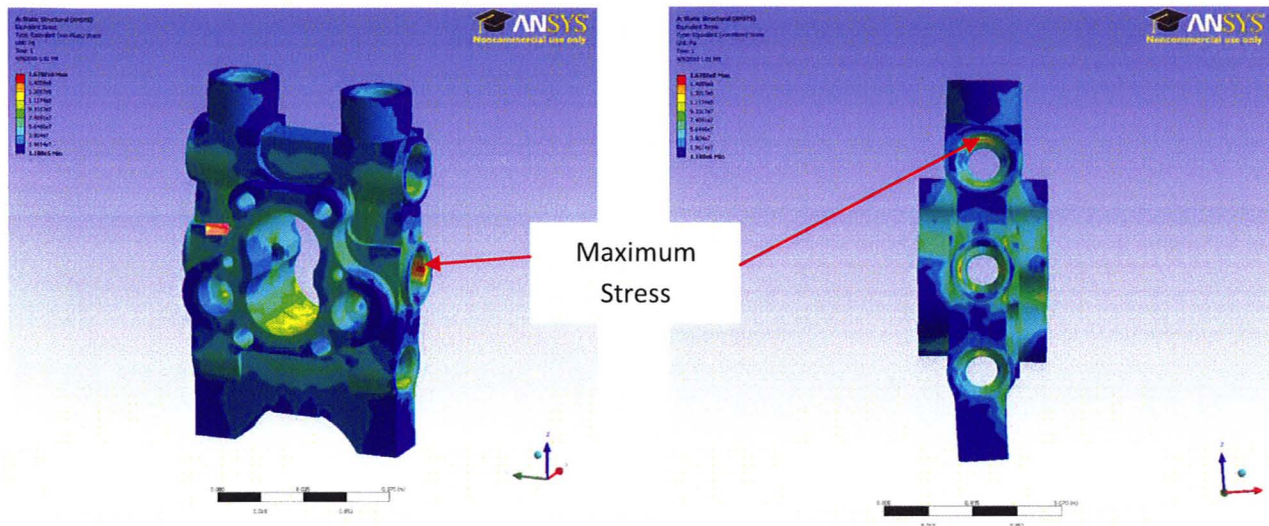


Figure 4.39. Stress distribution in the pump housing.

The results from the pump housing simulation can be seen in figure 4.40. This shows that the largest amount of stress occurs where the bolt heads and washers make contact with the hatch. The largest amount of stress is 128.57 MPa and the safety factor is 7.49, which is above the minimum required value of 6.

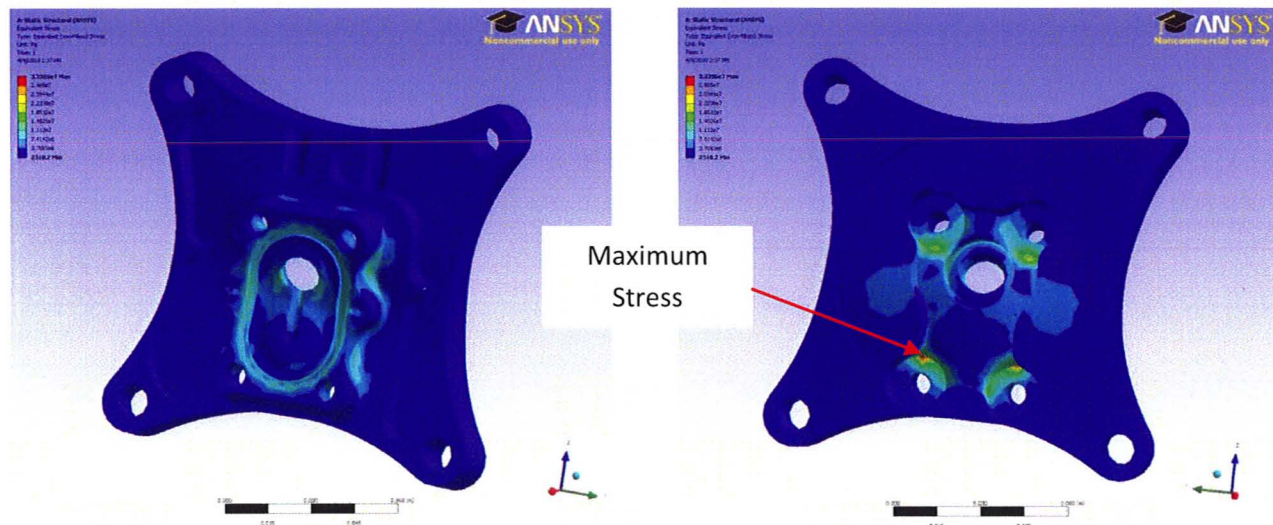


Figure 4.40. Hatch stress distribution.

These results show that the weakest portion of the assembly is in the pump housing. Although the acquired safety factor is slightly below 6 it was determined to be satisfactory for the final design.

4.8 Servomotor Drive Amplifier and System Controller

As previously mentioned the drive amplifier used to power the Siemens servomotor is a Simodrive 611U, which is also produced by Siemens. This drive receives 480VAC 3-phase with a maximum of 30 amperes and converts it into a Pulse-Width Modulated (PWM) signal that gets sent to the servomotor. The PWM signal is controlled using a $\pm 10V$ analog input signal. The source of the $\pm 10V$ comes from a data acquisition card which is connected to software that controls this input. The card used to control the Simodrive is a National Instruments PCI-6229 multifunction DAQ.

Figure 4.41 shows a depiction of the Siemens drive amplifier and the PC used to control the entire system. A full electrical diagram along with the specifications for each component in figure 4.41 can be seen in Appendix A. A description of select electrical components can also be seen in Appendix A.

All outputs are controlled and all inputs are received by this card which communicates with the Real-Time Windows Target (RTWT) toolbox in Simulink, which is a part of the Matlab software package. Simulink allows for real-time feedback control of a system if desired and can control several inputs and outputs at any given time. All four analog outputs are utilized in this system, two for controlling two of the servomotors and the others control the proportional valves described in section 5.5. The three gage and one differential pressure transducers utilize four of the single ended analog inputs. Six of the digital outputs are used to control the six on-off solenoids in the system while two outputs initialize the drive so that it can receive external signals. All of these are connected to a relay bank that allow 120VAC and 24VDC input voltage sources to power any load. This relay bank is a model CIO-ERB08, made my Measurement Computing.

There are four encoders used in the system, one linear encoder attached to the actuator and a rotary encoder attached to the back of each servomotor. The output of these encoders give a differential quadrature signal. To receive these types of signals the data acquisition card PCI-QUAD04 made by Measurement Computing was utilized. This card connects with RTWT and receives up to four differential quadrature inputs.

To parameterize the Siemens Servodrive that accepts the $\pm 10V$ signal from the PCI-6229 multifunction DAQ there is a PROFIBUS communication link between itself and the PC. This is a digital field bus communication protocol that allows a single control platform to communicate with multiple Servodrives over the same cable. To interface with the PC there is a PCI card installed that allows the computers' signals to be transmitted via the PROFIBUS protocol.

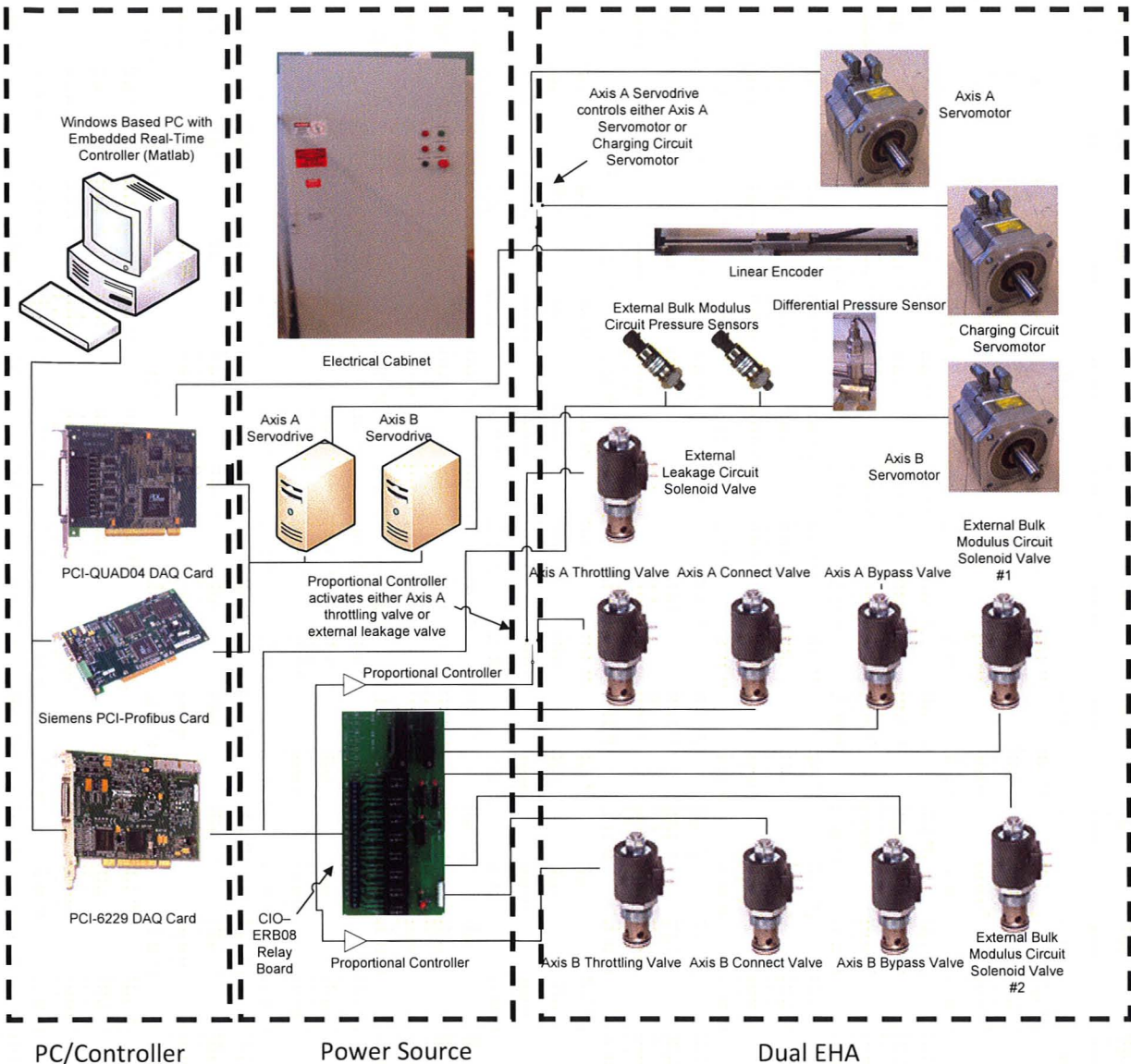


Figure 4.41. Dual EHA electrical and control configuration.

4.9 Conclusion

This chapter describes in detail the dual EHA prototype produced. This prototype is based off a leaner design made to attach to the rudder of the F-35 JSF but was modified with more commercially available components. This system also has the ability to incorporate fault conditions for future research purposes. The major parameters for control purposes that are determined from the system design have been also presented in this chapter.

Chapter 5 Experimental Determination of EHA Parameters

This section will evaluate the parameters of the EHA that are not available from the design itself. The parameters determined here are the leakage and damping coefficients. This chapter will outline the experimental processes used to determine these parameters and the theory behind varying of the bulk modulus of oil with respect to entrapped air.

5.1 Verification of the Hydraulic Gain

As previously stated the hydraulic gain of the EHA is given by the following equation:

$$K_h = \frac{AD_p}{A^2 + L_T B} \quad (5.1)$$

Assuming that leakage is negligible the hydraulic gain becomes $\frac{D_p}{A}$. Trials were performed to verify whether this relationship holds true. This was done by inputting a servomotor velocity and extracting the actuator velocity. Assuming the leakage is negligible the relationship between the pump and actuator velocity is shown by equation 5.2.

$$\dot{x} \approx \frac{D_p}{A} w_d \quad (5.2)$$

The plot of \dot{x} vs. w_d obtained from measurements can be seen in figure 5.1. The slope of this curve shows the hydraulic gain, which is 3.57×10^{-4} m/rad. The calculated value, according to equation 5.2, is 3.62×10^{-4} m/rad. Measurements confirm that the hydraulic gain is within the correct range and the small discrepancy shows that there is some leakage in the system. Note that this trial was performed with no load so the leakage was at the minimum.

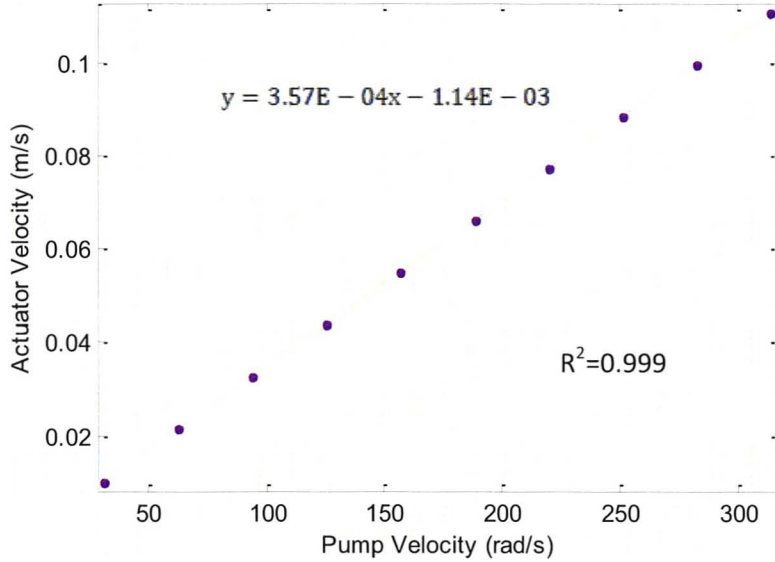


Figure 5.1. Measured actuator velocity vs. pump velocity.

5.2 Determination of the Overall Leakage Coefficient

This section describes the process in which the overall leakage coefficient, L_T , was acquired and reveals its magnitude at various pressures. It is assumed that the leakage flow in the EHA is laminar and therefore dependent on the pressure differential [22].

The experimental procedure used to determine the combined leakage of Axis A used a differential pressure sensor and linear encoder. Details of these transducers can be seen in appendix A. Axis A and B cylinders are coupled together. Axis A of the dual EHA is actuated while the pump and the cylinder in axis B are decoupled by closing its corresponding shut off valve. Axis B throttle shut off valve is open. As the axis A cylinder is actuated it will move the axis B cylinder and force its fluid through the axis B throttle valve. This throttle valve is controlled by a proportional solenoid that changes the orifice restriction by receiving an analog signal from the PCI-6229 data acquisition card. The increase in voltage increases the throttling which develops a larger pressure differential. The increase in pressure differential increased the leakage in axis A and this was calculated using the steady-state velocity extracted from the linear encoder. The equation used to determine the leakage is given by:

$$L_T = \frac{D_p w_d - A \dot{x}}{\Delta P} \quad (5.3)$$

Where ΔP is the pressure differential across the actuator chambers (Pa), which can also be described as $P_1 - P_2$. Each trial was performed at a constant velocity to eliminate the effects of the acceleration of mass and to minimize compressibility flow. A schematic of the experimental setup can be seen in figure 5.2.

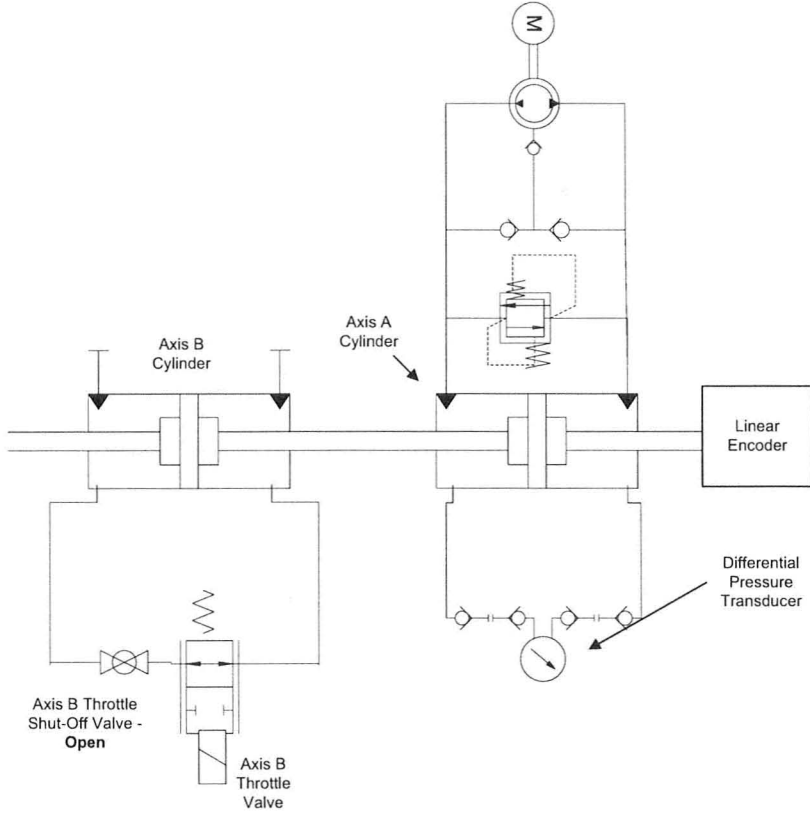


Figure 5.2. Schematic of setup used to determine the overall pump leakage.

A plot of the flow rate versus pressure for Axis A can be seen in figure 5.3. A constant pump speed of 104.7rad/s (1000rpm) was used for all trials, which equates to a demanded flow rate of 5.76E-05m³/s. Ten trials were performed to ensure repeatability of the setup. It was found that the data was repeatable within a small margin of error. Figure 5.3 shows the data from three of these trials. The plot shows that a linear relationship exists between pressure and leakage where the flow rate decreases as the pressure increases. The pump pressure was increased to a maximum value of 3.36E06Pa (487psi) in which the pump flow decreased to 3.39E-05m³/s.

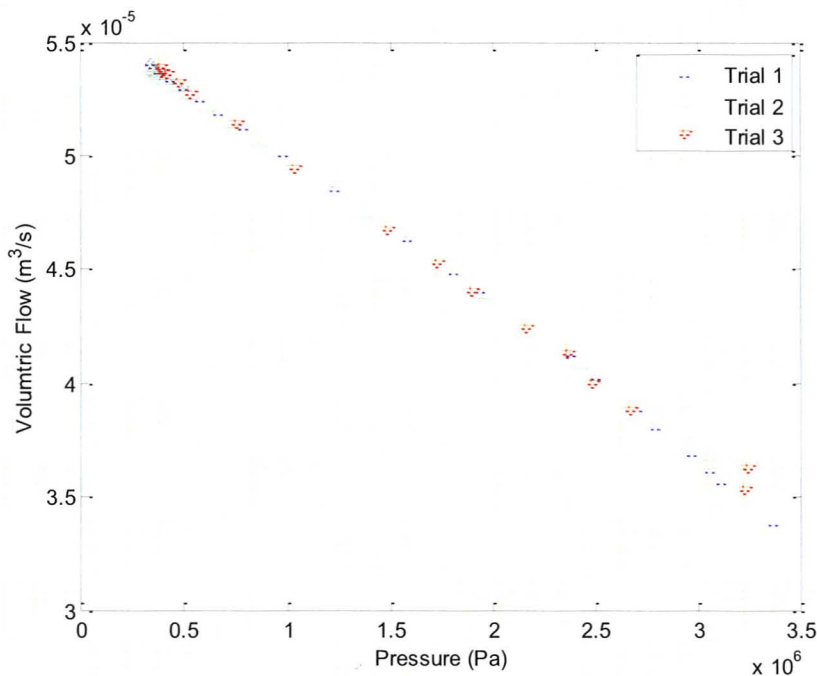


Figure 5.3. Flow vs. pressure at a pump speed of 1000rpm for Axis A.

A plot of the overall leakage versus pressure can be seen in figure 5.4. Figure 5.4 shows the linear trend between leakage and pressure using a least squared line fit. The slope of this line is the overall leakage coefficient for Axis A, which is $6.52E-12m^3/sPa$.

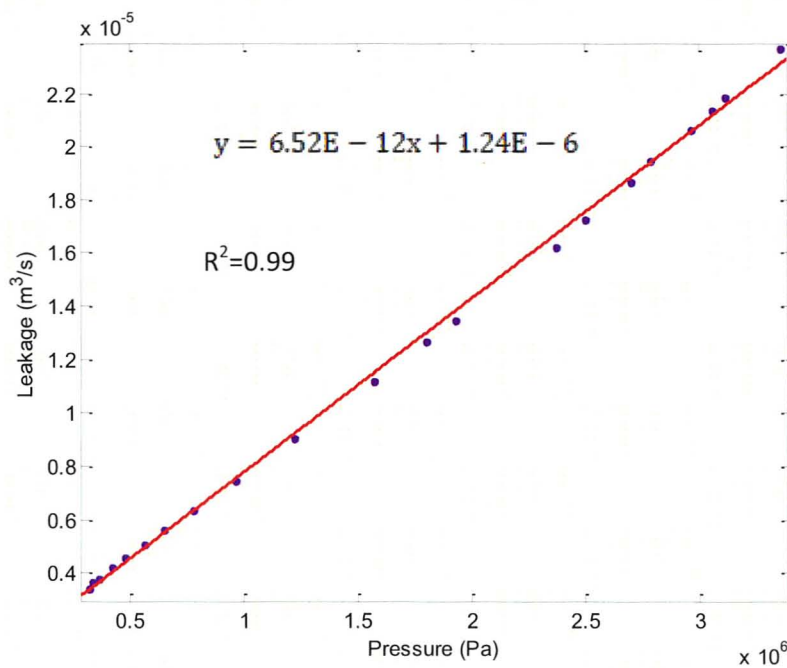


Figure 5.4. Leakage vs. pressure at a pump speed of 1000rpm for Axis A.

A plot of the volumetric efficiency versus pressure can be seen in figure 5.5. The formula used to derive the efficiency is as follows:

$$\varepsilon_V = 100 * \frac{A\dot{x}}{D_p w_d} \quad (5.4)$$

Where ε_V is the volumetric efficiency (%).

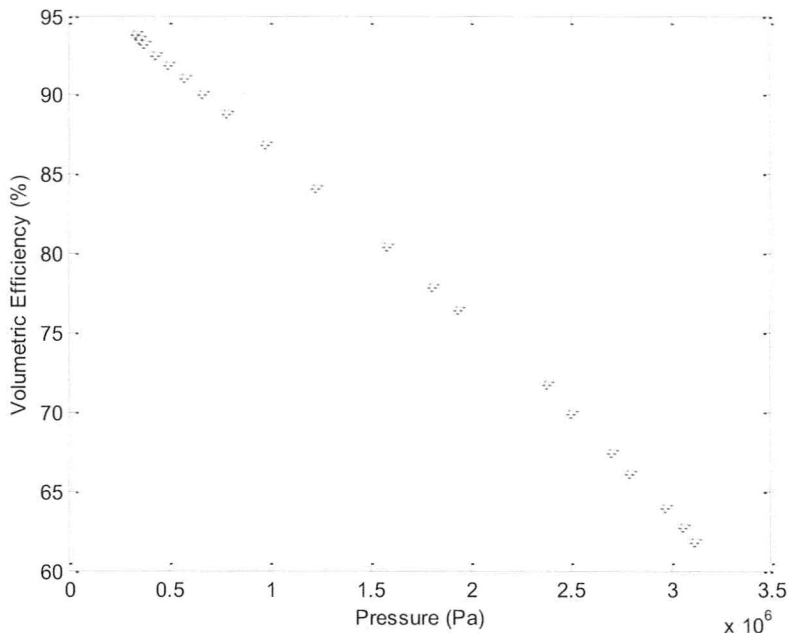


Figure 5.5. Volumetric efficiency vs. pressure at a pump speed of 1000rpm for Axis A.

The same process was used to determine the leakage coefficient for Axis B. Instead of the Axis A actuator driving the Axis B actuator the experiment was reversed. The differential pressure transducer was switched from Axis A to Axis B and the appropriate valves were opened and closed. Figures that show the relationship between flow, leakage and efficiency vs. pressure can be seen in Appendix B. The leakage coefficient of Axis B is $4.27E-12 m^3/s$.

It must be noted that the leakage of this system is much larger compared to regular hydraulic systems. In this study it can be assumed that the pump leakage accounts for the vast majority of the overall leakage and hence plots 5.3-5.5 include the pump leakage. The other sources of internal leakage are the Axis A throttle shutoff valve and the cylinder. These both contain positive seals between both chambers which give them much better sealing properties compared to the gear pump. There are three sources of leakage inside of a gear pump: in the gap between the gear face and bushings (traverse

surface gap), in the gap between the pump housing wall and teeth (radial gap) and between the two meshing gears where the fluid flows to the case drain [32]. This can be seen in figure 5.6

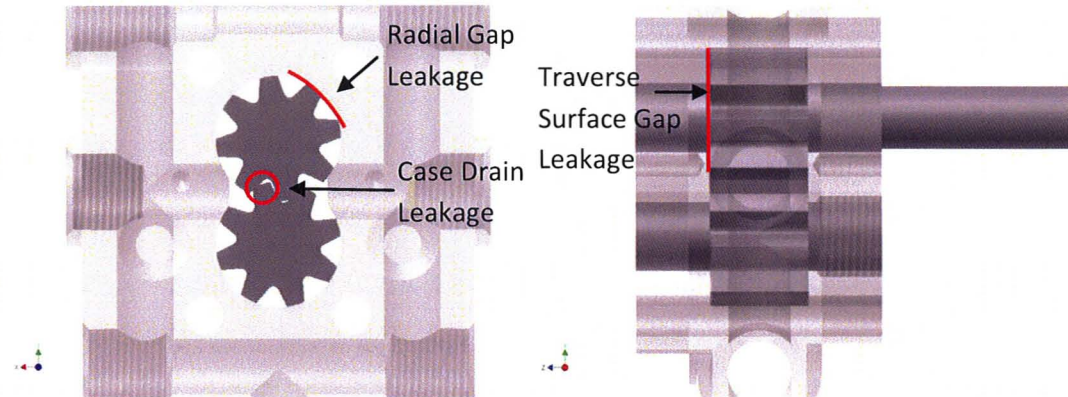


Figure 5.6. Leakage areas of an external gear pump.

Standard industrial external gear pumps tend to have efficiencies of 80-85% at higher pressures [14]. As mentioned in Chapter 4 the leakage of a pump is extremely sensitive to any increase in clearance between the gear teeth and casing. The high leakage is attributed to the inability to hold the tolerances needed to achieve high volumetric efficiency during the machining process. Figure 5.5 shows proof that the machining process must use submicron resolution cutting machines that are much more rigid than a standard mill or lathe.

5.3 Determination of the Cylinder Damping Coefficient

Equations 3.52 and 3.53 show that the damping coefficient of the cylinder plays a part in determining the EHA natural frequency and damping ratio. Damping inside of a cylinder can be modeled by determining the friction coefficients of the system. The three friction coefficients of the system are the static, boundary (or coulombic) and viscous friction. Of these three the most difficult to model mathematically is the static friction since it is dependent on how the piston and rod seals interact with the inner-bore of the cylinder at the microscopic level [33]. Knowing that these three coefficients exist and that for accurate control of the EHA low velocity friction must be characterized, it is assumed that the damping coefficient does not always have a linear relationship to actuator velocity.

Early friction models of a hydraulic cylinder were devised by Burenin, where he formulated that the friction of an actuator at non-zero velocities is a function of the coulombic and viscous friction. The mathematical relationship for the coulombic friction, which occurs at non-zero velocities but is independent of velocity at any time is given by [34]:

$$F_c = c_c P_{diff} d_o^2 \quad (5.5)$$

Where F_c is the coulombic friction force (N), P_{diff} is the pressure differential (Pa), c_c is the coulombic friction coefficient (dimensionless), and d_o is the diameter of the piston (m). The relationship for the viscous friction is given by [34]:

$$F_v = \mu c_v d_o \dot{x} \quad (5.6)$$

Where F_v is the viscous friction force (N), μ is the dynamic coefficient of viscosity (Kg/sm) and c_v is the loss factor for viscous friction (dimensionless).

A friction model has previously been developed for the EHA by Chinniah, et. al [4]. It assumes that the behaviour of the actuator friction at low speeds is quadratic. The general form of this equation can be seen in the equation below [22]:

$$F_f = (a|\ddot{x}|^2 + b|\dot{x}| + c) sgn(\dot{x}) \quad (5.7)$$

Where F_f is the friction force (N) and a, b and c are the friction coefficients that are determined experimentally. sgn is the sign function that multiples the function by 1 if the velocity is positive and -1 if the velocity is negative. These coefficients can be determined either by curve-fitting the experimental data or can be estimated online using model based techniques such as the Extended Kalman Filter (EKF) [22].

Recent developments in estimating friction have taken into account the irregularities of surface asperities in what is termed the pre-sliding region. This is the region where the cylinder starts from a zero to positive velocity but there is no sliding motion between the piston/rod seal and cylinder bore. Instead, there is a deflection of the seal which occurs in a highly non-linear fashion. This deflection of the seal can be compared to the contact between elastic bristles. As the bristles start to deflect they act as springs which gives rise to friction force [8]. Figure 5.7 depicts this phenomenon.

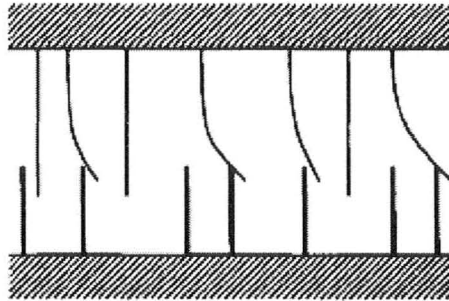


Figure 5.7. Friction interface between two surfaces at the microscopic level [35].

When the bristles have fully deflected the sliding regime has commenced. This occurs in a highly random fashion since it is dependent on the microstructure of the cylinder bore and the piston/rod seals. This means that the friction differs depending on the structure of the two surfaces interacting. The force in the pre-sliding regime is also not symmetric around zero velocity, which gives it a highly hysteretic nature. The most common model available that incorporates this phenomenon is the LuGre model. The global equation for the LuGre model is shown in equation 5.8 [35].

$$F_f = \sigma_0 \varphi + \sigma_1 \frac{d\varphi}{dt} + \sigma_2 \dot{x} \quad (5.8)$$

Where φ is the pre-sliding displacement of the seals (m), σ_0 is the micro-asperity stiffness of the contact between the seals and bore (N/m), σ_1 is the damping coefficient of the micro-asperities during the pre-sliding displacement (Ns/m) and σ_2 is the coefficient of viscous friction in the gross-sliding regime (Ns/m). The gross-sliding regime occurs when the piston/rod seals have stopped deflecting and their relative velocity to the cylinder bore is non-zero. Even when gross-sliding has commenced the effects of the first two terms of equation 5.8 can be non-zero. In both the pre-sliding and gross-sliding regimes $\frac{d\varphi}{dt}$ is significant and is described by equation 5.9 [35].

$$\frac{d\varphi}{dt} = \dot{x} - \frac{|\dot{x}| \sigma_0}{g(\dot{x})} \varphi \quad (5.9)$$

Where $g(\dot{x})$ is the Stribeck friction relationship. When the seal deflection approaches steady-state equation 5.9 takes the following form:

$$\varphi_{ss} = \frac{\dot{x} g(\dot{x})}{|\dot{x}|} = sgn(\dot{x}) g(\dot{x}) \quad (5.10)$$

Where φ_{ss} is the steady state piston/rod seal deflection. It must be noted that when the pre-sliding regime transfers to the gross-sliding regime the value of φ_{ss} is a function of the piston velocity. Equation 5.11 shows how the static and viscous frictions affect the Stribeck friction [36].

$$\sigma_0 g(\dot{x}) = F_c + (F_s - F_c) e^{-(\frac{\dot{x}}{v_s})^n} \quad (5.11)$$

Where v_s is the Stribeck velocity (m/s) and n is the Stribeck exponent. The Stribeck velocity and exponent are determined by least squares optimization to achieve the best fit. When the gross-sliding occurs the steady state friction can be described by equation 5.12.

$$F_{fss} = F_c + (F_s - F_c) e^{-(\frac{\dot{x}}{v_s})^n} + \sigma_2 \dot{x} \quad (5.12)$$

Where F_{fss} is the steady-state actuator friction (N). For this research the effects of pre-sliding friction in transient mode will be ignored and equation 5.12 is used as the actuator friction model. To derive a model for the friction it is beneficial to determine the static, coloumbic and viscous friction coefficients. To determine the static friction coefficient a step velocity input was given to the EHA in the range between 0.5-10V. In this trial, axes A and B pumps are both driving only axis A cylinder. This equates to an actuator velocity range of 0.011m/s-0.22m/s. The maximum pressure peak was extracted from each trial, which was assumed to be the static friction. Figure 5.8 shows the relationship between the static friction force and the step input velocity for the forward direction in Axis A.

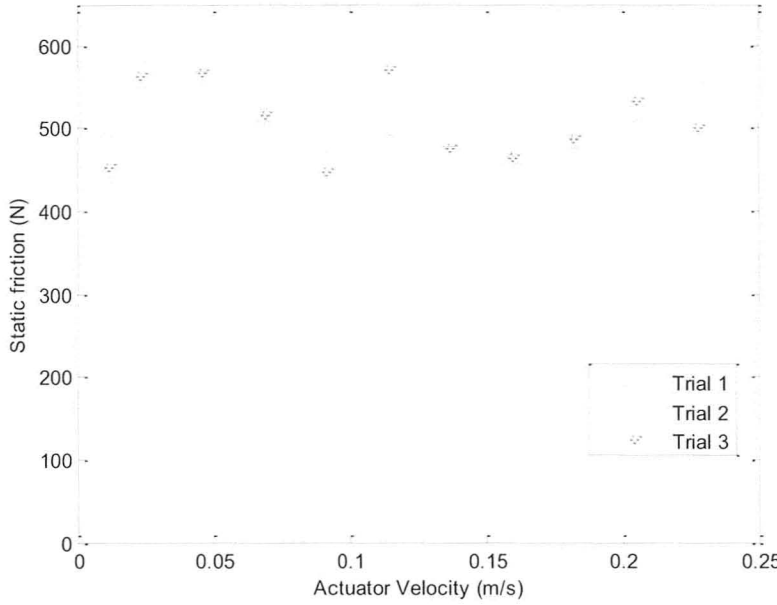


Figure 5.8. Static friction vs. velocity of actuator with no load for the axis A forward operating mode.

Figure 5.8 shows that the static friction does not increase with an increase in step velocity, which is expected. The average value of the friction was 510.4N with a standard deviation of 41.5N. The same trend existed for axis A in reverse and axis B in forward and reverse. This is a relatively large standard deviation but is expected in static friction measurements since the physical characteristics of the seal to bore contact are extremely hard to repeat. For this analysis it will be assumed that the static friction is 510.4N. The remaining static friction versus actuator velocity curves can be seen in Appendix B. The static friction for each operating condition and its standard deviation can be seen in table 5.1.

Table 5.1. Static friction and standard deviation for all operating modes.

Operating Mode	Static Friction	Standard Deviation
Axis A Forward	510.4N	41.5N
Axis A Reverse	448.0N	42.1N
Axis B Forward	467.7N	48.0N
Axis B Reverse	479.2N	43.9N

The coulombic friction coefficient is the value past the static friction value which is the lowest force needed to move the cylinder while in motion. It is expected that this value is lower than the static friction. To determine this value the cylinder was accelerated from 0 to 0.22m/s in two seconds using a

linear acceleration. The corresponding pressure was determined and plotted versus velocity. This can be seen in figure 5.9. The curves are compensated for the force due to the acceleration of the mass of the piston. Since the acceleration of the piston is 0.11m/s^2 (velocity increases from 0 to 0.22m/s in two seconds) and the mass of the piston is 3.688Kg , the force due to the acceleration piston is calculated using $\text{Force} = \text{Mass} \times \text{Acceleration}$. This calculated value is 0.406N and was subtracted from all calculated force values. Figure 5.9 shows that the friction of the piston goes down as the velocity increases. This is evidence of the Stribeck effect occurring in the cylinder. It also shows that the force due to the acceleration of the piston is negligible. As the velocity reaches its maximum value the force no longer decreases. This is where the coulombic friction occurs. The average coulombic friction value determined is 151.1N with a standard deviation of 3.2N . LuGre's model states that once this point is surpassed the friction will increase with velocity and viscous friction will dominate. In this setup 0.22m/s is the maximum achievable velocity. For the axis A forward there is no increase in friction with an increase in velocity. For this case the viscous friction coefficient cannot be determined.

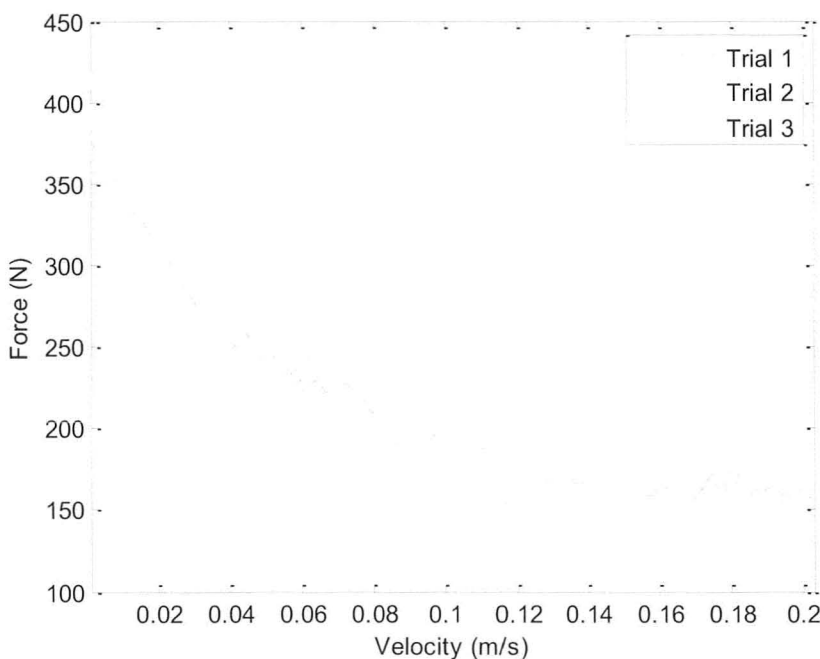


Figure 5.9. Actuator friction vs. velocity for the axis A forward operating mode.

Because of this equation 5.12 is used to model the overall friction but without the viscous friction coefficient, which is seen in equation 5.13.

$$F_{fss} = F_c + (F_s - F_c)e^{-(\frac{\dot{v}}{v_s})^n} \quad (5.13)$$

Figure 5.10 shows the best fit curve using equation 5.13. Through least squares optimization, the ideal values for the Stribeck velocity and exponent were 0.026m/s and 0.590 respectively. Therefore, the LuGre friction parameters for the actuator are:

- Static friction (F_s): 510.2N
- Coulombic friction (F_c): 151.1N
- Stribeck velocity (v_s): 0.026m/s
- Stribeck exponent (n): 0.590

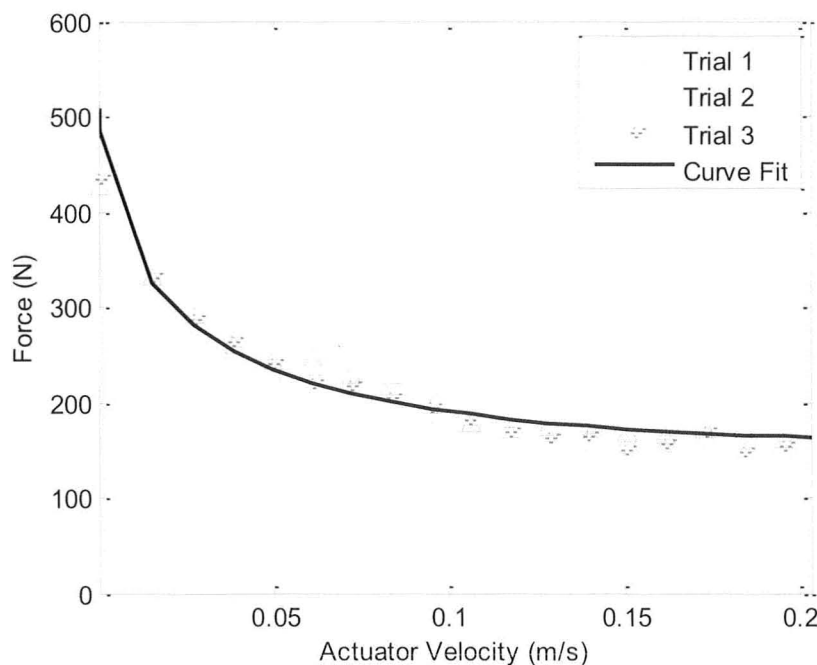


Figure 5.10. Actuator friction vs. velocity for Axis A forward operating mode.

Equation 5.14 shows equation 5.13 with these parameters inputted.

$$F_{fss} = 151.1 + 359.1e^{-\left(\frac{\dot{x}}{0.026}\right)^{0.590}} \quad (5.14)$$

For the axis A reverse and axis B forward and reverse operating modes at higher velocities, there was an increase in friction with an increase in actuator velocity. This made it possible to use the viscous damping coefficient for these cases. To model the friction equation 5.12 was used which includes the viscous damping coefficient. Figure 5.11 shows the friction versus the velocity and the best fit curve for the LuGre model for the axis A reverse operating mode. Note that for figure 5.11 the curve fit breaks

down at velocities lower than -0.18m/s. In this case there is a gradual increase in friction with the increase in speed but this rate has a very sudden change around -0.18m/s. This is an added non-linearity where the viscous friction becomes high and dominates the friction equation. This is unique to only this actuator in the reverse direction. Since the operating region in the remainder of this research is $\pm 0.11\text{m/s}$ (maximum speed for one pump driving one actuator) it was decided to create a curve fit that is more suitable for this area. For the Axis B forward and reverse operating modes similar plots can be seen in Appendix B. Table 5.2 shows the LuGre friction coefficients which were determined by least squares optimization for all operating modes.

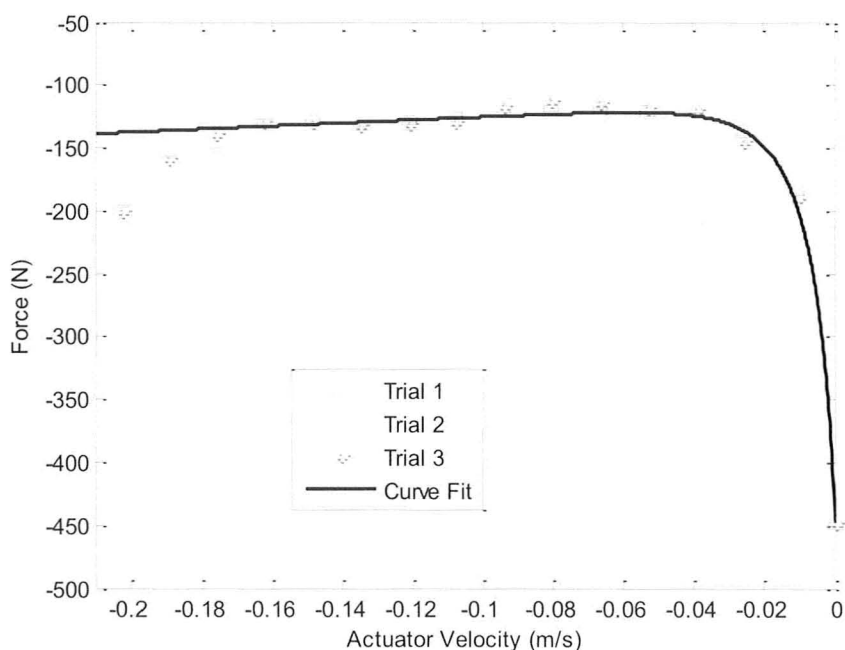


Figure 5.11. Actuator friction vs. velocity for Axis A reverse operating mode.

Table 5.2. LuGre friction parameters for all operating modes.

Operating Mode	Viscous Friction	Coulombic Friction	Stribeck Velocity	Stribeck Exponent	Static Friction
Axis A Forward	N/A	151N	0.026	0.590	510.2N
Axis A Reverse	123N	-113N	-0.007	0.776	-448.0N
Axis B Forward	138N	75N	0.010	0.743	467.7N
Axis B Reverse	109N	-72N	-0.016	0.835	-479.2N

The resulting equations for the damping coefficients for Axis A forward and reverse and Axis B forward and reverse can be seen in equations 5.15-5.18 respectively.

$$B_{A,For} = \frac{151.1 + 359.1e^{-(\frac{\dot{x}}{0.026})^{0.590}}}{\dot{x}} \quad (5.15)$$

$$B_{A,Rev} = \frac{113 + 335e^{-(\frac{\dot{x}}{-0.007})^{0.776}}}{\dot{x}} - 123 \quad (5.16)$$

$$B_{B,For} = \frac{75 + 397.2e^{-(\frac{\dot{x}}{0.010})^{0.743}}}{\dot{x}} + 138 \quad (5.17)$$

$$B_{B,Rev} = \frac{72 + 407.2e^{-(\frac{\dot{x}}{-0.016})^{0.835}}}{\dot{x}} - 109 \quad (5.18)$$

5.4 Determination of the EHA Bulk Modulus

The bulk modulus is an extremely important parameter to estimate if high accuracy is desired for the system. The bulk modulus is in essence the combined stiffness of the system and not just the stiffness of the working fluid itself. The factors that affect the stiffness of the system include:

- Volume and bulk modulus of the hydraulic oil
- Volume and pressure of entrapped air in the system
- Elasticity of material enclosing the hydraulic fluid and air

Since the housings for all components in the EHA prototype are metal and only steel tubing is used the compressibility effects due to the fluid enclosures is assumed to be negligible compared to the hydraulic fluid and air. The bulk modulus of a system is given by equation 5.19 [37].

$$\beta_e = -\frac{P_{diff}}{\Delta V/V_o} \quad (5.19)$$

Where ΔV is the change in volume of the system for a given change in applied pressure. The limitation of this equation is that it starts to break down when air is present in the system. Equation 5.20 gives an

estimate of the bulk modulus when entrapped air is present. It takes into account gas laws in conjunction with oil compressibility [38].

$$\beta_v = \frac{\left(\frac{P}{P_o}\right)^m + \delta}{\frac{\delta\beta_0}{nP} + \left(\frac{P}{P_o}\right)^m \beta_0} \quad (5.20)$$

Where β_v is the combined effective bulk modulus (Pa), P is the static pressure (Pa), P_o is atmospheric pressure (Pa), β_0 is the bulk modulus of oil (Pa), m is the air index of compression and δ is the air/oil volume ratio. The goal in designing hydraulic systems is to minimize the entrapped air as much as possible since a little amount can severely lower the overall bulk modulus of the system [39]. Figure 5.12 shows the relationship between static pressure and combined bulk modulus for a system with a varying percentage of entrapped air. Equation 5.20 is used to develop this figure.

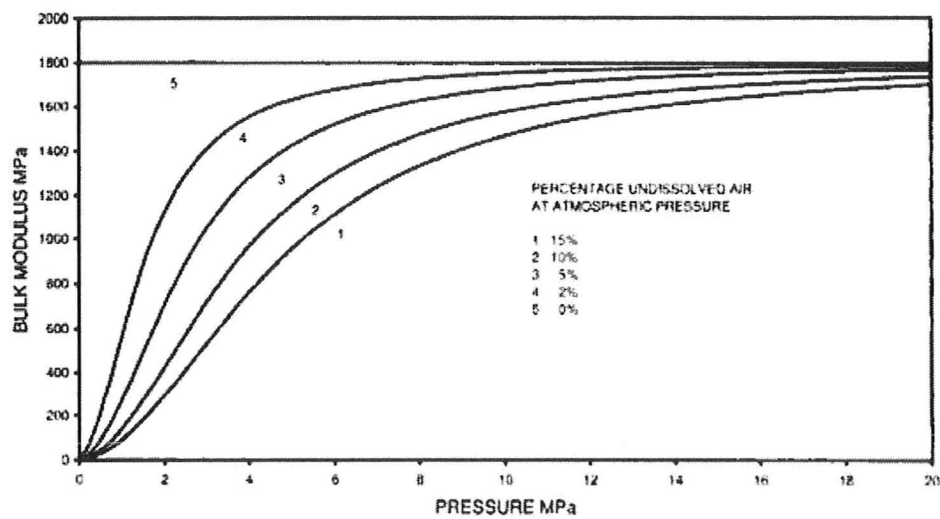


Figure 5.12. Effect of entrapped air on the bulk modulus of a hydraulic system [37].

Equation 5.21 shows another way of determining the overall bulk modulus of the system using a more simple relationship [38].

$$\frac{1}{\beta_v} = \frac{1 - \delta}{\beta_0} + \frac{\delta}{1.4P} \quad (5.21)$$

Note that the static pressure is multiplied by 1.4 to take into account adiabatic effects of air compression.

Entrapped air is always a big issue in hydrostatic systems since oil with entrapped air does not cycle back to a reservoir exposed to atmosphere where the air bubbles diffuse away. This is the case in open-loop systems. It is ideal to use equation 5.21 to determine the relationship between static pressure and bulk modulus but this requires knowledge of the air/oil volume ratio and the pure oil bulk modulus. The oil used in the EHA is AW32 but the pure bulk modulus varies between manufacturers.

The bulk modulus was not estimated in this analysis since the volume of entrapped air cannot be directly measured. Previous experiments performed by Chinniah, et. al, on the EHA used a bulk modulus of 2.10E+8 Pa [4]. This will be the value of the bulk modulus used in the remainder of this research.

5.5 Review

In review, the experimental coefficients for each axis of the EHA can be seen in table 4.3.

Table 5.3. Experimental EHA parameters for both Axes.

Parameter	Axis A	Axis B
Leakage Coefficient	$L_{T,A} = 6.52E-12 \text{ m}^3/\text{sPa}$	$L_{T,B} = 4.27E-12 \text{ m}^3/\text{s}$
Damping Coefficient, Forward Mode	$B_{A,For} = \frac{151.1 + 359.1e^{-(\frac{\dot{x}}{0.026})^{0.590}}}{\dot{x}}$	$B_{B,For} = \frac{467.7e^{-(\frac{\dot{x}}{0.015})^{0.526}}}{\dot{x}} + 487$
Damping Coefficient, Reverse Mode	$B_{A,Rev} = \frac{448e^{-(\frac{\dot{x}}{-0.010})^{0.356}}}{\dot{x}} - 720$	$B_{B,Rev} = \frac{479.2e^{-(\frac{\dot{x}}{-0.025})^{0.631}}}{\dot{x}} - 430$
Bulk Modulus	$\beta_{e,A} = 2.10E+8 \text{ Pa}$	$\beta_{e,B} = 2.10E+8 \text{ Pa}$

These parameters along with the parameters in table 4.21 are added to the EHA transfer function which was derived in chapter 3 and is shown in equation 5.22:

$$\frac{x(s)}{w(s)} = \frac{\frac{A\beta_e D_p}{V_o M}}{s^3 + \left(\frac{B}{M} + \frac{L_T \beta_e}{V_o}\right)s^2 + (A^2 + L_T B) \frac{\beta_e}{V_o M} s} \quad (5.22)$$

Equations 5.23-5.26 show the axis A forward, axis A reverse, axis B forward and axis B reverse transfer functions respectively:

$$TF_{A,For} = \frac{44.64}{s^3 + \left(1.27 + \frac{B_{A,For}}{3.688}\right)s^2 + (1.22E5 + 0.343B_{A,For})s} \quad (5.23)$$

$$TF_{A,Rev} = \frac{44.64}{s^3 + \left(0.83 + \frac{B_{A,Rev}}{3.688}\right)s^2 + (1.22E5 + 0.225B_{A,Rev})s} \quad (5.24)$$

$$TF_{B,For} = \frac{44.64}{s^3 + \left(1.27 + \frac{B_{B,For}}{3.688}\right)s^2 + (1.22E5 + 0.343B_{B,For})s} \quad (5.25)$$

$$TF_{B,Rev} = \frac{44.64}{s^3 + \left(0.83 + \frac{B_{B,Rev}}{3.688}\right)s^2 + (1.22E5 + 0.225B_{B,Rev})s} \quad (5.26)$$

Where $TF_{A,For}$, $TF_{A,Rev}$, $TF_{B,For}$ and $TF_{B,Rev}$ are the axis A forward, axis A reverse, axis B forward and axis B reverse transfer functions respectively. Note that the EHA now becomes non-linear due to the LuGre friction in each actuator.

5.6 Conclusion

Chapter 5 described the EHA parameters that cannot be determined mathematically. It was proven that the EHA has a relatively high internal leakage relative to common external gear pumps available on the market. It also showed that the EHA model is non-linear due to the actuator friction. It was also proven that the friction behaves in accordance with the LuGre model. Chapter 6 will investigate the acquisition of system models in different piece-wise linear regions using system identification techniques.

Chapter 6 EHA System Identification

In this section several linear models are determined experimentally by using a black-box approach to identifying transfer functions. By using this approach, transfer functions are obtained using feedback from the mechanical system and processed through algorithms that can give a very accurate model of the system. This process is known as system identification. This chapter will outline the models obtained for several piece-wise linear regions and the different methods for obtaining the order and transfer functions for the EHA.

6.1 System Identification Theory

System identification can provide a quick and accurate way of obtaining a linear transfer function [40]. Its advantages are its accuracy in capturing significant dynamics, speed of deriving the model and relevance. Its disadvantages are that it requires an experimental setup and it is a form of black-box modeling, meaning that the coefficients in the transfer function have no physical meaning. Modeling of the servomotor along with the overall EHA system (servomotor and hydraulic system) were performed in this research.

To commence system identification the input and output states for the desired transfer function must be known. The servomotor input and output are both in rad/sec for the system. The input signal is a voltage but needs to be scaled to be converted to velocity. The output is extracted as a position since the transducer is an encoder. The output is simply converted to velocity by taking the derivative and placing it through zero-phase filter, which eliminates the potential for lag in the filtered signal. This needs to be done since system identification is more effective when performed on a type zero system. Using the position from the encoder directly results in a type one system (which is the EHA type of transfer function derived in chapter 3).

Note that in equation 3.51, the hydraulic EHA model can be approximated as a third-order transfer function:

$$\frac{x(s)}{w(s)} = \frac{K_h w_{nh}^2}{s(s^2 + 2\zeta_h w_{nh}s + w_{nh}^2)} \quad (6.1)$$

Multiplying both sides of the equation by s yields:

$$\frac{sx(s)}{w(s)} = \frac{K_h w_{nh}^2}{s^2 + 2\zeta_h w_{nh}s + w_{nh}^2} \quad (6.2)$$

This shows that the hydraulic transfer function can be approximated by measuring the pump and actuator speeds. Therefore, the system identification process was performed in terms of velocity to obtain the transfer functions for both cases.

With this data the system was evaluated in the frequency domain by generating an Empirical Transfer Function Estimate (ETFE). The ETFE is computed by taking the Fast Fourier Transform (FFT) of the output and dividing it by the FFT of the input. A sampling interval of 0.001s was used. Once the ETFE was obtained a parametric model was fit to the data to get the overall transfer function.

There were four different forms of parametric models considered to obtain the transfer function. They were the AutoRegressive model with eXternal input (ARX), the AutoRegressive Moving Average model with eXternal input (ARMAX), Box-Jenkins (BJ) and Output Error (OE). All four use a regression technique to calculate the model. The ARX model uses the structure shown in figure 6.1 [40].

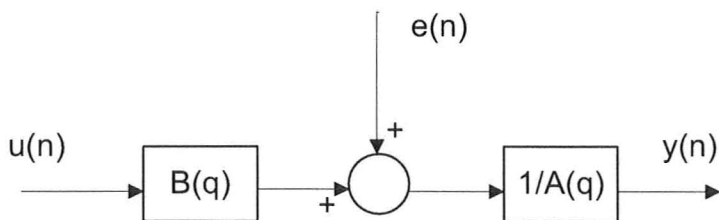


Figure 6.1. ARX model structure.

Where q is the time shift operator, $B(q)$ is the system model and the $1/A(q)$ is the noise model. The ARX model is a computationally efficient. It is a simple way of determining the model since it results in an equation that can be solved for obtaining model parameters. Its disadvantage is that the noise model is coupled to the denominator polynomial of the system model, making it very restrictive.

The ARMAX model uses the structure shown in figure 6.2 [40].

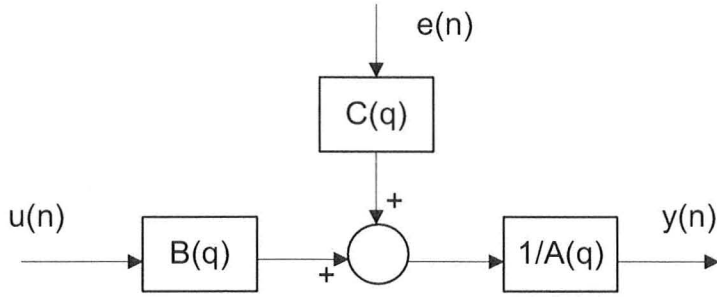


Figure 6.2. ARMAX model structure.

The ARMAX model extends on the ARX model in that it provides a more flexible transfer function in relation to noise with the use of $C(q)$.

The Box-Jenkins model uses the structure shown in figure 6.3 [40]. The Box-Jenkins method models the noise and dynamics of the system independently.

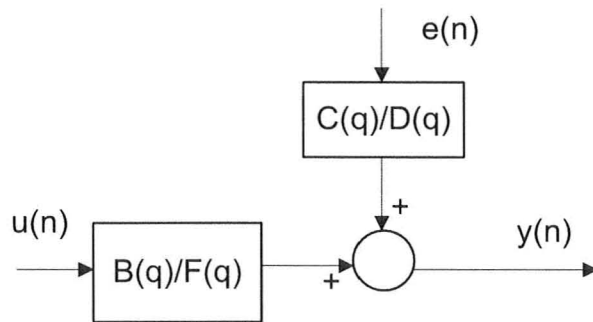


Figure 6.3. Box-Jenkins model structure.

The Output Error method does not take into account system or measurement noise disturbances within the system and models only the system dynamics. This is a preferred method to use when there is only white noise. The Output Error model uses the structure shown in figure 6.4 [40].

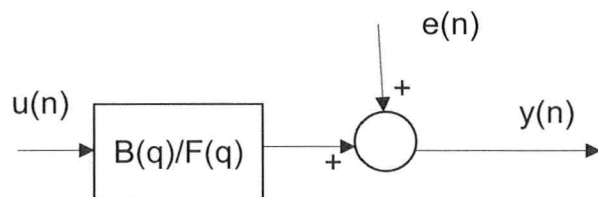


Figure 6.4. Output Error model structure.

Initial experimentation was performed using all four methods and the results from each were compared. It was found that the OE method provided the best results. Due to the minimal disturbances present in the system and given that the noise in the measurement was largely due to differentiation and aliasing, the OE method provided the best results.

For all of these methods the model structure and system order must be known before they can be identified. The order can be determined through several forms of analyses. They include [41]:

- Spectral analysis
- High order ARX analysis
- Impulse response analysis.

The two forms chosen for this analysis are the ARX and Impulse Response analysis. The high order ARX analysis generates models from a varying range of orders, typically 1-10. With each model there is a percentage output variance which is the percentage of the response that cannot be explained by the model. The model chosen with its corresponding order is typically the lowest order that contains an output variance of less than 0.5%, but this is dependent of the situation.

The impulse response method is also employed which uses a more systematic approach to determining the order instead of generating several models to see which one fits best. The basis behind this method involves sending an impulse to the system and recording the output. Since generating an impulse is difficult, a step input is commonly sent to the system and the output is differentiated.

The method used for obtaining the derivative of the step signal in this research is the central difference method which can be seen in equation 6.3.

$$f'(k) = \frac{f(k_s + 1) - f(k_s - 1)}{2T} \quad (6.3)$$

Where k_s is the time iteration, T is the sampling period (sec), f is the output and f' is the derivative.

The entire impulse response is the derivative of each point using equation 6.3. Equation 6.4 is the equation used to calculate the impulse response.

$$Im(k_s) = \frac{f(k_s + 1) - f(k_s - 1)}{2T\eta} \quad (6.4)$$

Where Im is the impulse response at sample k_s and η is the input magnitude (V).

To determine the order of the system the impulse response array is organized into a Hankel matrix (H_a), which can be seen in equation 6.5.

$$H_a = \begin{bmatrix} Im(1) & Im(2) & .. & Im(n) \\ Im(2) & Im(3) & .. & Im(n+1) \\ : & : & : & : \\ Im(n) & Im(n+1) & .. & Im(2n-1) \end{bmatrix} \quad (6.5)$$

The parameter n represents the size of the symmetrical Hankel matrix. If the length of the measured impulse response array is N then the relationship between the dimension of the Hankel matrix and N is $n=N/2$. The order of the system is equal to the number of linearly independent columns in the Hankel matrix. This can be determined by taking the rank of the Hankel matrix. The issue with this method is that noise is inherent in the impulse response data, especially since the impulse response is determined by differentiating the position reading from the encoder twice. To overcome this a process called Singular Value Decomposition (SVD) is used. SVD breaks down the Hankel matrix into the following form:

$$H_a = UV_d W^t \quad (6.6)$$

Where U and W are unitary matrices and V_d is a diagonal $n \times n$ matrix consisting of positive singular values, all on the diagonal. The order is determined by the number of significant non-zero singular values in V_d .

6.2 System Identification Initial Tests

System identification was performed only on Axis A with no loads.

To obtain accurate results in the system identification process the input signals used for the ETFE must contain a flat power spectrum in the frequency range of interest. The two types chosen here are a Pseudo-Random Binary Signal (PRBS) and a chirp signal. The PRBS signal is a binary set of step inputs with predefined minimum and maximum values. The amplitude of the PRBS changes randomly between two extremes given a switching rate. The switching rate determines the range of the flat power

spectrum of the PRBS, while the amplitude of the PRBS affects the signal-to-noise ratio. The chirp signal is a sine wave that increases its frequency as time increases. Both signals are rich in frequency content.

The first step in system identification is to determine the frequency range of interest. This is usually taken as ten times the bandwidth of the system, or the cross-over frequency, or the frequency range in which the signal-to-noise ratio is reasonably high to provide useful information. The frequency range of interest can be determined by inputting a signal to the system with a maximum frequency content equal to the Nyquist frequency, which is 3141rad/sec (500Hz). This was done using a PRBS signal with a voltage input of $\pm 2.5V$. The resulting ETFE for the servomotor and combined system can be seen in figures 6.5 and 6.6 respectively. Note that for the system identification process the inner-loop P and I gains for the servomotor have been set to 1 and 0 respectively.

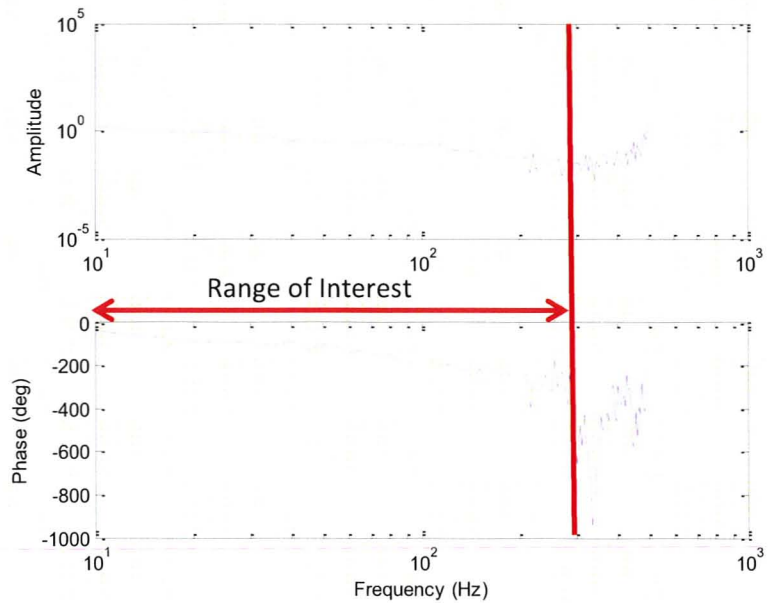


Figure 6.5. Break frequency test ETFE for the servomotor.

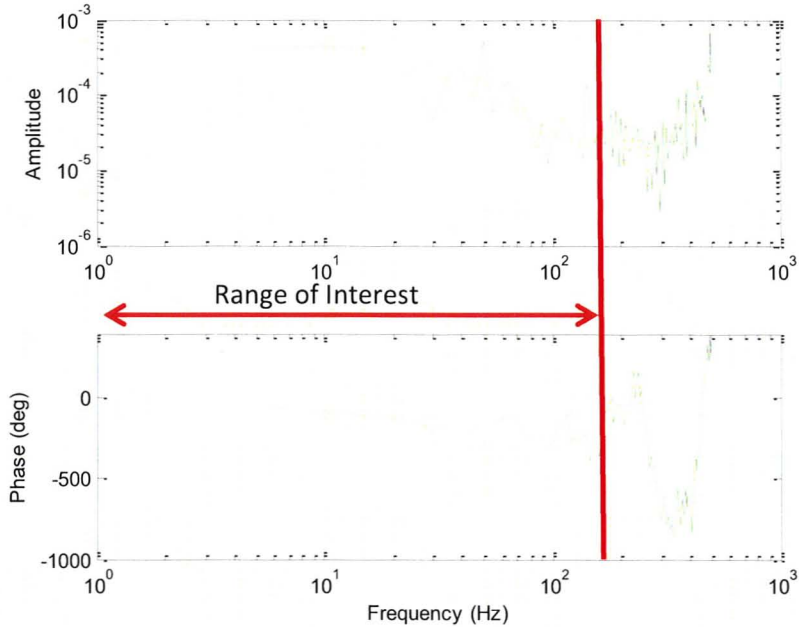


Figure 6.6. Break frequency test ETFE for the combined EHA system.

Both of these plots clearly show that the signal-to-noise ratio deteriorated beyond use at around 1571rad/sec (250Hz). Knowledge of this frequency limits the maximum useful frequency input that can be placed into the system because the signal-to-noise ratio degrades heavily thereafter.

With knowledge of the frequency range of interest, the input signal can be determined. In addition to consideration of the frequency content the amplitude of the signal needs to be determined. Ideally, the highest level of input signal should be chosen to maximize the signal-to-noise ratio while remaining within a piece-wise linear region and avoiding non-linearities such as saturation. This analysis was performed by using ETFE input signals between $\pm 1V$ - $\pm 10V$. Figures 6.7 and 6.8 show ETFE's of the servomotor and the combined system with the said input ranges using a PRBS signal of 785.40rad/sec (125Hz). All of these curves are placed through a 128 point size Hamming window to show a cleaner signal. In figure 6.8 the maximum voltage shown is 6V due to the large amount of torque required to move the actuator above this point causing the system to fault. These figures show the point in which saturation effects occur, which allows for the determination of the proper input voltage range to use for the rest of the system identification process. Figure 6.8 shows that the major limiting factor is the combined system in terms of the bandwidth. The bandwidth starts to decrease around $\pm 2V$. This is due to the limited amount of torque available to move the system at such high frequencies, which is a saturation effect. Knowing this the voltage range chosen for the rest of the identification process was $\pm 1.5V$ or a peak-to-peak amplitude of 3V. This is chosen for both system identification processes.

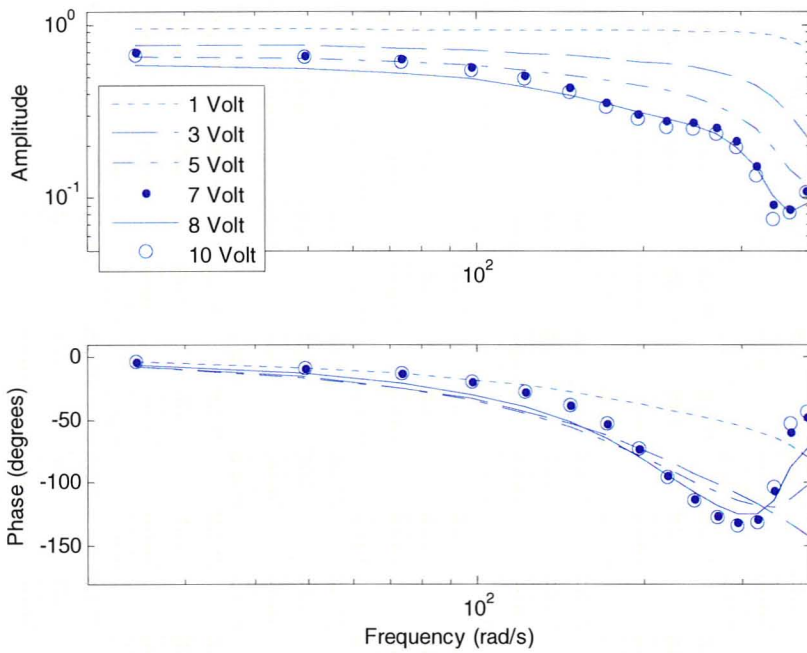


Figure 6.7. ETFE's for the servomotor using different input levels. Used to determine the highest input voltage range before saturation effects occur.

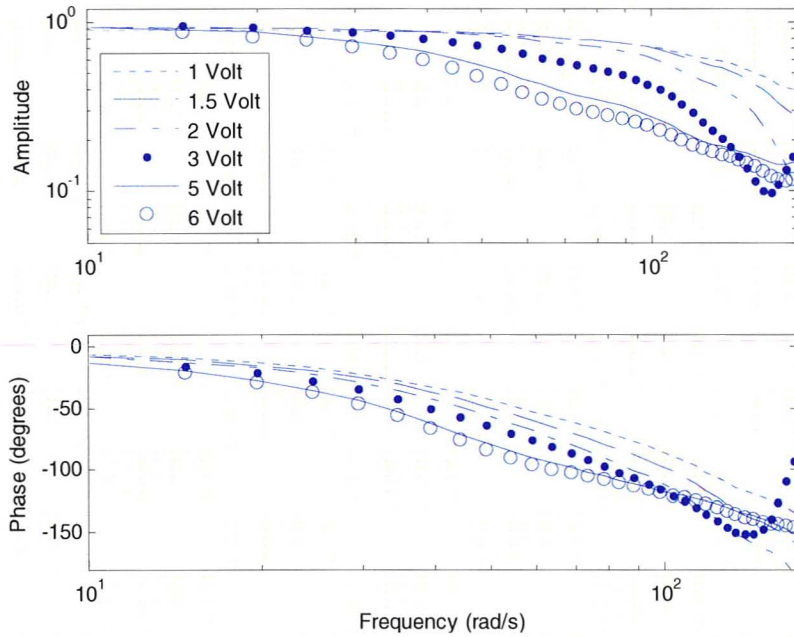


Figure 6.8. ETFE's for the combined EHA using different input levels. Used to determine the highest input voltage range before saturation effects occur.

The next step is to determine the piece-wise linearity for different operating regions of the system using the acquired input voltage range previously mentioned. This is performed by injecting a frequency rich signal at different operating points which is the same as adding a voltage bias. Choice of the type of

signal is dependent on any prior knowledge of the system. The only concrete knowledge of the dynamics given is the time constants of the Siemens servomotor found in its data sheet. These yield a motor bandwidth of 72.66rad/sec (11.56Hz). Based on this, the frequency content of the input signal should be at least ten times this value. It was decided to use an input signal for the rest of the simulations of at least 942.48rad/sec (150Hz). The resultant signal used was a $\pm 1.5V$ amplitude chirp signal with frequency input from 0.63-942.48rad/sec (0.1-150Hz), combined with a ± 0.25 PRBS of 450Hz, giving a flat power spectrum of 150Hz. The reason for this combination is that it takes advantage of the benefits of both the PRBS and chirp signal. Using this input superimposed on a fixed constant input of different magnitudes the piecewise linearity of the motor and combined system at different operating regions was determined. The ETFE's for all operating velocities for the servomotor and combined system can be seen in figures 6.9 and 6.10 respectively. All ETFE's have been filtered through a 128 point Hamming window.

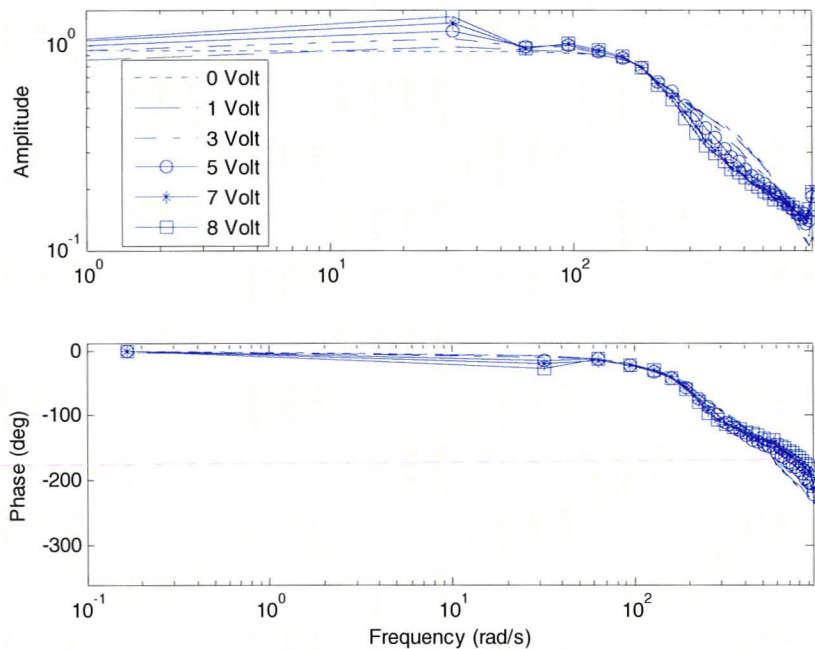


Figure 6.9. ETFE's to determine the piece-wise linearity of the motor.

Figure 6.9 shows that the servomotor is predominately linear throughout all operating regions.

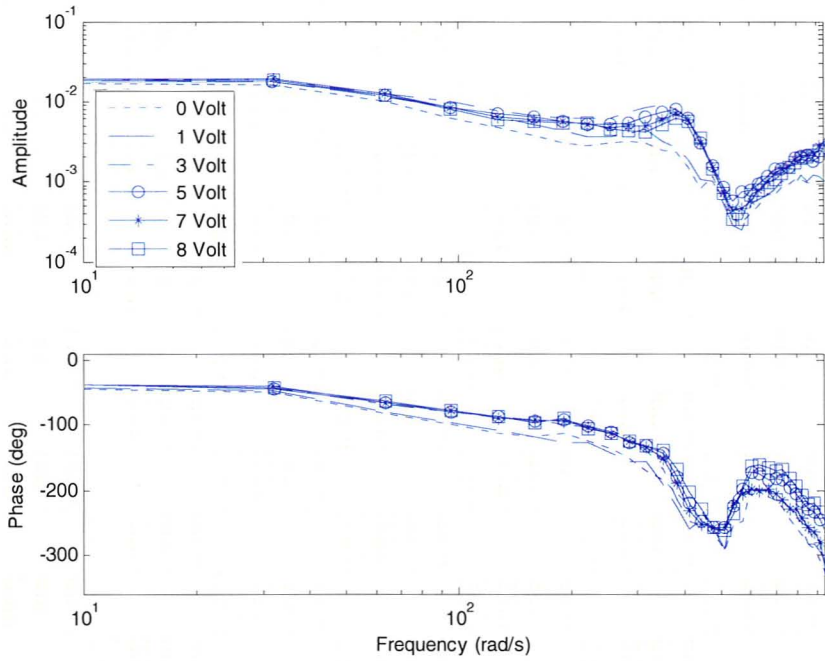


Figure 6.10. ETFF's to determine the piece-wise linearity of the combined system.

Figure 6.10 shows that there are two distinct piece-wise linear regions in the combined system. The first occurs when the input has a mean about zero. The other occurs at higher voltages. Figure 6.10 shows that at 1 Volt there is distinction between the two regions but it is believed that this is a transition. Knowing that the servomotor is linear in all regions and the combined system is not it can be assumed that this non-linearity is caused by the hydraulic system alone. One explanation for this is that the EHA is operating in the different modes explained when mathematically modeling the system in the literature review. Note that mode 1 occurs at higher velocities where there is symmetry on both ends of the pump/actuator. The system becomes non-linear in mode 2 at lower velocities where it is assumed the inlet pressure is equal to the case drain pressure, or $P_b \approx P_r$. There is no symmetry in this case. Another explanation includes the increased actuator friction at lower velocities seen in figures 5.10 and 5.11.

Other initial tests on the system included determining the delay and deadband of both the servomotor and the combined system. Table 6.1 shows this data.

Table 6.1. Delay and deadband of the servomotor and combined system.

	Delay	Deadband
Servomotor	1ms (1 sample)	0.0011V (3.46E-2 rad/sec)
Combined System	10ms (10 samples)	0.06V (6.82E-4 m/s)

To determine the order of the combined system the aforementioned high order ARX and impulse response method was used. For the ARX method the output above was placed through a 10th order zero-phase Butterworth filter with a break frequency of 942.48rad/sec (150Hz). For the impulse response method, a step input signal of 3V was used for each case which had a duration of one second. Figures 6.11 and 6.12 show the high order ARX analysis and SVD results for the servomotor and the combined system respectively.

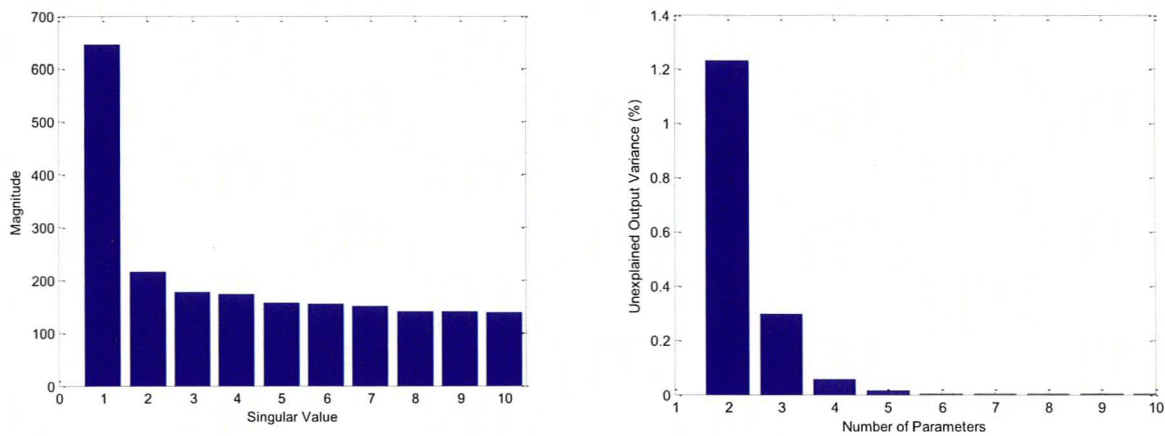


Figure 6.11. a) SVD and b) ARX-structure order estimates of the servomotor.

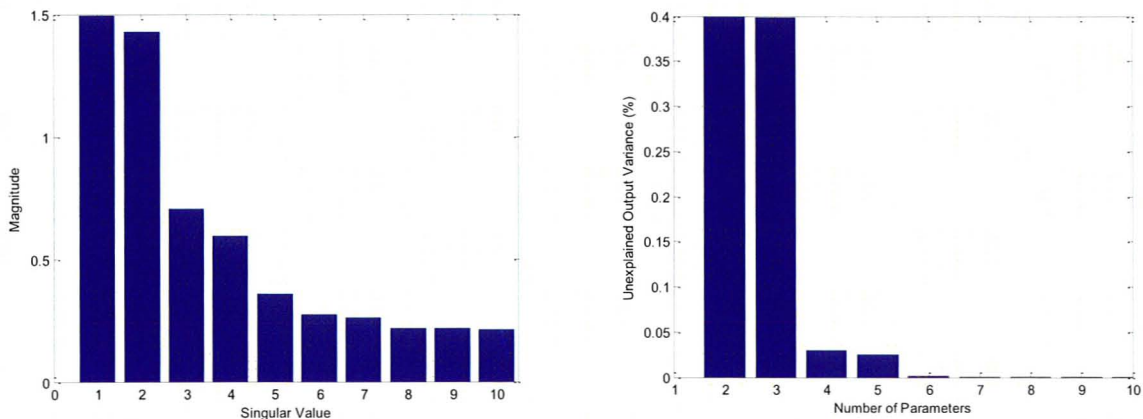


Figure 6.12. a) SVD and b) ARX-structure order estimates of the combined system.

Figure 6.11 clearly shows that the servomotor is a second order system with respect to velocity. This is interpreted by viewing the bar that shows the most significant drop in magnitude relative to the one before. Since the 2nd bar shows the most significant drop from the first for both the SVD and ARX-structure analysis this is evidence that this is a second order system. This confirms the servomotor model outlined in chapter 3.

Figure 6.12 shows that the combined EHA system has a higher order than the motor. There are two significant bars before there is a large drop in magnitude which is partially evident in the SVD case but very evident in the high order ARX case. This gives evidence that this is a predominately third order system when the inputs and outputs are both velocities. When the output variable is position the combined system can be viewed as fourth order. The SVD analysis does show that this is predominately a fourth order system but there are bars that show that there are some higher order dynamics in the system.

The above analysis indicates that the servomotor is dynamically significant to the system. Although it has been proved that the servomotor is second order, type zero when integrated into the system, it only adds another order to the combined system. Knowing this the combined system is assumed to be third order, type zero with respect to velocity or fourth order, type one with respect to velocity for the rest of this analysis.

Noise is inherent to this system and a model can be extracted from it. Figures 6.5 and 6.6 show that the system noise dominates above 1571rad/sec (250Hz) so the noise in the frequency range of interest is low enough to extract accurate system models. Although not significant in most cases it is still of interest to document the noise models. As explained in section 6.1, ARX, ARMAX and BJ models provide an estimation of the transfer function related to noise. ARX modeling is very restrictive and is not the best choice. ARMAX is best used where the majority of the noise is inputted to the system while Box-Jenkins is the most flexible and provides for system as well as measurement noise. There is input noise due to the ±10V analog command signal coming from the data acquisition card. There is also some noise caused by the amplification and signal conversion of the input from the Siemens drive. It was determined that the noise level from both of these sources is small. The majority of the noise comes from taking the derivative of the encoder signal to extract velocity. Because of this the Box-Jenkins method for determining the noise model was chosen. The Box-Jenkins method allows a system and noise model to be extracted. Using the same input signal as previously discussed, a system and noise model has been extracted for the servomotor and the combined EHA system using the orders

previously outlined. Equations 6.7 and 6.8 show the continuous Box Jenkins system models for the servomotor and combined system respectively. These were taken at zero mean velocity.

$$\frac{w(s)}{w_d(s)} = \frac{24.55s + 5.15E4}{s^2 + 307s + 5.59E4} \quad (6.7)$$

$$\frac{sx(s)}{w_d(s)} = \frac{-3.90E - 3s^2 + 1.56s + 623.4}{s^3 + 272.2s^2 + 3.67E4s + 1.74E6} \quad (6.8)$$

Equations 6.9 and 6.10 show the continuous Box Jenkins noise models for the servomotor and combined system respectively. These were taken at zero mean velocity.

$$\frac{n_m(s)}{e(s)} = \frac{2630s + 1.02E7}{s^2 + 293.60s + 2.11E4} \quad (6.9)$$

$$\frac{n_c(s)}{e(s)} = \frac{1.68s^2 + 568.30s + 3.56E5}{s^3 + 1250s^2 + 5.20E5s + 7.20E7} \quad (6.10)$$

Where n_m , n_c and e are the servomotor and combined system output noise respectively and e is the input error.

6.3 System Identification of the Servomotor

With all the information gathered about the system parametric models can be extracted from the data. A second order Output Error model is used to determine the transfer function of the servomotor. A motor ETFE centred around 0 Volts with the Output Error fit can be seen in figure 6.13.

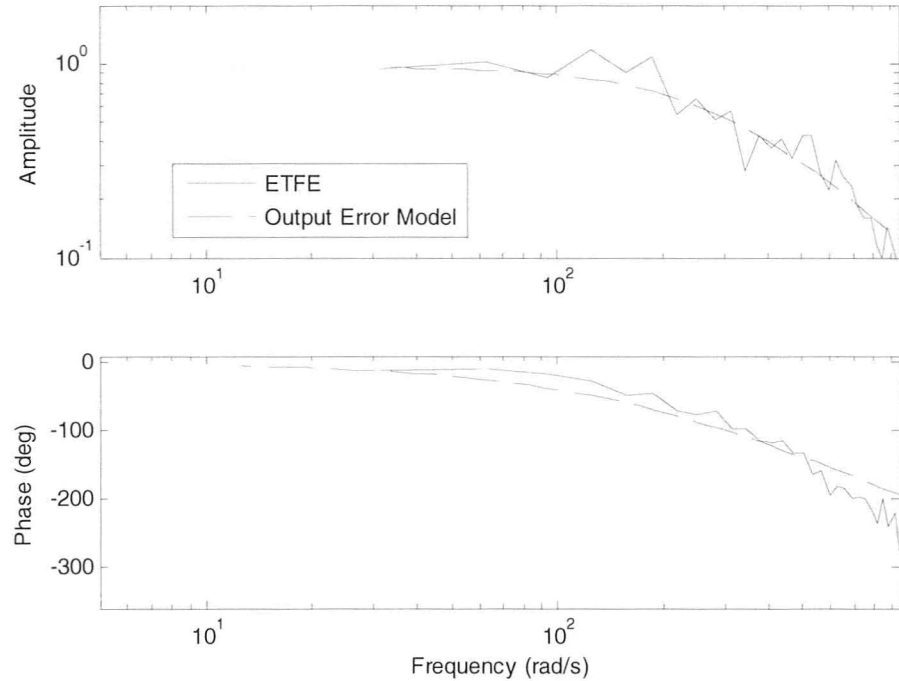


Figure 6.13. ETFE and Output Error model of the servomotor.

The corresponding transfer function for the servomotor can be seen in equation 6.11.

$$\frac{w(s)}{w_d(s)} = \frac{e^{-0.001s}(68.67s + 1.21E5)}{s^2 + 760.8s + 1.26E5} \quad (6.11)$$

The second order equation above has the following properties:

- Bandwidth: 209.0rad/s (33.3Hz)
- Poles: -517.9 and -242.9

Verification of this model was performed by comparing the actual output to the model output for a step, chirp and sawtooth input. Figures 6.14 and 6.15 show the comparison between the model response and the system response for a step and chirp signal respectively. The system response data was placed through a 10th order zero-phase filter with a cutoff frequency of 150Hz. The delay of 1ms was also incorporated in the model response curve for all cases. The step input used has a magnitude of 94.2rad/sec (3V) and its response can be seen in figure 6.14.

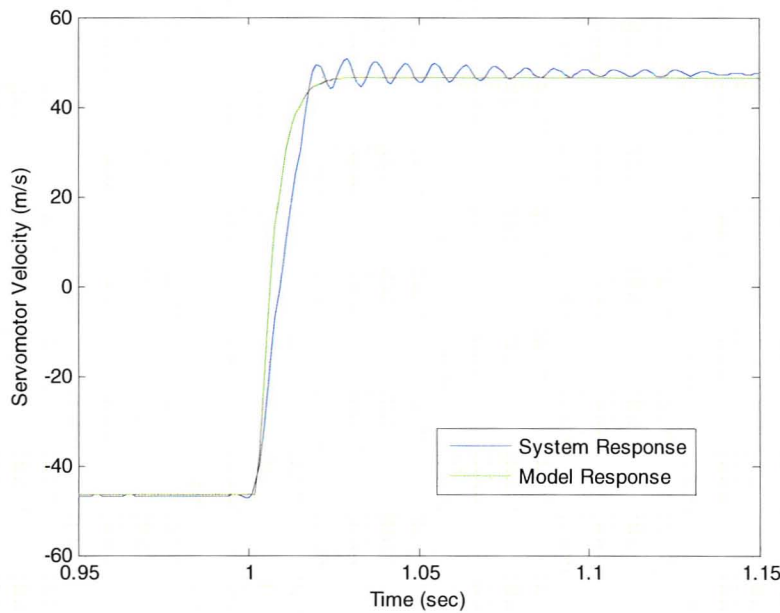


Figure 6.14. System response and model response for a 3V (94.2rad/sec) step input for the servomotor.

The chirp signal used had a frequency range between 0.1-50Hz in a time interval of 12.5sec. This output data was also placed through a 10th order zero-phase Butterworth filter with a cut-off frequency of 150Hz.

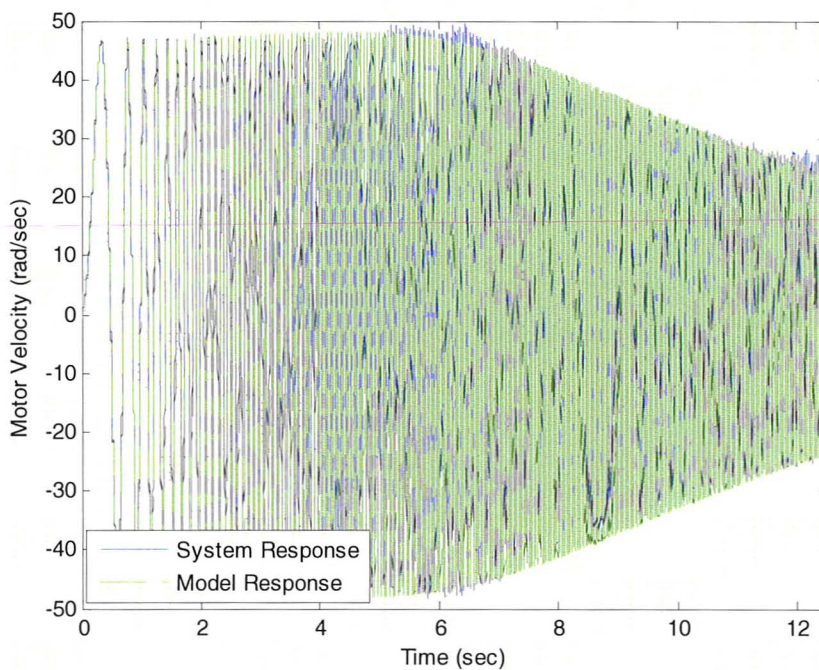


Figure 6.15. System response and model response for a $\pm 1.5V$ ($\pm 47.1\text{rad/s}$) chirp input for the servomotor.

Figures 6.16-6.18 show a closer view of the chirp response for various ranges.

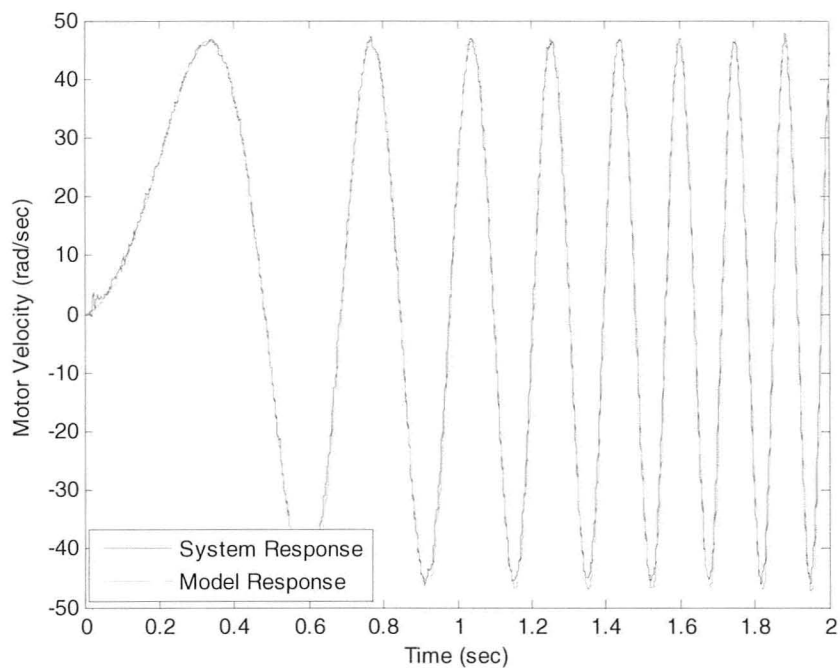


Figure 6.16. System and model response for a chirp input between 0-2 seconds.

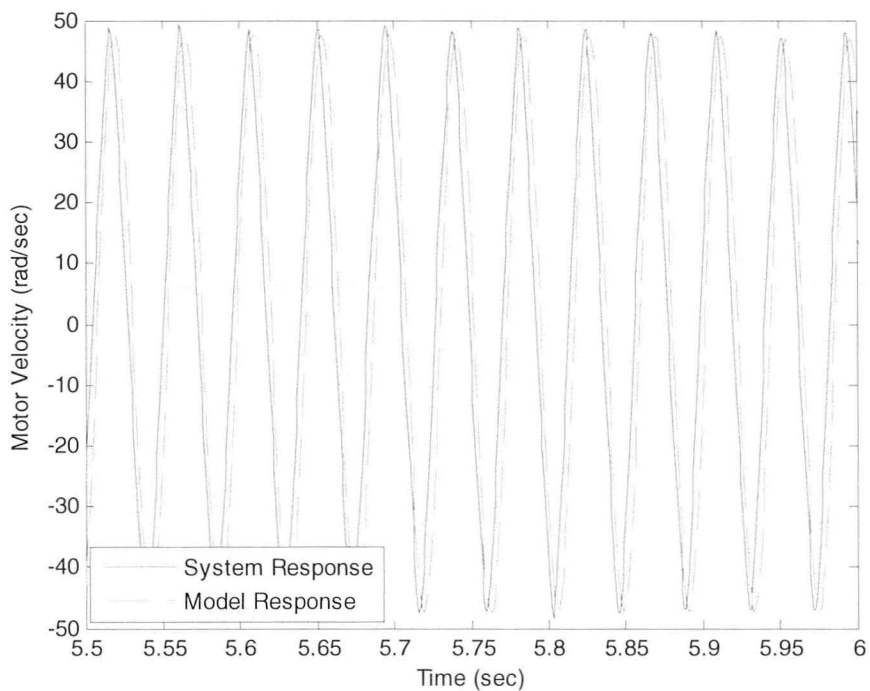


Figure 6.17. System and model response for a chirp input between 5.5-6 seconds.

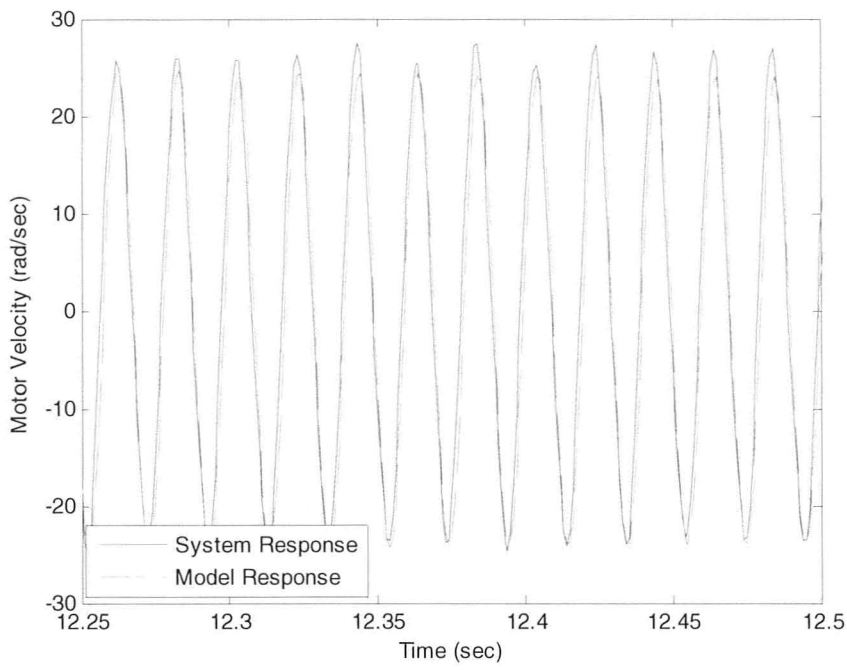


Figure 6.18. System and model response for a chirp input between 12.25-12.5 seconds.

Figure 6.19 shows the system and model response to a sawtooth input at 20Hz with a magnitude range of 0-3V (0-94.2rad/sec).

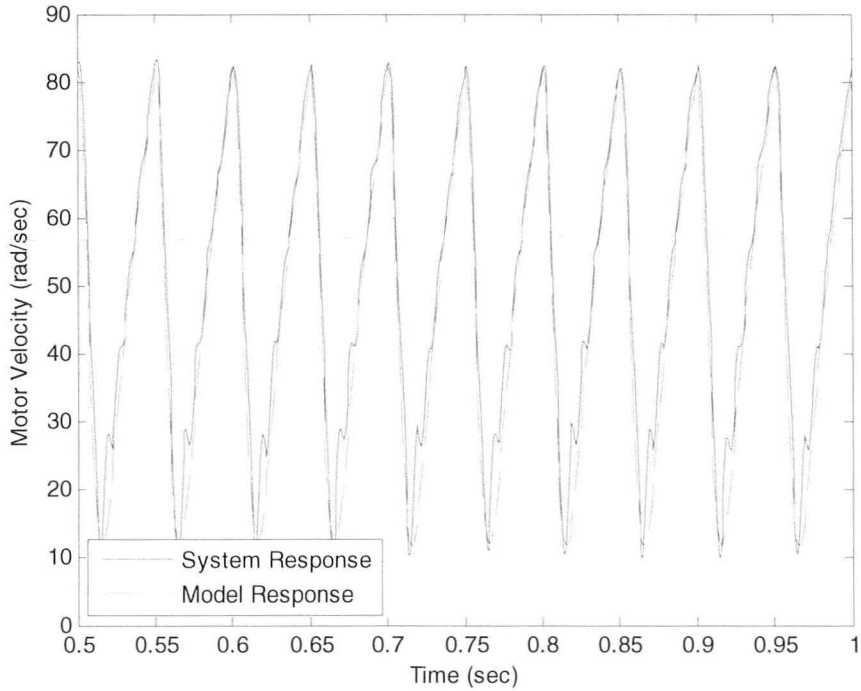


Figure 6.19. System and model response for a sawtooth input of 20Hz with a magnitude between 0-94.2rad/sec.

Figures 6.14 to 6.19 show that that system response and model response for all cases are very agreeable and the system response is very clean. The system response indicates the presence of higher order dynamics with lower levels of significance. It must also be noted that the identified model and the motor model derived by using the time constants provided by Siemens are very different. Although the source of this discrepancy is not known the identified model will be treated as the correct model since there is proper evidence to support it.

6.4 System Identification of the Combined EHA System

The next system identification process was performed for the first linear region of the combined system with a mean velocity of zero, which will be termed as the low velocity linear region. This is where stick-slip with the rod and piston seals and high friction become issues of concern. It is clear from figure 6.10 that this region has a lower bandwidth compared to the higher velocity regions. Using the same input signal used to develop figure 6.10, the ETFE and 3rd order Output Error model can be seen in figure 6.20. Note that at higher frequencies beyond the bandwidth of the system the signal breaks down, decreasing the signal-to-noise ratio. The signal breaks down since the high frequency inputs are operating in a region where the actuator cannot move due to static friction. This is clearly seen in figure 6.21 which is the response from a $\pm 1.5V$ input chirp signal with a frequency range of 0.63-942.48rad/sec (0.1-150Hz). This figure shows that the actuator does not move beyond 282.74rad/sec (45Hz) except for the higher frequency ranges which are caused by higher frequency dynamics in the system which are not of interest.

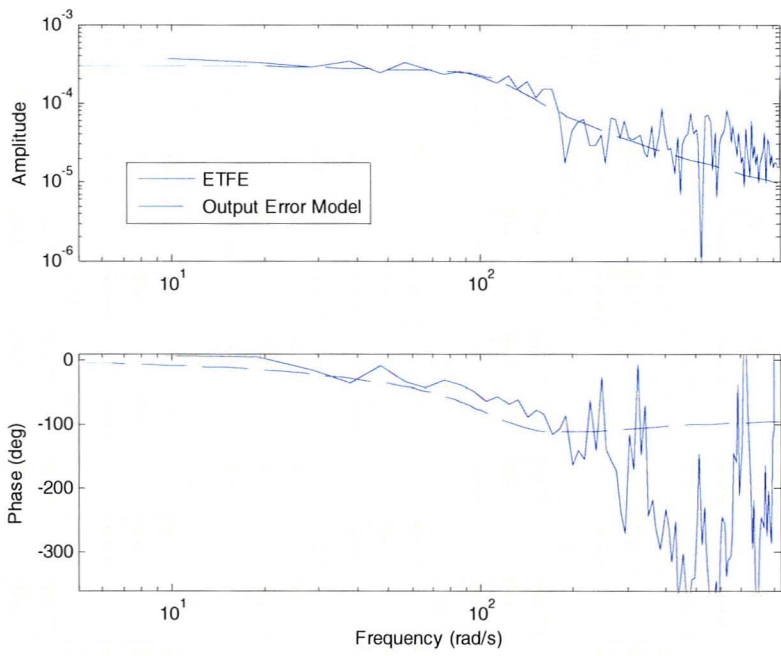


Figure 6.20. ETFE and Output Error model of the first piecewise linear region of the combined system.

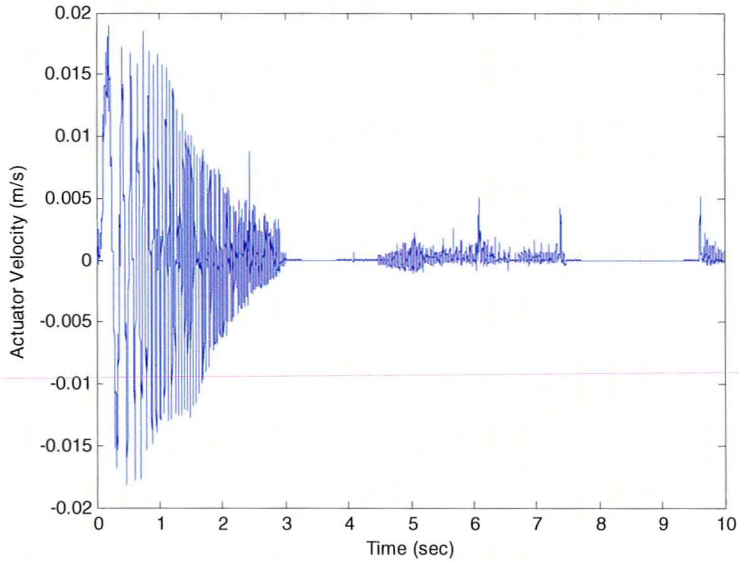


Figure 6.21. Chirp input response showing the system operating in the deadband of the first piecewise linear region.

The corresponding transfer function for the servomotor can be seen in equation 6.12. It is multiplied by $1/s$ to represent it as the demanded motor velocity as the input and actuator position as the output.

$$\frac{x(s)}{w_d(s)} = \frac{e^{-0.01s}(1.08E - 2s^2 + 2.562s + 242.6)}{s^4 + 144.8s^3 + 1.66E4s^2 + 6.50E5s} \quad (6.12)$$

The fourth order, type 1 equation with respect to velocity above (or third order, type zero with respect to position) has the following properties:

- Bandwidth: 105.6rad/sec (16.8Hz)
- Poles: $-44.5 \pm 98.3, -55.8$

Verification was performed using step, chirp and sawtooth responses. Figure 6.22 shows the step response of the low speed linear range using an input beginning at -1.5V and ending at 1.5V.

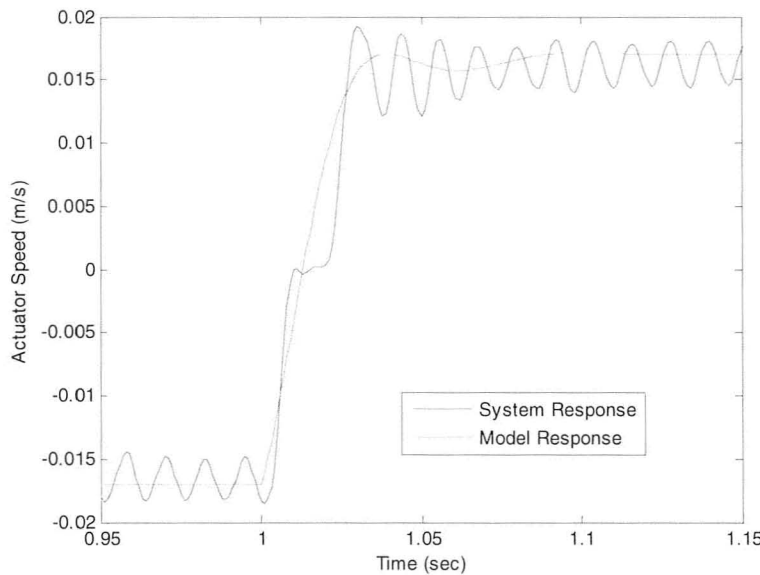


Figure 6.22. System and model response for the low velocity linear range in the combined system.

Figure 6.22 shows the system response slightly flatlines at zero velocity. This could be attributed to the static friction and stick-slip nature of the rod and piston seals during changes between positive and negative velocities, which was discussed in chapter 5. The chatter before and after the step change results from running the actuator at this low speed where friction is high.

Figures 6.23-6.26 show the system and model response to a $\pm 1.5V$ magnitude chirp input with a frequency range of 0.63-188.50 rad/sec (0.1-30Hz) in a 5 second window. These figures show that the model response is a good fit up until the higher frequency portion which is seen in figure 6.26. Although there is a large phase shift in figure 6.26 the input frequency is between 0.63-169.65 rad/sec (27-30Hz) which is substantially larger than the bandwidth.

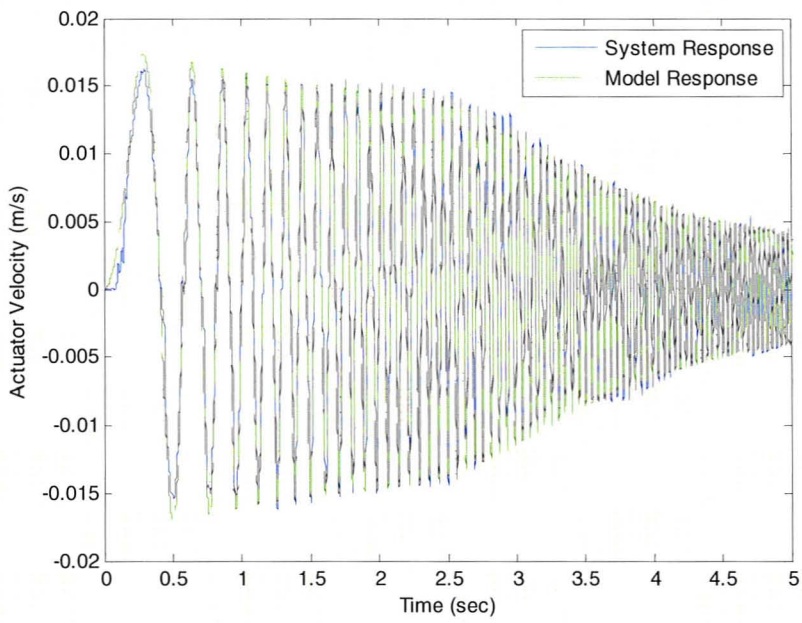


Figure 6.23. System response and model response for a $\pm 1.5V$ ($1.71E-2\text{m/s}$) chirp input for the combined system low velocity linear region.

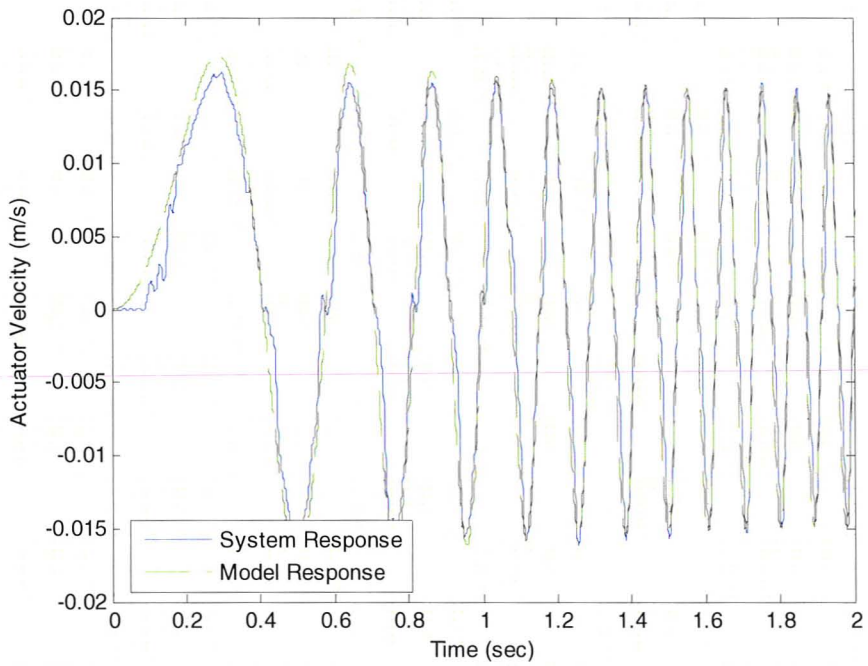


Figure 6.24. System response and model response for a $\pm 1.5V$ ($1.71E-2\text{m/s}$) chirp input for the combined system low velocity linear region, 0-2 seconds.

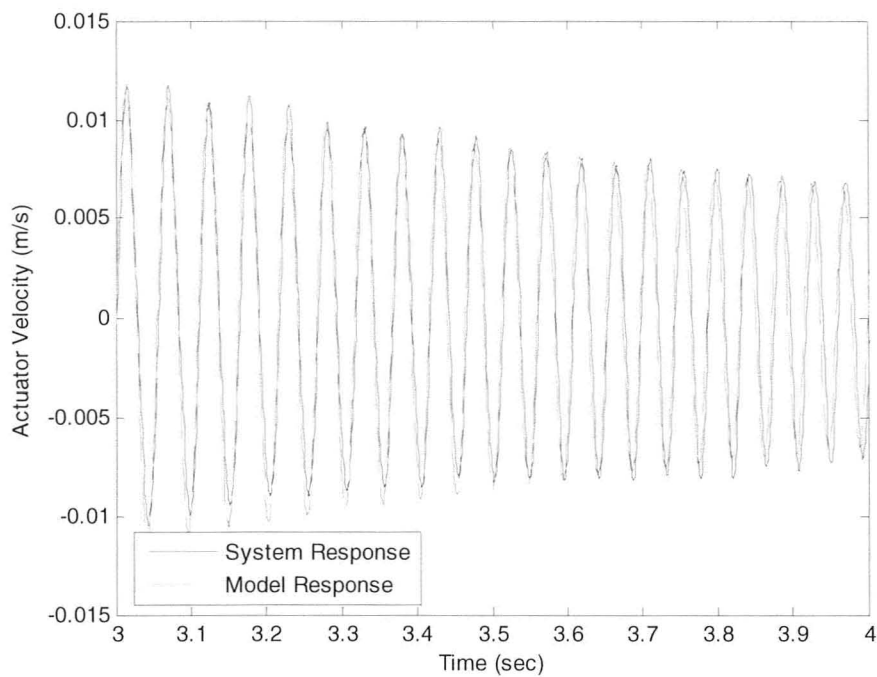


Figure 6.25. System response and model response for a $\pm 1.5V$ ($1.71E-2\text{m/s}$) chirp input for the combined system low velocity linear region, 3-4 seconds.

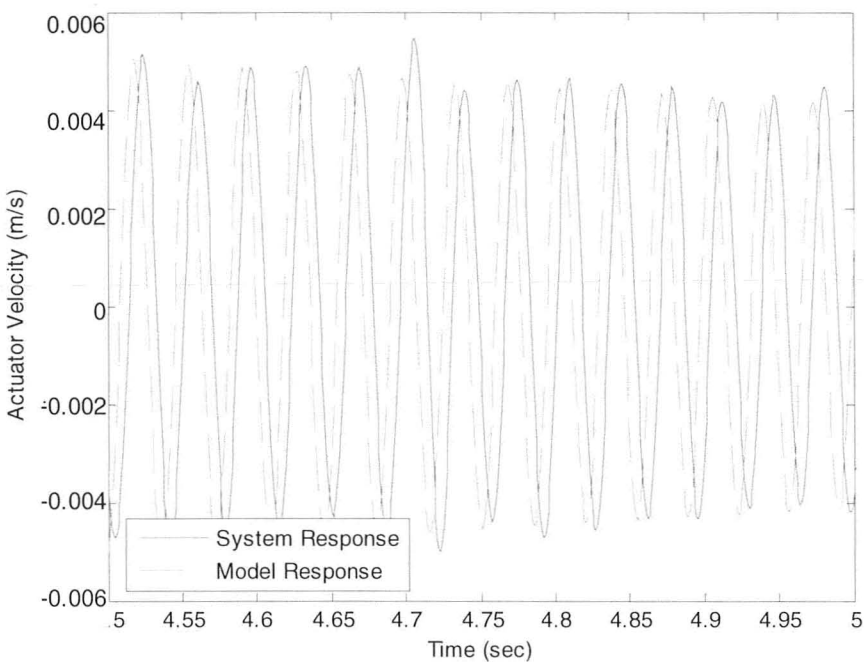


Figure 6.26. System response and model response for a $\pm 1.5V$ ($1.71E-2\text{m/s}$) chirp input for the combined system low velocity linear region, 4.5-5 seconds.

Figure 6.27 shows the system and model response for the low velocity linear region using a sawtooth input of 100.53rad/sec (16Hz). The system response shows a slight deviation from the model response with a curvature that occurs just before the system changes from a negative to positive velocity. This is evidence of a nonlinearity that occurs when the change in velocity is more gradual than sudden. This could also be attributed to the static friction and stick-slip nature of the rod and piston seals during changes between positive and negative velocities.

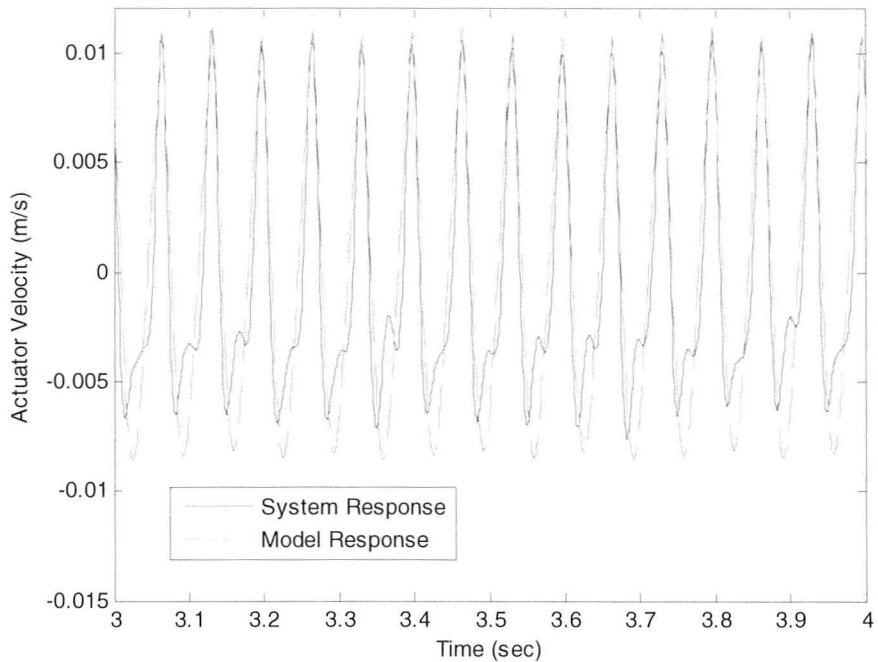


Figure 6.27. System response and model response for a sawtooth input of 16Hz with a magnitude between $\pm 1.5V$ ($1.71E-2m/s$).

The next region evaluated for the combined EHA system was high velocity linear region. This region uses the same inputs as the low velocity region but has a mean velocity of 8.375V ($9.52E-2m/s$). Figure 6.28 shows the ETFE and Output Error parametric model response for this region.

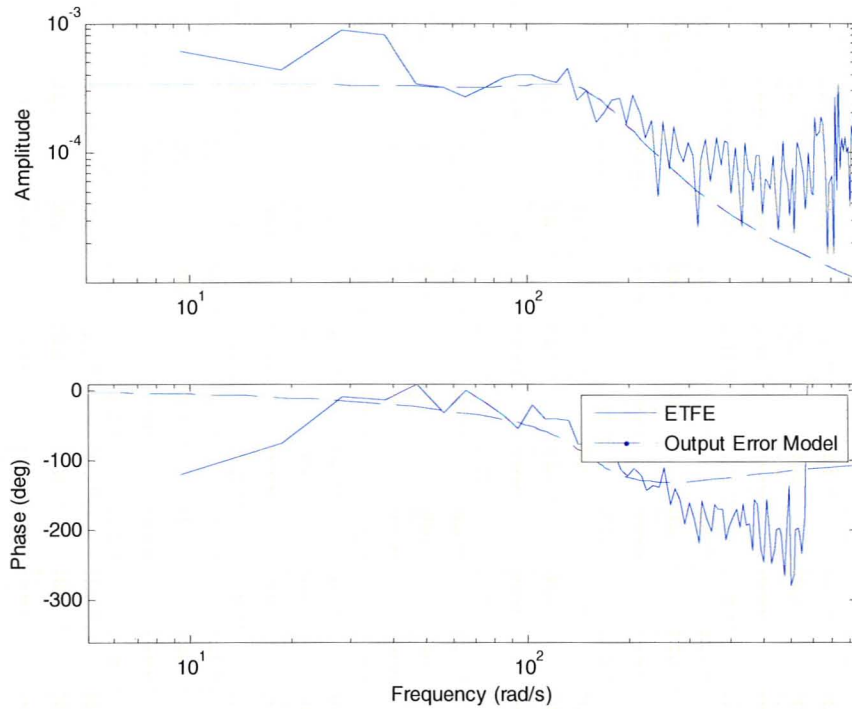


Figure 6.28. ETFE and Output Error model for the high velocity linear region for the combined system.

The corresponding transfer function for the combined EHA system for the high velocity linear region is:

$$\frac{x(s)}{w_d(s)} = \frac{e^{-0.01s}(9.43E - 3s^2 + 4.37s + 648.80)}{s^4 + 185.5s^3 + 3.14E4s^2 + 1.91E6s} \quad (6.13)$$

Equation 6.13 has the following properties:

- Bandwidth: 170.0 rad/s (27.04 Hz)
- Poles: $-50.9 \pm 142.3i, -83.8$

Figure 6.29 shows the system and model response for a step input that starts at 6.75V and ends at 9.75V (7.68E-2 m/s and 1.11E-1 m/s). Figures 6.30-6.33 show the system and model response for a chirp input with a frequency range of 0.63-201.06 rad/sec (0.1-32 Hz) over a time interval of 2.75 seconds. The time duration in this case needed to be lower in order to avoid position saturation of the actuator. Figures 6.30 and 6.33 show that at higher frequencies the mean system response velocity starts to slope down and the fit between the system and model response breaks down. As seen in chapter 4 the damping at an actuator velocity of 7.68E-2 m/s (6.75 volts) is higher than at an actuator velocity of 11.09E-2 m/s (9.75 volts). The increased damping at lower velocities causes the actuator to respond slower especially

at higher frequencies. This is an example of the non-linearity of the system caused by the aforementioned friction characteristics. Although this deviation is significant it begins at approximately 144.51rad/sec (23Hz, slightly lower than that bandwidth) and is deemed acceptable since it occurs at higher frequencies where the signal-to-noise ratio is typically low.

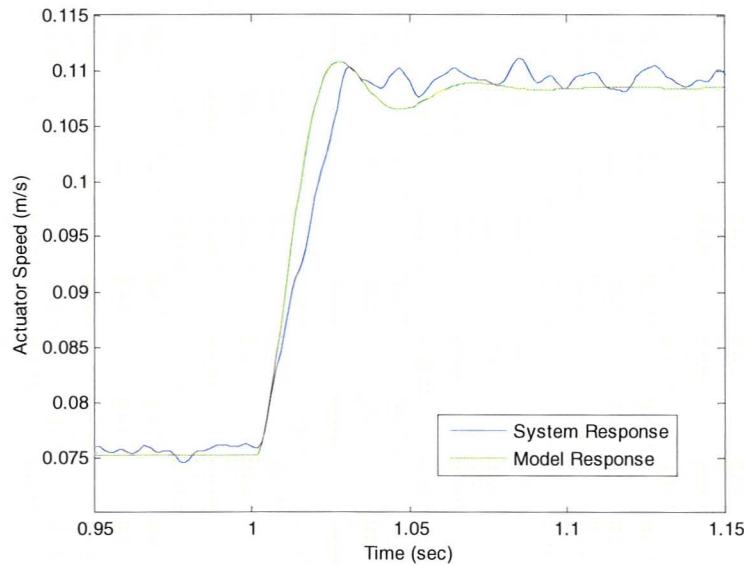


Figure 6.29. System and model step response for the high velocity linear range in the combined system.

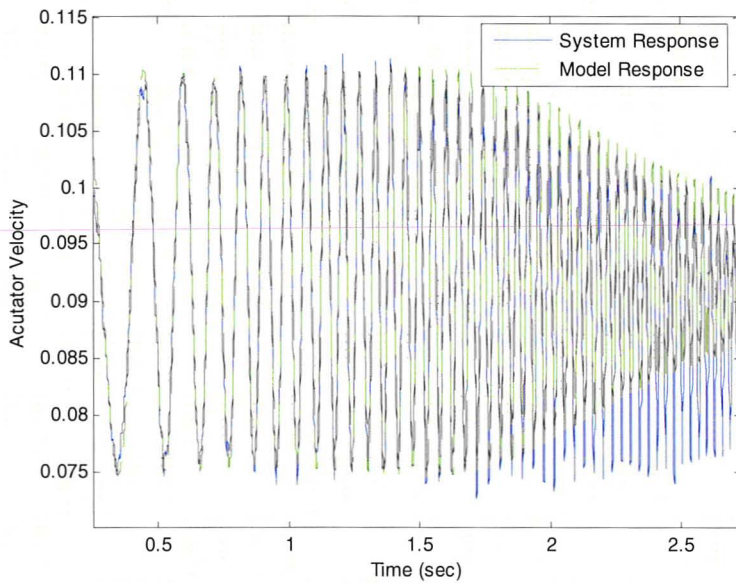


Figure 6.30. System and model chirp response for the high velocity linear range in the combined system.

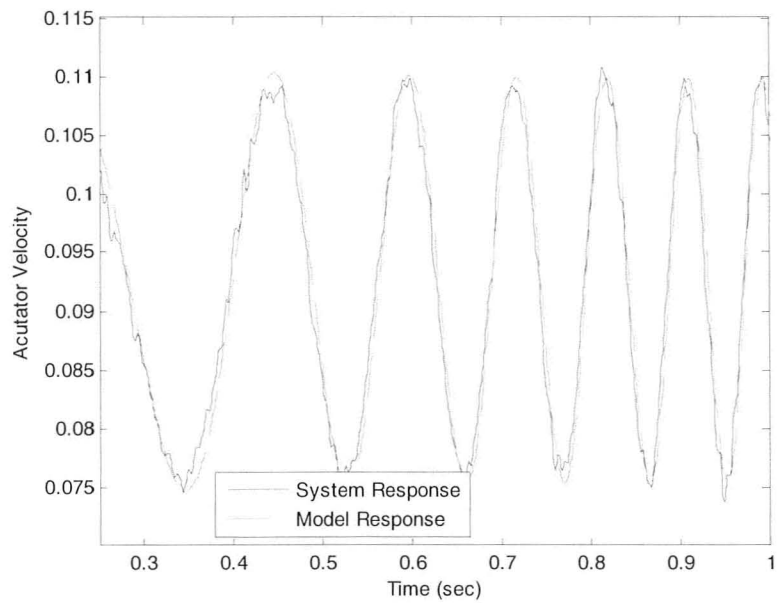


Figure 6.31. System and model chirp response for the high velocity linear range in the combined system, 0-1 seconds.

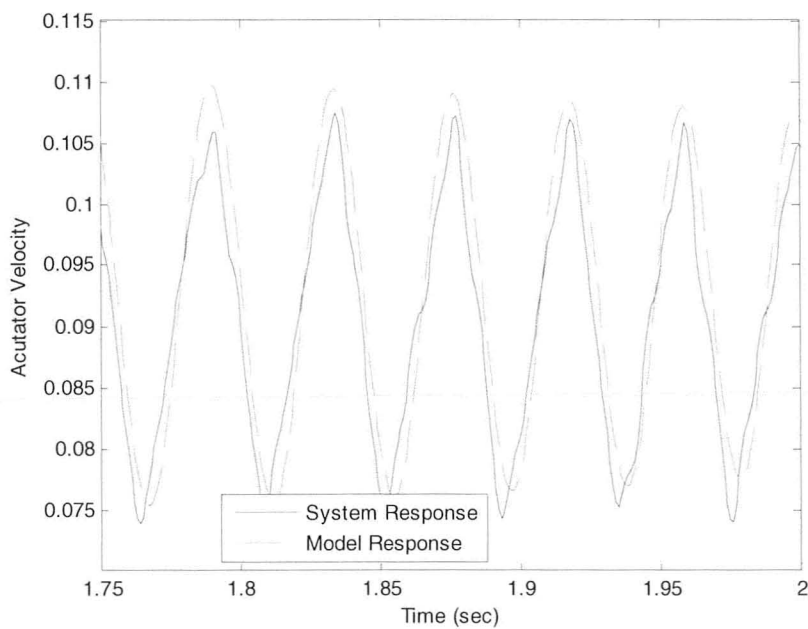


Figure 6.32. System and model chirp response for the high velocity linear range in the combined system, 1.75-2 seconds.

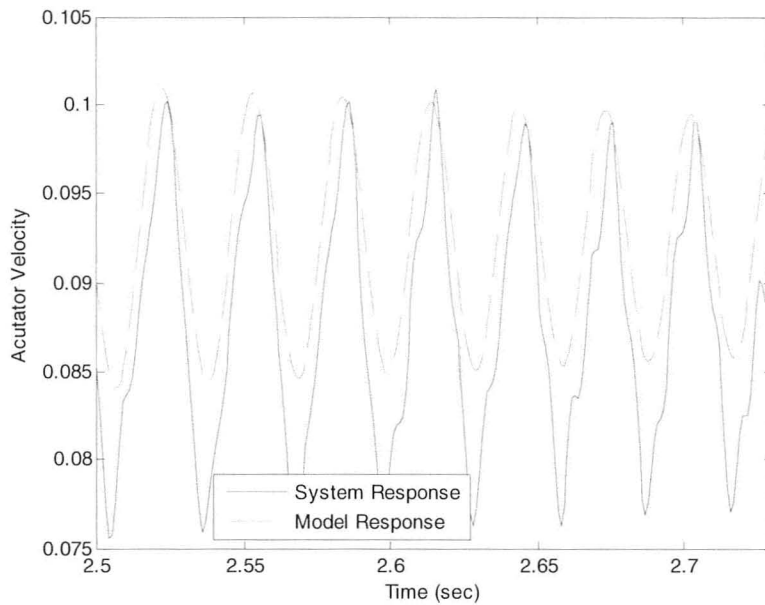


Figure 6.33. System and model chirp response for the high velocity linear range in the combined system, 2.5-2.75 seconds.

Figure 6.34 shows the system and model response for the high velocity linear region using a sawtooth input of 125.66rad/sec (20Hz) between 6.75-9.75 Volts. The system and model response show a good fit but there is a slight deviation when the velocity ramps up from the minimum. This also shows how the friction in the system adds non-linearity.

Above, system identification for the combined system in the high velocity region compared to the low velocity region shows two major conclusions. As the mean velocity increases the system bandwidth increases and the degree of symmetry about the mean input velocity breaks down. Both of these characteristics can be explained by the actuator friction/damping. Figures 5.10 and 5.11 show that friction is greatest around zero velocity, which decreases the bandwidth of the system. At higher mean velocities the friction decreases and the bandwidth subsequently increases. These figures also show that the friction is not symmetric about non-zero mean velocities, which accounts for the lack of symmetry in the system response in the high velocity region.

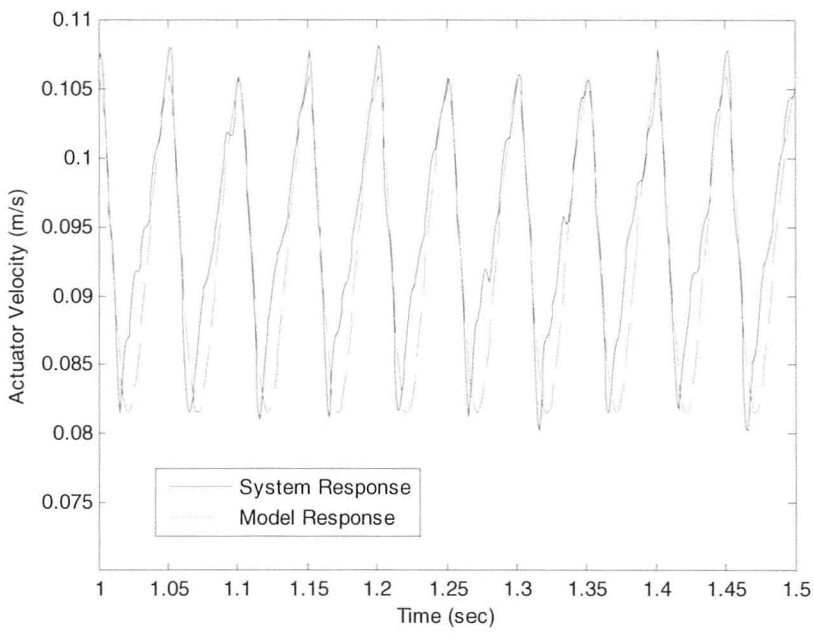


Figure 6.34. System and model sawtooth response for the high velocity linear range in the combined system.

6.5 Review

The identified system models for the low velocity and high velocity piece-wise linear regions in the combined EHA system can be seen in equations 6.14 and 6.15 respectively.

$$\frac{x(s)}{w_d(s)} = \frac{e^{-0.01s}(9.43E - 3s^2 + 4.37s + 648.80)}{s^4 + 185.5s^3 + 3.14E4s^2 + 1.91E6s} \quad (6.14)$$

$$\frac{x(s)}{w_d(s)} = \frac{e^{-0.01s}(1.08E - 2s^2 + 2.562s + 242.6)}{s^4 + 144.8s^3 + 1.66E4s^2 + 6.50E5s} \quad (6.15)$$

The mathematical models for the EHA determined in chapter 4 are shown below:

$$TF_{A,For} = \frac{44.64}{s^3 + \left(1.27 + \frac{B_{A,For}}{3.688}\right)s^2 + (1.22E5 + 0.343B_{A,For})s} \quad (6.16)$$

$$TF_{A,Rev} = \frac{44.64}{s^3 + \left(0.83 + \frac{B_{A,Rev}}{3.688}\right)s^2 + (1.22E5 + 0.225B_{A,Rev})s} \quad (6.17)$$

$$TF_{B,For} = \frac{44.64}{s^3 + \left(1.27 + \frac{B_{B,For}}{3.688}\right)s^2 + (1.22E5 + 0.343B_{B,For})s} \quad (6.18)$$

$$TF_{B,Rev} = \frac{44.64}{s^3 + \left(0.83 + \frac{B_{B,Rev}}{3.688}\right)s^2 + (1.22E5 + 0.225B_{B,Rev})s} \quad (6.19)$$

Analysis should be performed in future research to determine how well the identified and mathematical models compare in different operating modes.

6.6 Conclusion

This chapter provided a system model for the servomotor and models for different piece-wise linear regions for the combined EHA system using system identification techniques. This showed that the servomotor is dynamically significant to the combined EHA system. It also showed that as the mean velocity of the actuator increased the system bandwidth increased for the combined EHA system. The cause of this was that the actuator follows a LuGre model for friction, causing the friction to critically decrease as the velocity increases in the region of interest.

Chapter 7 Control of the Electro-Hydrostatic Actuator

In this chapter a digital filter is presented that can be used for feeding back several states to a controller. The theory and design of this filter is shown. This chapter also introduces a basic closed-loop proportional controller implemented into a single EHA to control the position of the actuator. The design process and results will be presented.

7.1 State Conversion for Feedback Purposes

If the measurement of the encoder position was continuous and free of system and measurement noise the velocity could be extracted by simply taking the derivative. In this system the position feedback is free of noise but is in discrete form. As previously discussed taking the derivative of a discrete signal yields noise. The amount of noise depends on the rate of change of the position and the sampling period, but in almost all cases the velocity signal is unusable for feedback. To extract a clean and accurate velocity of the position measurement there are two options. The first is using a model based estimator such as the Kalman filter. The Kalman filter and other model based estimators (such as the Extended Kalman filter) have proven to give very accurate results but require prior knowledge of the system dynamics. The other option is to take the derivative of the discrete position signal and pass it through an Infinite Impulse Response (IIR) filter to eliminate the resulting high frequency noise. An IIR filter is a simple and robust way of eliminating noise and only requires knowledge of the bandwidth of the system. The IIR filter is an effective way of obtaining multi-state feedback for more advanced control algorithms. Although multi-state feedback control was not performed in this research the appropriate IIR filter to obtain these states for future research is presented below.

7.1.1 Design of an IIR filter

There are many forms of IIR filters which include Chebyshev, Butterworth and Elliptic types. For this analysis a Butterworth filter is employed. The magnitude function of the lowpass Butterworth filter can be seen in equation 7.1.

$$|J(iw)| = \frac{1}{\sqrt{1 + \left(\frac{w}{w_c}\right)^{2p}}} \quad (7.1)$$

Where J is the filter response magnitude, w_c is the cut-off frequency (rad/s) and p is the order of the filter. The major parameters needed to design a Butterworth filter are the cutoff frequency, the passband gains, stopband gains and frequency range of the passband and stopband. The cutoff frequency occurs when the magnitude experiences a 3dB drop, or where $|J(iw)| = \frac{1}{\sqrt{2}}$. Equation 7.2 shows the continuous transfer function for a Butterworth filter [42].

$$J(s) = \frac{1}{a_n s^p + a_{n-1} s^{p-1} + \dots + a_1 s + 1} \quad (7.2)$$

Where a_n to a_1 are the filter coefficients. The order of the filter determines the effective distance between the passband and stopband. The higher the order, the lower this distance is. It is advantageous to have a high order so that signals above the cutoff frequency are reduced further in magnitude. The issue with a higher order is the phase shift. The phase shift of the filter is a function of the cutoff frequency and the order. To remove the phase shift the data is passed through the IIR filter twice. In its second filtering, the output data stream is reversed such that the last measurement is placed through the filter first. In the forward direction the phase shift is introduced but is removed by reverse filtering the data. This strategy is referred to as zero-phase filtering but can only be used for off-line applications such as system identification. In applications such as filtering a feedback signal used for real-time control, zero-phase filtering cannot be performed and a phase shift will be present in the filtered signal. Therefore, when filtering for real-time control the filter order must be low so that it removes as much of the noise as possible without adding a significant phase shift. Through analysis, it was determined that a 2nd order Butterworth filter provided sufficient filtering of the signal without adding too much phase shift that would degrade the performance of the system.

The cutoff frequency for IIR filter should be ideally five to ten times the value of the bandwidth of the system. The system identification process for the high velocity linear region in the previous section yielded a bandwidth of 169.90rad/sec (27.04Hz). Many trials were attempted using a filter with a bandwidth of 850rad/sec (135.28)Hz but it was found that the resulting feedback signal was too noisy, causing chattering in the servomotor. Because of this it was decided to design a more aggressive filter that had a bandwidth approximately twice the value of the bandwidth of the high velocity linear region transfer function, which is 350rad/sec (55.7Hz).

An example of a continuous second order transfer function for a Butterworth filter can be seen in equation 7.3. Its Bode plot with a bandwidth of 350 rad/s can be seen in figure 7.1.

$$J(s) = \frac{122500}{s^2 + 494.9s + 122500} \quad (7.3)$$



Figure 7.1. Bode plot for a lowpass Butterworth filter with a bandwidth of 350rad/sec.

Since all experiments are performed in discrete time intervals equation 7.3 must be converted to a z-transform. This is accomplished by using the Bilinear transform, otherwise known as Tustin's method, which is shown in equation 7.4 [42].

$$s = \frac{2}{T_s} \frac{z - 1}{z + 1} \quad (7.4)$$

The resultant discrete Butterworth IIR filter used for control purposes is shown in equation 7.5.

$$J(z) = \frac{5.28E - 2z^{-1} + 4.39E - 2z^{-2}}{1 - 1.514z^{-1} + 0.61z^{-2}} \quad (7.5)$$

7.2 Design of a Closed-Loop Controller

A basic closed-loop position controller was designed for a single Axis of the EHA to demonstrate the closed-loop performance. The output from the linear encoder in this case did not need to be filtered before being fed back to the controller since the position reading of a differential quadrature encoder gives a very clean signal. Refer to Appendix A for details on the differential quadrature linear encoder used in this research. It was decided to use the Ziegler-Nichols method for tuning a proportional controller. This is performed by increasing the proportional gain to a value where the output starts to oscillate at the final set point. This value is termed as the critical gain. To obtain the final proportional gain the critical gain is simply divided by two [45]. The final set point of the step input is 0.1m. Through experimentation it was found that the ultimate gain had a value of 33750 and the corresponding proportional gain was 16875.

This is an aggressive form of controller and it was found though experimentation that a saturation effect occurred. This was the velocity of the servomotor and it was found that it was at a maximum for a portion of the transient response. The step input and transient response can be seen in figure 7.2.

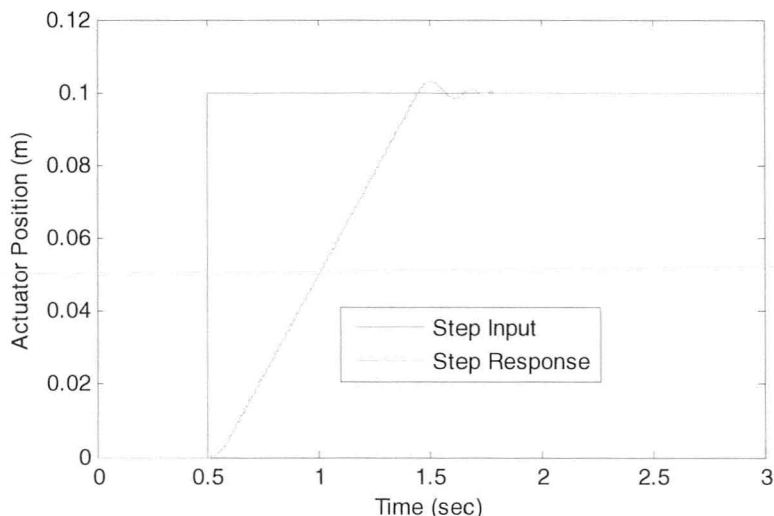


Figure 7.2. Step input and response for a proportional controller.

Taking the derivative of the position measurement and filtering the signal using equation 7.5 the resulting actuator velocity can be seen in figure 7.3.

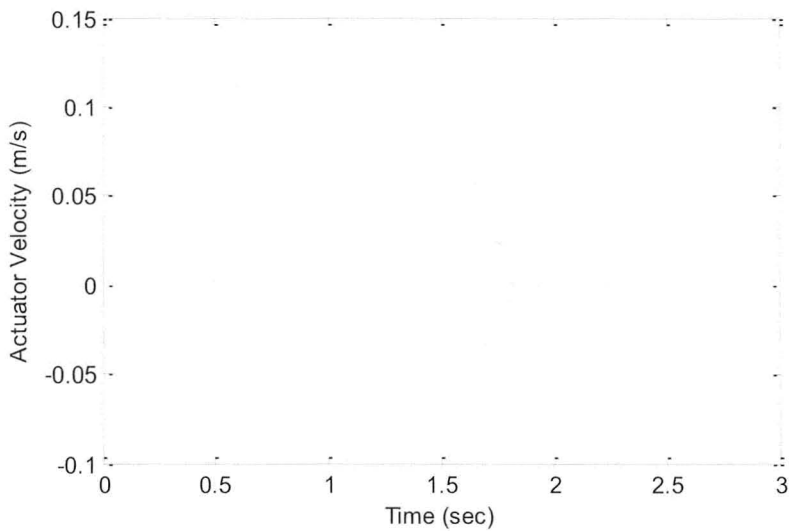


Figure 7.3. Resultant velocity of the step response shown in figure 7.2.

Figure 7.3 shows that the velocity saturates between approximately 0.6-1.4 seconds. Since the maximum velocity of the actuator when using a single pump is 0.117m/s (corresponding to 314.59 rad/sec or 3000rpm for the servomotor) a step input will cause this effect in many cases, depending on the aggressiveness of the controller.

The steady state error of this response is $-21\mu\text{m}$. This shows that even with a basic outer-loop proportional controller an accurate response can be achieved. The inner-loop proportional and integral gains here were set to 1 and 0 respectively, which were the same values used in system identification.

7.3 Conclusion

In this chapter a digital filter was presented that can be used for real-time feedback of several states into a controller. Analysis showed that the bandwidth of the filter should be no higher than 350rad/sec, even though this is less than five times larger than the bandwidth of the identified model for the high velocity piece-wise linear model for the combined EHA determined in chapter 6. A basic closed-loop position control analysis was also performed on the EHA which used an aggressive proportional controller.

Chapter 8 Conclusions and Recommendations

8.1 Summary

The objective of this research was to design and manufacture a dual Electro-Hydrostatic Actuator (EHA) prototype. This design was partly based on incorporating the performance specifications for the Parker dual EHA on the F-35 Lightning rudder and partly based on incorporating equipment that can simulate fault conditions for future research. Basing the design on the performance specifications outlined by Parker provides a prototype that is more comparable to common EHA systems currently in industry. The incorporation of equipment that simulates fault conditions in the EHA allows for further research on creating algorithms that can detect these faults (i.e. increased internal leakage, increased friction, etc.).

Once the prototype was completed parameter identification was performed to identify the leakage and damping coefficients of the system. These parameters are significant in terms of the overall performance of the EHA when using a mathematical approach to designing control strategies. System identification was also performed on the EHA which provided insight into the linearity, order and bandwidth of the servomotor and combined EHA system for different piece-wise linear regions. An identified model was captured for each piece-wise linear region as well.

The final objective of this research was to design a filter to feedback several states to a controller and to implement a basic controller for the combined EHA to control the actuator position.

8.2 Outcomes

A dual EHA that is lighter and incorporates the same performance characteristics as the Parker F-35 EHA was designed with a final weight savings of 12%. A prototype was produced which incorporates all of the previous design with the exception of the choice of its electrical motors. This prototype was augmented with several components and sub-assemblies which provide the following functions:

- Inducing fault conditions.
- Off-line filtration for fluid conditioning.
- Extra fluid capacity when priming the system.

The fault conditions that can be simulated by the system are as follows:

- External leakage.
- Internal leakage.
- Varying bulk modulus.
- Increased friction/damping.

A real-time controller was added to the dual EHA which has the ability to control the aforementioned fault conditions within a wide range of operating conditions.

Investigation into the internal leakage of both axes of the EHA revealed that the pumps manufactured are inefficient compared to industrial available external gear pumps. It was determined that the machining techniques used cannot achieve the tolerances required to machine highly efficient external gear pumps. It was determined that the leakage in Axis A and B could be estimated using a coefficient. This coefficient was different for both axes.

Investigation into the system friction showed that it behaves in a non-linear fashion for both axes. It was determined that the magnitude of the friction in both directions for both axes can be approximated by using a LuGre model. Experiments were performed to determine the static, coulombic, and viscous friction coefficients for each operating mode, which allowed for a LuGre model to be applied by curve-fitting to measured data. More significantly, it was determined that for the useful operating region of the EHA ($\pm 10V$ or $\pm 0.117m/s$) at no point does the friction increase with the actuator velocity. The resultant damping lies within the Stribeck region. As a result, in a no-load condition, the EHA performance acts in a non-linear fashion.

System identification techniques were applied to the EHA prototype. Investigation showed that the Siemens servomotor behaved in a linear fashion and the combined EHA system exhibited two major piecewise linear regions. The first of these linear regions occurred when the mean velocity was zero. The second piecewise linear region occurred at actuator velocities above approximately $2.27E-2m/s$ ($2V$). System identification also showed that the servomotor is 2nd order while the combined EHA is 4th order, type 1. This occurs when the inner-loop proportional and integral gains are 1 and 0 respectively. When identifying the models for each piece-wise linear region of the combined EHA the 2nd piece-wise linear region where the mean velocity was non-zero yielded a transfer function with a bandwidth that was higher than the bandwidth of the transfer function of the model taken at zero mean velocity. It is clear that this is caused by the higher system damping, the non-linear stick-slip phenomenon and the lack of symmetry between both chambers that occurs when operating close to zero mean velocity.

System identification proved that the EHA is non-linear mainly due to the LuGre damping exhibited in the actuator.

Finally, a digital filter was determined that can be used to feedback several states to a controller. It was shown that to feedback an appropriate signal the order of the filter should be no larger than 2 and the bandwidth should be 350rad/sec. A proportional controller was also implemented that showed an accurate step response can be achieved without the implementation of additional control parameters. It also revealed that the maximum velocity of the actuator can be a concerning saturation effect in future experiments.

8.3 Conclusions

The conclusions from this research showed that dual EHA can function properly with the new inner-circuit shared between each pump and that one axis can function when the other is idle. The research also showed that this custom pump housing exhibits higher leakage than typical industrially available external gear pumps, proving that its performance is extremely sensitive to increased clearances between the gear and its enclosure walls.

It can also be concluded that the combined EHA acts in a non-linear fashion due to the non-linear LuGre friction that exists in the actuator. System identification proved this by yielding two piece-wise linear regions.

It was found also through system identification that the combined model of the EHA prototype is 4th order, type 1. This shows that without tuning the inner-loop PI gains the servomotor is dynamically significant.

8.4 Recommendations for Future Research

Potential areas for future research include:

- Fault condition analysis. This prototype is designed to simulate 4 different types of fault conditions that can be controlled and regulated through the real-time controller.
- Perform experiments to determine the bulk modulus of each axis. This can be performed by parameter estimation using techniques such as the Extended Kalman Filter (EKF) or the Smooth Variable Structure Filter (SVSF).

- Build the full lumped dual EHA design that incorporates the Infranor motors and new dual actuator.
- Investigate issues due to elevated temperature on the EHA, which will affect the damping of the system due to a changing oil viscosity index.
- Apply several high-level control algorithms such as Sliding Mode Control (SMC) to the EHA along with other controllers to determine how accurate the position response can be. Tuning of the inner-loop proportional and integral gains can also increase the accuracy of the position response.
- Apply several control algorithms using potential torque inputs to the servomotor. The Siemens Servodrive can control the servomotor in velocity mode or torque mode. All experiments performed in previous research and this study used velocity inputs to the servomotor. Torque inputs to the EHA could be investigated to see if there is any advantage over velocity inputs.
- Investigate the performance of the EHA when exposed to varying loads. Increased mass and/or increased damping should be added to investigate the effects on the performance of the EHA.
- Perform system identification on the combined EHA with the inner-loop controller for the servomotor tuned to different proportional and integral gains.

The prototype developed is very suitable for fault condition simulations, which makes this the major contribution of this research. The parameters experimentally determined allow for further insight into fault and parameter identification since they can be applied directly to the mathematical model. It also provides an effective training platform for future students who desire to increase their knowledge in control, hydraulics and system identification.

References

- [1] Federal Aviation Administration, *Chapter 4 - Flight Controls*, in Pilot's Encyclopedia of Aeronautical Knowledge, Skyhorse Publishing, New York, NY, pp. 1-4, 2007.
- [2] Maxwell C.J. et al., "Electro-hydraulic actuation of primary flight control surfaces," in IEEE Colloquium on all Electric Aircraft, London U.K, pp. 1-5, 1998.
- [3] McRuer D., Graham D., "A Flight Control Century: Triumphs of the Systems Approach," Journal of Guidance, Control and Dynamics, 27(2), pp. 161-173, 2003.
- [4] Department of Aerospace Engineering. "Chapter 6 – Flight Control Systems," Aircraft Systems Lecture Notes, Polytechnic University of Milan, pp. 1-11.
- [5] Nachtwey P., 2010, "Choosing the Right Valve," [Online], Available: <http://www.hydraulicspneumatics.com/200/Issue/Article/False/13913/Issue>.
- [6] Thayer W.J., 1965, "Transfer Functions for Moog Servovalves," [Online], Available: http://www.servovalve.com/technical/new_tb_103.pdf.
- [7] Habibi S.R., "Lecture on Hydraulic Systems," Control Systems - ME 4R03 Lecture Notes, Department of Mechanical Engineering, McMaster University, pp.3-14, 2006.
- [8] Ludovic A., "Boeing 767 Systems Review," [Online], Available: http://www.smartcockpit.com/data/pdfs/plane/boeing/B767/instructor/B767_Hydraulics.pdf.
- [9] Navarro R., "Performance of an Electro-Hydrostatic Actuator on the F-18 Systems Research Aircraft," NASA Dryden Flight Research Centre, Edwards, CA., TM-97-206224, 1997.
- [10] Jensen S.C., Jenny G.D., and Dawson D., "Flight Test Experience with an Electromechanical Actuator on the F-18 Systems Research Aircraft," NASA Dryden Flight Research Centre, Edwards, CA., 2E, 1993.
- [11] Moog Inc., 2010, "System Integrator for Lockheed Martin F-35," [Online], Available: <http://www.moog.com/markets/aircraft/military-aircraft/fighter-trainer/system-integrator-for-lockheed-martin-f-35/>.
- [12] Habibi S.R., Roach J. and Luecke G., "Inner-Loop Control for Electro-Mechanical (EMA) Flight Actuation Systems," Journal of Dynamic Systems, Measurement and Control, 130, pp. 1-13, 2008.
- [13] Botten S.L., Whitley C.R. and King A.D., "Flight Control Actuation Technology for Next-Generation All-Electric Aircraft," Technology Review Journal – Millennium Issue, pp. 55-68, 2000.
- [14] Eaton Hydraulic Training Services, *Industrial Hydraulics Manual*, Eaton Hydraulics Training, Eden Prairie, MN, 2006.

- [15] Manring N.D. and Luecke G.R., "Modeling & Designing a Hydrostatic Transmission with a Fixed-Displacement Motor," *Journal of Dynamic Systems, Measurement and Control*, 120, pp. 45-50, 1998.
- [16] Habibi S.R. and Goldenberg A.A., "Design of a New High Performance ElectroHydraulic Actuator," *IEEE/ASME Transactions on Mechatronics*, 5 (2), pp. 158-164, 2000.
- [17] Habibi S.R. and Singh G., "Derivation of Design Requirements for Optimization of a High Performance Hydrostatic Actuation Systems," *International Journal of Fluid Power*, 1(2), pp. 11-29, 2000.
- [18] Habibi S.R., Burton R., and Sampson E., "High Precision Hydrostatic Actuation Systems for Micro and Nano Manipulation of Heavy Loads," *Journal of Dynamic Systems, Measurement and Control*, 128, pp. 778-787, 2006.
- [19] Watton, J., *Fluid Power Systems*, Prentice-Hall, Englewood Cliffs, NJ, 1989.
- [20] Fox R.W., McDonald A.T., and Pritchard P.J., *Introduction to Fluid Mechanics*, John Wiley and Sons, Inc., Hoboken, NJ, p. 338, 2004.
- [21] Merritt, H. E., *Hydraulic Control Systems*, Wiley, New York, 1967.
- [22] Chinniah, Y., "Fault Detection in the EHA using the EKF," Ph.D. thesis, University of Saskatchewan, 2004.
- [23] Control Systems Division – Military, "Electrohydrostatic Actuation Systems," Parker Aerospace, Parker Hannifin Corporation, Irvine, CA, 2006.
- [24] A.K. Steel Corporation, 2007, "Product Data Sheet: 15-5PH Steel," [Online], Available: http://www.aksteel.com/pdf/markets_products/stainless/precipitation/15-5_PH_Data_Sheet.pdf.
- [25] The Infranor Group, 2010, "AC Servomotor HDD/ICM-Series," [Online], Available: <http://ch.infranor.com/dynasite.cfm?dsmid=83414&pid=112&ppid=112>.
- [26] Hawe Hydraulic, 2009, "Check Valves Type RK/RB, RC, RE, and ER," [Online], Available: http://www.hawe.de/download/catalog/en/K_RK.pdf.
- [27] Hawe Hydraulic, 2009, "Hydraulic Miniature Accumulators Type AC," [Online], Available: http://www.hawe.de/download/catalog/en/K_AC.pdf.
- [28] Hydraforce Inc., 2010, "Hydraforce Product Guide," [Online], Available: http://www.hydraforce.com/pdf/HF_PG_10_Web.pdf.
- [29] Siemens Automation Inc., 2006, "Configuration Manual 12/2006 Edition," [Online], Available: http://www.automation.siemens.com/doconweb/pdf/SINAMICS_1008_E/PFK7S.pdf?p=1.

- [30] R+W America, 2008, "Model BK2: Backlash-Free, Torsionally Stiff Metal Bellows Coupling," [Online], Available: http://www.rw-america.com/bellows_couplings/bellow-coupling-bk2-t.php.
- [31] ANSYS Inc., 2007, "Programmer's Manual for ANSYS," [Online], Available: www1.ansys.com/customer/content/.../110/ansys/aprog110.pdf.
- [32] Hong X. et al., "Research of Internal Leakage Theory Model in Exterior Meshing Gear Pump," in *International Conference on Intelligent Human-Machine Systems and Cybernetics*, Nanjing, China, 2009, pp.331-334.
- [33] Armstrong-Hélouvry, B., Dupont P. and Canudas de Wit, C., "A Survey of Models, Analysis Tools, and Compensation Methods for Control of Machines with Friction," *Automatica*, 30(7), pp.1083-1138, 1994.
- [34] Burenin V.V., "Computing the Damping Coefficients of Hydraulic Cylinders," [In Russian], Khimicheskoe i Neftyanoe Mashinostroenie, 7, pp.12-13, 1985.
- [35] C. Canudas de Wit, H. Olsson, K. J. Astrom and P. Lischinsky (March 2005). "A new model for control of systems with friction," *IEEE Transactions on Automatic Control*, 40(3), pp. 419-421, 1995.
- [36] Yanada H., Sekikawa Y., "Modeling the Dynamic Behaviors of Friction," *Journal of Mechatronics*, 18, pp. 330-339, 2008.
- [37] Akers A., Gassman M., Smith R.J., "Hydraulic Power System Analysis," CRC/Taylor & Francis, Boca Raton, FL, 2007.
- [38] Watton J., *Modeling, Monitoring and Diagnostic Techniques for Fluid Power Systems*, Springer, New York, 2007.
- [39] Akkaya A.V., "Effect of Bulk Modulus on Performance of a Hydrostatic Control System," *Sadhana - Academy Proceedings in Engineering Sciences*, 31(5), pp. 543-556, 2006.
- [40] Ljung L., *System Identification: Theory for the User*, Prentice Hall, Upper Saddle River, NJ, 1999.
- [41] Shih-Ho W., T.F. Lee and R. Zachery, "System Identification via Singular Value Decomposition," *IEEE International Conference on Acoustics, Speech, and Signal Processing*, (5), pp.2638-2641, 1996.
- [42] Oppenheim A.V., Schaffer R.W., Buck J.R., *Discrete-Time Signal Processing*, Prentice-Hall, Upper Saddle River, NJ, 1999.
- [43] Fagor Automation Inc., 2008, "Fagor Linear and Rotary Encoders," [Online], Available: http://www.fagor-automation.com/Products/Brochures/General_Feedback.pdf.
- [44] Centikunt S., *Mechatronics*, John Wiley and Sons, Inc., Hoboken, NJ, 2007.
- [45] Nise N.N., *Control Systems Engineering*, John Wiley and Sons, Inc., Hoboken, NJ, 2004.

Appendix A – Description of Electrical Components and Full Electrical Diagram of the Siemens Servodrive

A.1 Sensors Used for System Analysis

This section will describe the sensors used for the experimentation performed in this research. These sensors include a differential pressure sensor, an absolute pressure sensor, a rotary encoder and a linear encoder.

A.1.1 Differential Pressure Transducer

A differential pressure transducer is employed to measure the difference in cross-port pressure between both sides of the actuator. The method of attachment of the transducer to the actuator can be seen in figure A.1. Quick connect couplings are employed to allow the transducer to be easily switched from one actuator to the other.

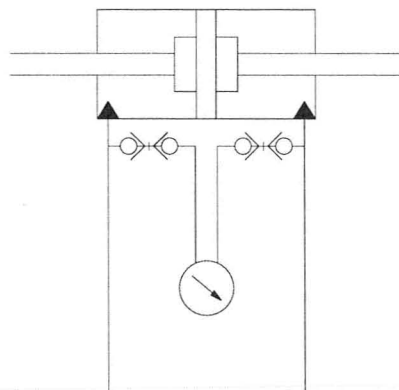


Figure A.1. Differential pressure transducer attached to the actuator.

The type of differential pressure transducer employed is a diaphragm type, manufactured by Omegadyne Inc. As the pressure increases the diaphragm is slightly displaced. This displacement corresponds to a proportional electrical output, which is relayed to a data acquisition card. A depiction of the pressure transducer can be seen in figure A.2.

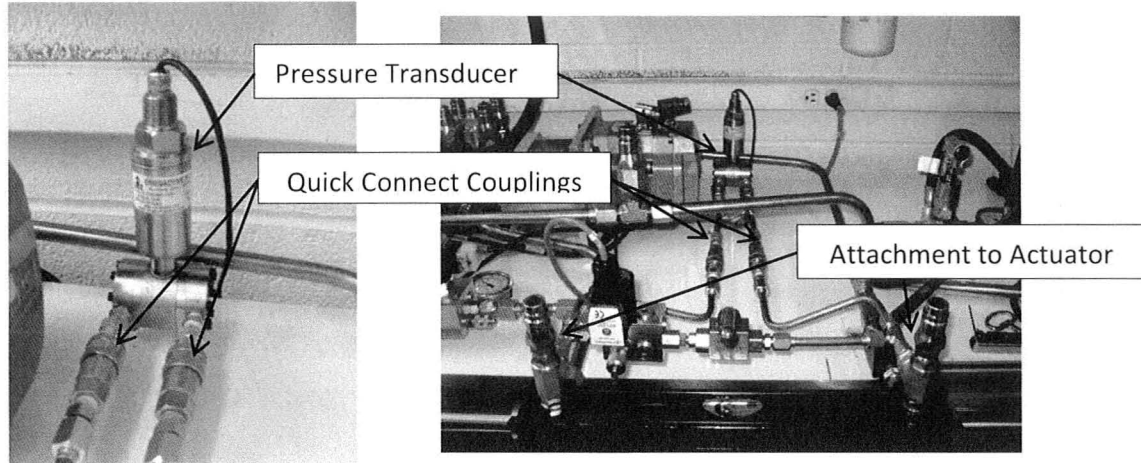


Figure A.2. Omegadyne PX80B0-1KDI differential pressure transducer.

Its specifications are as follows:

- Measurable pressure range: 0-6.895MPa (0-1000psi)
- Allowable line pressure: 10.34Mpa (1500psi)
- Burst Pressure: 41.36MPa (6000psi)
- Output: 4-20mA

The PCI-6229 data acquisition card accepts 0-10V analog inputs so the current output must be switched to voltage. This was performed by placing a 499Ω resistor between the input channel and the ground. The relationship between input amperage to voltage is provided by equations A.1 and A.2:

$$V_{low} = I_{low}R \quad (A.1)$$

$$V_{low} = 4.0E - 3 * 499 = 1.996V$$

$$V_{high} = I_{high}R \quad (A.2)$$

$$V_{high} = 20.0E - 3 * 499 = 9.980V$$

Where V_{low} is the lowest voltage attainable (V), V_{high} is the highest voltage attainable, I_{low} is the lowest current available from the sensor (A), I_{high} is the highest current available from the sensor (A),

and R is the impedance of the resistor connecting the input channel to ground (Ω). Since the voltage is proportional to the pressure a relationship between the two can be found.

$$Sensitivity = \frac{6.895E + 6Pa - 0Pa}{9.980V - 1.996V} = 8.636E + 05 \text{ Pa/V} \quad (\text{A.3})$$

At 0 Pa of differential pressure the voltage output is 1.996V meaning the linear curve relating voltage to pressure must be shifted. The final relationship between voltage and corresponding pressure is shown in equation A.4:

$$P_{diff} = 8.636E + 05V - 1.724E + 06 \quad (\text{A.4})$$

Where P_{diff} is the pressure differential of the sensor (Pa).

A.1.2 Linear Incremental Optical Encoder

A high precision optical encoder is used to measure the positional output of the actuator. The form of encoder is a linear incremental differential quadrature type. The encoder manufacturer is Fagor Automation and has the model code MX-35-5. The encoder measures displacement by emitting pulses that occur once there is a small movement of the reader head [43]. The reader head consists of an infrared light, a grid and a photo-diode receptor. In between the light and the grid is a graduated glass scale with engraved chrome lines with a specific pitch. The reader head, which is attached to the actuator, moves along the glass scale. As this occurs, there is relative movement between the glass and the grid. This movement changes the intensity of the infrared light in a sine wave fashion, which is converted into electrical signals by the receptor. The electrical signals are in the form of a pulse, which are counted by the PCI-QUAD04 data acquisition card. Each count corresponds to a distance travelled by the actuator.

The quadrature function of the encoder means that there are two channels that accept pulses from the encoder, where each channel has its own graduated track. Each track has scales with an equal pitch but are referenced 90° out of phase. These tracks are usually termed A and B. This allows the counter to be able to track the direction of motion as well as the displacement. This also increases the resolution of the encoder by a factor of 4. In addition to tracks A and B there is a track that holds a chrome line which is referred to as an index, or I. There are several indexes on the encoder scale that are equally spaced apart. This is typically used to find the absolute position of the encoder by a home

motion sequence if needed [44]. This is not employed in this research. This concept can be seen in figure A.3.

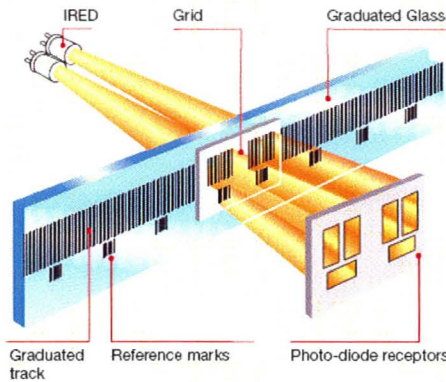


Figure A.3. Principle components of a linear encoder [43].

The differential function of the encoder indicates that there are complementary channels to A, B and I that act to minimize noise. These channels are termed \bar{A} , \bar{B} and \bar{I} . These channels emit a pulse at the same phase as their complement but at an opposite voltage. As the signals travel though their respective wires they pick-up the same amount of noise. When the signals reach the data acquisition card they are subtracted from one another then divided by two. This in effect cancels the noise added to the resultant signal.

The performance characteristics of the MX-35-5 linear encoder are as follows:

- Accuracy: $\pm 5\mu\text{m}$
- Resolution: $1\mu\text{m}$
- Maximum speed: 1m/s
- Moving force: $\leq 2\text{N}$
- Range of measurement: 0.35m

A depiction of the linear encoder can be seen in figure A.4. Note that to attach the encoder to the actuator shaft there is a linear rail that acts as a buffer. As the rod in a cylinder oscillates it tends to rotate if the piston/rod assembly has any axial misalignment. The linear rail eliminates this degree of freedom without adding any stress to the reader head of the encoder.

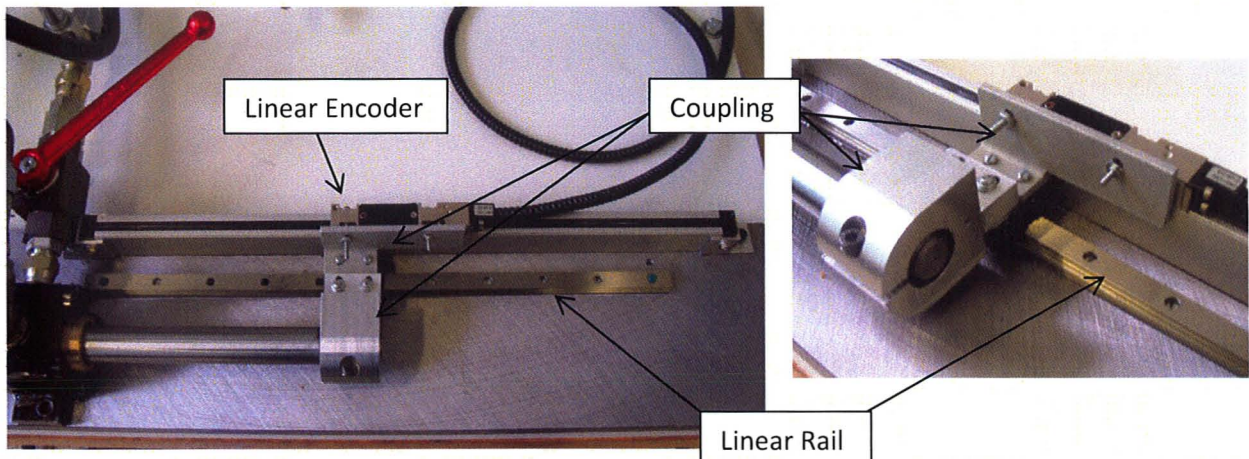


Figure A.4. Fagor MX-35-5 encoder with linear rail and actuator shaft coupling.

A.1.3 Rotary Incremental Optical Encoder

A high precision rotary optical encoder is employed in each servomotor to feedback velocity in the inner-loop. Rotary encoders work on the same principle as linear encoders. The main difference is that the graduated glass scale is circular and is attached to the shaft of the motor, meaning that it moves opposed to the reader head [44]. The encoder used for this analysis is built in with the Siemens servomotor and is of the rotary incremental differential quadrature type. The performance characteristics of this encoder are as follows:

- Resolution: 16384lines/rev (14 bits)
- Maximum Speed: 628.3rad/s (6000 rpm)

It must be noted that an encoder is a position measuring device and the state required for the feedback loop is velocity. Velocity must be extracted from the position of the encoder.

A.2 Noise Characteristics of the Transducers

Noise characteristics are apparent in both the analog differential pressure transducer and the encoders used for position feedback. This section presents an investigation of the noise in these components.

A.2.1 Noise Characteristics of the Rotary Encoder

As previously discussed it is imperative to take the derivative of the encoder position signal to extract the velocity. The main issue with this is taking the derivative of a discrete signal introduces noise into the output. To characterize this noise a step input of 3V (94.24rad/sec) was given to the motor. The derivative was then taken to extract velocity. A power spectral density analysis was then performed on

the unfiltered velocity to determine if there are any peaks which could deteriorate the output. The steady state step output can be seen in figure A.5 and its power spectral density can be seen in figure A.6. Note that the sampling time was 0.001sec. Figure A.6 shows the spectral analysis up to the Nyquist Frequency.

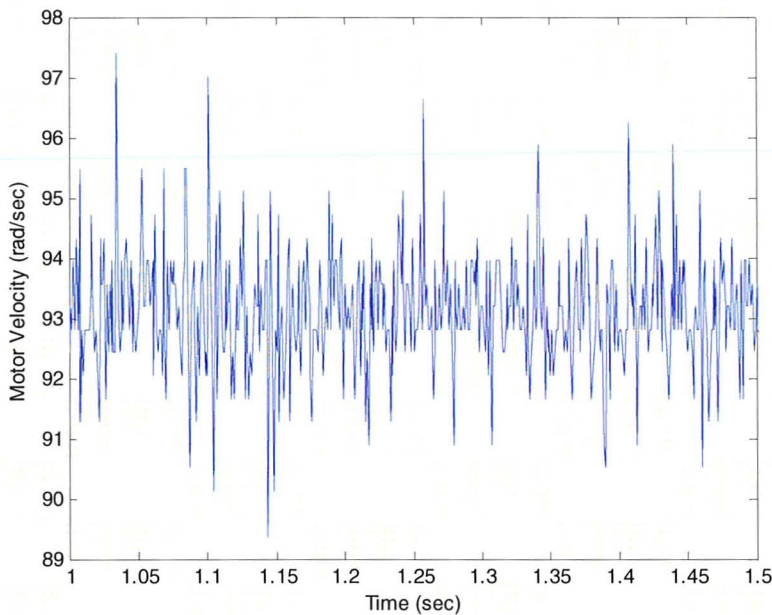


Figure A.5. Rotary encoder velocity signal using 3V (94.24rad/sec) step input.

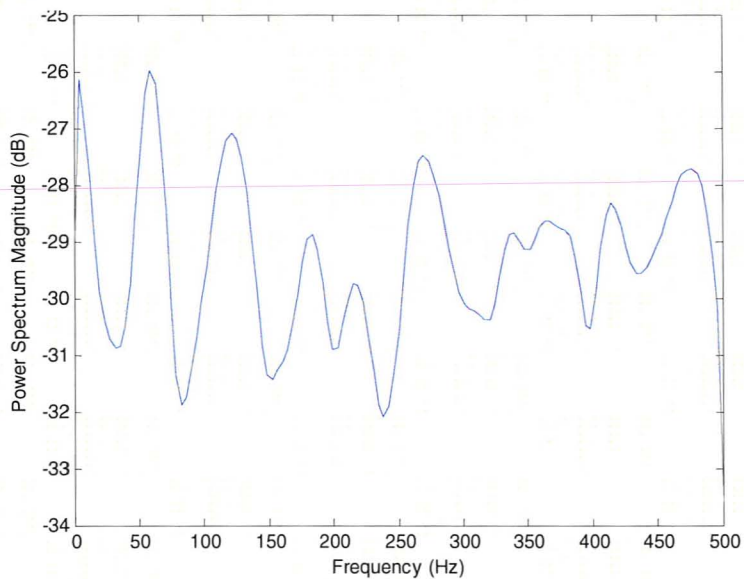


Figure A.6. Power spectral density of the rotary encoder velocity signal.

Figure A.6 shows that there are no peaks in the rotary encoder velocity signal that are of any concern.

A.2.2 Noise Characteristics of the Linear Encoder

Using the same input signal and sampling time in determining the noise characteristics of the rotary encoder the power spectral density for the derivative of the linear encoder signal was determined. As seen in chapter 5 the velocity of the linear encoder is extracted for system identification purposes. The steady state output of the actuator can be seen in figure A.7 while its power spectral density can be seen in figure A.8.

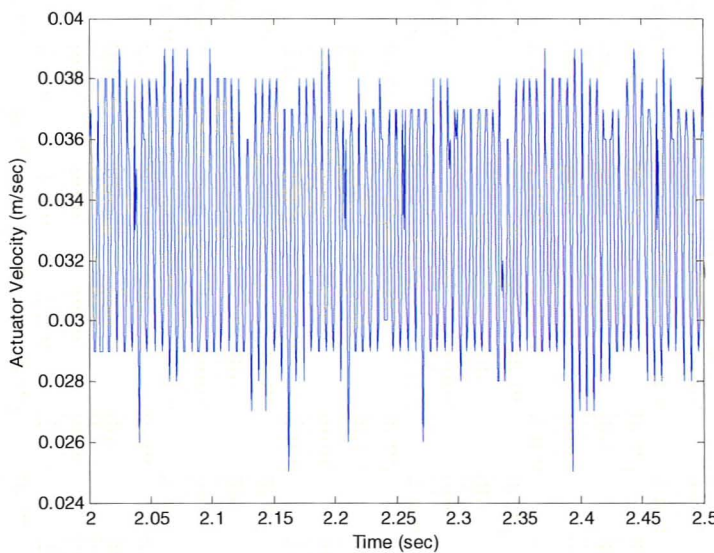


Figure A.7. Linear Encoder velocity signal using 3V (3.41E-2m/s) step input.

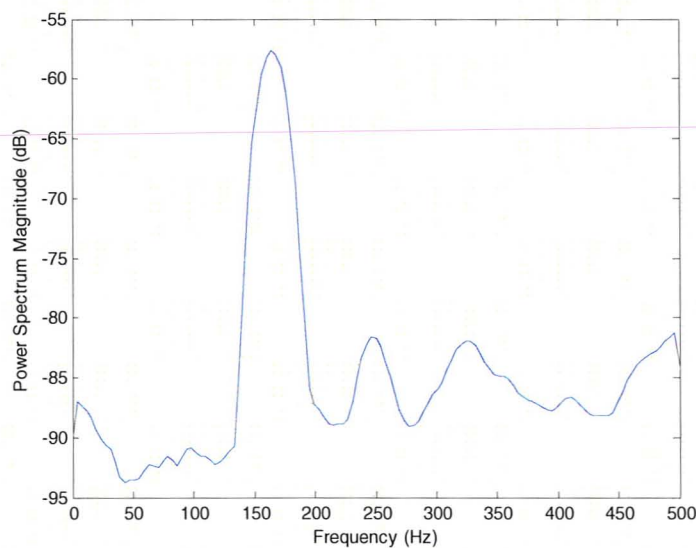


Figure A.8. Power spectral density of the linear encoder velocity signal.

Figure A.8 shows there is a large peak at around 165Hz. This is a concern if the peak is close to the system bandwidth.

A.2.3 Differential Pressure Noise Characteristics

The differential pressure transducer provides an analog output, meaning there will be some noise in its response. Figure A.9 shows a plot of the measurement noise in volts when there is no motion in the actuator. The power spectral density of the noise is shown in figure A.10. The noise was sampled at a frequency of 1000Hz.

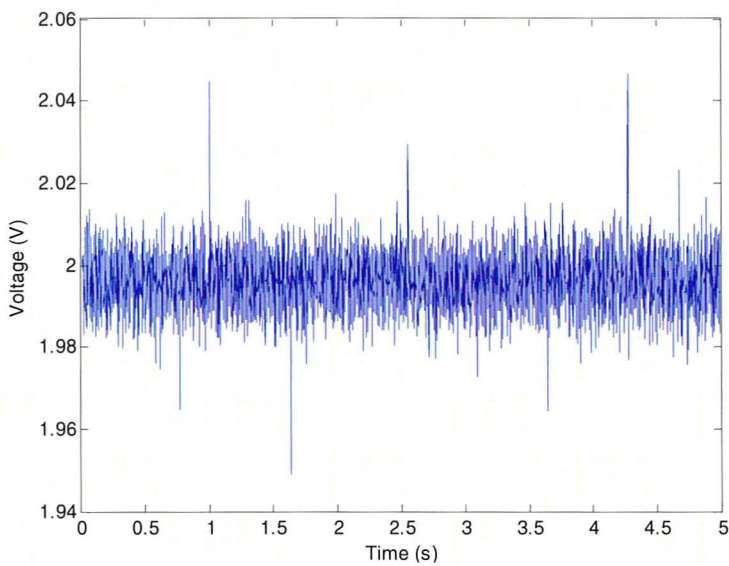


Figure A.9. Measurement noise in the differential pressure transducer.

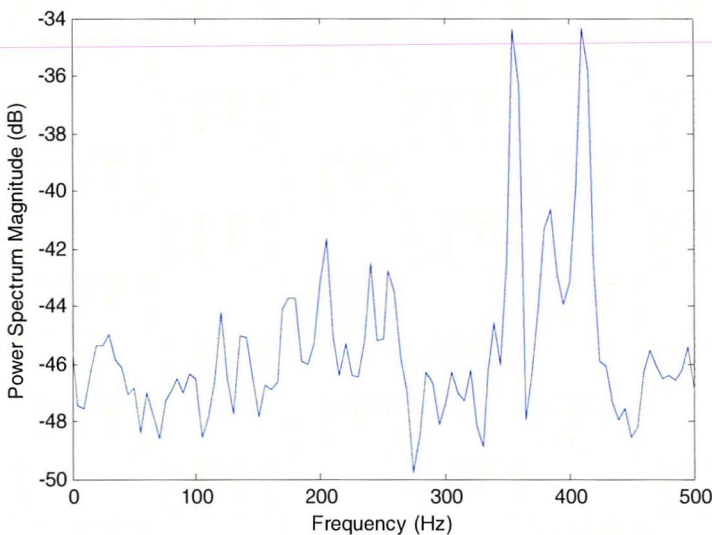


Figure A.10. Power spectral density of the measurement noise in the differential pressure transducer.

Figure A.10 shows that there are two dominant peaks at 355Hz and 410Hz. It is unclear what the source of this noise is but is located at such a high frequency that it will not affect results within the frequency range of interest. In the frequency range of interest (0-150Hz) the noise is considered as white.

A.3 Data Acquisition Cards (DAQ)

A.3.1 National Instruments PCI-6229 Multifunction DAQ

The primary data acquisition card used for this system is the National Instruments PCI-6229 multifunctional DAQ. This card contains some of the following features:

- 4 analog outputs, 16 bit resolution ($\pm 10V$)
- 32 single ended analog inputs or 16 differential, 16 bit resolution ($\pm 10V$)
- 48 programmable digital inputs or outputs (TTL, $\pm 5V$)

A depiction of this card can be seen in figure A.11.

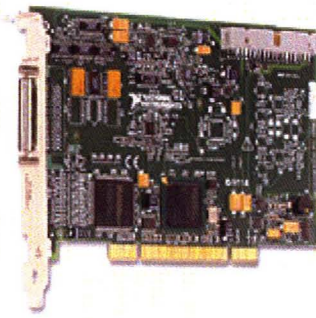


Figure A.11. National Instruments PCI-6229 multi-function data acquisition card.

This card provides the primary control signal for the EHA servomotors (analog outputs). It uses the analog inputs for feedback from all pressure sensors and digital outputs to control all relays and solenoids. Please refer to the manufacturer's manual for greater details.

A.3.2 Measurement Computing PCI-QUAD04 Encoder DAQ

As previously discussed the encoders used for this research are a differential quadrature type. The PCI-6229 has the ability to accept single-ended quadrature signals but not differential. It also does not incorporate anti-dithering circuitry. Dithering can cause consecutive pulses to emanate from a single channel (i.e. A or B) when the encoder head is vibrating at a high frequency. This yields a false count. The PCI-QUAD04 includes a differential quadrature function as well as anti-dithering circuitry. Using the PCI-6229 DAQ card was attempted but it was noticed that there were issues with dithering, especially

with the linear encoder. Because of this the PCI-QUAD04 DAQ card has been employed. Figure A.12 shows a depiction of this DAQ card.

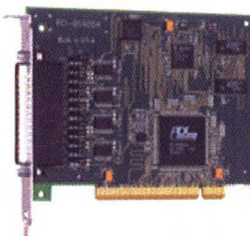


Figure A.12. Measurement Computing PCI-QUAD04 encoder data acquisition card.

A.3.3 Siemens PCI-Profibus Interface Card

The Siemens Servodrive essentially receives the analog output from the PCI-6229 DAQ card, amplifies it and converts it into a pulse-width modulated signal. To parameterize the Servodrive to change variables such as the inner-loop PI controller, the maximum rms torque allowed, initializing digital inputs/outputs, etc., there must be a communication protocol between the PC and the Servodrive. The communication protocol is Profibus. This is a digital protocol that is commonly used in automation technology. The benefit of this protocol is that several drives in parallel can be communicated with via a single communication line. The program used to parameterize the Servodrive is SimComU. A depiction of the PCI interface card that links the Servodrives via profibus is seen in figure A.13.

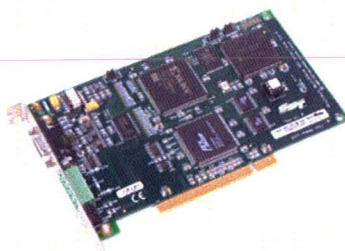


Figure A.13. Siemens PCI-Profibus Interface Card.

A.4 EHA Electrical Circuit Diagram

Figure A.14 shows a complete electrical diagram for the EHA

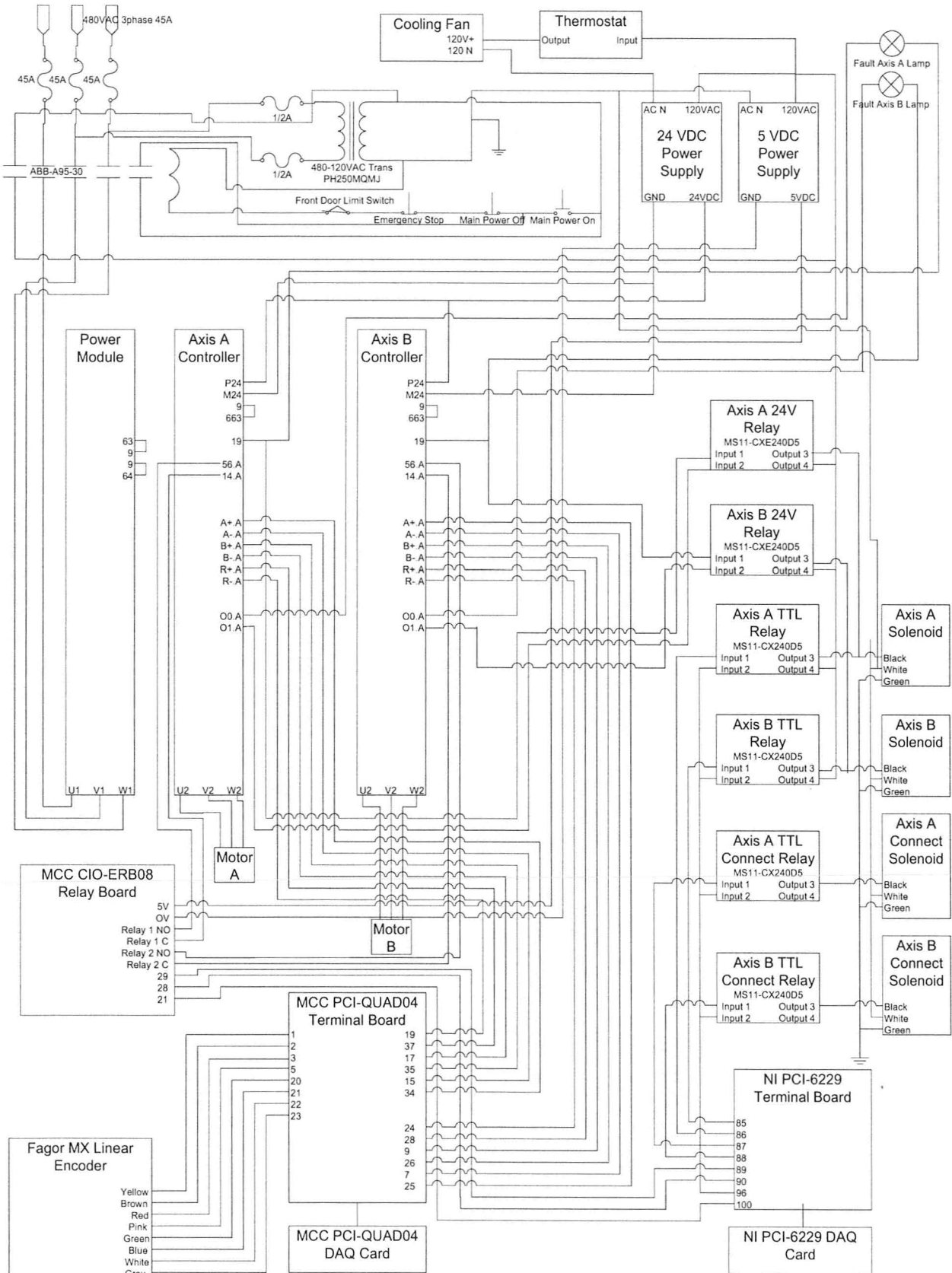


Figure A.14. EHA electrical diagram.

Appendix B – Additional Friction and Internal Leakage Data

Figures B.1 though B.3 show the static friction plots with respect to actuator velocity for the Axis A reverse, Axis B forward and Axis B reverse modes respectively.

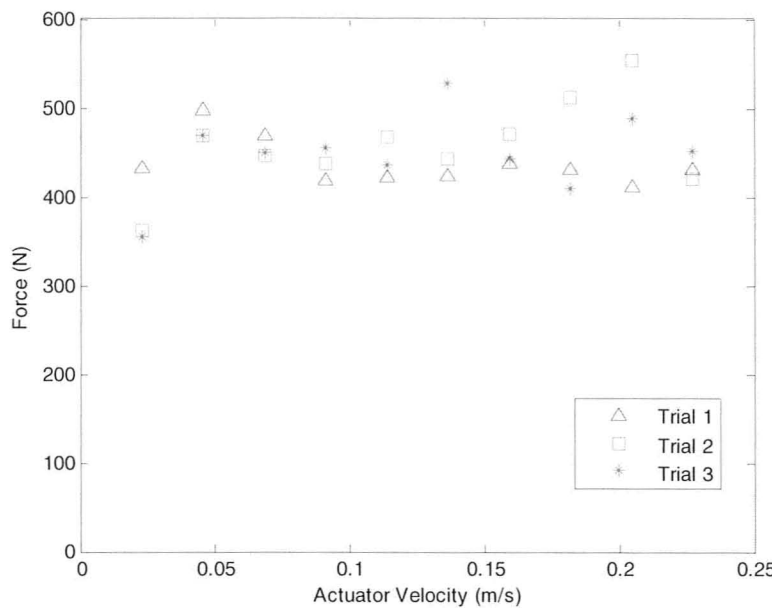


Figure B.1. Static friction vs. velocity for Axis A reverse operating mode.

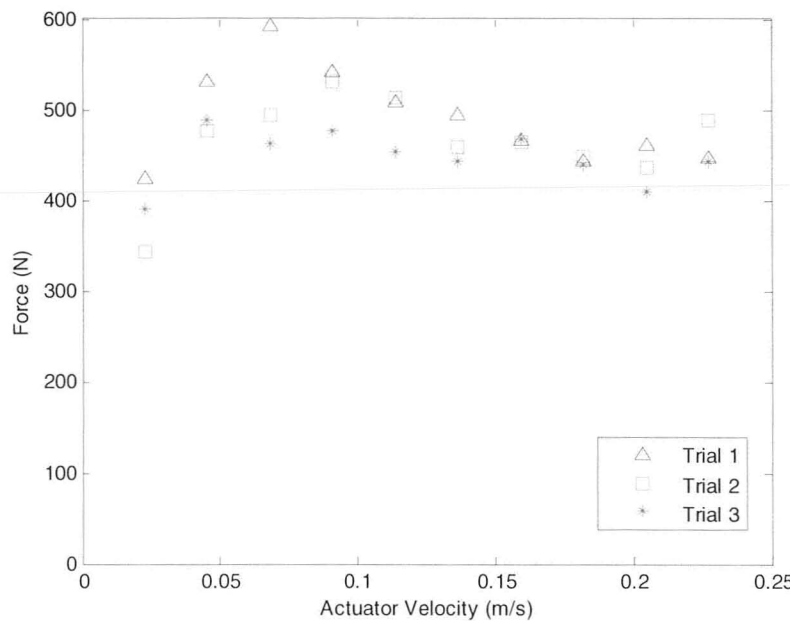


Figure B.2. Static friction vs. velocity for Axis B forward operating mode.

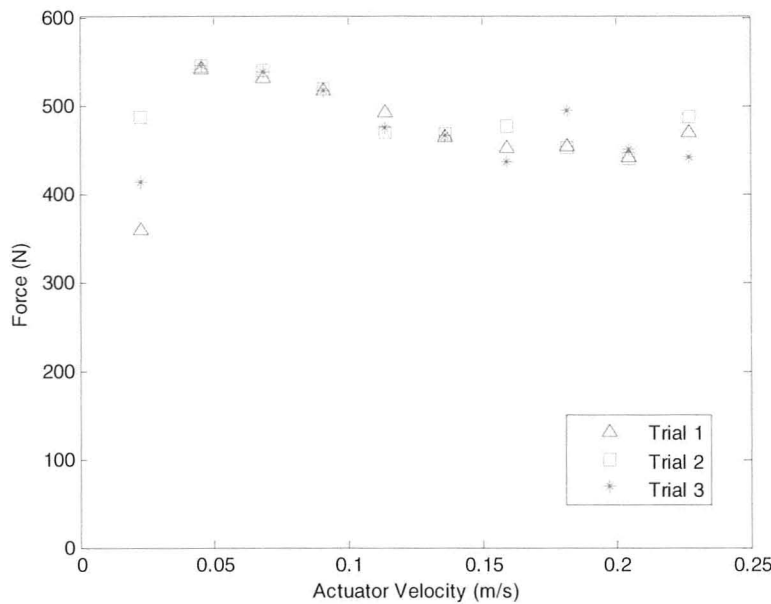


Figure B.3. Static friction vs. velocity for Axis B reverse operating mode.

Figures B.4 and B.5 show the LuGre friction versus actuator velocity for both the forward and reverse operating mode in actuator B.

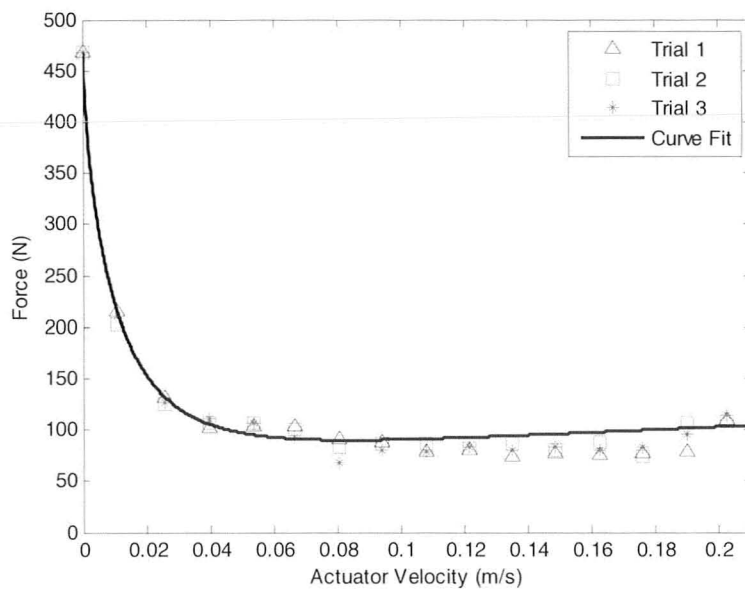


Figure B.4. Actuator friction force vs. velocity for Axis B forward operating mode.

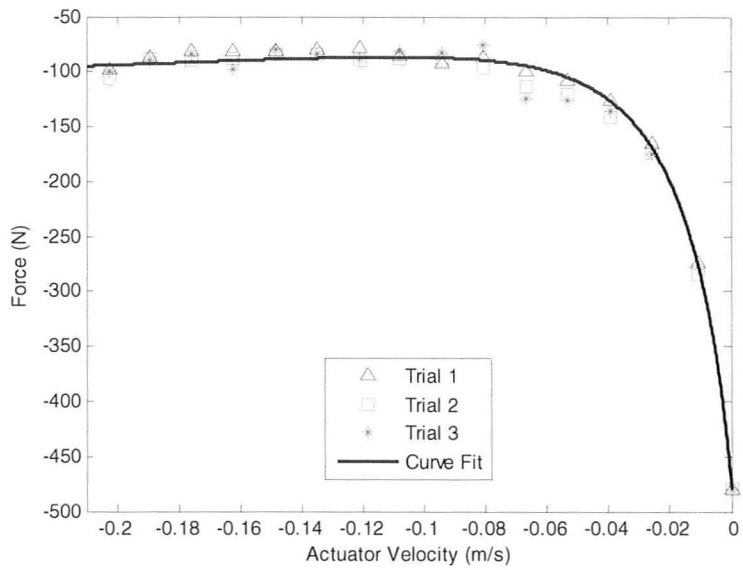


Figure B.5. Actuator friction vs. velocity for Axis B reverse operating mode.

Figures B.6 through B.8 show the volumetric flow versus the resistance pressure, the leakage flow versus the resistance pressure and the volumetric efficiency versus resistance pressure for Axis B respectively.

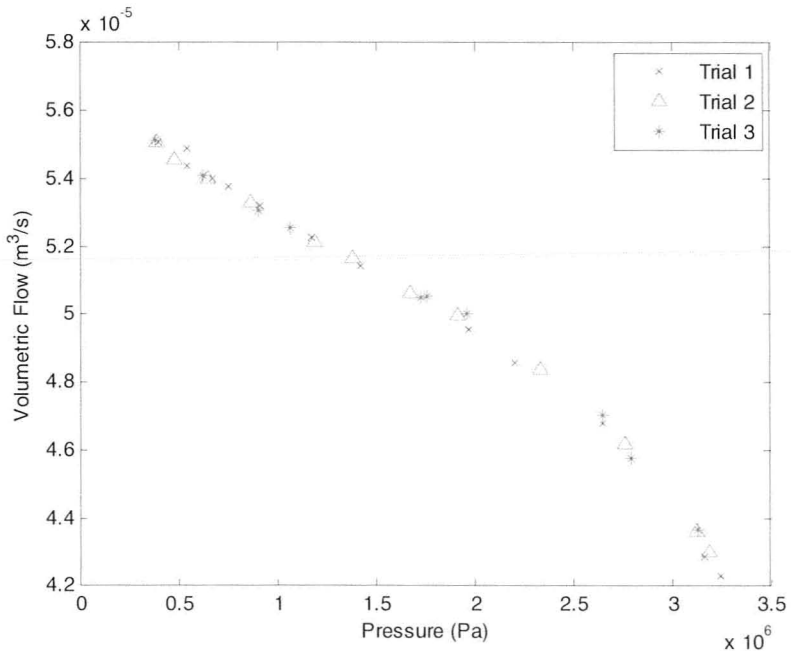


Figure B.6. Volumetric flow vs. pressure for axis B.

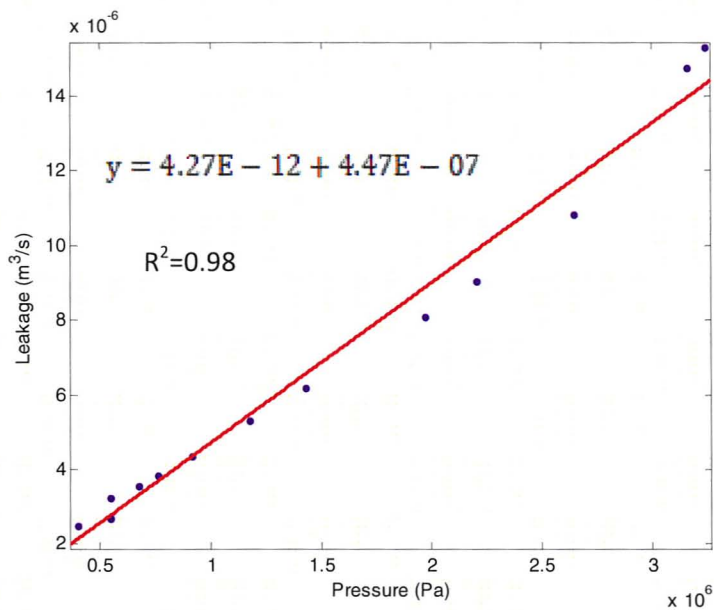


Figure B.7. Leakage flow vs. pressure for axis B.

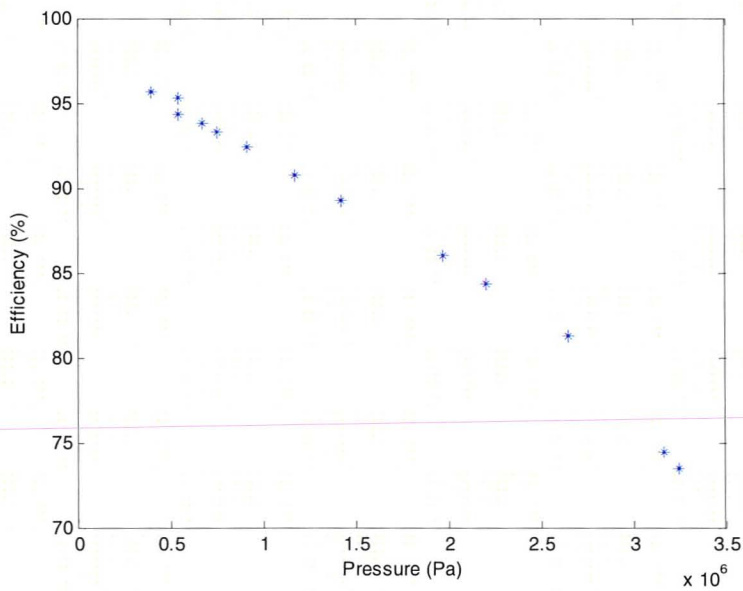


Figure B.8. Volumetric Efficiency vs. pressure for axis B.